DISS. ETH NO. 24099

THE EFFECTS OF EXPLOSIONS ON SNOW

A thesis submitted to attain the degree of

DOCTOR OF SCIENCES of ETH Zurich

(Dr. sc. ETH Zurich)

presented by

STEPHAN SIMIONI

MSc ETH Civil Eng, ETH Zurich

born on 10 February 1984

citizen of Winterthur ZH

accepted on the recommendation of

Prof. Dr. Jürg Dual
Dr. Jürg Schweizer

2017

Contents

Zusammenfassung

In den allermeisten Gebirgsregionen mit ganzjähriger oder saisonaler Schneedecke stellen Lawinen eine grosse Gefahr dar. Grosse Lawinen, welche während oder direkt nach Grossschneefällen spontan abgleiten, können Infrastruktureinrichtungen wie Eisenbahn, Strassen oder Siedlungen gefährden. In Skigebieten können spontane oder durch Skifahrer ausgelöste Lawinen darunter liegende geöffnete Pisten erreichen. Diese Risiken konnten durch die künstliche Lawinenauslösung drastisch reduziert werden, indem Lawinen präventiv während Zeiten von geringer wirtschaftlicher Bedeutung durch Explosionen ausgelöst werden. Die durch die Explosion erzeugte Zusatzlast auf die Schneedecke, kann zum Bruch innerhalb der Schneedecke und folglich zu einer Lawine führen. Traditionellerweise wurden die Sprengladungen von Hand oder aus dem Helikopter in potentielle Anrissgebiete geworfen. Nicht zuletzt der Lawinenwinter 1999 in der Schweiz zeigte das grosse Potential der künstlichen Lawinenauslösung und führte zur Weiterentwicklung dieser Methode mit der Einführung fixer Sprenginstallationen. Mit diesen Systemen können Lawinen dann ausgelöst werden, wenn die Auslösewahrscheinlichkeit am höchsten ist: während oder kurz nach Grossschneefällen. Herkömmliche Methoden hingegen können in diesen Situationen kaum oder nur sehr spät eingesetzt werden. Die fixen Sprenginstallationen werden im Anrissgebiet aufgestellt. Eine Explosion erfolgt durch Zünden von Sprengstoff oder einer Gasmischung. Die Systeme sind typischerweise an einen festen Standort gebunden und es können nur einzelne oder wenige Sprengpunkte mit einem System bedient werden. Deshalb muss der Ort und die Wirkung des Systems sorgfältig analysiert werden. Bis jetzt ist aber die Wirkung verschiedener Explosionen auf die Schneedecke nicht genügend erforscht.

Das Ziel dieser Arbeit ist es, die Prozesse bei der künstlichen Lawinenauslösung über und in der Schneedecke besser zu verstehen. Grossmassstäbliche Versuche wurden mit normalen Sprengladungen (spherical/solid explosives) und einem mobilen Gaszündrohr (directed gas explosion) durchgeführt und die Luftdrücke über der Schneedecke und die Beschleunigungen in der Schneedecke auf einem flachen Versuchsgelände gemessen. Zusätzlich haben wir Versuche an operationellen Lawinenauslösesystemen durchgeführt und auch die Bodenerschütterung gemessen. Um die Prozesse in der Schneedecke besser zu verstehen, haben wir in kleinmassstäbliche Versuchen sowohl die Beschleunigungen als auch die Ankunftszeit der Wellen gemessen. Wir haben daraus die elastischen Eigenschaften und Bruchausbreitungsgeschwindigkeiten bestimmt, welche für die

Auslösung von Schneebrettlawinen massgebend sind. Schliesslich haben wir die Messungen mit einem komplexen Modell verglichen, welches die Wellenausbreitung im Schnee modelliert.

Die Resultate der grossmassstäblichen Versuche zeigten, dass der Luftdruck und die davon abgeleiteten Parameter mit der Distanz vom Sprengpunkt stark abnahmen. Die Beschleunigungen in der Schneedecke und die daraus abgeleiteten Grössen nahmen mit der Distanz vom Sprengpunkt und der Tiefe in der Schneedecke stark ab. Die Beschleunigungen in einer gewissen Tiefe in der Schneedecke nahmen mit der Distanz ähnlich stark ab wie der Luftdruck über der Schneedecke. Die gerichtete Gasexplosion erzeugte eine ähnliche Wirkung innerhalb eines Sektors von ca. 70° um die Zündrohrachse. In einem Winkel von 90° zur Zündrohrachse waren die absoluten Luftdruckwerte nahe des Sprengpunktes tiefer als in der Achse, nahmen aber weniger stark ab. Dies führte zu Linien gleichen Druckes, welche nahe an der Sprengung eine elliptische Form und weit weg eine Kreisform hatten. Letzteres wird auch bei herkömmlichen Sprengladungen erwartet.

Wir beobachteten zwei verschiedene Arten des Bruches in der Schwachschicht in der Schneedecke, welche durch unterschiedliche Prozesse ausgelöst wurden: Die Brüche an einem Beobachtungsort wurden entweder durch die Bruchausbreitung oder durch die direkte Einwirkung der Sprengung über der Schneedecke verursacht. Die Experimente an einem operationellen Gaszündrohr zeigten, dass die Resultate der Versuche im Flachfeld gut mit denjenigen am operationellen System übereinstimmten. Flachfeldversuche sind demnach gut geeignet, um verschiedene Explosionsarten zu vergleichen. Die durch das operationelle System erzeugten Bodenbeschleunigungen waren klein im Vergleich zu den in der Schneedecke gemessenen Beschleunigungen. Die Wellenausbreitungsgeschwindigkeiten und die tiefen Amplituden lassen darauf schliessen, dass die Wellen hauptsächlich durch die Luft und anschliessend durch die Schneedecke auf den Boden übertragen wurden. Die Ausbreitung über das Fundament des Gaszündrohrs war demnach nicht massgebend.

Die Resultate der kleinmassstäblichen Versuche zeigen ähnliche Werte wie frühere Laborexperimente. Die Dämpfung war nicht abhängig von der Schneedichte im beobachteten Dichtebereich. Aufgrund der ausgeprägten Schichtung der Schneedecke und den daraus folgenden Änderungen der Eigenschaften benachbarter Schichten ergab sich eine grosse Streuung in den Resultaten. Da mit dem Hammerschlag keine perfekt ebenen Wellen erzeugt wurden, wurden vertikale und horizontale Dämpfungskomponenten gemessen. Die starke Schichtung ist wahrscheinlich ein weiterer Grund für die starke Dämpfung von Wellen im Schnee. Im Schnee breiten sich zwei Kompressionswellen, die eine durch das Eisgerüst und die andere durch den Porenraum, und eine Scherwelle durch das Eisgerüst aus. Die gemessene Dämpfung entsprach der Dämpfung der zweiten Kompressionswelle im Porenraum. Die gemessenen Geschwindigkeiten entsprachen der Kompressionswelle durch das Eisgerüst. Aufgrund der kurzen Distanzen zwischen den Messpunkten,

welche aufgrund der starken Dämpfung gewählt werden mussten, konnten die verschiedenen Wellentypen nicht unterschieden werden. Unsere Messausrüstung erlaubte es zum ersten Mal, die Bruchausbreitung in Stabilitätsversuchen direkt in der Schneedecke zu messen. Die Resultate lassen vermuten, dass verschiedene Wellen bei der Bruchausbreitung beobachtet werden: Die erste Welle, welche der tatsächlichen Bruchausbreitung entspricht und die zweite Welle, welche durch die Setzung des Schneebretts nach dem Bruch der Schwachschicht entspricht (Kollapswelle).

Die Daten der Feldexperimente wurden zudem für ein Modell verwendet, welches Schnee als poröses Material darstellt. Erste Resultate lassen darauf schliessen, dass die Modellierung der Wellenausbreitung in einem porösen Medium die vielversprechendste Methode ist. Das Modell überschätzte allerdings die Beschleunigungen in der Schneedecke, wahrscheinlich als Folge von Vereinfachungen in der Geometrie, welche zu einer zu geringen Dämpfung im Modell führte.

Diese vorliegende Arbeit hat zu einem besseren Verständnis der Wellenausbreitung in Schnee beigetragen. Wir haben die Unterschiede und Gemeinsamkeiten zwischen einer normalen Sprengladung und einer Explosion mit Gas aufgezeigt. Beide Arten der Explosion haben eine ähnliche Wirkung. Ein umfangreicher Datensatz zur Wirkung von Explosionen auf Schnee liegt nun vor. In einem weiteren Schritt sollten die Daten aus den Feldversuchen für die Verbesserung der Modellierung der Wellenausbreitung in und über dem Schnee verwendet werden.

Summary

Snow avalanches are a major hazard in mountainous regions with seasonal or perennial snowpacks. Large spontaneous avalanches during or after storms may reach and destroy vital infrastructures such as railway lines, roads or settlements. Ski areas are threatened by spontaneous or skier-triggered avalanches. Artificial triggering of avalanches by explosions has decreased these risks significantly. Avalanches can preventively be triggered during times of minor economic loss. The explosions create a surcharge on the snowpack that may lead to failure and consequently to an avalanche. During the past decades, charges have mainly been delivered by hand or helicopter. Past catastrophic avalanche winters as e.g. the year 1999 in Switzerland showed the high potential of the method and led to new developments: remotely controlled fixed installations. These systems allow triggering an avalanche at times when the triggering possibility is highest: during or directly after a storm – when usually conventional delivery methods cannot be employed. They are installed at fixed positions in avalanche starting zones. An explosion is created by remotely igniting solid explosives or a gas mixture. However, as the systems are limited to a single or a few detonation points per system, the location and effect of these systems need to be carefully chosen. Yet, the effect of different types of explosions on snowpacks is not sufficiently known.

This thesis aims at improving our understanding of the processes above and in the snowpack involved in artificial triggering of avalanches using explosions. We performed large scale field experiments using solid spherical explosives and a mobile gas exploder (directed gas explosion) as sources and measured air pressures and snowpack accelerations on flat terrain. We performed experiments near operational avalanche control systems to validate the importance of the flat field experiments and also measured ground accelerations. To better understand the processes within the snowpack, we conducted small scale experiments and measured accelerations and wave arrival times to assess snowpack attenuation and wave speeds. On small snow blocks (< 1 m^3), we performed in situ measurements to derive elastic properties and crack propagation speeds relevant for slab avalanche release.

The results of the large scale field experiments showed that the air pressure and derived parameters were decreasing strongly with distance from the point of explosion. Snowpack accelerations and derived parameters strongly decreased with distance from the explosion and depth within the snowpack. Accelerations at a certain depth within the snowpack decreased similarly

with distance as the air pressure. The explosions produced by solid explosives showed similar results as those performed with a gas mixture. The directed gas explosion caused similar loading for angles within a forward cone of about 70°. At 90° from the exploder axis, the air pressure was lower close to the point of explosion but decreased less strongly with distance from the point of explosion. This resulted in elliptically-shaped isolines of air pressure close to the explosion and circle-shaped isolines at far distances as expected with unconfined solid explosives.

Far from the point of explosion, we observed different weak layer failure within the snowpack caused by different processes. They were either caused by crack propagation or the direct impact of the explosion above the snowpack. The experiments at the operational gas exploder showed that our flat field experiments were in good agreement with these systems and hence the flat field experiments were the correct choice to compare different types of explosions. Ground accelerations were small compared to the accelerations within the snowpack. The wave propagation speeds and the low amplitudes suggest that the waves were mainly transmitted from the air to the snowpack and hence the ground rather than over the foundation of the exploder or over areas with a lacking snowpack.

The small scale experiments resulted in similar attenuation values as observed in lab experiments. The attenuation was not depending on snowpack density in the observed density range. However, we observed large scatter in the results due to snowpack layering including changes in snow properties between adjacent layers. As the source using a hammer did not cause perfectly plane waves, vertical and horizontal components were measured. The effect caused by the strong layering may be an additional cause for the strong wave attenuation within snowpacks. Three different types of waves occur in snow: compressional waves in the ice skeleton and the pore space and shear waves in the ice skeleton. The measured attenuation was mainly attributed to the second compressional wave that is strongly attenuated. Wave speeds, however, were related to the fast wave within the ice skeleton. However, due to the short distances between the measuring locations required due to the strong attenuation, the different wave types could not be distinguished. First measurements at small snow blocks as used for crack propagation experiments showed that our method of acoustic wave measurement using accelerometers was suited to derive crack propagation speeds. Signal analysis suggests that there might be different types of waves in crack propagation experiments that could not be observed so far: One wave corresponding to the actual crack propagation and a second wave resulting from settling of the slab that follows weak layer failure – also called collapse wave.

A modeling approach that was based on our experimental data and considered snow as porous material was developed by other researchers. Preliminary results suggest that modeling wave propagation in a porous medium may be the most promising approach to assess the effect of

explosions for complex geometries. However, the model overestimated the observed accelerations due to the simplifications of the snowpack leading to too low attenuation.

With this thesis, we gained an increased understanding of the different waves propagating through the snowpack, and their behavior. We learnt about the effects of a directed gas exploder compared to spherical explosives. Further, we produced a comprehensive dataset on the effect of explosions on the snowpack. In a further step it will be required to use this data to improve modeling of explosions and snow.

1 Introduction

1.1 Snow and avalanches

Snow avalanches are gravitational mass movements such as landslides, debris flows and rock avalanches. However, their existence is limited to mountainous regions with either perennial or seasonal snowpacks. Many of these regions are either populated, of industrial importance, e.g. for mining, or vital transport corridors in particular for people, goods and energy. The exposure of humans to avalanche terrain leads to at least about 200 fatalities annually worldwide (Meister, 2002). The long-term annual mean of fatalities due to snow avalanches in Switzerland is 25 (Tschirky et al., 2000). Only considering the last two decades, this number has decreased to 23 fatalities annually. Whereas until the middle of the 20th century people in the European Alps mainly died in settlements or on transport corridors as roads or railways, these days most of the fatalities are recreationists performing winter backcountry activities.

This shift over the past decades in the Alps is the result of extensive avalanche mitigation measures that were put in place following major avalanche catastrophes striking settlements and infrastructure. In less developed mountain areas such as the Himalayas, however, snow avalanches hitting unprotected settlements is still the main reason for fatalities.

Avalanche mitigation can be divided into active and passive, permanent and temporary methods (Wilhelm et al., 2001). Temporary passive measures include avalanche warning and seasonal road closures. Hazard mapping, e.g. to limit construction and presence in endangered areas, is the main permanent passive measure. Active permanent measures consist of engineering works as e.g. defense structures in avalanche release areas, catching and deflecting dams in the avalanche path or runout zone or snow sheds to protect roads and railways (McClung and Schaerer, 2006). Temporary active measures consist of evacuations, road closures and artificial avalanche release. Engineering works are expensive and sometimes not desired for aesthetic reasons. Long road closures and evacuation are disliked and can lead to high economic loss. To protect settlements and avoid evacuations, defense structures in combination with hazard mapping remain the prime mitigation measures. However, for protecting transportation corridors artificial avalanche release has become increasingly important due to its low cost and flexible use. It is nowadays not only the standard measure to protect ski runs, but also widely employed to preventively release avalanches threating roads and railway lines, and occasionally even parts of settlements (Fig. 1-1).

Fig. 1-1: Typical situation where artificial avalanche release (here a fixed system) is used to protect humans and infrastructure.

1.1.1 Snow

Snow is a unique material. It consists of air, ice and sometimes water. It is the only material in nature found at very high homologous temperatures, i.e. close to the melting point and is extremely porous (Schneebeli, 2002). The ice content of seasonal snow ranges from as low as 5% up to around 50%. The high homologous temperature and the porosity define its unique mechanical and thermal behavior. The material is highly strain-rate dependent and is characterized by very low strength (Shapiro et al., 1997).

A snowpack consists of many different layers, a result of a steadily changing environment defined by the actions of wind, temperature, precipitation, short- and long wave radiation and the perpetual change of layers due to metamorphism of snow crystals (McClung and Schaerer, 2006) (Fig. 1-2). This combination of mechanisms is essential to form a snowpack that is prone to avalanche formation including weak layers and slabs. Weak layers are formed under high temperature gradients within the snowpack or at the snow surface including high vapor fluxes. Typical weak layers include faceted crystals, surface or depth hoar (Schweizer et al., 2016a). Slabs are formed by the compaction and sintering of snow layers.

Fig. 1-2: Translucent profile showing typical snowpack layering (Photo: J. Schweizer).

1.1.2 Avalanche formation

There are two main types of avalanches: loose-snow and slab avalanches (Fig. 1-3). Loose-snow avalanches release from a point in relatively non-cohesive snow surface layers and are usually harmless. Slab avalanches, on the other hand, include the release of a cohesive slab above a weak layer (Fig. 1-4). Damage accumulation by an additional load on the snowpack caused e.g. by a skier or new snow, and subsequent failure localization in the weak layer below the slab leads to an initial crack (Schweizer et al., 2016a). The onset of crack propagation within the weak layer follows this initial failure, provided the initial failure is sufficiently large and the weak layer-slab combination is prone to crack propagation. This process is followed by dynamic crack propagation on the slope scale. At some point, the slab will fail in tension. If the terrain is sufficiently steep, i.e. above 30°, friction may be overcome and the whole slab detaches. Slab avalanche release therefore comprises four steps: (i) failure initiation in a weak layer underlying a cohesive snow slab, (ii) the onset of crack propagation, (iii) dynamic crack propagation through the weak layer across the slope, and (iv) tensile failure – equivalent to crack arrest, followed by sliding of the slab (Schweizer et al., 2016a) (Fig. 1-5). Dry-snow slab avalanches are causing the majority of fatal accidents. Slab avalanches can develop into disastrous powder avalanches which are the main danger for settlements and infrastructure, given the terrain is sufficiently steep and the snowpack conditions are suitable. Slab and loose-snow avalanches can develop in dry and wet snowpack conditions. For wet-snow avalanches, the failure is

induced in a 0° isothermal snowpack by the reduction of strength by water penetrating the snowpack either due to rain or snowpack melting. Whereas dry-snow slab avalanches are well studied, wet snow avalanche release mechanisms are poorly understood. The release of a slab avalanche requires an additional load or a reduction in the weak layer strength at a given load. The additional load may be new snow resulting in natural avalanches or an artificial load as a skier or an explosion. Explosions are used to trigger avalanches deliberately (Fig. 1-6).

Fig. 1-3: The two main avalanche types: (a) slab avalanche and (b) loose snow avalanche (Photos: J. Schweizer).

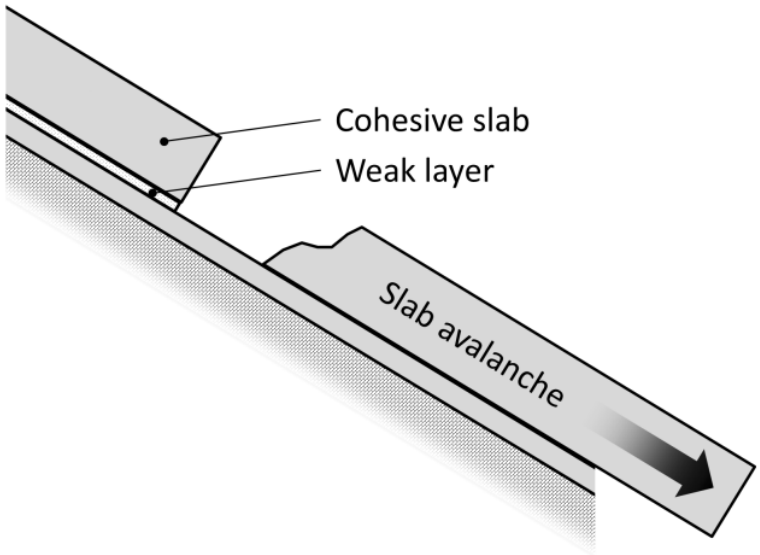

Fig. 1-4: Schematic of snow slab avalanche release (Schmid, 2015).

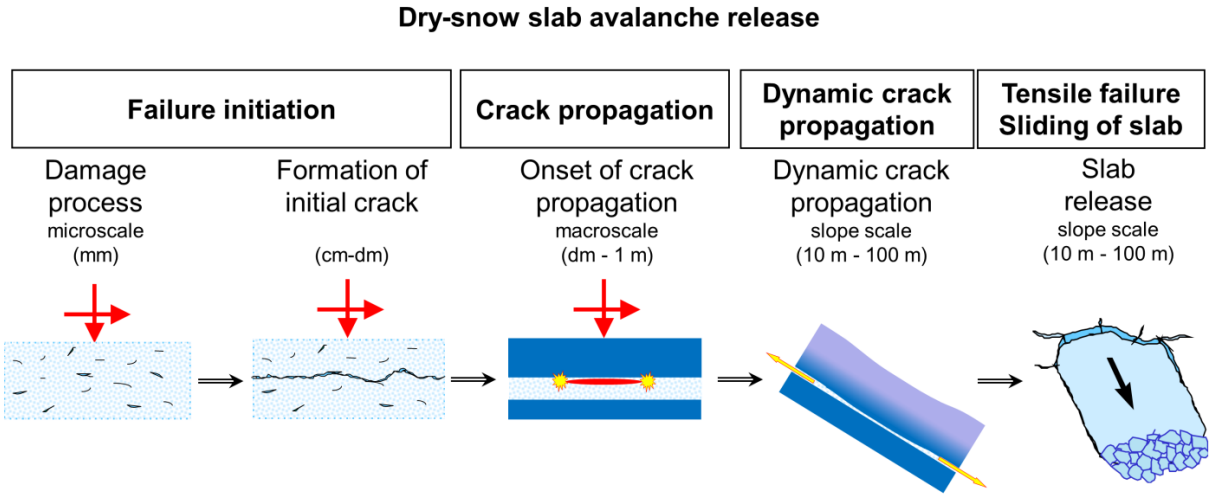

Fig. 1-5: Conceptual model of dry-snow slab avalanche release including the four stages of (i) failure initiation in a weak layer underlying a cohesive snow slab, (ii) the onset of crack propagation, (iii) dynamic crack propagation through the weak layer across the slope, and (iv) tensile slab failure arrests the propagating crack in the weak layer, followed by sliding of the slab; red arrows indicate mixed-mode loading (Schweizer et al., 2016a).

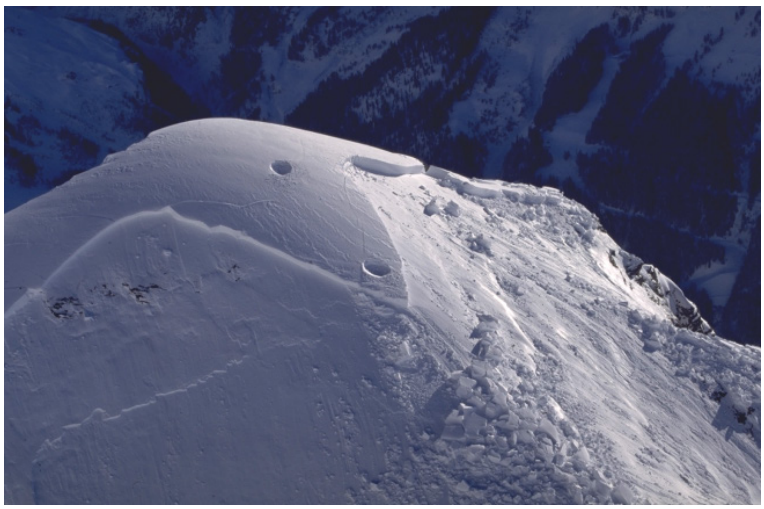

Fig. 1-6: Craters formed by the detonation of solid explosives and subsequent avalanche release with crown (Photo: J. Schweizer).

1.1.3 Artificial avalanche release

The aim of artificial avalanche release is to reduce the risk to people and infrastructure and indirect costs of closures of certain areas by the controlled release of smaller, less destructive avalanches at times of minor economic loss, e.g. at night. Artificial release has been applied for decades in ski resorts to protect ski runs and lifts from avalanches. The catastrophic avalanche winter of 1999 in Switzerland and other parts of the Alps showed that large catastrophic avalanches can be prevented provided frequent triggering resulted in small to medium-sized avalanches. However, large avalanches causing destruction to infrastructure and settlements were in some cases artificially

released (SLF, 2000) (Fig. 1-7). This was mainly due to the fact that triggering was not possible due to long storm periods resulting in large new snow amounts and hence deep slabs. It is therefore crucial to be able to release avalanches during bad weather and at night-time.

Fig. 1-7: Damaged house by an artificially released avalanche during the catastrophic avalanche winter of 1999 (Photo: J. Schweizer).

Many different methods exist to artificially release avalanches, all of them include explosions which result in an additional load on the snowpack required to release an avalanche as described above (McClung and Schaerer, 2006). Solid explosive charges are in particular used in artificial release, deployed by hand charging e.g. by ski patrol, helicopter charging or other means. Military mortars, howitzers or bazookas are used around the world to trigger avalanches. Bomb trams allow deploying solid explosives at different locations. Fixed avalanche control installations have become increasingly used during the last years (Fig. 1-8). They allow avalanches to be released under any given conditions from the valley-bottom. They either drop a solid explosive charge (SE) that is triggered above the snowpack or ignite a gas mixture within a pipe that causes an explosion (directed gas explosion – DGE) loading the snowpack. Some are able to throw a charge over some tens of meters. Other shooting/throwing devices with larger ranges are the avalancheur that shoots an arrow loaded with solid explosives or the avalanche pipe that throw solid explosive charges. In order to understand the effect of these systems on snowpack stability, understanding the processes that lead from an explosion to the release of an avalanche is crucial.

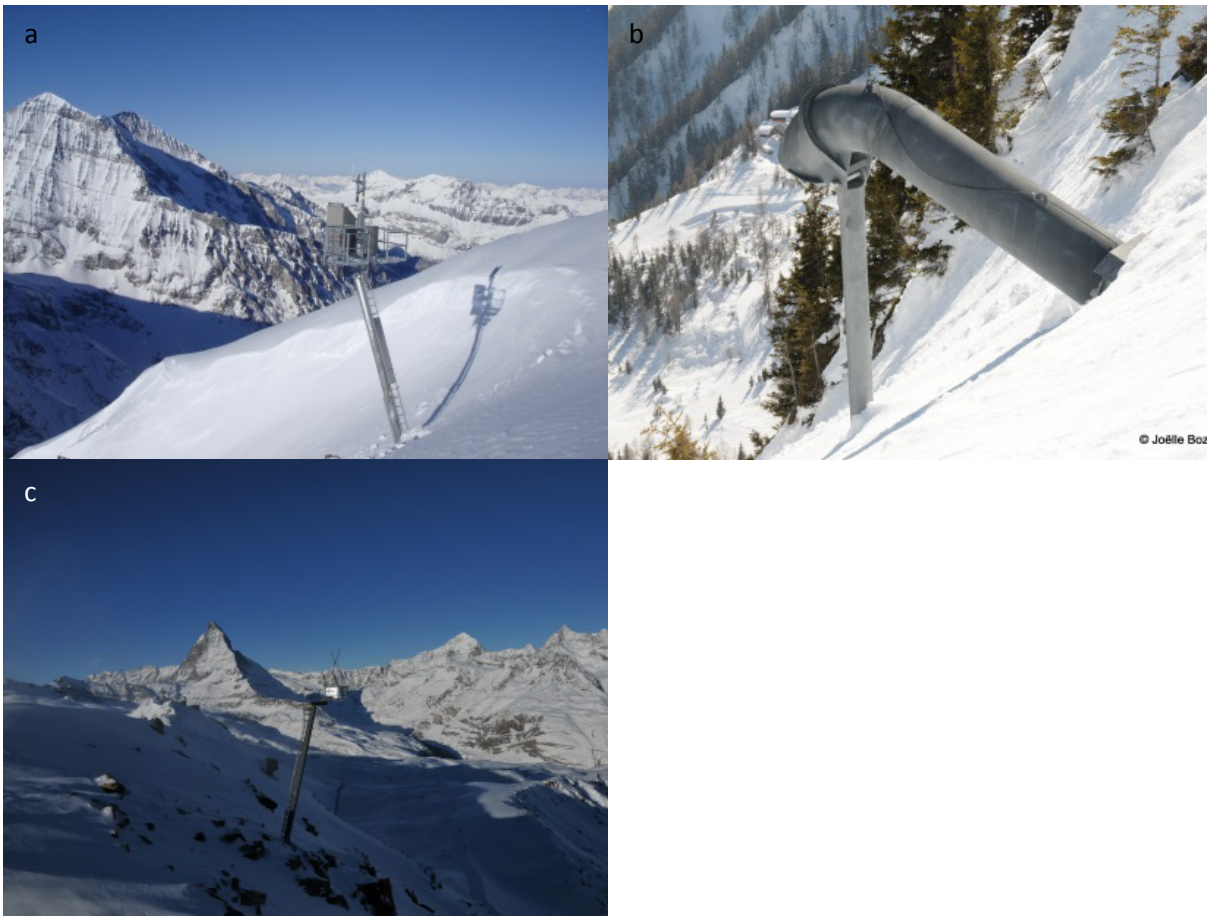

Fig. 1-8: Typical fixed avalanche release installations working with (a,c) solid explosives (SE) and (c) gas (DGE).Photos by Inauen-Schätti, Joëlle Bozon (TAS) and wyssen avalanche control.

1.2 Objectives and outline

Due to the relevance of avalanches as a natural hazard and the increasing popularity of preventive triggering of avalanches by explosions, in particular by remotely controlled fixed installations, it is important to improve our understanding of the effect of artificial triggering methods. This includes the processes in the air above a snowpack and within a snowpack following an explosion – so far the only effective method to trigger avalanches artificially.

Hitherto, few studies have investigated wave propagation in snowpacks at large scale and at distances outside the shock region. None of the research has investigated wave propagation basics such as wave speeds and attenuation in field experiments. No attention has been paid to recording actual failure initiation due to explosions as this has not been feasible so far. A detailed comparison of different types of explosions as caused by solid explosives or gas mixtures has not been performed, in particular because of the large and diverse study site and extensive equipment required. A comparison between flat field experiments and experiments on slopes has not been performed yet.

The aim of this study was therefore to assess the effect of various artificial avalanche triggering methods by developing a measuring system, measuring wave propagation in snowpacks caused by explosions, and recording and evaluating failure due to explosions.

To reach this overall aim the following objectives were defined:

(a) *Develop measuring equipment and layout to assess the effect of explosions*

Develop a measuring setup that can be used to measure the effect of explosion at different distances and depths from the point of explosion.

(b) *Quantify wave propagation above and in a snowpack caused by explosions*

Perform small and large scale experiments on different geometries using explosions and other sources to measure the response of the snowpack to the dynamic loading, i.e. to characterize wave propagation processes in snow. Measure the attenuation and wave propagation speeds for different snowpack properties. Use compact cameras to record weak layer failure in snow. Explain different types of weak layer failure and their cause. The results are required to better understand wave propagation caused by explosions.

(c) *Measure the effect of an explosion used by operational avalanche control systems (spherical explosive and directed gas explosion) on snowpacks and ground*

Perform measurements near operational gas exploders to assess whether flat field experiments are suitable to evaluate the effect of operational control systems.

Perform measurements near operational gas exploders to assess the effect of ground accelerations caused by an explosion. Investigate the cause of the ground vibration and the probability of triggering avalanches by ground vibration.

These three main objectives are fundamental to better understand artificial triggering and to assist in better planning of remote avalanche control systems.

The outline of the thesis follows from the above-mentioned objectives.

In Chapter 2 the state of the art is summarized.

Chapter 3 includes the description of the field sites used in the various studies. Furthermore, an outline of the methods is given.

Chapter 4 describes the measuring setup and results of large flat field experiments using spherical explosives and gives potential wave propagation characteristics, the loading of the snowpack and different types of weak layer failures.

Chapter 5 introduces a prototype exploder (directed source DGE) to investigate the effect of gas explosions. In this chapter, the results using this gas exploder affecting the snowpack on flat study sites is investigated.

In chapter 6, we describe the experiments performed on slopes using operational gas exploders and we compare the results with the experiments on a flat study site. We further discuss the use of in-slope experiments.

Chapter 7 gives insight into ground accelerations caused by explosions. We discuss the results comparing the findings to the effect of explosions on snowpacks and to past results on ground accelerations. We assess the probability whether ground accelerations are suitable to trigger avalanches.

In chapter 8 we describe small scale experiments used to derive mechanical properties as wave speeds and snow attenuation and perform measurements of crack propagation speeds.

In the appendices, we include publications that are not a primary part of this thesis or which were addressed to a different, mainly non-scientific audience.

Appendix A treats the comparison of two different solid explosives used in artificial avalanche release.

In Appendix B, we investigate the shape of the isolines of equal pressure using a directed gas exploder and compare it to the spherical explosion of an unconfined solid explosive.

Appendix C assesses different types of weak layer failures for different snowpack conditions using a novel approach to detect weak layer failure.

In Appendix D we further give insight into stresses calculated from field experiments and discuss different weak layer failure types.

Appendix E discusses a model for wave propagation and compares the model results to experimental findings.

In Appendix F we describe the flat field gas exploder experiments and discuss whether the air pressure or derived parameters may be used as approximations for the effect within the snowpack.

Appendix G gives on overview over our research, the resulting published and planned publications and their integration into this thesis.

2 State of the art

During the past decades, many studies were performed on explosions and snow, wave propagation in snow and mechanical properties of snow. In the following sections, we give insight into the most important research relevant for this study. However, comparisons among various sets of data are difficult due to different objectives, varying measuring techniques and snow conditions (Sommerfeld, 1982). Still, there are many important findings that allow conclusions to be drawn on the most relevant aspects. They are discussed in more details in the following sections. In general, the response of snow to explosive loading is a complex problem (Johnson et al., 1994), in particular due to the high homologous temperature, the low strength, the porous structure, the high compressibility and the characteristics of the snowpack and the explosive.

2.1 Explosions

To create the impulse used to load the snowpack in artificial avalanche release, explosions are used (Fig. 2-1). The basic concept of explosions is described below. For more details, the reader is referred to Cooper (1996).

Fig. 2-1: Explosion caused by solid avalanche explosives on a flat study site.

Explosions are chemical reactions that release large amounts of energy in the form of pressure and heat within a short period. They cause waves that propagate through the surrounding medium. Close to the point of explosion, there exist shock waves. Shocks are characterized by a propagation speed higher than the sound speed of the medium and abrupt changes in pressure, particle velocity, temperature and density of the medium (Cooper, 1996). Shock waves can be described by the Rankine-Hugoniot equations. With increasing distance from the point of explosion, the shock develops into an elastic (acoustic) wave due to geometrical spreading and other effects propagating at the speed of sound of the material. When hitting a material boundary, the energy of the wave is partly transmitted to the other material and partly reflected, resulting in different wave modes

depending on material properties, the incident wave mode and angle and impedance differences of the materials.

The creation and cancellation of a shock can be described as follows (Cooper, 1996):

1. Shock waves occur when a material is stressed far beyond its elastic limit by a pressure disturbance.
2. The pressure-wave speed increases with pressures above the elastic limit and hence a pressure-disturbance “shocks-up”.
3. The underpressure wave that moves into the shock wave travels faster than the shock front and hence the shock is attenuated from behind. This leads to an elastic wave as described in the following section.

2.2 Wave propagation principles

The calculation of stresses and strains is not a primary aim of this study. Still, it is important to introduce the main principles of wave propagation in order to understand the wave types that exist, how they propagate and to understand the experimental results. An overview over wave propagation in elastic, isotropic continua is given here. For more details, the reader is referred to e.g. Achenbach (1973) or Vollmann and Dual (2012).

The kinematic relations connect the displacement field and the strain tensor:

$$\varepsilon_{ij} = \frac{1}{2}\left(u_{i,j} + u_{j,i}\right) \tag{2.1}$$

where ε_{ij} is the strain, $u_{i,j}$ the derivative of the displacement component in direction i with respect to the direction j in indicial notation.

To relate the stresses to the strains, constitutive laws are required which in our case is linear elasticity. This results in:

$$\sigma_{ij} = \lambda \varepsilon_{\mathrm{kk}} \delta_{ij} + 2\mu\varepsilon_{ij} \tag{2.2}$$

where λ and μ are the Lamé parameters and δ_{ij} is the Kronecker delta.

The next step is to establish the dynamic equilibrium:

$$\sigma_{ij,j} = \rho u_{i,tt} \tag{2.3}$$

where ρ is the density and t the time.

Combining the above equations yields the wave equations, a set of partial differential equations:

$$\sigma_{ij,j} = (\lambda + \mu) u_{k,ki} + \mu u_{i,kk} = \rho u_{i,tt} \tag{2.4}$$

The displacement fields can be expressed with potential functions:

$$\underline{u} = \underline{\nabla}\varphi + \underline{\nabla} \times \underline{\psi} \tag{2.5}$$

with the scalar potential φ and the vector potential $\underline{\psi}$.

The displacement field is then expressed in indicial notation in Cartesian coordinates:

$$u_i = \varphi_{,i} + \varepsilon_{ijk}\psi_{k,j} \tag{2.6}$$

where ε_{ijk} is the permutation symbol.

The above equation is substituted into the differential wave equation and yields:

$$\left((\lambda + 2\mu)\varphi_{,kk} - \rho\varphi_{,tt}\right)_{,i} + \varepsilon_{ilm}\left(\mu\psi_{m,kk} - \rho\psi_{m,tt}\right)_{,l} = 0 \tag{2.7}$$

It follows that the ψ-waves do not contribute to the dilatation.

The term $\psi_{i,kk}$ represents the local rotation as defined in elasticity.

We can write the displacement fields in terms of derivatives of a local derivative of the scalar and the vector potential and we get differential equations for rotation-free and for isochore waves that propagate uncoupled in our case.

The rotation-free part gives

$$c_1^2\Delta\varphi = \varphi_{,\mathrm{tt}} \tag{2.8}$$

where

$$c_1 = \sqrt{\frac{\lambda+2\mu}{\rho}} \tag{2.9}$$

is the speed of the first (primary) wave.

The isochore part leads to

$$c_2^2\Delta\underline{\psi} = \underline{\psi}_{,\mathrm{tt}} \tag{2.10}$$

where

$$c_2 = \sqrt{\frac{\mu}{\rho}} \tag{2.11}$$

is the speed of the secondary wave.

The speed of the first wave is higher than of the second wave for materials as metals or snow.

For plane waves and in structures, depending on the geometry, the primary and secondary waves have different speeds. In beams, the longitudinal wave propagates with

$$c_0\,(k) = \sqrt{\frac{E}{\rho}} \tag{2.12}$$

and the flexural wave propagates at a speed of

$$c_b\,(k) = \sqrt{\frac{E}{\rho}}\sqrt{\frac{I_3}{A}}k \tag{2.13}$$

where k is the wave number, E the Young's modulus, I_3 is the moment of inertia, A the surface of the cross-section and k the wavenumber.

For experiments with explosions in air above a snowpack, idealized as a semi-infinite linearly elastic solid, we have to understand the influence of the angle of the incident wave on wave transmission and reflection. In our case, the solid is the snowpack. In a typical case, an incident P-wave in the fluid above the snowpack, i.e. air, is caused by the air pressure wave of an explosion. The

incident wave causes a reflected P-wave in the air, a P-wave in the continuum and an S-wave in the continuum. All these waves propagate at different angles measured from the normal axis on the surface of the snowpack assuming plane waves. Their amplitude ratios and angle can be determined based on the incident angle and amplitude using parameterizations of the waves and boundary conditions. For a detailed derivation the reader is referred to Vollmann and Dual (2012)

The amplitude ratios are

$$A_r = \frac{-n_1\varepsilon+\delta}{\delta+r_1\varepsilon} A \tag{2.14}$$

$$A_s = \frac{2c_2\lambda_f p_1 p_2 (r_1-n_1)}{\delta+r_1\varepsilon} A \tag{2.15}$$

$$A_t = \frac{c_1\lambda_f (n_1-r_1)(s_1^2-s_2^2)}{\delta+r_1\varepsilon} A \tag{2.16}$$

with

$$\delta = 2c_2\lambda_f p_1 p_2 s_2 + c_1\lambda_f p_1 (s_1^2 - s_2^2) \tag{2.17}$$

$$\varepsilon = c_f((\lambda + 2\mu p_1^2)(s_2^2 - s_1^2) - 4\mu p_1 p_2 s_1 s_2 \tag{2.18}$$

$$c_f = \sqrt{\frac{\lambda_f}{\rho_f}} \tag{2.19}$$

$$c_1 = \sqrt{\frac{\lambda+2\mu}{\rho}} \tag{2.20}$$

$$c_2 = \sqrt{\frac{\mu}{\rho}} \tag{2.21}$$

$$\underline{n} = \begin{pmatrix} \cos\Theta \\ \sin\Theta \\ 0 \end{pmatrix} \tag{2.22}$$

$$\underline{r} = \begin{pmatrix} -\cos\Theta_\mathrm{r} \\ \sin\Theta_\mathrm{r} \\ 0 \end{pmatrix} \tag{2.23}$$

$$\underline{p} = \begin{pmatrix} \cos\Theta_\mathrm{p} \\ \sin\Theta_\mathrm{p} \\ 0 \end{pmatrix} \tag{2.24}$$

$$\underline{s} = \begin{pmatrix} \cos\Theta_\mathrm{s} \\ \sin\Theta_\mathrm{s} \\ 0 \end{pmatrix} \tag{2.25}$$

$$\underline{s'} = \begin{pmatrix} -\sin\Theta_s \\ \cos\Theta_s \\ 0 \end{pmatrix} \tag{2.26}$$

where A_r, A_s and A_t are the amplitudes of the reflected P-wave, the transmitted S-wave and the transmitted P-wave and A is the amplitude of the incident wave. λ and μ are the Lamé parameters of the solid. λ_f is the Lamé parameter of the fluid. ρ and ρ_f are the densities of the solid and the fluid. $\underline{n}$, $\underline{r}$, $\underline{p}$ are the unit vectors of the P-waves' propagation directions. $\underline{s}$ and $\underline{s'}$ are the unit vectors of the

S-wave propagation and S-wave displacement directions. Θ, Θ_r, Θ_p and Θ_s are the angles of the propagation direction of the waves with reference to the normal axis of the snow surface.

The energy reflection coefficient is equal to

$$e_r = \left(\frac{n_1\varepsilon+\delta}{\delta+r_1\varepsilon}\right)^2 \tag{2.27}$$

The relation between the different angles is

$$\Theta = \Theta_r \tag{2.28}$$

$$\sin\Theta_p = \frac{c_1}{c_f}\sin\Theta \tag{2.29}$$

$$\sin\Theta_s = \frac{c_2}{c_f}\sin\Theta \tag{2.30}$$

where c_f is the P-wave velocity in the fluid.

For $c_f < c_1$ there is a critical case at which no P-wave is caused in the solid. The same is observed for $c_f < c_2$. In these cases, there is only a surface wave created required to fulfill the boundary conditions.

2.3 Wave propagation in porous media and modeling

As snow is porous, the entire wave propagation process is more complex than the case for an elastic solid described above. To understand the effects of explosions and other dynamic impulses on a snowpack, it is best to use a model which gives an idea about the processes in snow.

Snow has been modeled as a continuum to model snow acoustics, which is simpler, but has the shortcoming that it is inadequate to answer the question of two different propagation media (Sommerfeld, 1982). Continuum models have been used with success to determine bulk mechanical properties (Sommerfeld, 1982). Only few of the measurements include densities of seasonal snow covers, though.

In seasonal snow covers with densities below 200 kg m^{-3}, pore air might be more important in sound propagation (Sommerfeld, 1982). Biot (1956a) developed a model to describe the acoustic wave propagation in porous media composed of a solid skeleton and a viscous fluid in the pore space. His model was applied to snow by Johnson (1982) using the solution by Deresiewicz and Rice (1962) for plane waves in a homogeneous isotropic linear-elastic material (s. 2.3.1). In snow, the porous character is given by the ice matrix and the air (and/or water) in the pores. The Biot model predicts the existence of three different wave types: Two uncoupled longitudinal waves and one transversal wave. The first longitudinal wave propagates in the ice skeleton and is also called the fast wave due to the high speed of sound compared to air. The transversal wave also propagates in the ice skeleton. The second longitudinal wave propagates within the pore space. The propagation speeds of the wave types are different and depend on mechanical properties of snow. Whereas the first longitudinal wave and the transversal wave are only slightly dispersive, the second longitudinal wave, also called

slow wave, is dispersive. All waves are attenuated within the snow, increasingly with increasing frequency with the slow wave being much stronger attenuated than the other waves. The low attenuation within the ice skeleton reported by Johnson (1982) was in contrast to experimental data, probably due to the neglected friction loss within the ice skeleton (Sommerfeld, 1982). Johnson (1982) showed that a large portion of the acoustic energy transmitted across the air-snow interface was transmitted through the pore system as a dilatational wave of the second kind. One of the main complexities of the model is the requirement for more than 10 material parameters of snow. These were parameterized by Sidler (2015) depending on snow porosity or density. However, this is only an approximation due to the complex geometry of snow. Sidler (2015) showed speeds and attenuation that were in good agreement with earlier studies. He also reported that at very high porosities, i.e. low densities, the speed of the first longitudinal wave was becoming slower than the speed of the second longitudinal wave in the pore space. Capelli et al. (2016) used the solution of Deresiewicz and Rice (1962) for the high-frequency range of Biot's equations with the parameters reported by Sidler (2015) and found that wave speeds were in good agreement with their experimental results and that the measured attenuation coefficients were between those modeled for the fast and the slow wave. However, they report that the applicability of Biot's model is limited due to the large number of parameters needed that are difficult to relate to snow properties.

A stress-wave model was reported and showed that dilatational and shear waves could interact with a weak bedding layer causing dilatational and shear stresses in the layer (Johnson, 1980). He showed that impedance differences at boundaries had a great influence on the propagation of the stress waves to the bedding layer.

Johnson (1990) stated that shock wave attenuation in snow is affected by the shock amplitude, the geometry, the duration of the shock and the mechanical properties of the material. He established simple snowpack attenuation models based on the principle of momentum modeling using different impulses. These models were initially used to analyze the dynamic behavior of porous media (Herrmann, 1971) in which the material compacts to a final density at negligible stresses. After the compaction, the pressure impulse (momentum) of the shock wave uniformly spreads over the volume of material behind the advancing shock wave. The stress wave is lengthened in time and reduced in amplitude as more of the material is compacted. The attenuation is then caused by momentum spreading and losses are attributed to plastic deformation. However, fracturing and release waves were not considered. Johnson (1990) predicted the attenuation to be proportional to x^{-2} for plane waves and x^{-6} for spherical waves with his model, where x is the distance from the center of the blast. This is in contrast to the results by Brown (1981) with attenuation proportional to $x^{-1.2}$ for plane waves and Mellor (1977) who reported attenuation proportional to x^{-3} to x^{-4} for spherical waves, probably due to the simple snow compaction model applied by Johnson (1990) which only

considered one step compaction. On the other hand, Mellor (1977)'s values of the exponent might result from propagation outside the range of shock where pressure decay is due to viscous dissipation and geometric spreading which produce much less attenuation than compaction predicted by Johnson (1990)'s model.

Brown (1981) used jump equations to evaluate shockwave propagation in snow and concluded that this is a viable way since one can avoid the expensive and complicated numerical solution of the wave equation. He showed that snow strongly attenuates plastic stress waves. The wave amplitude reduced to about 10 % of its original amplitude within a distance of 10 cm. His results of the pressure attenuation are in good agreement with experimental results, though there was a lack of good shockwave data (Brown, 1981). For weaker shockwaves, the attenuation of the numerically solved wave equation and the jump equations were in good agreement but diverged for stronger shocks. This might be due to the simplification introduced with the jump equations or numerical instability at the solution of the wave equation (Brown, 1981). The attenuation and the change of the wave speeds showed similar trends with the two approaches. Johnson et al. (1994) used finite element modeling to compare shock wave attenuation for plane and spherical waves and concluded that their results for plane shockwaves were in agreement with the results obtained by a simple momentum model and with the measurements performed.

As computational power increased, finite element models became increasingly used in snow mechanical research (Podolskiy et al., 2013). For example, Haehnel and Shoop (2004) used a capped Drucker-Prager model with different snow parameter sets to model snow under dynamic loading. Their results gave upper and lower boundaries for the experimental data they used as a basis. Miller et al. (2011) performed finite element modeling on seasonal snow based on pressure-density data by Johnson et al. (1993). He used mechanical properties summarized in Mellor (1975). A shock equation of state was used by Miller et al. (2011) to model the volumetric constitutive behavior of snow subject to blast loading. A linear elastic-brittle failure constitutive relationship was used to model the deviatoric behavior. Their results are of great interest since they were able to show stress and strain distributions within the snowpack. They showed a shear stress concentration above a weak layer and snow densification. The results by Miller et al. (2011) on detonation height agreed with those from Gubler (1977). However, insight into why a suspended charge is better in avalanche control than a surface blast could not yet be provided. Miller et al. (2011) also showed that there was a near surface pressure intensification due to reflection enhancement as suggested by Mellor (1973), however, they modeled snow as an elastic solid and not as a porous material. They suggested that the impulse of the blast, i.e. the integrated air pressure over time, rather than peak air pressure was a contributor in increasing dynamic snowpack response at far field. Their model did not consider the porous

character of the snowpack which actually results in different wave types. They stated that further field experiments were needed to calibrate the models.

Nicolas et al. (1985) developed a simple two-parameter model to predict the propagation of acoustic waves in the air above a snowpack. He showed changes at lower frequencies with changes in the layer thickness. The model showed good agreement with field measurements for higher frequencies. For frequencies below 200 Hz, the measurements agreed better with a theory based on semi-infinite porous ground. They reported that a very thin layer decreased the sound pressure level more effectively than a thick layer with the reason being unclear.

Cardu et al. (2008) introduced a coupled stress and energy criterion for the release of artificially triggered dry snow slab avalanches. They propose to revise the TNT-equivalent approach because the equivalent does not include tensional or energetic considerations. In addition, the duration of the induced stress and the underpressure should be considered. Cardu et al. (2008) suggest quantifying the specific fracture energy using different solid explosives.

2.3.1 Biot's equations of motion and solution for plane waves

We give an overview over the Biot's equations. For more details, the reader is referred to Biot (1956a), Biot (1956b), Johnson (1982), Sidler (2015) and Capelli et al. (2016).

The constitutive relations for linear-elastic porous media are (Biot, 1956a; Johnson, 1982):

$$\sigma_{ij} = (Ce + Q\epsilon)\delta_{ij} + 2Ne_{ij} \tag{2.31}$$

$$s = Qe + R\epsilon \tag{2.32}$$

where e and ϵ are the strain tensors of the solid and the fluid, respectively, C is an elastic constant and N is the shear modulus of the solid. s is the fluid pore pressure. R describes the pressure on the fluid required to force a certain volume of the fluid into the aggregate while the volume stays constant. Q describes the coupling of the volume change of the fluid and of the solid.

The equations of motion are

$$N\underline{\nabla}^2\underline{u} + \underline{\nabla}\left((C+N)\underline{\nabla}\cdot\underline{u} + Q\underline{\nabla}\cdot\underline{U}\right) = \frac{\delta^2}{\delta t^2}\left(\rho_{11}\underline{u} + \rho_{12}\underline{U}\right) + b(\eta)\frac{\delta}{\delta t}\left(\underline{u} - \underline{U}\right) \tag{2.33}$$

$$\underline{\nabla}\left(Q\underline{\nabla}\cdot\underline{u} + R\underline{\nabla}\cdot\underline{U}\right) = \frac{\delta^2}{\delta t^2}\left(\rho_{12}\underline{u} + \rho_{22}\underline{U}\right) - b(\eta)\frac{\delta}{\delta t}\left(\underline{u} - \underline{U}\right) \tag{2.34}$$

where $\underline{u}$ is the displacement vector of the solid skeleton, $\underline{U}$ the displacement vector of the fluid. ρ_{11}, ρ_{12} and ρ_{22} are coefficients for the inertial effect of the moving fluid and are related to the solid and fluid mass densities. $b(\eta)$ defines the dissipation caused by fluid friction and is related to the porosity, the permeability and the fluid viscosity. Θ is a function of the characteristic pore size and the frequency.

The solution by Deresiewicz and Rice (1962) for plane waves is given using two scalar potentials and a vector potential. They show that longitudinal waves of the first and second kind and the transversal waves affect the displacements in the fluid and the solid which means that the motions are coupled. The parameters C, N, R and Q can be determined from measurable coefficients (Johnson, 1982) such as the shear modulus, the compressibility, the permeability, the tortuosity etc. Sidler (2015) suggested to express the parameters in simplified form to depend on snow porosity only.
The propagation speeds and the attenuation can be derived from the complex wave number k. The speeds are given by $c_i(\omega) = \omega/\mathrm{Re}(k_i(\omega))$ and the spatial attenuation by $\alpha_i(\omega) = \mathrm{Im}\big(k_i(\omega)\big)$. ω is the angular frequency and Re and Im denote the real and the imaginary part, respectively.

Stoll and Kan (1981) reported that the refraction angles for waves in a semi-infinite porous saturated soil below water were always smaller than the incident angle (Fig. 2-2). This means that there was no overcritical case which would be in contrast with the solution in the continuum described above. However, it is not clear whether this concerned the angles of all three types of waves caused in the half space.

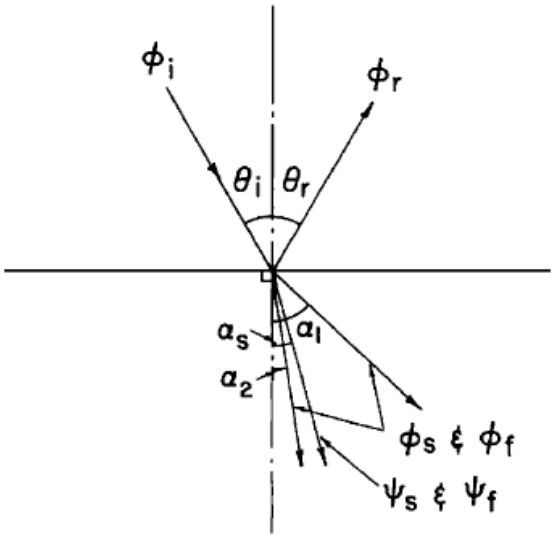

Fig. 2-2: Typical wave reflection and transmission behavior with a liquid (or gas) above a semi-infinite porous half space (horizontal line) with incident and reflected waves and the three refracted waves in the porous medium (Stoll and Kan, 1981).

2.4 Artificial avalanche release (large range effects)

Experimental research on the effect of spherical explosions affecting the snow cover with varying solid explosives, detonation heights and snowpacks was performed by Gubler (1977). His findings are still considered the cornerstone of avalanche control methods. Gubler (1977), for example, showed that in case of a dry snowpack, which is the typical situation in avalanche control, detonation points

one to two meters above the snowpack were most effective. One reason for this finding might be wave fusion of the shock wave at shorter distances which increases the loading of the snowpack (Mellor, 1973). Johnson et al. (1994) reported the same findings. They also stated that the increase of the elevation above 2 m $kg^{-1/3}$, where the distance is scaled by the charge mass, did not have an improved effect on maximum far field snow surface pressures which is in agreement with Gubler (1977). Buried charges have a strictly localized effect (< 10 m from point of explosion) due to the attenuation of snow as a porous material and the large fraction of energy dissipated in crater formation (Miller et al., 2011). Ueland (1993) showed that there was no measurable displacement for sensors at distances ranging from 20 to 80 m from the point of explosion. Still, Gubler (1977) suggested an effective range of 17 to 120 m with a 1 kg charge depending on snow stability. The effective range was defined by Gubler (1977) as the distance up to which it is possible to induce a failure in a given weak layer within the snowpack assuming a shear strength of the weak layer of 1-10 kPa. He concluded that the effective range was proportional to the square root of the charge size. Gubler (1993) proposed an effective radius of an avalanche control method based on the stress at the depth of the weak layer corresponding to the load by a skier. He stated that within this range the minimum additional stress at the weak layer caused by a skier was around 100 Pa, in most cases 300 Pa – which seems low. This resulted in an effective range of approx. 85 m for a charge of 1 to 1.5 kg. The effective radius is still widely used to determine the area in which the pressure is sufficient to fracture an existing weak layer. However, the load required to release an avalanche by dynamic explosive loading is not actually known, and obviously depends on the snowpack conditions under consideration. This leads to very different effective ranges depending on stability reaching from 17 to 120 m (Gubler, 1977) and 50 to 100 m (Gubler, 1983) with a 1 kg charge. Ueland (1993) concluded that larger charge sizes were required for isothermal snow conditions and that using fewer large charges was more effective than a large number of smaller charges.

Gubler (1976) also showed that one should target zones with shallow snow depths in case an explosion above the snowpack should not be possible. This is given by the fact that shallow snowpacks are usually less stable and the weak layer is located closer to the surface. Gubler (1977) concluded that the sonic boom by an aircraft with amplitudes of maximum 100 Pa would not be sufficient to release an avalanche. This is in agreement with the findings by Reuter and Schweizer (2009).

Bair (2013) analyzed datasets on the natural and artificial avalanche release. He reported an overall explosive yield of 25%. He also suggested that results of Extended Column Tests (ECT) were indicative of avalanche activity for artificially released avalanches. On days when the crack propagated across the entire column, the number of avalanches was higher and the avalanches were larger than on days when the ECT did not indicate propagation. Waiting after a storm before

releasing avalanches significantly decreased the number of avalanches and their sizes. It is therefore important to trigger avalanches during or directly after a storm or to wait until the snowpack is stable again, which is often no option.

There has been little research performed on directed gas explosions (DGE). LaChapelle (1977) showed alternate methods to artificially release avalanches like gas mixtures causing explosions, inflation of buried airbags, the application of high-energy vibrations and the modification of the snow-ground interface to increase gliding. Liebermann et al. (2002) then updated the original principles on a gas exploder. Berthet-Rambaud (2009) developed a test protocol to investigate the effect of gas exploder explosions.

2.5 Effect of explosions at short range

Johnson et al. (1994) conducted experiments with sheet explosives on the snow surface to measure shockwave attenuation with buried stress gauges and found very high attenuation proportional to $x^{-1.6}$ in snow, where x is the distance from the detonation point. They showed that outside the region of compacted snow stresses are transmitted as acoustic waves and attenuated proportional to $x^{-0.7}$ for plane waves in snow and x^{-1} for spherical waves in air above a seasonal snowpack.

Frigo et al. (2010) performed experiments on a flat study site using solid explosives and tried to derive mechanical properties. They could show snow compaction close to the point of explosion using a georadar. Frigo et al. (2012) investigated the effect of explosions near the blast and showed that the size of the crater increased with increasing charge mass and decreasing charge elevation. Similarly, Binger et al. (2006) investigated craters formed by explosions and assessed the influence of charge and blasting cap orientation. Wooldridge et al. (2012) performed stability tests before and after explosions close to the detonation point and showed a decrease of stability using compression tests after the explosion.

The pressure from an air shock is primarily transmitted onto the snowpack through the air space, i.e. the second longitudinal wave which is coupled to the ice frame. This wave is according to Johnson et al. (1994) mainly responsible for peak stresses near the snow surface (Johnson 1992). This is also related to the fact that the uncompacted snow impedance is close to the impedance of air.

Ueland (1993) conducted a series of explosions and recorded the response of the snowpack with seismographs and showed that shockwaves attenuated very rapidly and that the P-wave travelling directly through the snowpack from the point of explosion is negligible except in the immediate vicinity of the explosion. The air, however, is much more efficient in transmitting shockwaves. Ueland (1993) stated that most of the movement of the snowpack is caused by the wave travelling through the air and striking the snow surface which then causes a transversal wave. Consecutive shots at the same location did not cause significantly different amplitudes and no measurable settling was

recorded at any of the sensor locations. Ueland (1993) showed that shockwaves attenuate faster in isothermal snow. Gubler (1977) stated that the air pressure wave penetrates the snowpack almost unchanged. A negative pressure phase is only observed at larger distances (Mellor, 1965).

Small-scale laboratory experiments with a gas gun at 2 to 40 MPa and initial snow densities ranging from 100 to 520 kg m^{-3} revealed that compaction was depending on initial snow density and that significant strain hardening occurred once a critical density was reached which was in the range of 480 to 680 kg m^{-3} (Johnson et al., 1993). Very small stresses were needed to compact snow up to this critical density. At low densities, the snow deformed along distinct paths due to the low initial particle bond strength. At the critical density, particle bonds had sufficient strength. At higher densities, the ice particles “flowed” into the remaining void space through plastic deformation processes. These different behaviors show the complexity of snow under high amplitude dynamic loading (Johnson et al., 1992).

Albert (1983) reviewed inelastic stress wave propagation in snow reporting that snow is a viscoplastic material supporting the propagation of elastic and elasto-plastic waves, but not supersonic shock waves. He suggested values for the scaled radius of plastic deformation of 1.6 m $kg^{-1/3}$ and 1.2 m $kg^{-1/3}$ for charges fired in and above snow, respectively.

The most recent study on the impact of explosions onto the snowpack was performed by Bones et al. (2012) and Binger and Miller (2016) based on equipment developed by Tichota et al. (2010). They performed tests on dry hard and soft snow slabs and measured accelerations and air overpressures at short distance from the detonation point ranging from 3 to 7 m. Their results revealed an increasing impact of explosions on the snowpack up to an optimum height of the charge above the snow surface at short distances and are in agreement with the findings by Gubler (1977) and Johnson et al. (1994). Bones et al. (2012) and Binger and Miller (2016) showed that the positive and negative air pressure wave impulses were similar. They stated that the air overpressure and impulse increase with increasing charge height up to 1 m with a charge size of 1 kg. With a smaller charge, overpressure and impulse increased up to an elevation of 1.5 m. They showed higher air pressures for the sensor at the snow surface than for the elevated sensor because of shock reflection. All accelerometers showed increased acceleration with increased charge height. The vertical attenuation was proportional to $d^{-0.4}$ and $d^{-1.3}$ for different slabs where d is the depth within the snowpack and the attenuation in the snowpack was independent of charge height. The attenuation of the acceleration was stronger in moist than in dry snow and the radial attenuation was stronger than the vertical regardless of the snow type. In addition to the attenuation with depth within the snowpack, the air pressure and accelerations also decayed strongly with distance from the point of explosion.

2.6 Ground accelerations (directed gas explosions)

The influence of ground accelerations on avalanche release has not been investigated in depth. Ground waves might become relevant at far distances due to the lower attenuation compared to snow, but amplitudes may not be sufficient at these distances to cause weak layer failure (Ueland, 1993). Based on field experiments, Suriñach et al. (2011) investigated the ability of the vibrations of a commonly used gas exploder caused by recoil or by the air pressure wave transmitted to the snowpack and hence to the ground to trigger avalanches beyond the commonly assumed effective radius of the respective system. They measured vibrations in the vicinity of an operational gas exploder. They recorded two wave groups, one longer wave travelling at 3180 m s^{-1} and the other with a distinct N-shape travelling at 331 m s^{-1}. These speeds correspond to the P-waves in basement rock and sound waves in air. They interpreted that the first wave was generated beneath the Gazex and transferred through the ground. They stated that there was no wave transmitted through the snowpack over the entire distance as this wave would not be recordable after a distance of 2.6 m. The second wave presumably propagated through the air and was then recorded by the sensor within the snowpack. The main frequencies of the first wave were in the range of 10 to 20 Hz, those of the second wave in the range of 20 to 40 Hz. High frequencies attenuated with distance. Peak ground accelerations at the measuring locations (> 130 m) derived from the geophone signals were about 6 times lower than acceleration values that are according to Schweizer (1999) required for avalanche release with a critical acceleration criterion. The amplitudes of the snowpack acceleration caused by the sound waves were higher than those caused by the ground wave by up to one order of magnitude. Johnson et al. (1994) showed that snow surface and ground seismic waves are only secondary effects and do not contribute significantly to the stresses in the snow cover which is in agreement with Ueland (1993) findings who also stated that ground waves were controlling at larger distances due to the lower attenuation but were of too low amplitude to trigger avalanches Pérez-Guillén et al. (2014) showed an example where an avalanche might have been triggered by an earthquake. However, they were not sure as peak ground accelerations were rather low. Albert and Orcutt (1990) reported sound wave amplitudes being 10 times higher than those of the ground waves. Only at very large distances, Suriñach et al. (2011) reported comparable values of sound and ground wave amplitudes, but amplitudes were low. Albert et al. (2013) showed for different grounds that the wave propagating through the air and being transferred to the ground always resulted in higher amplitudes than the wave propagating directly through the ground at higher speeds.

Chernouss et al. (2002), Chernouss et al. (2006) and Podolsky et al. (2008) reported ground accelerations caused by large explosions in an open pit mine and developed a model for the influence of ground accelerations on snowpack stability. They performed lab experiments with a shaking table showing the decrease of shear strength during shaking.

2.7 Influence of snowpacks on air pressure waves

Albert et al. (2008) determined the influence of a snow cover on blast noise propagation above it and on acoustic sensors. Snow is an extreme case in ground impedance and by far the most absorptive naturally occurring ground cover. Acoustic responses vary over short periods of time as a result of snow cover property changes (Albert and Hole, 2001). Using pistol shots, Albert et al. (2008) showed that the acoustic attenuation was greater for snow than for any other ground material. Attenuation reached around -30 dB within 100 m. Larger attenuation is expected under different snow conditions. A snowpack has a significantly different influence on waves travelling above it than has bare ground. Johnson et al. (1993) showed the influence of a snow cover on blast noise propagation using microphones at distances ranging from 100 m to 1500 m from the C4 charge. Mellor (1965) stated that the reflected air pressure from a snow surface was around 30% lower than from a rigid surface.

2.8 Wave attenuation and speeds – laboratory experiments

Different methods were used in the laboratory to determine the attenuation of waves propagating in snow: Marco et al. (1998) measured the impedance of snow which resulted in attenuation coefficients. The transmission loss of snow layers with different thicknesses was used by Reiweger et al. (2015), Ishida (1965) and others. A review on the measuring methods and results is given in Capelli et al. (2016). They also performed propagation experiments with small scale samples. Most experiments were performed with frequencies below 10 kHz whereas Capelli et al. (2016) measured at frequencies higher than 10 kHz.

Capelli et al. (2016) measured the attenuation of signals produced by pencil lead fractures and piezo elements with different snow sample lengths. Although comparison is difficult due to different measuring techniques and the consequent measurement of the attenuation of different wave types, their results were in good agreement with other studies reporting attenuation coefficients of 0.05 to 3.5 dB cm^{-1}, independent of density. Depending on the wave type, the structure and density of the snow can cause opposite effects on damping, i.e. some waves might have higher damping at lower densities and higher damping at high densities and vice versa.

Capelli et al. (2016) also reported and reviewed measurements on the wave propagation speed in snow (Fig. 2-3). Depending on the wave type, speeds can either increase or decrease with increasing density: Waves within the pore space decrease with increasing density and are between 250 and approx. 100 m s^{-1}. The longitudinal and transversal waves within the ice skeleton increase with increasing density and are in the range of 250 to 2500 m s^{-1} with the longitudinal wave being faster (Capelli et al., 2016).

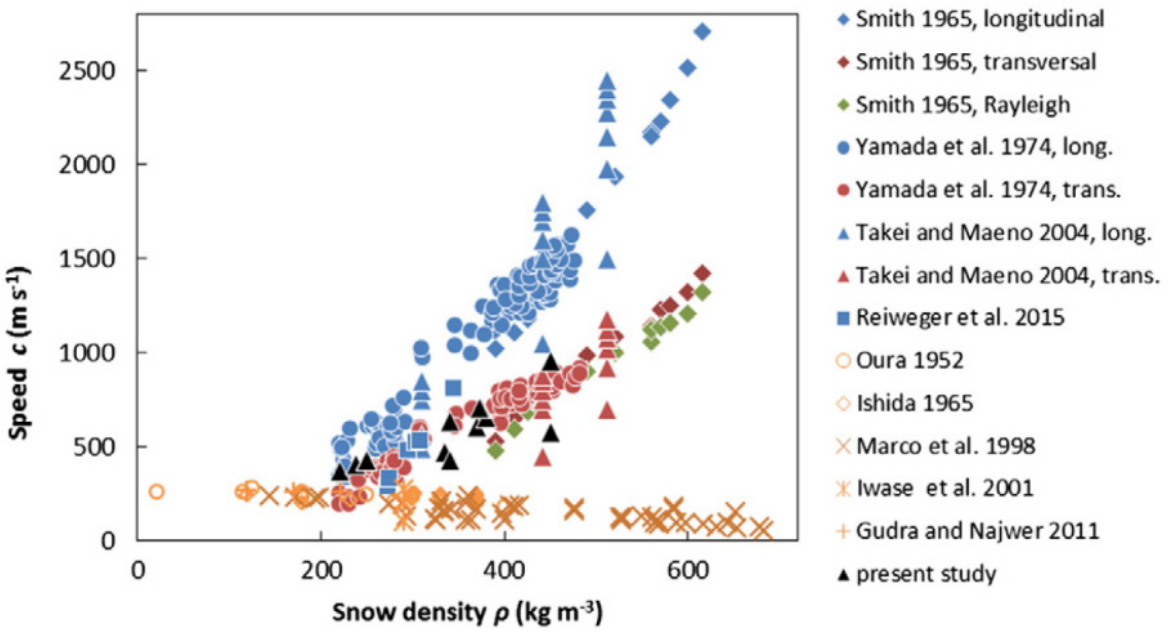

Fig. 2-3: Review of the wave speeds in snow by Capelli et al. (2016). The colors indicate the fast wave (blue), the slow wave (orange) and the transversal wave (red). Speeds were measured on different snow grain types and hence defer at the same density. Frequencies are in the range of approx. 50 Hz to 30 kHz.

2.9 Elastic moduli

Different methods exist to determine the elastic behavior of snow. True elastic moduli may only be determined using dynamic (low-amplitude) testing as many of the other methods result in elastic moduli that include plastic deformation as it is difficult to perform quasi-static and static experiments that do not cause plastic deformation. Quasi-static experiments as uniaxial compression tests were often used to determine the elastic behavior (Mellor, 1975; Scapozza, 2004; Shapiro et al., 1997). Furthermore, dynamic methods using e.g. rheometers and pulse wave propagation were used. Scapozza and Bartelt (2003) reported that field measurements of the wave propagation velocity yielded the most consistent results for the elastic modulus (constrained or P-wave modulus). However, most of these experiments were performed on high-density snow (Gerling, 2016). Using micro computed tomography scanning, it was possible to perform finite element simulations on the actual structure of snow samples (Schneebeli, 2004). It has also been suggested that an elastic modulus – referred to as Young's modulus – of snow can be derived from the penetration resistance signal as obtained with a snow micro-penetrometer (SMP) (Johnson and Schneebeli, 1999; Löwe and van Herwijnen, 2012). However, these SMP-derived values seem not directly related to the true elastic properties but include plastic deformation (Reuter et al., 2013). They have been related to the bulk modulus of the slab as observed with PTV (particle tracking velocimetry) in propagation saw tests (Reuter et al., 2015a; van Herwijnen et al., 2016b); the latter is known to include non-elastic

parts of deformation due to the complex deformation behavior at the tip of the SMP and plastic deformation during bending of the slab in PTV.

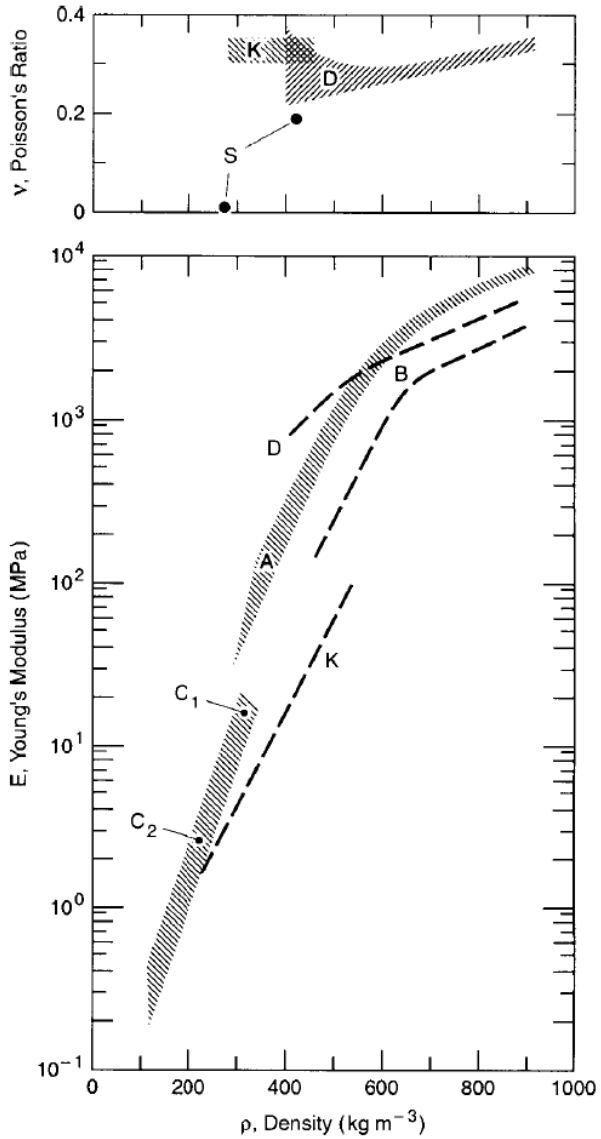

Fig. 2-4: Poisson's ratio and Young's modulus of snow over its density range. The different curves give values from different studies. Shapiro et al. (1997), modified from Mellor (1975).

Young's modulus was most often described as a function of density. As the microstructure has an important influence on snow mechanics this leads to large scatter in the data. Furthermore, viscous effects and the complex and unclear snow behavior during some experiments lead to further scatter. The Young's modulus of snow for a given density therefore scatters over three orders of magnitude and a large scatter is also observed within different fit parameters that often use exponential functions to describe the Young's and constrained modulus depending on snow density (Gerling, 2016; Mellor, 1975) (Fig. 2-4).

2.10 Crack propagation speed

Johnson et al. (2004) reported the crack speed of a whumpf at 20 m s^{-1} using seismic instruments on the surface. Hamre et al. (2014) measured crack propagation speeds from video stills involving artificial release of avalanches by spherical explosives and reported crack propagation speeds that were above all other studies with an average speed of 97 m s^{-1}. Speeds were increasing with increasing spherical explosive charge sizes. Alternatively, crack speeds were observed in propagation saw tests (van Herwijnen et al., 2016a). This resulted in crack propagation speeds between 10 and 30 m s^{-1} depending on the snowpack properties.

2.11 Summary

Wave propagation in snow is complex and depends on many different parameters. On one side, the characteristics of the source (e.g. explosion) are relevant. On the other side, snow is a very low density and compressive material with low strength. The porous character has a large influence on wave propagation and causes different wave types. The description of wave propagation in snow requires many parameters due to the complex microstructure of snow. As snow can have different mechanical properties at the same density, the parameterization of these properties is difficult. The different waves in snow are differently attenuated, have different amplitudes and different wave speeds. Because of the strong attenuation, measurements at large distances where the different waves could be distinguished due to a time lag are difficult. In addition, direct stress measurements within the snowpack are hardly feasible due to the porosity. Modeling wave propagation in snow is difficult and hence extensive studies including comparison to field results are lacking. The description of wave propagation in elastic continua is only given to understand the wave propagation principles but are not directly applied in this study that mainly focuses on the experimental approach.

3 Methods and study sites

3.1 General measurement methods

Measuring the response of a snowpack to loading by explosions can be done in different ways. The differences before and after an explosion can be recorded by conventional means as snow profiles or with a snow micro-penetrometer (SMP) to detect differences in layering, density and mechanical parameters. These methods are suitable for close ranges where plastic, large deformations can be expected. At larger distances from the point of explosion, these methods will not give significant results. Other techniques are required to get an understanding of the waves propagating above and in the snowpack and to register small deformations and possible failure. One method to track changes in the snowpack is to use cameras that record the pit wall within a snow pit. However, there are limitations for this method in snow. Small deformations are best measured with accelerometers buried/inserted in the snowpack at different distances and depths. This method can be supplemented by microphones recording the air pressure above the snowpack and pressure sensors measuring pressures within the snowpack. In addition, seismic sensors can be used to assess the effect of ground accelerations. All of the above methods were used for our experiments, with a focus on measuring with accelerometers, microphones and cameras. The measuring techniques and sensors are described in more details in the chapters where they are applied.

3.1.1 Air pressure above snow surface

For all air pressure measurements, two microphones with different peak ranges from the same manufacturer were used. These were Larcor 160 dB and 5 PSI microphones with an upper frequency limit of 10 and 1 kHz, respectively, as already used by Binger and Miller (2016). The microphones were installed directly above the snow surface, i.e. a few centimeters, with a few exceptions. The microphones were installed at the far end of the snowpit at some tens of centimeters from the pit wall in the undisturbed snowpack.

3.1.2 Accelerations within snowpack

Different ADXL accelerometers with peak ranges of 1.7 g, 5 g, 18 g and 70 g were used to measure snowpack accelerations. Low-pass filters with a limit of 2.2 kHz were installed in the data acquisition systems. The sensors measured accelerations in two directions, i.e. in a radial direction from the explosion and in the vertical direction.

3.1.2.1 Manufacturing of accelerometers

The accelerometers were fixed in a two-piece mold with the two measuring axes in the plane perpendicular to the longest extension of the sensor. The mold was filled with a two-component mixture that reacted and hardened to foam with an overall density of the sensor of approx. 200 kg m^{-3} to match an expected average density of the seasonal snow observed at our study sites.

3.1.2.2 Placement of the accelerometers

Snow pits were dug to install the sensors. Holes were drilled with a pipe into the wall parallel to the expected wave propagation direction. The sensors were then inserted and aligned with a guiding rod. The hole had a slightly smaller diameter at the end than the sensor to achieve better coupling. The middle snow pit was usually aligned on a certain axis from the point of explosion. The first and the last pits were slightly offset in opposite directions from the axis to obtain an undisturbed snowpack between the explosion and the pit wall, such that the sensors were installed in an undisturbed part of the snowpack.

3.1.3 Weak layer failure detection

Compact cameras, mainly action cameras from GoPro®, were used to identify weak layer failures. The cameras were installed in the snow pit used for the acceleration measurements recording the pit wall. Markers were inserted into the pit wall as reference points and to obtain a contrast for the focus of the cameras (van Herwijnen and Jamieson, 2005). The frame rate was usually set to 240 frames per second. Weak layer failures were assessed by manually assessing the video stills.

3.1.4 Traditional snow characterization

Traditional snow profiles were performed during all test days with a few exceptions (Fierz et al., 2009). These profiles showed the layering of the snowpack at a single location. Per test day, one profile was performed. The profile was then qualitatively compared to the snowpack layering in the other snow pits.

3.1.5 Snow density measurement

Densities were measured with depth at every few centimeters using a Denoth probe (Denoth, 1989), if possible at more than one location to assess the uniformity of the snowpack. Where the snowpack was expected to be moist or wet, additional manual density profiles were performed using a density cutter (Proksch et al., 2016). This is required as the dielectric constant measured by the Denoth device depends on the snow density and wetness. If the snow is dry, the density can be directly determined from the signal.

3.1.6 Data acquisition

Data were acquired using National Instruments cDAQ systems in each snow pit. The systems contained several A/D modules which could accommodate 8 channels each at a sample frequency of 100 kHz per channel. The measurements could be performed simultaneously on all channels. The accelerometers and microphones were connected to these modules.

In addition, digital modules were used to trigger the measuring system. A trigger cable connected to all measuring systems was used to trigger all systems simultaneously.

Data were transferred via wireless networks or network cables to a central computer used for data acquisition.

3.1.7 Triggering

Different methods were used to trigger the data acquisition. Manual triggering was used where no electronics were required to produce the source or where it was not possible to modify the system to trigger the source. This was the case for all experiments using hammers, operational avalanche release systems and for propagation saw tests. For the other systems, automatic triggering was used: The activation of the explosion created an impulse triggering the data acquisition system.

3.1.8 Ground acceleration measurement

Ground accelerations were measured using single-axis geophones SM-6 with a resonant frequency of 8 Hz and manufactured by Input/Output Inc. The geophones were installed at different distances from the point of explosion either buried in soil or mounted on rock for better coupling at the bottom of the snowpack. The measurements were running continuously at a sampling frequency of 800 Hz. Data were transmitted directly to an on-site computer and hence to the institute via the network of the artificial snow production steering and internet. These measurements were not only used to measure ground accelerations, but in particular to detect avalanches.

3.2 Data evaluation

Different methods were used for the different purposes in this thesis. Below, an overview is given on the main data evaluation techniques used in almost any of the following chapters. The methods are described in more detail in the respective chapters where the methods are applied.

3.2.1 Air pressure measurements

The maximum of the measured air pressures was used to determine the decay with distance from the explosion. Their frequency spectra, the maximum increase per time (derivative of the air pressure) and an equivalent of the energy of the air pressure wave were used to compare different explosions and the change of the wave forms with distance from the explosion. Fits of the different parameters were used to describe their behavior.

3.2.2 Acceleration measurements

The maximum accelerations were used to determine the decay of the different components (vertical and horizontal) with depth within the snowpack and distance from the point of explosion. They were

integrated over time to receive displacement velocities and displacements. An energy equivalent of the waves propagating through the snowpack was used to describe the wave propagation behavior. Attenuation coefficients for the small scale experiments for different snowpack densities were calculated using the energy equivalent. Propagation speeds were determined using the arrival times of the wave at the accelerometers. Crack propagation speeds were determined similarly.

3.2.3 High speed imaging

The videos from the cameras used for the evaluation of weak layer failures were processed to single video stills. These were analyzed manually to determine weak layer failure within the snowpack.

3.3 Study sites

All experiments were performed outside in various study sites. The study sites can be divided into flat field and slope study sites for large scale experiments and small scale study sites for the experiments on smaller snow blocks with simpler geometries.

3.3.1 Flat field large scale study site

One flat field study sites was chosen for the different types of field experiments. The advantage of a flat field site is that consecutive experiments under uniform conditions can be performed without the risks for equipment and personnel that would exist in slopes prone to avalanches. The site had to meet several requirements. The study site had to be level and sufficiently large. A seasonal snowpack with a rather long period with dry snow conditions was crucial. The study site had to be remote and allow an unobstructed view in all directions to safely perform experiments and not endanger people. Access roads were required due to heavy equipment and explosives transport. Further, explosive storage had to be as close as possible to the sites. The seasonal snowpack, the good accessibility and the low traffic were competing goals.

3.3.1.1 Military firing range Hinterrhein

The military firing range of Hinterrhein is located at 1630 m a.s.l. directly at the north portal of the San Bernardino tunnel in the Rheinwald valley in the canton of Grisons, Switzerland (46.52° N and 9.17° E). The site lies directly north of the major alpine divide and receives major precipitation mainly from the South due to orographic lifting. The firing range has a total extent of 3 km by 0.3 km with the area used for the experiments corresponding to 50’000 m^2. Experiments could be performed in parallel for different types of explosions on a level site. The fact that the site is a military firing range allowed undisturbed experiments to be performed. The crane used for the mobile gas exploder could be erected directly at the study site thanks to roads at closest distance. The firing range of

Hinterrhein was used for large-scale experiments. The low elevation resulted in short experimental periods with often warm and stable snowpacks.

Fig. 3-1: Overview over one of several flat field study plots at the firing range of Hinterrhein. Photo by Oliver Pelzer.

3.3.2 Small scale study sites

Small scale study sites were used to perform experiments on smaller snow blocks to better understand wave propagation principles which are difficult with large scale experiments due to the special propagation characteristics. The high elevation of all small scale sites yields a longer season with often more suitable snow conditions, i.e. a more unstable snowpack compared to the site at Hinterrhein.

3.3.2.1 Flüelapass

The study site on the summit of Flüelapass close to Davos in the Canton of Grisons, Switzerland, is located at an elevation of 2375 m a.s.l. The coordinates are 46.75° N and 9.94°. It is accessible during most of the season when the snow is cleared off the road. The study site is not totally level, but sufficient for small scale experiments triggering only small charge sizes up to approximately 0.5 kg Fig. 3-2). As the mountain pass is closed for traffic during the experimental season, experiments could safely be performed.

Fig. 3-2: Overview of the study site and an experiment at the Flüelapass.

3.3.2.2 Weissfluhjoch study site

The study site at Weissfluhjoch is located in the Parsenn ski area in Davos in the Canton of Grisons, Switzerland (Fig. 3-3). It is a major study site of the WSL Institute of Snow and Avalanche Research SLF (Marty and Meister, 2012). It is located at an elevation of 2540 m a.s.l., is flat and is easily accessible on skis. Its coordinates are 46.83° N and 9.81° E. Bi-weekly snow profiles are performed at the study site to monitor the development of the snowpack. The site was mainly used for small scale experiments to investigate the wave propagation principles on simple geometries.

Fig. 3-3: Flat field study site Weissfluhjoch, used for small scale experiments. Photo by Lino Schmid

3.3.2.3 Steintälli study site

The Steintälli study site is located at 2442 m a.s.l. at a weather station in a larger terrain bowl (Fig. 3-4). The coordinates are 46.81° N and 9.79° E. The study site is mainly flat directly around the

weather station. It is accessible on skis only and the small basin is used for research on snowpack stability and its variability (Reuter et al., 2015b). The site was used for small scale experiments during experiments to track the evolution of snowpack stability.

Fig. 3-4: Overview over the basin, where the Steintälli flat field study is located. The red star indicates the location of the study plot. Photo by W. Steinkogler.

3.3.3 Slope study sites

A slope study site was chosen to assess operational avalanche control systems. This was mainly required to compare the prototype used at the study site of Hinterrhein to operational gas exploders but also to test the effect of ground accelerations induced by the gas exploders on avalanche release.

3.3.3.1 Jakobshorn

The Jakobshorn study site is located in a ski resort close to Davos in the Canton of Grisons, Switzerland, and lies at an elevation of approximately 2500 m a.s.l (Fig. 3-5). The coordinates are 46.78° N and 9.85° E. Four operational gas exploders are installed at this study site between the Jakobshorn and Brämabüel in a WSW-facing slope to protect a ski traverse starting at the Brämabüel upper terminus. Experiments to compare our flat field experiments to operational gas exploders were performed at the first (northernmost) gas exploder with the most level slope. Gas exploder 2 was used to assess the effect of ground accelerations induced by the gas exploder on avalanche release. This slope is rather gully-shaped and uneven with the gas exploder standing on a rock outcrop. The terrain hindered the use of this study site for comparison experiments.

Fig. 3-5: Slope study site Jakobshorn.

4 Field measurements of snowpack response to spherical explosive loading

4.1 Introduction

Avalanche control by explosives has become a key temporary preventive measure in avalanche mitigation. To protect ski runs, power lines and occasionally exposed parts of settlements, avalanches are triggered artificially – often using explosives – during or shortly after storms (McClung and Schaerer, 2006).

The explosion causes a shock wave that propagates radially outward from the point of the explosion in the air as well as in the snow. With increasing distance from the point of explosion, it eventually behaves like an elastic wave for which the propagation speed is independent of the pressure amplitude (Mellor, 1973). The actual process leading from an explosion to an avalanche is not well understood (Frigo et al., 2012). The induced waves propagating in the snowpack lead to a temporary increase of strain. If the strength of a weak layer within the snowpack is locally exceeded, failure can occur and subsequent crack propagation may lead to the release of a slab avalanche.

Whereas avalanche control is successfully applied in practice – mainly based on extensive experience, few studies, experimental or theoretical, exist that investigated the effect of avalanche control by explosions on a snowpack, and in particular the complex behavior of snow under high dynamic loading. Comparison among the various sets of data is difficult due to different objectives, varying measurement techniques and snow conditions (Sommerfeld, 1982).

The most extensive study on the effect of explosions affecting the snow cover was performed by Gubler (1977). His experiments included varying solid explosives, detonation heights and snowpack conditions and the resulting findings are still considered state of the art in avalanche control. One of the most relevant results of Gubler (1977), also stated by Mellor (1973), was the observation that charges triggered above the snowpack are most effective in triggering avalanches.

Johnson et al. (1994) conducted experiments with sheet explosives on the snow surface to mimic plane-wave propagation and measure shock wave attenuation with buried stress gauges and found very high attenuation with distance from the explosion. Ueland (1993) showed that shock waves attenuate faster in isothermal snow whereas there is less attenuation in dry snow (Gubler, 1977).

Experiments with a gas gun revealed that snow compaction due to the explosion depends on initial snow density and that significant strain hardening occurs once a critical density is reached (Johnson et al., 1993). Johnson et al. (1993) and Johnson et al. (1994) focused on the effects at short distances from the blast. Frigo et al. (2012) also focused on short distances and in particular investigated the influence of different solid explosives and their placement on crater formation. They derived empirical laws for crater depth and diameter. Binger et al. (2006) assessed snowpack

compression dependency on detonator orientation. They reported increased layer compression with the blasting cap oriented down.

More recently, Bones et al. (2012) performed tests on dry hard and soft snow slab layers applying the measurement techniques introduced by Tichota et al. (2010) and measured air pressure above the snow surface and accelerations within the snowpack at distances ranging from 3 to 7 m from the point of explosion. They found increasing accelerations in the snowpack with increasing elevation of the spherical explosive charge above the snow surface confirming the findings by Gubler (1977) and Johnson et al. (1994). Bones et al. (2012) showed that attenuation rates of the peak accelerations in the snowpack were largely independent of the distance from the charge. Tichota et al. (2010) concluded that a buried charge does not have a widespread effect beyond the crater in moist snow conditions and mentioned the complex non-linear snow response. Wooldridge et al. (2012) conducted compression tests before and after explosions close to the point of explosion and found that compression test scores decreased. Frigo et al. (2010) performed experiments on a flat field including georadar, seismic and vibration measurements to derive snowpack characteristics, mechanical properties of the snowpack and record wave propagation.

In practice, the key question is to know how far from the point of explosion the snowpack has been sufficiently loaded so that the slope can be considered safe. Gubler (1993) proposed to define the effective range of an avalanche control method to be the radial distance from the point of detonation where the additional stress at the depth of the weak layer is larger or equal to the load of a skier. Mellor (1973) suggested the stress to be larger than 3.5 kPa, whereas Gubler (1976) considered a value larger than 1 kPa as sufficient to initiate weak layer failure, and eventually release an avalanche. Obviously, the minimal load required to release an avalanche by dynamic explosive loading will depend on the properties of the slab and the weak layer, and a fixed stress value might not fully reproduce the complexity of the problem.

The effect of ground accelerations induced by an explosion on or above the snowpack on avalanche release has not been investigated in depth. Ground accelerations might become relevant for avalanche triggering at large distances from an explosion due to the lower attenuation in soil compared to snow. However, amplitudes may not be sufficient at large distances to cause weak layer failure (Ueland, 1993). Based on field experiments, Suriñach et al. (2011) concluded that the vibrations of a commonly used gas exploder through the foundation are not sufficient to trigger avalanches beyond the effective range of the system. Chernouss et al. (2006) also investigated the effect of ground accelerations on avalanche release but due to explosions in an open-pit mine.

Several studies investigated the attenuation of blast noise propagation over snow and bare soil (Albert et al., 2008; Albert and Hole, 2001; Albert et al., 2013). They found that a snowpack significantly increases attenuation of acoustic waves above ground. Johnson et al. (1993) showed the

influence of a snow cover on blast noise propagation from C4 charges using microphones at distances ranging from 100 m to 1500 m.

Few studies have tried to model the effect of an explosion on the snowpack. Johnson (1982) used a porous model for wave propagation in snow solving Biot's equations considering the two dilatational waves and the shear wave in snow which are propagating through the ice skeleton and the pore space and which are attenuated differently. Johnson (1990) estimated shock wave attenuation in snow with a momentum model used for porous media. Miller et al. (2011) recently proposed a model for shock wave propagation in and above a snowpack caused by explosions. They showed how stress concentrations around a weak layer develop and compared model results of air pressure to data from an open air blast. Cardu et al. (2008) developed a coupled stress and energy criterion for the artificial release of slab avalanches.

Comprehensive field measurements covering a large range of distances from the point of explosion and measuring the snowpack's response at different distances simultaneously with modern measuring techniques have not been performed so far. Weak layer failure detection in avalanche control experiments was not feasible so far and hence measurements of how weak layers fail caused by an explosion are lacking.

We developed the experimental setup based on the findings by Bones et al. (2012) and Tichota et al. (2010) to measure the influence of an explosion on a seasonal snowpack. During the winter 2013-2014 we performed a series of detailed measurements with commonly employed solid avalanche control explosives used in Switzerland. Our goal was to measure acoustic wave propagation in the snowpack and to record air pressure and acceleration as a function of charge elevation, charge size, receiver location and snowpack conditions while measuring simultaneously at different distances from the point of explosion. Our results should contribute to an improved understanding of the complex wave propagation principles in a snowpack and serve as a base for modelling. Furthermore, we aimed at introducing a method to detect weak layer failure during avalanche control experiments using explosives.

4.2 Methods

4.2.1 Study site

A military firing range in the Swiss Alps directly north of the alpine divide was chosen as study site. The site is characterized by a plane level field with a total area of about 55,000 m^2 at an elevation of 1680 m a.s.l. Roads directly besides the site allow for good accessibility. A flat level study site was chosen to ensure good reproducibility of the experiments; it allows to compare different methods under comparable conditions and to perform safe and precise measurements at the intended

location. Flat study sites have already been previously used (e.g. Binger et al., 2006; Bones et al., 2012; Frigo et al., 2010).

4.2.2 Meteorological conditions during winter 2013-2014

During the winter 2013-2014, snow depth was well above average as recorded at 10 km distance from the study site at the observer station of Splügen (1457 m a.s.l.). The maximum snow depth at Splügen was 144 cm, whereas we recorded a snow depth of up to 187 cm at the study site during the test days directly at the location of the experiments. The relatively thick snowpack did not include any persistent weak layers during the entire winter and can be classified as generally stable (Schweizer and Wiesinger, 2001). The relatively smooth topography was leveled out by snowfall and snow drift. Snow depth varied slightly, but the snowpack layering was spatially rather uniform.

4.2.3 Experimental data winter 2013-2014

We performed 37 experiments on eight test days with dry (6 days) and wet (2 days) snowpack conditions. For each experiment, we measured air pressure near the snow surface at three different horizontal distances from the point of explosion and snowpack acceleration at approximately the same horizontal distances and three depths within the snowpack (Fig. 4-1). We recorded high speed videos in each snow pit to perform particle tracking (see below) in order to assess weak layer failure. Coordinates of pit locations were measured by differential GPS at the position of the microphone. Positions of the acceleration sensors were measured relative to the position of the microphone.

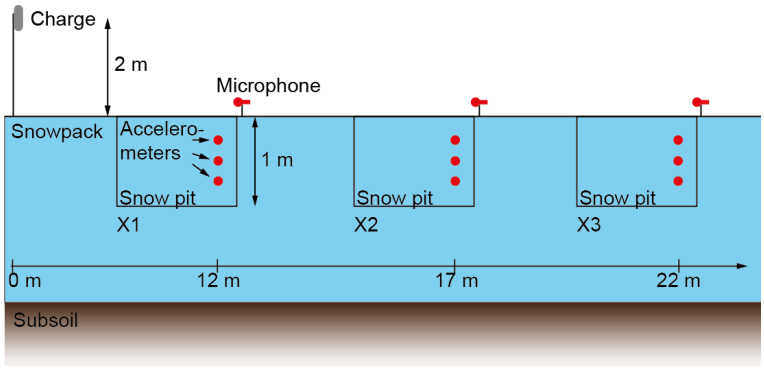

Fig. 4-1: Longitudinal section of an exemplary measuring layout indicating snow pits X1 to X3 with increasing distance from the point of explosion, charge location, microphones and accelerometers at different distances from the point of explosion and depths within the snowpack. As an example, the charge was elevated at 2 m, the horizontal location of the charge is 0 m, the snow pits X1 to X3 were located at 12, 17 and 22 m horizontal distance from the point of explosion, respectively. Snow pit depth was usually about 1 m.

4.2.4 Air pressure measurement

Microphones, as employed by Tichota et al. (2010) and Bones et al. (2012), with an upper pressure limit of 34.5 kPa and manufactured by Larcor were used to measure near-surface air pressure resulting from the explosion at different distances from the point of explosion above the snow surface. For all tests and all pits, air pressure was measured 5 to 10 cm above the snow surface. On one test day, two measurement setups were used in one pit to measure air pressure in addition at 0.96 m above the snow surface.

Propagation speeds of the air pressure wave were calculated from the air pressure arrival times at the different microphones.

4.2.5 Acceleration measurement

Two-directional accelerometers (Analog Devices ADXL203, AD22293, AD22037, and ADXL001) were used to measure accelerations within the snowpack (Table 4-1). All sensors except the ADXL 001 are dual-axis sensors. Two ADXL001 single axis sensors were mounted perpendicularly on a board to be able to measure strong accelerations in two directions. The accelerometers were sealed in foam cylinders in a similar way as described in Gubler (1976); the foam consisted of a two-component mixture with a density corresponding to an average snow density of 200 kg m^{-3} (Fig. 4-2). We installed the accelerometers within cut-out cavities in the snowpack (Fig. 4-3) that were slightly smaller in radius at the tip than the sensor to ensure good coupling to the snowpack. A guiding rod was used to place and align the sensor within the cavity. After the measurement the sensors were recovered with a cord fixed to the sensor (Gubler, 1976). Three accelerometers were installed in each snow pit at depths ranging from 0.13 to 0.22 m for the uppermost sensor, 0.43 to 0.53 m for the middle sensor and 0.78 to 0.93 m for the lowest sensor with the exception of one test day when all sensors were buried about 0.35 m deeper than the values given above. Accelerations were measured in radial (horizontal) and vertical directions.

Table 4-1: Accelerometer specifications (www.analog.com).

	ADXL203	AD22293	AD22037	ADXL001-70
Range (g)	+/- 1.7	+/- 6	+/- 18	+/- 70
Sensitivity (mV/g)	1000	312	100	24
Resonant frequency (Hz)	5500	5500	5500	>20000

Fig. 4-2: Acceleration sensor sealed in foam cylinder (length: 20 cm, diameter: 6 cm).

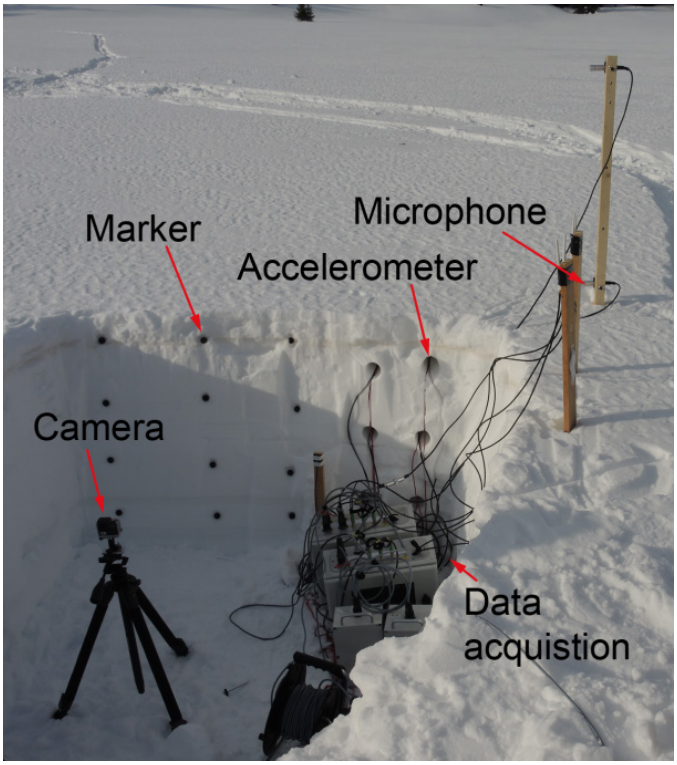

Fig. 4-3: Measuring equipment in a snow pit. Markers and camera are used for particle tracking velocimetry and failure identification. The three (in this example six) accelerometers are installed within the snowpack in the cavities of the pit wall. The charge is triggered left of the picture and air pressure waves hence propagated through the air from left to right.

4.2.6 Recording weak layer failure

Particle tracking has previously been used to record snowpack deformation during snow instability tests (e.g. van Herwijnen et al., 2010). Commodity compact cameras manufactured by GoPro were installed in each snow pit on tripods and recorded the pit wall at 240 frames per second with a

resolution of 848x480 pixels during the explosion. The specific camera model was chosen due to its low cost, acceptable frame rate and resolution. Markers were installed at the pit walls for particle tracking. The single video stills allowed weak layer failure due to movement of the snowpack to be identified visually. Failure depth within the snowpack can be determined when distances between markers measured at the pit wall change. The time of the explosion was recorded by LED lights flashing at the time of triggering the data acquisition and the explosion.

4.2.7 Data acquisition

In each snow pit a box containing the data acquisition device and wireless transmission equipment was installed. Data were acquired with several National Instruments cDAQ-9184 (AD converter) recording devices as previously used by Bones et al. (2012) installed in each snow pit. NI 9215 modules were employed to record the signals simultaneously, whereas NI 9402 modules were used for triggering the data acquisition.

Data were recorded at a sampling frequency of 20 kHz and were wirelessly transmitted to a central field computer for data storage. The wireless equipment allowed for efficient installation of the instrumentation and reduced the wired connections to a single data acquisition trigger cable between the snow pits.

4.2.8 Snowpack characterization

A complete snow profile (Fierz et al., 2009) including layer characteristics and density was recorded on each of the test days in one of the measurement pits. In addition, snow density was measured in each of the three snow pits using a capacity probe (Denoth, 1994). Manual density was also recorded layer by layer if possible. Measurements were taken at intervals of 5 cm or 10 cm starting from close to the snow surface down to the bottom of the pit (approximately 1 m for all experiments) or the bottom of the snowpack. The depth of the pit was chosen with respect to the fact that repeated artificial triggering rarely leads to large slab thickness and that slab thicknesses involved in skier-triggered avalanches hardly exceed 1 m (van Herwijnen and Jamieson, 2007).

4.2.9 Spherical explosives and triggering

Spherical slurry explosive charges were used for this study (Table 4-2). Charge sizes employed in manual avalanche control in Switzerland are in the range of 1.5 to 3.5 kg. Charge sizes installed in fixed avalanche control installations in Europe mainly range between 4.25 and 5 kg.

For the experiments, the solid explosives were triggered electrically using a blasting machine. The electrical current to ignite the charge was also used to trigger the data acquisition system and to define the time of the detonation.

Table 4-2: Solid explosive characteristics.

Explosive name	Alpinit
Explosive type	Slurry
Explosive density (kg m^{-3})	1200
Explosive energy (kJ kg^{-1})	5610
Detonation speed (m s^{-1})	4900

4.2.10 Wave arrival time

The arrival time of the wave with the strongest amplitude recorded with the accelerometers and the microphones was determined using an STA/LTA (short time average/long time average) algorithm, where short and long time averages of the signals are compared and a certain threshold is implemented which defines the start (Withers et al., 1998); in addition, the arrival time was checked visually and corrected if required.

4.3 Results

4.3.1 Snowpack

The thick snowpack during winter 2013-2014 was relatively warm with snow temperatures in the range of -2 to -1°C on the days with a dry snowpack. The snowpack was isothermal during the last two test days. Stability tests on the flat study site (Schweizer and Jamieson, 2010) indicated good snowpack stability. A summary of snowpack characteristics is shown in Table 4-3. Little variation in density was observed between the three density profiles on each test day. Hence the snowpack was considered spatially uniform. Snowpack densities were in the range of 75 to 495 kg m^{-3}, usually increasing with depth with some less dense, weaker layers and some ice crusts with ice density.

Table 4-3: Snowpack characteristics of all tests during winter 2013-2014 including snow depth, wetness and stability class (according to Schweizer and Wiesinger (2001)).

Date	Field site	Snow depth (cm)	Snowpack wetness	Stability class
12 Feb 2014	HINT	153	dry	good
18 Feb 2014	HINT	176	dry	good
25 Feb 2014	HINT	177	dry	good
27 Feb 2014	HINT	187	dry	good
25 Mar 2014	HINT	145	wet	good
26 Mar 2014	HINT	151	wet	good

4.3.2 Air pressure

A typical measurement of near-surface air pressure for three different distances from the point of explosion is shown in Fig. 4-4. A sharp increase in pressure is followed by a strong decrease and a negative pressure pulse. Finally, a strongly damped oscillation can be observed. Distortion can be seen in the shape of the air pressure wave. Higher frequencies are attenuated more strongly with increasing distance from the point of explosion (Fig. 4-4). The maximum air pressures of all experiments from winter 2013-2014 are shown in Fig. 4-5. To compare experiments with different charge sizes, distances were scaled. As we always used the same type of spherical explosives, this was done by scaling the distance x by the cube root of the charge mass m (kg) (Bones et al., 2012; Cooper, 1996):

$$x' = x\, m^{-\frac{1}{3}}\, (m\, kg^{-\frac{1}{3}}) \tag{4.1}$$

When the air pressure is plotted in a double-logarithmic plot against the scaled distances from the point of explosion, the measurements gather along a straight line suggesting a power law relation (Bones et al., 2012). We therefore fitted a power law to each experiment for the maximum positive p_{max} and negative air pressure p_{min}

$$p = a\, x'^{-b} \tag{4.2}$$

where x' is the distance from the point of explosion, scaled by the solid explosive mass (m $kg^{-1/3}$), a and b are parameters. The maximum air pressure decayed with $x'^{-1.1}$ to $x'^{-2.1}$ with a mean exponent b of 1.66 (Fig. 4-5).

For the first pit, charge elevation was considered in the calculation of the air pressure propagation speed. Propagation speeds reached 547 m s^{-1} for the microphone locations closest to the point of explosion down to 332 m s^{-1} for the largest distances (Table 4-4 and Fig. 4-6).

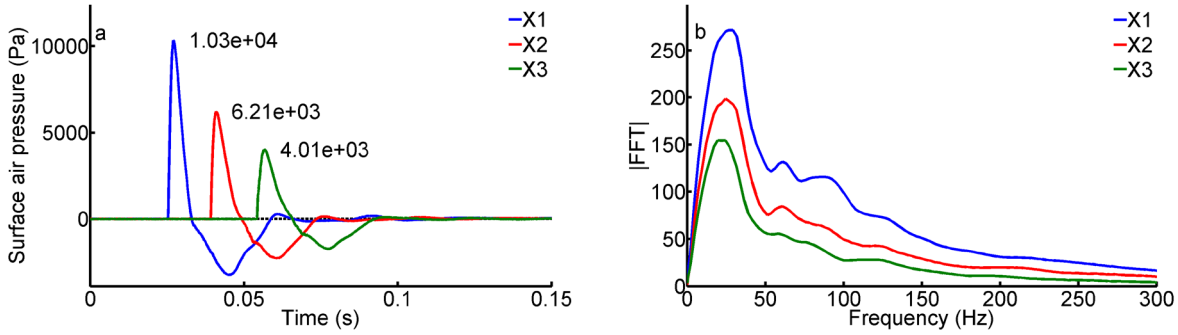

Fig. 4-4: (a) Typical air pressure waves and (b) their frequency content (right, Fast Fourier Transform: FFT) measured at three different distances from the blast (X1: 12.3 m, X2: 17.3 m, X3: 22.5 m). Data from 27 February 2014, test 1.

.

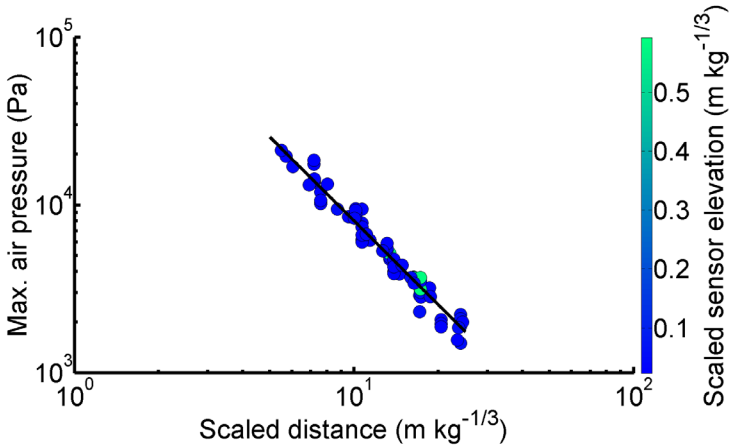

Fig. 4-5: Maximum air pressure of all experiments vs. scaled horizontal distance from the point of explosion. Marker fill color shows the elevation of the microphone above the surface (N = 25). The line indicates a power law fit according to equation (2) with exponent b = -1.66.

Table 4-4: Summary of all experiments indicating charge elevation, charge mass, air pressure wave propagation speed (c_{air}) between the point of explosion X0 and pit X1, pit X1 and pit X2, and pit X2 and pit X3. The distances were horizontally measured between the point of explosion and the respective pit. Systems with same distances during a test indicate two microphones at the same distance.

Date	Test no.	Charge elevation (m)	Scaled charge elevation (m $kg^{-1/3}$)	Charge mass (kg)	Distance (m)			c_{air} (m s^{-1})		
					X1	X2	X3	Det-X1	X1-X2	X2-X3
6 Feb 2014	1	2	1.17	5	19.2	29.4	41.2	397	340	352
6 Feb 2014	2	2	1.17	5	19.2	29.4	41.2	396	338	352
6 Feb 2014	3	1	0.58	5	19.2	29.4	41.2	407	332	332
6 Feb 2014	4	0	0.00	5	19.2	29.4	41.2	386	336	349
12 Feb 2014	1	1.85	0.91	8.5	9.6	19.5	29.7		327	
12 Feb 2014	2	1.85	1.08	5	9.6	19.5	29.7		326	
12 Feb 2014	3	1.85	1.08	5	5.5	15.3	25.4			
12 Feb 2014	4	1.5	0.88	5	21.9	31.9	41.8		331	
18 Feb 2014	1	2	1.17	5	20.0	30.0	40.0	366	370	333
18 Feb 2014	2	3	1.75	5	15.0	25.0	35.0	398	379	335
18 Feb 2014	3	2	1.17	5	15.0	25.0	35.0			
18 Feb 2014	4	2	1.17	5	15.0	25.0	35.0	410	369	338
18 Feb 2014	5	1	0.58	5	15.0	25.0	35.0	415	369	334
25 Feb 2014	1	2	1.23	4.25	17.3	28.0	28.0	436	347	
25 Feb 2014	2	2	1.23	4.25	17.3	28.0	28.0	437	345	348
25 Feb 2014	3	2	1.17	5	17.3	28.0	28.0	435	351	355
25 Feb 2014	4	3	1.85	4.25	17.3	28.0	28.0	432	351	355
25 Feb 2014	5	2	1.23	4.25	12.3	23.0	23.0			
25 Feb 2014	6	2	1.17	5	12.3	23.0	23.0	494	359	363
25 Feb 2014	7	2	1.17	5	12.3	23.0	23.0	518	359	363
27 Feb 2014	1	1	0.62	4.25	12.3	17.3	22.5	490	358	343
27 Feb 2014	2	1	0.62	4.25	12.3	17.3	22.5	497	355	345
27 Feb 2014	3	1.9	1.17	4.25	12.3	17.3	22.5	496	364	347
27 Feb 2014	4	2	1.23	4.25	12.3	17.3	22.5	472	362	344
27 Feb 2014	5	2	1.17	5	12.3	17.3	22.5	505	363	347
27 Feb 2014	6	3	1.75	5	12.3	17.3	22.5	497	370	351
27 Feb 2014	7	3	1.75	5	12.3	17.3	22.5	505	366	349
27 Feb 2014	8	2	0.93	10	12.3	17.3	22.5	534	377	
25 Mar 2014	1	2	1.47	2.5	11.8	21.7	32.1	452	347	333
25 Mar 2014	2	2	1.17	5	11.8	21.7	32.1	481	349	333
25 Mar 2014	3	2	1.02	7.5	11.8	21.7	32.1	534	355	335
25 Mar 2014	4	2	0.93	10	11.8	21.7	32.1	547	358	339

26 Mar 2014	1	1	0.74	2.5	12.2	17.2	22.8	452	350	339
26 Mar 2014	2	2	1.17	5	12.2	17.2	22.8	489	352	
26 Mar 2014	3	2	1.17	5	12.2	17.2	22.8	495	352	
26 Mar 2014	4	1	0.62	4.25	12.2	17.2	22.8	521	352	
26 Mar 2014	5	1	0.62	4.25	7.0	11.9	17.6		373	
26 Mar 2014	6	0	0.00	8.5	7.0	11.9	17.6		373	

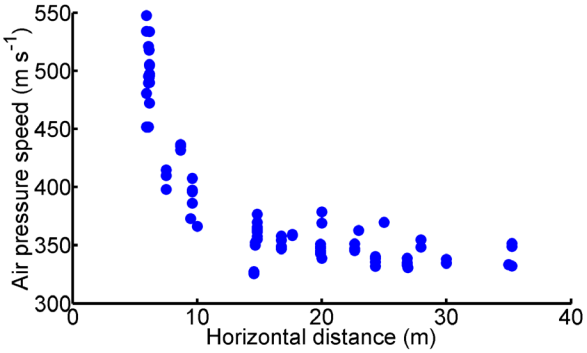

Fig. 4-6: Decrease of the air pressure speeds to sound speed with unscaled distance from the point of explosion.

4.3.3 Acceleration, displacement velocity and displacement

Vertical accelerations decreased strongly with depth in the snowpack and horizontal distance from the point of explosion (Fig. 4-7). The depths of the sensors were scaled due to the different charge masses used for the experiments. At the top sensors, vertical maximum accelerations ranged from more than 500 m s^{-2} for short distances of 7 m or large charge sizes of 8.5 kg to 10 m s^{-2} for large distances up to 41.8 m and small charge sizes of 2.5 kg. Maximum accelerations at the deepest sensors correspondingly ranged from 50 m s^{-2} to 2 m s^{-2} with increasing distance from the first to the last pit. The uppermost accelerometer in each pit and in each experiment showed a high frequency first peak which was distorted and attenuated at the locations of the lower accelerometers (Fig. 4-8). During some of the experiments, before the arrival of the distinct high amplitude wave, a first low amplitude high frequency wavelet was observed (Fig. 4-9). This first wave was not visible at deeper sensor locations (Fig. 4-8). The first prominent wave was usually superimposed by waves with smaller amplitudes and during some experiments followed by waves with small amplitudes that arrived later at the sensor (Fig. 4-9). During some experiments, a second major wave reached or even exceeded the amplitude of the first wave (Fig. 4-10). The horizontal signals show the same features as the vertical accelerations but with smaller amplitudes (Fig. 4-8). The frequency content illustrates the decay in the higher frequency range with increasing depth within the snowpack (Fig. 4-11).

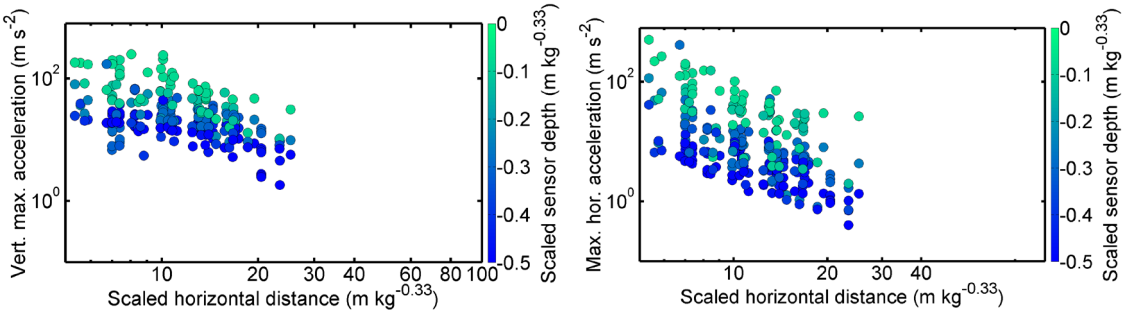

Fig. 4-7: (a) maximum vertical and (b) horizontal accelerations of all experiments with increasing scaled horizontal distance from the point of explosion. Marker fill color shows the scaled accelerometer depth below snow surface.

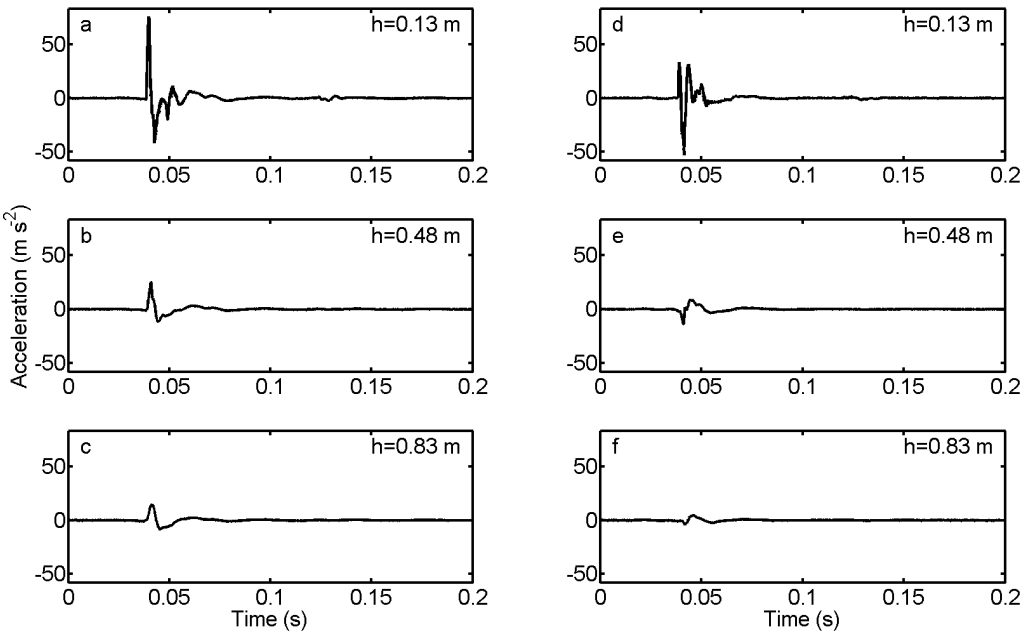

Fig. 4-8: Vertical (a, b, c) and horizontal (d, e, f) accelerations with increasing depth at a horizontal distance of 17.3 m from the point of explosion. Data from 27 February 2014, test 1.

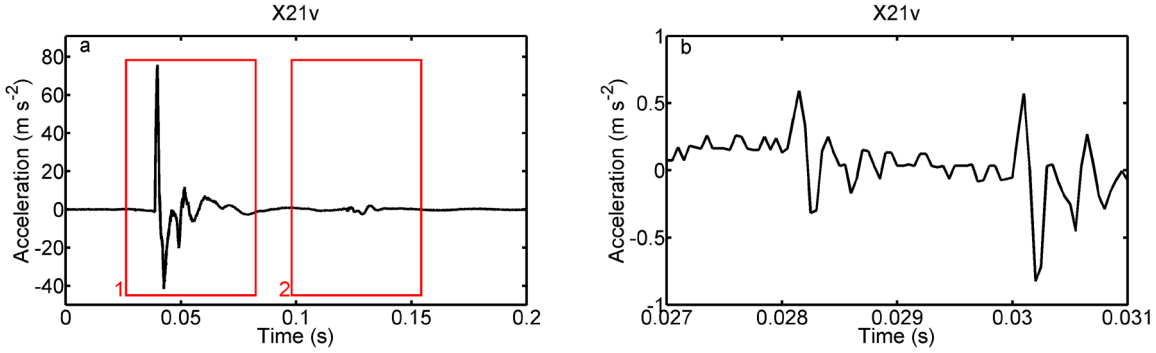

Fig. 4-9: (a) Example of vertical acceleration at 0.13 m below the snow surface and 17.15 m horizontal distance from the point of explosion. In panel 1 a wave arrives preceding the main, high amplitude wave. In panel 2 the arrival of a later wave propagating through the snowpack is highlighted. (b) Excerpt showing the wave preceding the main, high amplitude wave (in panel 1 of Fig. 4-9a). Data from 27 February 2014, test 1.

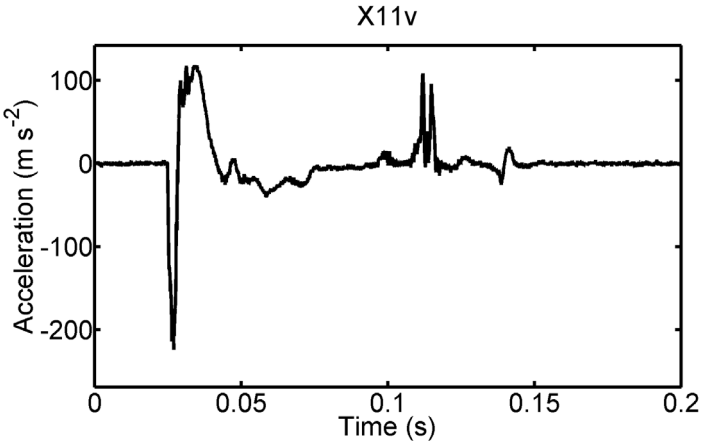

Fig. 4-10: Vertical acceleration at 0.13 m below the snow surface at the first snow pit with a distinct second wave with similar positive amplitude as the first wave. Data from 27 February 2014, test 4.

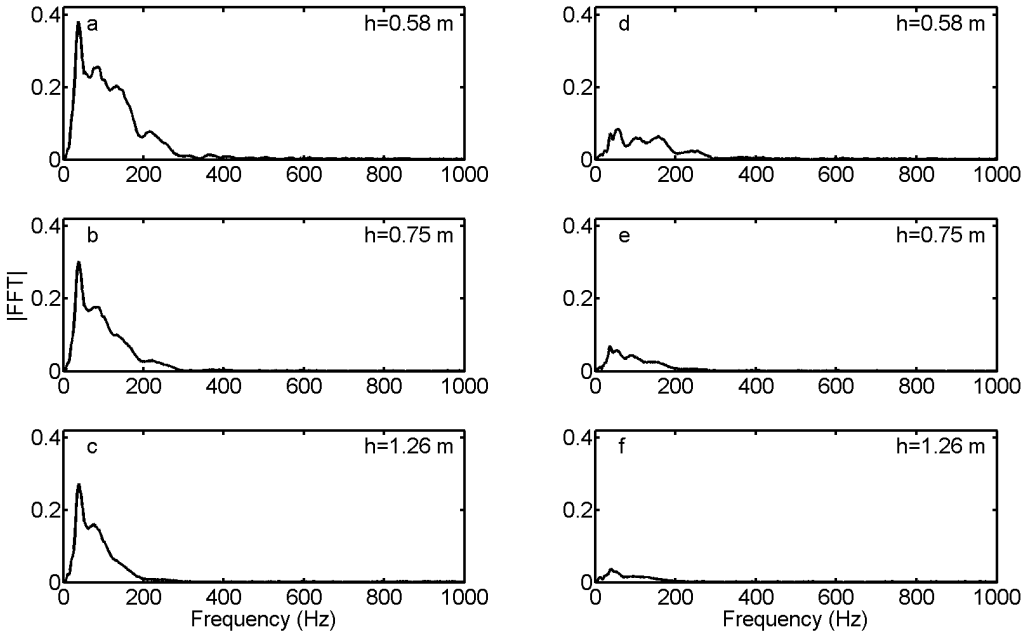

Fig. 4-11: Frequency content of the vertical (a, b, c) and horizontal (d, e, f) accelerations with increasing depth from top to bottom, at a horizontal distance of 20.0 m from the point of explosion. Data from 18 February 2014, test 1.

For each pit, vertical and horizontal components of the acceleration were plotted against the depth of the respective sensor and fitted to a power law (Fig. 4-12). As the depth of the sensors slightly varied from pit to pit, the acceleration was then calculated for a given depth for each pit of a single experiment using these power law functions. This procedure allowed the decrease of the acceleration in a given depth with distance from the point of explosion to be determined – by again fitting a power law relation. At a depth of 0.3 m $kg^{-1/3}$ below the snow surface, for which the fits were calculated, vertical minimum and maximum accelerations on average decreased proportional to $x'^{-1.3}$ and $x'^{-1.0}$, respectively, but scatter was large. Horizontal minimum and maximum accelerations

decreased more strongly proportional to $x'^{-2.1}$ and $x'^{-1.9}$, respectively. Considering minimum, maximum, horizontal and vertical accelerations, the decay of accelerations between consecutive tests with equal charge mass and charge elevation above the snow surface was for most tests approximately the same considering slight variations in charge elevation, charge masses and horizontal position of the point of explosion.

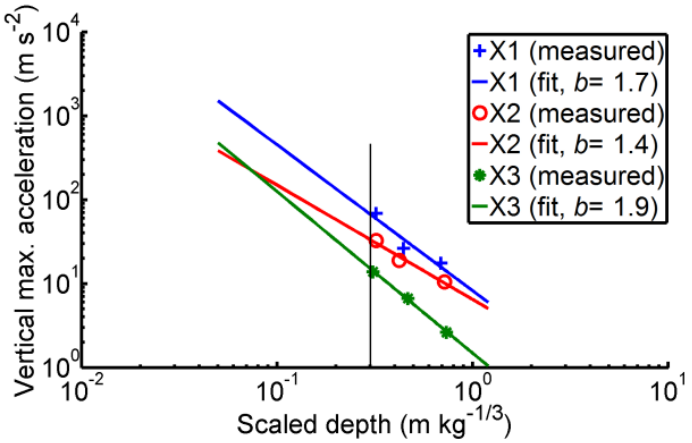

Fig. 4-12: Measured and fitted (power law) maximum vertical acceleration with scaled sensor depth within the snowpack at three different scaled horizontal distances from the point of explosion (X1: 8.2 m, X2: 14.4 m, X3: 20.3 m) on 18 February 2014, test 3.

Displacement velocity is the speed, with which a particle in the snowpack moves due to loading by a wave as e.g. caused by an explosion. Displacement velocity is derived by integrating the snowpack acceleration with respect to time. Velocity was calculated for all experiments. Fig. 4-13 shows typical velocities for a certain distance from the point of explosion. Velocities were usually largest close to the surface and in vertical direction and decayed with depth within the snowpack with a few exceptions. As for the accelerations and the air pressures, a power law was fitted to describe the relation between displacement velocity and depth of the sensor within the snowpack. Then, these functions were again fitted with a power law using the scaled horizontal distance from the point of explosion and a certain depth within the snowpack. Vertical minimum and maximum displacement velocities decayed proportional to $x'^{-1.2}$ and $x'^{-0.8}$, respectively. The respective horizontal displacement velocities decreased proportional to $x'^{-1.8}$ and $x'^{-1.9}$, respectively. The accelerations and displacement velocities were well reproducible for consecutive tests with the same measuring setup and charge masses.

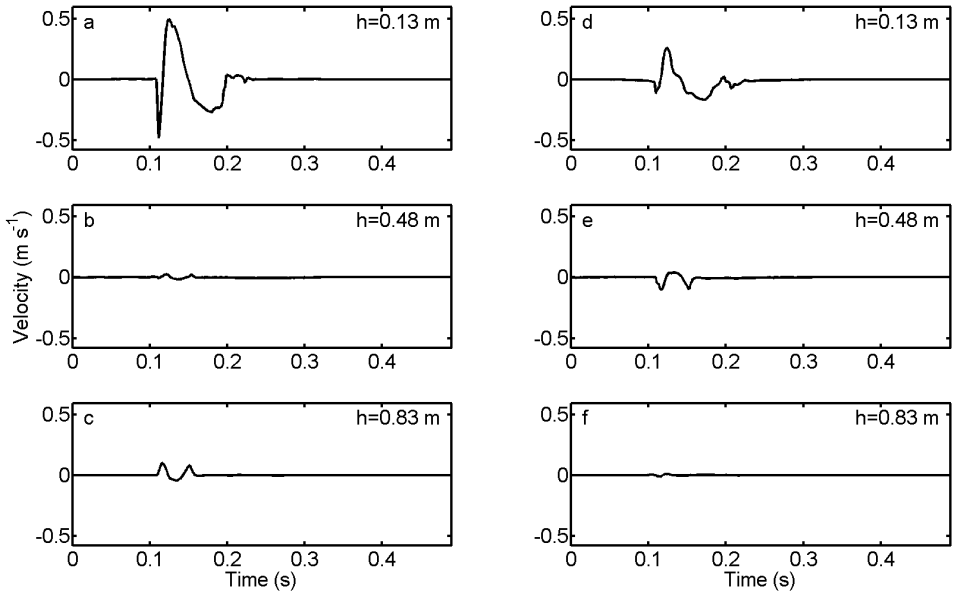

Fig. 4-13: Example of vertical (a, b, c) and horizontal (d, e, f) displacement velocity with increasing depth (top to bottom) at a horizontal distance of 12.3 m from the point of explosion. Data from 27 February 2014, test 4.

Displacements in vertical and horizontal directions of the different sensors were calculated by integrating displacement velocity with respect to time. Because sensor noise caused increasing displacement even after the wave had passed, the signal was cut manually before and after the main contributions of the displacement velocity to displacement.

Maximum displacement reached a maximum of a few millimeters but decreased strongly with depth within the snowpack (Fig. 4-14). Final, remaining displacement was in the range of a few millimeters for the uppermost sensors but usually small for all other sensors. As for acceleration, displacement velocity and air pressure, a power law was used to fit the maximum and minimum displacement amplitude with increasing depth. Then, a power law was used to determine maximum displacement depending on the horizontal distance from the point of explosion.

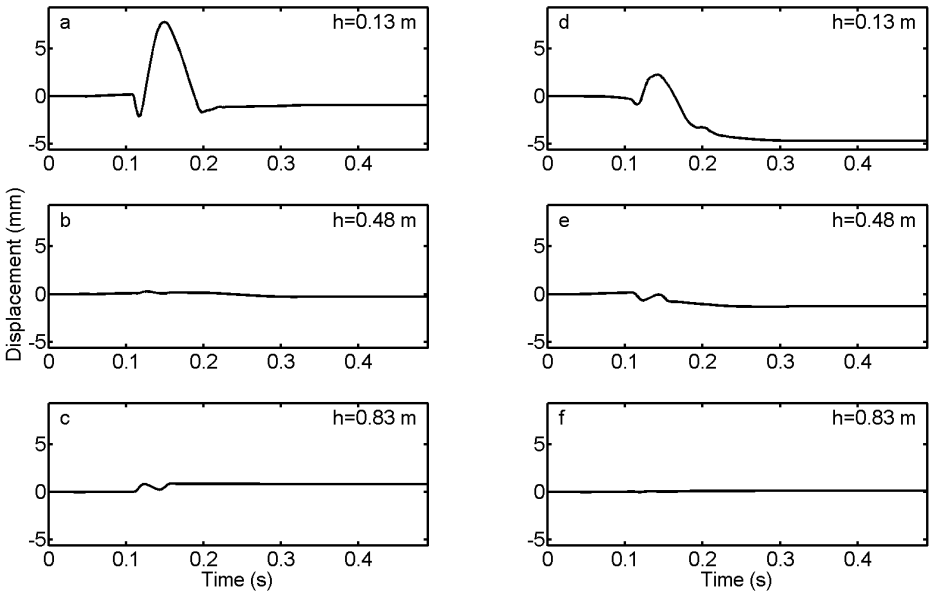

Fig. 4-14: Example of vertical (a, b, c) and horizontal (d, e, f) displacement with increasing depth (top to bottom) at a horizontal distance of 12.3 m from the point of explosion. Data from 27 February 2014, test 4.

Final vertical and horizontal displacements were in the range of 10^{-4} to 10^{-5} m, with some measurements up to a maximum of 1 cm.

Microphones were installed slightly displaced horizontally from the accelerometers by a distance of 0.35 m up to 1.35 m in order to not disturb the snowpack above the sensors. With a few exceptions, the high amplitude wave within the snowpack arrived 5 to 16 ms earlier at the accelerometers than the air pressure wave at the microphone. Often, a second major wave (Fig. 4-8 a to c and Fig. 4-10) was visible in the signal. This wave decayed in amplitude with distance and depth within the snowpack. The time delay of this wave compared to the first high amplitude wave was between 0.05 and 0.09 s.

4.3.4 Weak layer failure

We made 106 observations of pit walls with cameras during the winter season 2013-2014. We observed 20 failures, some of them including multiple failures at different depths (Fig. 4-15). Most failures were observed in non-persistent weak layers since no prominent weak layers existed in the generally stable snowpack. Failures occurred immediately after arrival of the air pressure wave which could be identified by a snow spray. In most cases, failure layers were close to the snow surface but occasionally failures deep in the snowpack (up to 1 m below the snow surface) were recorded in tests with either large charge sizes or pits close to the point of explosion. Only 6 failures were observed with depths larger than 0.5 m below the snow surface.

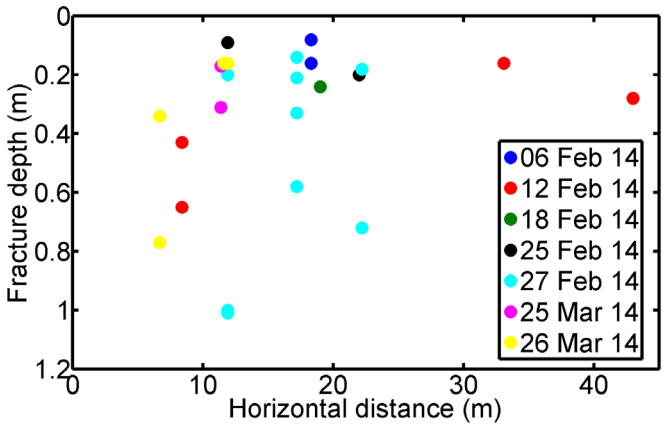

Fig. 4-15: Points indicating the maximum horizontal distance from the point of explosion and depth below snow surface where failures were observed.

4.4 Discussion

4.4.1 Air pressure

Air pressure showed a typical decay while travelling above the snow surface. The decay is due to a combination of shock wave transition, spherical spreading as well as a change in reflection of wave energy off the porous snow surface. The amplitude of a spherical wave decays proportional to r^{-1}, where r is the radius from the source. We observed a decay proportional to $x'^{-1.1}$ to $x'^{-2.1}$. The stronger decay than in the case of a spherical spreading is caused by charge elevation which causes a different incident angle on the snowpack and hence a different reflection and a different effect on the air pressure measured; in addition, snow surface properties contribute to the variation.

The wave velocities above the speed of sound, increasing with decreasing distance from the point of explosion indicate that we measured to some extent in the range of shock propagation, which is a non-adiabatic process and causes a stronger decay. Miller et al. (2011) numerically modeled the effect of explosions on a snowpack. Their modeled air pressure was higher than the predicted open air pressure. Our values of air pressure were in the range of an open air blast as shown in Miller et al. (2011). Low density snow at the top of the snowpack and hence the porous interface has a similar impedance as air and does not reflect the incoming wave strongly which is why the expansion is more similar to an open air blast.

We measured lower air pressure values than Mellor (1965) reported, probably due to less effective spherical explosives used in our experiments which is indicated by the very high detonation speeds he mentioned. The air pressures reported in Mellor (1973) but originally measured by Ingram (1962) were also higher than our data possibly as well due to the different type of spherical explosive used. Ingram (1962) showed a decay of air pressure which corresponds reasonably well with our results (Table 4-5). We measured a stronger decay than Gubler (1976) who used a charge of 1 kg of

Plastex detonated 1 m above the snow surface. Albert and Hole (2001) investigated blast noise propagation above a snowpack which is in very good agreement with our data. They suggested that rather the influence of the snowpack is relevant for the magnitude of the decay than shock effects close to the point of explosion.

Air temperatures measured during the experiments were ranging from -4 to 0°C so that the sound speed in air is expected to range from 329 to 331 m s^{-1}. In the vicinity of the point of explosion, air pressure wave speeds were (markedly) higher than the sound speed (Table 4-4). Further from the point of explosion, wave speeds decreased and were in the range of the expected sound speed. Speeds peaked at 547 m s^{-1} for distances measured between the point of explosion and the closest pits (5.5 to 19.2 m) decreasing to 332 m s^{-1} between pits furthest from the point of explosion (17.6 to 41.8 m). Speeds at closer range indicate that we measure to some extent within the range of inelastic shock expansion as shock propagation speeds are higher than the speed of sound.

Table 4-5: Power law exponent b for the air pressure decay reported in different studies.

	Exponent *b*
Ingram (1962), Mellor (1973)	1.43
Gubler (1976)	1.125
Albert and Hole (2001)	1.5 to 1.9
Present study	1.1 to 2.1

4.4.2 Acceleration, displacement velocity and displacement

For explosions above the surface, Gubler (1976) reported ice lattice accelerations for a snowpack deeper than 1.2 m and the sensor at depths smaller or equal to half the snow depth. Our results show comparable values for the middle accelerometer in Fig. 4-8 considering the larger charges employed in our experiments. Maximum vertical accelerations with scaled distance from the point of explosion decayed proportional to x'^{-1} on average at 0.3 m $kg^{-1/3}$ depth within the snowpack for the experiments performed under dry snowpack conditions – but scatter was large. Maximum horizontal accelerations decreased even more rapidly with distance proportional to $x'^{-2.1}$ on average. A strong decay in amplitude of radial accelerations was also observed for close ranges from the point of explosion by Bones et al. (2012) ranging from $x'^{-1.25}$ to x'^{-3} depending on the scaled charge height. Consecutive testing with same charge sizes and charge elevations above the snowpack had neither a significant influence on maximum acceleration nor maximum air pressure. The snowpack was probably not affected sufficiently to cause any difference in the wave propagation characteristics

directly above or within the snowpack. Only at short ranges settlement of the snow surface due to compaction could be observed after subsequent experiments. Actual crater formation was only observed for zero or small charge elevation above the snow surface which is in agreement with the results of Strange et al. (1961) and Frigo et al. (2012) who show decreasing crater size with increasing charge elevation.

The complex wave propagation characteristics in snow caused by a point source explosion above the snowpack hamper the interpretation of the recorded signals from only few selected locations. In a snowpack, three different wave modes occur as described by Johnson (1982). In addition, surface waves exist caused by the shallow incident angle of the air pressure wave at the investigated distances from the point of explosion. Furthermore, these three different wave types travelling within the snowpack and the surface waves are generated by the air pressure hitting the surface at each point between the point of explosion and the measurement location – so that the recorded signal is a superposition of many different waves and wave types. It is therefore not possible to determine with certainty which of the many waves observed in the accelerometer signal corresponds to which kind of wave mode and where it originated from. With the size of the acceleration sensor, we presumably measured a combined acceleration of the ice lattice and the air wave within the pores. The contribution of these to the overall acceleration is not known. The wave which was arriving before the high amplitude wave in some experiments could not be seen in all of the experiments due to the probably very low amplitude in the range of signal noise. The early arrival time might correspond to the high velocity of the first dilatational wave through the ice skeleton; however, one would not expect such low amplitudes for this type of wave. The waves that arrived later at the sensor might originate from the air pressure wave hitting the snow surface at different locations and being partly transmitted into the snowpack.

Maximum and final displacements recorded at the top sensors within the snowpack were higher than those buried deeper. Horizontal final displacement was probably due to low density snow close to the surface that was deformed, whereas vertical final displacement was mainly due to compaction of the snowpack. As no persistent weak layers existed that could have failed and collapsed, large vertical displacements were not observed; instead we only recorded small values of vertical displacement in the range of 10^{-4} to 10^{-5} m. Due to higher densities in greater depths within the snowpack and consequently higher elastic moduli, displacements were negligible in these regions. Very high displacements, in one case we measured almost 1 cm, were probably caused by snow densification in the low density snow at the top of the snowpack or by collapse of a layer. As there were hardly any persistent weak layers present that would allow for the latter, the first reason is more likely.

Gubler (1976) calculated displacement velocities and displacement from acceleration data. His vertical displacement velocities decayed much stronger ($x'^{-1.39}$) with horizontal distance from the point of explosion than our data suggest ($x'^{-0.51}$ on average). However, the data presented by Gubler (1976) resulted from measurements at a depth of half or smaller than half the snow depth from the surface. The strong decay with depth within the snowpack might influence the spreading at a certain depth with horizontal distance from the point of explosion. The decay of the horizontal displacement velocity presented by Gubler (1976) is in good agreement with our findings ($x'^{-1.8}$ and $x'^{-1.9}$ on average, respectively).

Vertical displacements measured by Gubler (1976) for a sensor 'at half or less than half the depth' of the snowpack from the surface was ranging from 4×10^{-4} to 4×10^{-5} m. This is in good agreement with what we measured except for the top sensors if close to the point of explosion.

4.4.3 Acceleration – air pressure relation

In the vast majority (21) of the 25 experiments with pressure and acceleration measurements, the exponent of the fitted power law was smaller for the maximum vertical acceleration at 0.3 m scaled depth ($x'^{-1.0}$) compared to the air pressure ($x'^{-1.6}$), the difference being 0.71 on average (Fig. 4-16). We believe that this is due to waves along the surface that expand cylindrically within the snowpack. The amplitude of a cylindrical wave should decay with $x^{-0.5}$. Higher decay rates are presumably due to a mixed spherical-cylindrical expansion and due to attenuation of the wave within the snowpack.

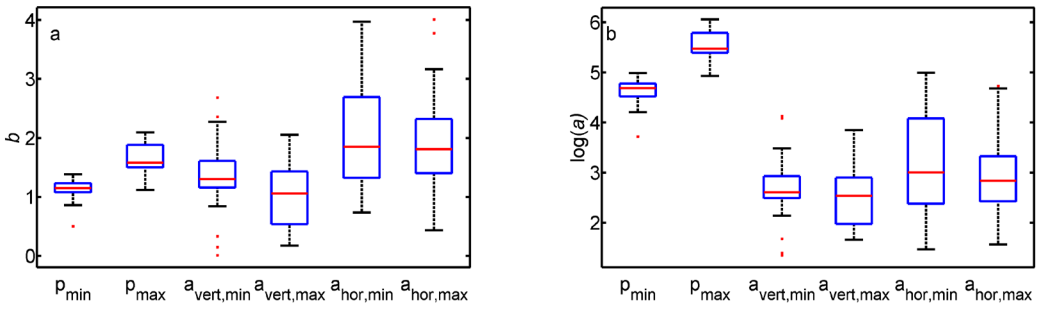

Fig. 4-16: Parameters of power law fits: (a) coefficients b and (b) log(a) for air pressure and acceleration with scaled horizontal distance from the point of explosion. Boxes span the interquartile range from 1st to 3rd quartile with a horizontal line showing the median. Whiskers extend to the most extreme data points not considered outliers (red dots) within 1.5 times the interquartile range above the 3rd and below the 1st quartile. Number of cases varies between 25 and 29.

4.4.4 Wave arrival time

The minimum time an air pressure wave needs to cover the horizontal distance between a point on the snow surface directly above the accelerometer and the microphone is the ratio of the maximum microphone offset divided by the highest air pressure speed measured (547 m s^{-1}). This yields a time

delay of 2×10^{-3} s which is shorter than the arrival time delay of the wave at the microphone compared to the accelerometer. Arrival of the first high amplitude wave was expected to be before the air pressure wave for the top sensors because the wave arriving at the sensor was resulting from the air pressure waves hitting the snow surface at a shallow angle of incidence closer to the point of explosion. Due to the higher density of the snow compared to air, the wave travelled faster within the snowpack. Lower sensors showed the same arrival time differences. This was probably due to the increasing density and hence velocity with depth within the snowpack which compensated for the longer distances the wave travelled. During some experiments there were waves before the major wave with very weak amplitude compared to the main wave (Fig. 4-9). These waves may be explained either by the fast dilatational wave travelling through the ice skeleton (Johnson, 1982) or a wave along the surface that propagates as a cylindrical wave at higher velocity than the air pressure wave but is attenuated strongly with depth within the snowpack.

The second high amplitude wave (Fig. 4-10) is not believed to be the result of a reflection at the snow-soil interface, where a large impedance mismatch is expected, as the amplitudes of the waves decay strongly with depth within the snowpack. We believe that these waves were slow waves (Johnson, 1982) travelling through the pore space of the snowpack or shear waves.

Ground accelerations did not seem to have had an influence on the snowpack as accelerations and derived parameters strongly decayed with depth and no waves with decreasing amplitude from bottom to top were recorded that exceeded the waves caused by the air blast transferred to the snowpack.

4.4.5 Weak layer failure

Very close to the point of explosion, the shock caused by a standard charge (e.g. a few kilograms TNT equivalent) will be sufficiently strong to fail almost any given weak layer down to the relevant depth for avalanche release. However, a weak layer may not exist or the slab-weak layer combination may not be prone to crack propagation at a close distance. Hence it is important whether a given explosion is strong enough to cause a weak layer to fail further away from the point of explosion, i.e. rather in the range of elastic wave propagation.

During the experiments in winter 2013-2014 we observed that weak layer failure was always immediate after the air pressure wave had passed the point of observation. With increasing distance from the point of explosion, failure became less frequent.

In the single experiment described by Simioni and Schweizer (2013; cf. Appendix C), even at 25 m from the point of explosion, the observed weak layer failure occurred 0.4 s after the arrival of the air pressure wave at the point of observation (pit). We suppose that the failure in this single experiment from the season 2012-2013 was not caused by the incident air pressure wave impacting

on the snow surface close to the pit. The short distance and the high wave velocities in snow would not account for the time delay between the snow spray caused by the passing air pressure wave and the observed failure at the weak layer. Failure was rather caused by the air pressure wave impinging on the snow surface closer to the point of explosion and being partly transferred to the snowpack. One of the excited wave modes (dilatational or shear) then locally failed the weak layer and crack propagation started. The low velocity of crack propagation, previously reported values were in the range of 8 to 42 m s^{-1} (van Herwijnen and Birkeland, 2014; van Herwijnen and Schweizer, 2011), was then responsible for the time delay.

Hence, there seem to be two distinctly different types of mechanisms causing weak layer failure at distances of several tens of meters from the point of detonation. The relatively poor snowpack stability during winter 2012-2013 compared to the winter 2013-2014 supports this finding. During winter 2013-2014 no crack propagation occurred, but failure was caused directly by the air pressure wave at the distance where the failure observation was made. The good snowpack stability conditions did not favor crack propagation.

Weak layer failure was not detected above 14 m $kg^{-1/3}$ scaled horizontal distance from the point of explosion. During some experiments, no failure was observed close to the point of explosion even if failure was detected further from the point of explosion. Either, a suitable weak layer was not present closer to the point of explosion, or, more likely, failure could not be detected by visual inspection. Failure close to the snow surface was detectable because the slab was slightly lifted by the negative pressure impulse. Deeper in the snowpack failure was usually only visible with major vertical displacement (collapse). When failure only occurred at the farer pit locations, we assumed that the same layer was failing at closer pit locations because of the spatially uniform snowpack though it could not be observed.

The observed rare occurrence of failures deeper in the snowpack – six out of 20 – and further from the point of explosion corresponded well with the low accelerations, displacement velocities and displacements measured at these locations.

4.5 Conclusions

We performed field experiments using spherical avalanche control explosives on a flat, snow-covered study site. We measured near-surface air pressure at different distances from the explosion using three locations on each test ranging from 7 m to 43 m horizontal distance. Within the snowpack, we recorded snowpack accelerations at these distances and at different depths within the snowpack ranging from 0.1 m to 1.3 m below the snow surface. We monitored pit walls at these locations with high speed cameras to visually identify weak layer failure. Due to the generally good stability of the snowpack, only few failures were observed, mainly at closer range from the point of explosion.

Air pressure decreased rapidly with scaled distance from the point of explosion proportional to $x'^{-1.66}$, indicating the influence of the snowpack on the decay of the amplitude. Air pressure wave propagation speeds were well above sound speed for short distances from the point of explosion due to non-linear effects in shock wave propagation (up to 547 m s^{-1}). Wave propagation speeds decreased with distance to sonic level. Accelerations decreased rapidly with depth within the snowpack and, for a given depth, with distance from the point of explosion (on average proportional to x'^{-1} at 0.3 m scaled depth for vertical maximum accelerations) due to geometrical spreading and attenuation due to the poro-elastic character of snow. Air pressure usually decayed stronger than maximum vertical acceleration. This finding indicates that some wave modes within the snowpack propagate as waves along the surface and expand cylindrically. Vertical accelerations were usually stronger in amplitude than horizontal ones.

The air pressure waves arrived at the microphones with a time delay compared to the arrival time of the waves within the snowpack at the top accelerometers, taking into account the horizontal offset of the microphone. This delay was expected due to higher wave velocities within the snowpack. However, waves at lower sensors did not arrive significantly later than at the top sensor. This, together with the strong decay within the snowpack, probably indicates a wave along the surface in the uppermost snow layers or surface wave propagating along the snowpack. However, the typical exponential decay with depth of a surface wave was not observed. Early low amplitude waves observed might be due to the fast wave mode propagating through the ice lattice. Later waves, as often observed, might be due to a slow wave, probably travelling through the air pores, rather than due to reflections lower in the snowpack as their amplitude decreased strongly with depth and time delays were large. Consecutive testing with equal charge sizes and charge elevations did not result in different air pressure or acceleration response.

Displacement speeds were usually less than 1 m s^{-1} for the top sensor and decayed strongly with depth within the snowpack and distance from the point of explosion. Compared to the top sensor, the middle and bottom sensors showed negligible displacement speeds.

Maximum displacements reached 1 cm for the top sensors during some experiments but were usually smaller (10^{-4} to 10^{-5} m). Displacements were negligible deeper in the snowpack. Final displacements were in the same range as the maximum displacements. The resulting small displacements were due to the absence of persistent weak layers with notable collapse heights.

Whereas our setup and instrumentation allows recording the response of the snowpack to spherical explosive loading with good accuracy and high temporal resolution and hence provides insight into the complex wave propagation behavior in and above a snowpack, detailed propagation patterns cannot be observed with a few measuring locations only.

Failure evaluation using high speed cameras has to our knowledge not been used in avalanche control experiments using explosives and seems to be a method with relevant informative content. Even under conditions with no persistent weak layer but mainly failures at layer interfaces with hardly any collapse height, the method allowed to determine weak layer failure by visually inspecting the single video stills individually. The method allowed distinguishing between two types of weak layer failure: (1) failure caused by the direct impact of the air pressure wave above the point of observation, and (2) failure caused by crack propagation initiated at a distance closer to the point of explosion than the point of observation as manifested by an arrival time delay.

Though the markers inserted into the pit wall would allow for particle tracking, the snow spray caused by the air pressure wave and single markers moving relative to the pit wall did not allow the pit wall displacements to be evaluated quantitatively. Furthermore, in order to use the recordings for particle tracking, the frame rate of our cameras was too low compared to the propagation speed of dilatational and shear waves in a snowpack and the snow spray inhibited real time tracking. However, particle tracking may still be useful for determining the total displacements.

We will continue performing field experiments on avalanche control to cover different snowpack conditions, new types of spherical explosives and different control techniques including gas exploders. In addition, we will use our data to model wave propagation caused by explosions and deflagrations employing different modeling techniques (e.g., Miller et al., 2011; Sidler et al., 2010). Small scale experiments are planned to gain a better understanding of wave propagation principles in a snowpack.

5 Snowpack response to directed gas explosions on level ground

5.1 Introduction

The artificial release of avalanches is a key active control measure in avalanche mitigation. Compared to engineering works such as e.g. snow sheds avalanche control by artificial release of avalanches is less costly and compared to snow supporting structures in starting zones the visual impact is minor. Hundreds of fixed avalanche control installations have been installed during the last decade. In principle, they allow avalanche control services to trigger avalanches under any given meteorological conditions and at any time of day. The weather independence is highly relevant as the yield of artificial avalanche release is highest during or directly after a storm (McClung and Schaerer, 2006) and operational constraints often inhibit artificial release during periods of good weather or daylight. However, the point of explosion cannot be adjusted easily for most systems, as the installations are fixed to the ground.

To trigger an avalanche artificially, an explosion is caused by igniting either solid explosives or a gas mixture, either propane-oxygen or hydrogen-oxygen (Berthet-Rambaud, 2009). For fixed avalanche control systems working with gas, the two gases are mixed within a steel pipe that is open on one side and directed with the opening inclined towards the snowpack (Liebermann et al., 2002). The explosion causes a shock and/or subsequently an elastic wave that is propagating outwards from the point of explosion. The air pressure wave is partly transferred to the snowpack depending on snowpack conditions: The mechanical properties of the snow (e.g. porosity), the snow-air-interface and the incident angle of the wave influence the part of the wave energy that is transferred to the snowpack (Bouzidi and Schmitt, 2012). The waves generated within the snowpack may then lead to failure and an avalanche might be released.

Since the pioneering works of Mellor (1973) and Gubler (1977), most studies performed on the effects of an explosion on a snowpack in relation to artificial avalanche release focused on near field effects where shock waves are dominant (e.g., Binger et al., 2006; Frigo et al., 2012; Johnson et al., 1994; Johnson et al., 1993). These authors all used solid explosives, investigated shock waves propagating through a snowpack and showed the strong damping effect of snow.

Recently, Binger and Miller (2016) measured air overpressure above a snowpack and snowpack accelerations within a distance of 7 m from the point of explosion, i.e. in the near field. Their study is based on the experiments of Tichota et al. (2010) and Bones et al. (2012). Reported attenuation coefficients of shock and acoustic wave propagation in snow ranged from x^{-1} to $x^{-1.9}$, where x is the distance from the point of explosion. Moreover, Wooldridge et al. (2012) performed stability tests before and after explosions to assess their influence on snowpack stability.

At larger distances from the point of explosion than in the shock range, i.e. larger than about 20 to 30 m according to Simioni et al. (2015; cf. Chap. 4), Frigo et al. (2010) performed experiments on a flat study site to assess the effect of an explosion on a snowpack. The most extensive studies in

this range were performed by Gubler (1977) and Simioni et al. (2015; cf. Chap. 4). The main differences between these studies were that Simioni et al. (2015; cf. Chap. 4) measured at different distances simultaneously and performed acceleration measurements at different depths within the snowpack. Hence they could not only describe the decay of the air pressure and snowpack accelerations with distance from the point of explosion, but also the decay with depth within the snowpack. On the other hand, Gubler (1976) provided estimates on the stresses and stability within the snowpack and showed the increased effect by elevating the charge from the snow surface. Cardu et al. (2008) developed a stability criterion for the artificial release of avalanches comprising stress and energy criteria. Simioni et al. (2014b; cf. Appendix E) observed weak layer failure during their explosion experiments and reported two different types of failure: one caused by the direct impact of the air pressure wave above the snowpack and one caused by crack propagation initiated closer to the point of explosion.

With regard to ground waves caused by explosions, Ueland (1993) stated that the amplitude of ground vibrations was too low to trigger avalanches at larger distances. Albert and Orcutt (1990) showed that the amplitudes of the acoustic wave transferred to the snowpack were 10 times higher than those of the ground waves transmitted to the snowpack. Suriñach et al. (2011) showed that vibrations caused by the explosion of a gas exploder propagating through the ground may not be sufficient to trigger avalanches at large distances (>100 m) and that vibrations caused by sound waves propagating through the air and through the snowpack are usually larger than those propagating directly through the ground.

To model the wave propagation in snow Johnson (1982) adapted the model by Biot (1956a) to snow and stated the existence of three different wave types. Miller et al. (2011) showed the effect of charge elevation and stress concentrations around a weak layer using a finite element code developed for explosions. Simioni et al. (2014b; cf. Appendix E) applied a two-dimensional pseudo-spectral method solving Biot's equations to field experiments using spherical explosives (Sidler, 2015) and showed the propagating wave within the snowpack and failure locations.

In a different context, not related to artificial release, the influence of a snowpack on acoustic wave propagation was investigated. For example, Albert (2001) showed that the acoustic response above a snowpack may vary within a short period of time (hours to days) as snow surface properties change. Albert et al. (2008) reported that acoustic waves above a snowpack were attenuated by as much as -30 dB within a distance of 100 m.

Whereas many studies on the effect of an explosion on the snowpack were performed using solid explosives as source, no studies exist that systematically investigated the effect of a directed gas explosion on a snowpack. The only studies involving gas exploders were performed by Suriñach et al. (2011) who focused on ground accelerations and Berthet-Rambaud (2009) who developed a

test protocol to investigate the effect of gas exploders. Hence, the detailed effect of such an explosion on a snowpack is essentially unknown, despite years of successful operational use of gas exploder systems.

Our goal was to investigate the effect of a directed gas explosion triggered above snow. We used a mobile gas exploder, a simple steel pipe suspended from a crane. To assess the propagation characteristics of the air pressure wave and its effect within the snowpack we measured air pressure and snowpack accelerations. Measurements were performed along two axes to assess the shape of the impact of a directed gas explosion which is not radially symmetric.

5.2 Data and methods

5.2.1 Study site

Experiments were performed at the same military firing range as described in Simioni et al. (2015; cf. Chap. 4); it is located at an elevation of 1680 m a.s.l. just north of the Alpine divide in the Eastern Swiss Alps. The study site is flat and level to guarantee reproducible conditions. Furthermore, the deployment of the measuring equipment was safe and relatively fast due to the level ground.

5.2.2 Experiments

During the winter 2014-2015 we performed 13 gas exploder experiments on the test site in Hinterrhein (Table 5-1). As these were the first experiments with a mobile gas exploder, the experimental setup had not yet been fully developed. Due to the lack of accurate manometers, precise gas volume measurements were not available for these experiments. During the following winter 2015-2016 we performed another 22 gas exploder experiments on three test days at Hinterrhein. In addition, 14 experiments were performed on 15 June 2016 above bare ground. Table 5-1 compiles the key experimental data, namely date, test number, mass of the gas mixture, incline of the exploder, angle between the first (gas exploder) and second measurement axis and horizontal distances of the measuring locations from the point of explosion.

Table 5-1: Summary of all experiments indicating date, test number, mass of the gas mixture, incline of the exploder, angle between the first (gas exploder) and second measurement axis and horizontal distances of the measuring locations from the point of explosion. Test numbers marked with an asterisk (*) are experiments for which no exact mass measurement is available. These masses were interpolated from the air pressure measurements based on the results of the other experiments. Experiments on 15 June 2016 were performed above bare ground.

Date	Test no. (-)	Exploder elevation (m)	Gas mass (kg)	Exploder incline (°)	Angle 2nd axis (°)	Distance (m)					
						X1	X2	X3	Y1	Y2	Y3
10 Mar 2015	1*	1.4	0.87	39	27	17.0	27.1	36.0	16.5	26.4	36.4
10 Mar 2015	2*	1.4	0.44	39	27	17.0	27.1	36.0	16.5	26.4	36.4
10 Mar 2015	3*	1.4	0.25	39	27	17.0	27.1	36.0	16.5	26.4	36.4
10 Mar 2015	4*	1.4	0.47	39	27	17.0	27.1	36.0	16.5	26.4	36.4
10 Mar 2015	10*	1.4	0.37	39	27	17.0	27.1	36.0	16.5	26.4	36.4
10 Mar 2015	11*	1.4	0.31	39	27	17.0	27.1	36.0	16.5	26.4	36.4
10 Mar 2015	12*	1.4	0.57	39	27	17.0	27.1	36.0	16.5	26.4	36.4
11 Mar 2015	1*	1.57	0.12	28	23	12.0	17.2	22.1	11.6	16.3	21.3
11 Mar 2015	2*	1.57	0.61	28	23	12.0	17.2	22.1	11.6	16.3	21.3
11 Mar 2015	3*	1.57	0.80	28	23	12.0	17.2	22.1	11.6	16.3	21.3
11 Mar 2015	4*	1.57	0.54	28	23	12.0	17.2	22.1	11.6	16.3	21.3
11 Mar 2015	13*	1.57	1.49	28	23	12.0	17.2	22.1	11.6	16.3	21.3
16 Feb 2016	1	1.77	0.54	30	37	19.2	34.3	49.2	17.7	32.7	47.6
16 Feb 2016	2	1.77	0.58	30	37	19.2	34.3	49.2	17.7	32.7	47.6
16 Feb 2016	3	1.77	1.09	30	37	19.2	34.3	49.2	17.7	32.7	47.6
16 Feb 2016	4	1.77	1.04	30	37	19.2	34.3	49.2	17.7	32.7	47.6
16 Feb 2016	5	1.77	1.43	30	37	19.2	34.3	49.2	17.7	32.7	47.6
16 Feb 2016	6	1.77	1.41	30	37	19.2	34.3	49.2	17.7	32.7	47.6
16 Feb 2016	7	1.77	1.57	30	37	19.2	34.3	49.2	17.7	32.7	47.6
16 Feb 2016	8	1.77	1.63	30	37	19.2	34.3	49.2	17.7	32.7	47.6
16 Feb 2016	9	1.77	1.82	30	37	19.2	34.3	49.2	17.7	32.7	47.6
17 Feb 2016	1	1.3	1.04	37	29	16.3	25.8	35.1	16.1	26.2	36.1
17 Feb 2016	2	1.8	1.13	36	29	16.3	25.8	35.1	16.1	26.2	36.1
17 Feb 2016	3	1.8	1.30	36	29	16.3	25.8	35.1	16.1	26.2	36.1

17 Feb 2016	4	1.8	1.24	36	29	16.3	25.8	35.1	16.1	26.2	36.1
17 Feb 2016	5	1.8	1.61	36	29	16.3	25.8	35.1	16.1	26.2	36.1
17 Feb 2016	6	1.8	1.61	36	29	16.3	25.8	35.1	16.1	26.2	36.1
17 Feb 2016	7	1.8	1.87	36	29	16.3	25.8	35.1	16.1	26.2	36.1
17 Feb 2016	8	1.8	1.89	36	29	16.3	25.8	35.1	16.1	26.2	36.1
18 Feb 2016	1	1.4	1.36	32	29	16.0	25.6	34.9	15.7	25.9	35.7
18 Feb 2016	2	1.4	1.30	32	29	16.0	25.6	34.9	15.7	25.9	35.7
18 Feb 2016	3	1.4	1.55	32	29	16.0	25.6	34.9	15.7	25.9	35.7
18 Feb 2016	4	1.4	1.50	32	29	16.0	25.6	34.9	15.7	25.9	35.7
18 Feb 2016	5	1.4	1.75	32	29	16.0	25.6	34.9	15.7	25.9	35.7
15 Jun 2016	1	1.4	1.30	34	90	14.1	22.0	28.4	15.3	23.2	30.0
15 Jun 2016	2	1.4	1.27	34	90	14.1	22.0	28.4	15.3	23.2	30.0
15 Jun 2016	3	1.4	1.32	34	90	14.1	22.0	28.4	15.3	23.2	30.0
15 Jun 2016	4	1.4	1.15	34	90	14.1	22.0	28.4	15.3	23.2	30.0
15 Jun 2016	5	1.4	1.12	34	90	14.1	22.0	28.4	15.3	23.2	30.0
15 Jun 2016	6	1.4	1.48	34	90	14.1	22.0	28.4	15.3	23.2	30.0
15 Jun 2016	7	1.4	1.47	34	90	14.1	22.0	28.4	15.3	23.2	30.0
15 Jun 2016	8	1.4	1.49	34	90	14.1	22.0	28.4	15.3	23.2	30.0
15 Jun 2016	9	1.4	1.50	34	90	14.1	22.0	28.4	15.3	23.2	30.0
15 Jun 2016	10	1.4	1.44	34	90	14.1	22.0	28.4	15.3	23.2	30.0
15 Jun 2016	11	1.4	1.48	34	90	14.1	22.0	28.4	15.3	23.2	30.0
15 Jun 2016	12	1.4	1.54	34	90	14.1	22.0	28.4	15.3	23.2	30.0

5.2.3 Gas exploder

A prototype gas exploder, manufactured by TAS that produces the Gazex® gas exploder (Liebermann et al., 2002; Stoffel et al., 2015), was used for the experiments. It was suspended from a crane. The gas exploder consisted of a steel pipe that was open at one side (Fig. 5-1). Its overall length was 2.5 m and its inner diameter 0.8 m. The total volume of the pipe was approx. 1.25 m^3. The opening could be closed with a soft plastic lid using a steel ring and screws to prevent gas heavier than air from flowing out of the tube. The exploder weighed approx. 800 kg. Three suspension points on the exploder were used to hang it up at a certain elevation and incline. The incline was set by adjusting

the length of the suspension chains. Two fastening points were installed to guy the exploder to the counter weights which prevented the tube from moving heavily due to the recoil. One or two counter weights, ranging from 1.9 to 2.3 t, were placed laterally (5 to 7 m) and axially (1 to 1.5 m) offset on either side of the exploder. The incline of the pipe was slightly influenced by pulling the gas exploder backwards to reach a certain pretension of the guy wires.

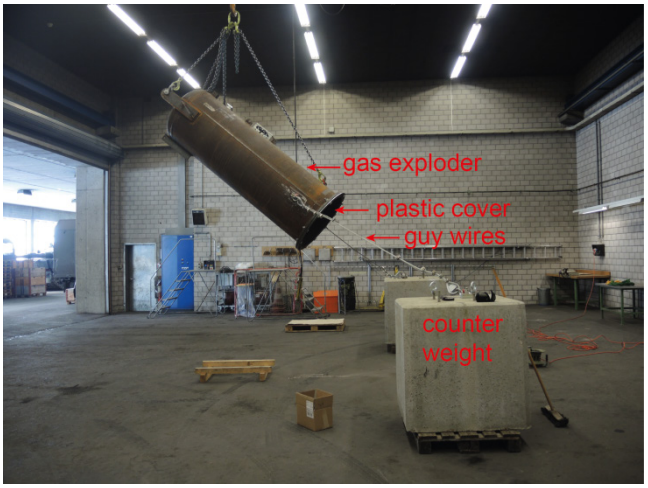

Fig. 5-1:View of the gas exploder, suspended from a crane. The pre-tensioned guy wires are connecting the gas exploder to the counterweights. The lower end of the tube is closed by a plastic cover.

The front bottom of the pipe was elevated between 1.4 and 1.8 m from the snow surface or the bare ground (Table 5-1). The angle between the inclined exploder and the level snow surface or the ground ranged from 30 to 36° (Table 5-1). Operational gas exploders are installed with angles of 28 to 48° between the inclined pipe and the snow surface.

5.2.4 Gas

The entire gas installations were provided by the manufacturer of the mobile gas exploder. As the propane-oxygen gas mixture is heavier than air, the opening of the pipe had to be closed as described above. The tube opening was not tightly closed so that the air could flow out while the pipe was filled with gases (Fig. 5-1). A tight closure would lead to an overpressure in the gas exploder and rupture of the plastic lid and hence total outflow of the mixture before the explosion.

The two different gases were supplied through independent, almost identical setups: The gas flowed from the gas bottle to a larger tank and was set to the required pressure using manual valves and pressure gauges (Fig. 5-2). After reaching the required tank pressure, the bottle valves were closed to prevent additional gas from flowing into the tank during outflow to be able to measure the gas quantity consumed during one experiment. The gas tanks valves were opened and gas flowed out for a set period using an electronic trigger. The gas flowed through long pipes to the gas exploder

where the two gases were mixed. This procedure guaranteed in combination with check valves at the gas exploder that there was no ignitable mixture in any part of the system except the gas exploder.

Fig. 5-2: Pressure reduction tanks for oxygen (blue) and propane (metallic). The gas bottles can be seen in the background.

5.2.5 Gas quantity

A handheld trigger, provided by the manufacturer of the mobile gas exploder, was used to fill the mobile gas exploder and to ignite the mixture with spark plugs that were installed within the pipe. The gas quantity was determined with a time relay to set the opening time of the outflow valves at the gas tanks. With the ignition of the gas mixture, data acquisition was started.

The released gas quantity of either gas was calculated according to the ideal gas law:

$$m_{\mathrm{GAS}} = \frac{\Delta p_{GAS}\, V_{\mathrm{tank}}}{R_S\, T}\ (\mathrm{kg}) \qquad (5.1)$$

where Δp_{GAS} is the pressure difference (Pa) in the tank before and after releasing the gas, V_{tank} is the volume of the pressure reduction tank (m^3), R_S is the specific gas constant of the respective gas (J kg^{-1} K^{-1}) and T is the gas temperature (K).

The gas volume at ambient pressure and temperature at the test site was calculated as:

$$V_{\mathrm{GAS}} = \frac{m_{\mathrm{GAS}}\ R_S\, T_{\mathrm{atm}}}{p_{\mathrm{atm}}}\ (\mathrm{m}^3) \qquad (5.2)$$

where p_{atm} and T_{atm} are the atmospheric air pressure (Pa) and the ambient temperature (K) at the test site.

The total gas amount equals the sum of the gas masses or volumes of the two gases oxygen and propane.

On all test days with snow, experiments with different gas volumes were performed. The initial pressure in the tanks was set according to the manufacturer's recommendations. The relative pressure in the oxygen tank was 6.5 bar and 1.4 bar in the propane tank. The time period (t_0) the gas valves were opened was selected between 0.5 and 3.5 s. Normally, two consecutive tests were

performed with the same opening time, i.e. gas volume. Within the opening time of the valves the gas pressure in the oxygen tank dropped by 72 to 256 kPa and by 18 to 60 kPa in the propane tank. Outside air temperatures ranged from -3 to -2 °C. The gas temperature in the tanks was assumed to be equal to the outside air temperature. The oxygen and propane gas masses were determined using the above measurements and the respective gas constants which are $R_{s_{\text{oxygen}}} = 259.8\, J\, kg^{-1}K^{-1}$ and $R_{s_{\text{propane}}} = 188.5\, J\, kg^{-1}K^{-1}$ according to equation (1). The gas quantities ranged from 0.40 to 1.45 kg oxygen and 0.14 to 0.47 kg propane with the ratio of propane to oxygen of approx. 1/3 (Table 5-1). The ambient air pressure p_{atm}, measured several times per day, varied between 829 and 837 hPa. The gas volumes of the two gases in ambient air were calculated using the exact gas measurements and were between 0.43 and 1.51 m^3; the maximum gas volumes were hence larger than the exploder volume. Oxygen from the ambient air is needed for the explosion as the ratio of the propane to oxygen mass taken from the gas tanks is larger than an explosive mixture. For comparison, we only gave the propane and oxygen masses taken from the gas tanks and did not consider the oxygen mass used from the ambient air. The heat of combustion of propane is 50.33 MJ kg^{-1}. Hence the maximum heat of combustion during the experiments was 23.7 MJ.

For the tests during the winter 2015-2016, exact pressure measurements were available. For the experiments during the winter 2014-2015, no exact gas measurements were available. The gas quantities of these experiments were derived from the air pressures caused by the explosion measured at various distances above the snowpack and hence back-calculated using the results from the experiments with gas measurements.

During the test day above bare ground without a snowpack, the relative pressure was set as in the tests with snow. The time period the valves were opened were 1.5, 2.0 and 2.5 s. These values corresponded to pressure drops in the oxygen tank between 150 and 210 kPa and 37 and 57 kPa in the propane tank. Using the ideal gas law and ambient pressure and air temperatures, the resulting gas masses ranged from 0.84 to 1.13 kg oxygen and 0.28 to 0.43 kg propane. These gas masses correspond to volumes between 0.67 and 1.26 m^3 in total.

5.2.6 Experimental setup

The gas exploder causes a directed explosion (Fig. 5-3), i.e. it is to be expected that the loading of the snowpack in the axis and in front of the exploder is different than at other angles from this axis. It is therefore not sufficient to perform measurements along the exploder axis only as is usually done when solid explosives with a spherical propagation behavior are tested (e.g. Binger and Miller, 2016). As a consequence, measurements were performed along two axes in a horizontal plane seen from above (Fig. 5-4). The first axis (X-axis) was in the direction of the pipe; the second axis (Y-axis) was selected such that the snowpack between the two axis was undisturbed and the field of view

from the exploder was not obstructed by the counterweights (Fig. 5-4). For the experiments above snow, the angle between the X-axis (exploder axis) and the Y-axis ranged from 23 to 37° (Table 5-1) and was limited by the positions of the counterweights. Larger angles would have led to a bias in the measured effect as the counterweights would have reflected the propagating wave partially. For the tests above bare ground, the angle between the two axes was 89° such that the pressure wave from the gas explosion could propagate unobstructed behind the counterweights. This was not feasibly above snow.

Fig. 5-3: View of the gas exploder during an experiment. Photo by M. Hiller.

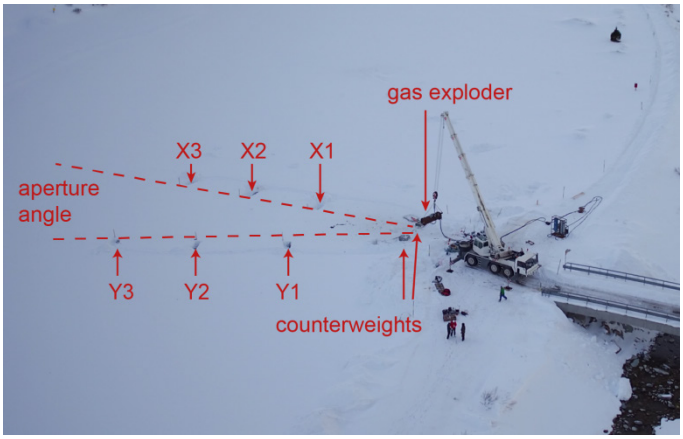

Fig. 5-4: Aerial view of the gas exploder and the crane. The 6 measuring pits are indicated with X1 to Y3.

Three measuring locations were used on each axis at different distances from the point of explosion which was determined as the open tip of the gas exploder (Fig. 5-5). Differential GPS was used to determine the positions of the gas exploder and the snow pits where the microphones for the air pressure measurement and the accelerometers for snowpack acceleration measurements were installed. The distance of the accelerometers from the microphone and the depth of the sensors within the snowpack were measured manually. The second microphone on the X-axis was

installed directly in the axis of the gas exploder. The first and the third microphones were installed slightly offset to obtain an undisturbed snowpack between the gas exploder and the sensors. This offset also resulted in a slight offset of the accelerometers such that there was no disturbed snowpack between the gas exploder and the accelerometers. The accelerometers were installed slightly closer to the point of explosion than the microphones with a few exceptions to prevent any interference of the accelerometer with the post of the microphone. The offset ranged from 5 cm further away from the microphone to 90 cm closer to the point of explosion.

The distances of the microphones from the point of explosion ranged between 11.6 and 49.2 m (Table 5-1); scaled with the total gas mass the corresponding distances ranged from 9.0 to 89.6 m $kg^{-0.65}$ (s. 5.2.10. for the calculation of the scaling factor).

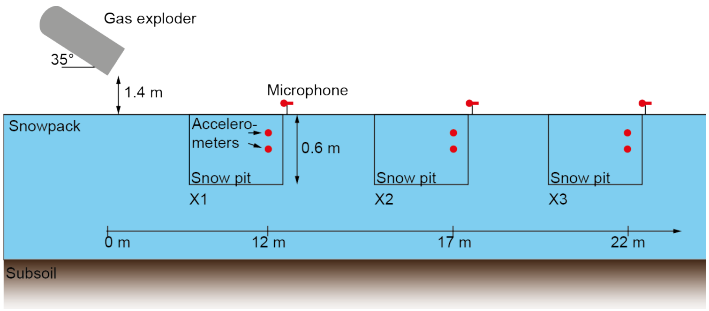

Fig. 5-5: Longitudinal section of an exemplary measuring layout indicating snow pits X1 to X3 on the X-axis with increasing distance from the point of explosion, gas exploder location, microphones and accelerometers at different distances from the point of explosion and depths within the snowpack. As an example, the gas exploder was elevated at 1.4 m with an incline of 35°, the horizontal location of the charge is at 0 m, the snow pits X1 to X3 were located at 12, 17 and 22 m horizontal distance from the point of explosion, respectively. The measuring layout is equal on the second axis; figure after Simioni et al. (2015; cf. Chap. 4).

5.2.7 Air pressure measurement

Microphones with an upper pressure limit of 34.5 kPa and a frequency limit of 1,000 Hz (Binger and Miller, 2016; Simioni et al., 2015; cf. Chap. 4) were used to measure near-surface air pressure resulting from the gas explosion at different distances from the point of explosion above the snow surface. Surface air pressure was measured at a maximum of 5 cm above the snow surface. Air pressure wave speeds were determined using the arrival times of the air pressure signal at the different microphones. For the experiments above bare ground, the microphones were installed at an elevation of 30 cm to 1 m above the ground.

5.2.8 Acceleration measurement

Snowpack accelerations were measured with two-directional accelerometers sealed into foam cylinders to closely match snow density (Table 5-2) (Simioni et al., 2015; cf. Chap. 4). Accelerometers were installed at different depths within the snowpack and at approximately the same distances

from the point of explosion as the air pressure measurements were performed (Fig. 5-4). Sensors were inserted into the undisturbed snowpack by first cutting out a hole up to one meter back from the snow pit wall.

No acceleration measurements were performed for the experiments above bare ground, as the accelerometers were not suitable for ground acceleration measurement.

Table 5-2: Accelerometer specifications (www.analog.com) (Simioni et al., 2015; cf. Chap. 4).

	ADXL203	AD22293	AD22037	ADXL001-70
Range (g)	+/- 1.7	+/- 6	+/- 18	+/- 70
Sensitivity (mV/g)	1000	312	100	24
Resonant frequency (Hz)	5500	5500	5500	>20000

5.2.9 Data acquisition

Data were acquired using the same setup as described in Simioni et al. (2015; cf. Chap. 4) with National Instruments cDAQ systems in each snow pit. Data acquisition modules allowed sampling up to 100 kHz per channel simultaneously. Other modules were used to trigger the data acquisition. However, due to the additional axis, six instead of three data acquisition systems were used. Data were transmitted via network cables.

5.2.10 Data evaluation

With solid explosives, a scaling factor is commonly used to consider different charge masses and their effect on surface air pressure at a certain distance (Simioni et al., 2015; cf. Chap. 4). For a confined gas explosion in a mobile gas exploder, no scaling factor exists. Therefore, a scaling factor was calculated for explosions with different gas volumes with the reference gas mass of 1 kg:

$$x' = x\, {m_\mathrm{G}}^{-a_\mathrm{G}} \quad (\mathrm{m\ kg}^{-a_\mathrm{G}}) \tag{5.3}$$

The following procedure was used to obtain the best scaling factor: The scaling factor a_G was varied within a certain range. Then, x' was calculated for each a_G. Maximum air pressure values of all experiments were then fitted against this scaled distance. The fit with the highest coefficient of determination R^2 determined the best value of a, which was subsequently used for gas mass scaling.

The scaling factor was determined using the experiments with precise gas measurements. The factor was then used to estimate the gas masses for the experiments without precise gas measurements based on the maximum air pressure measured at a given distance.

In addition to the maximum air pressure, the maximum air pressure derivative $p_{,t_\mathrm{max}}$ was calculated, i.e. the strongest increase of the air pressure per time that occurs on the first flank:

$$p_{,t_{\max}} = \left(\frac{\mathrm{d}p}{\mathrm{d}t}\right)_{\max} \quad (\mathrm{Pa\ s^{-1}}) \tag{5.4}$$

where p is the measured air pressure and t is time.

The decay of the air pressure with increasing distance was calculated using the measured distances (x) and the maximum air pressure at each location. For all experiments and all axes, a power law as in Bones et al. (2012) and Simioni et al. (2015; cf. Chap. 4) was fitted to the maximum air pressure with distance from the point of explosion:

$$p_{\max}^{\mathrm{X,Y}} = 10^{a}\, x'^{-b} \quad (\mathrm{Pa}) \tag{5.5}$$

where superscripts X or Y stand for the measuring axis and max for the maximum value of the air pressure.

Power laws were also fitted for the maximum air pressure increase per time $p_{,t_{\max}}$.

A simple energy equivalent of the air pressure was used to show the decay of the energy with distance from the point of explosion. This energy equivalent was derived by integrating the squared air pressure:

$$p_{\mathrm{energy}} = \int p^2\ \mathrm{dt} \quad (\mathrm{Pa^2\ s}) \tag{5.6}$$

Maximum vertical and horizontal accelerations within the snowpack were fitted against the scaled depth z' of the sensors in the snowpack measured from the snow surface in the same way as done with the horizontal distance from the point of explosion (Simioni et al. (2015; cf. Chap. 4). For each distance where accelerations were measured a power law fit for the maximum vertical and horizontal accelerations was obtained. These power laws were then used to fit a power law of the accelerations with distance from the point of explosion at a certain depth within the snowpack:

$$a_{\mathrm{s,max}}^{\mathrm{X,Y,pit}} = 10^{a}\, z'^{-b}\ (\mathrm{m\ s^{-2}}) \tag{5.7}$$

$$a_{\mathrm{s,max}}^{\mathrm{X,Y}} = 10^{a}\, x'^{-b}\ (\mathrm{m\ s^{-2}}) \tag{5.8}$$

Snowpack displacement velocities v and displacements d were determined by integrating the acceleration data once or twice over time, respectively. The maximum values of these quantities were fitted against depth within the snowpack and then against the distance from the point of explosion as done with the accelerations (Simioni et al., 2015; cf. Chap. 4). The decay exponents of the different quantities were then compared.

The equivalent of the wave energy within the snowpack was calculated by integrating the squared displacement velocity with time:

$$v_{\mathrm{energy}} = \int v^2\ \mathrm{dt}\ (\mathrm{m^2\ s^{-1}}) \tag{5.9}$$

To compare the decay of the energy with depth within the snowpack to literature values (Capelli et al., 2016), the logarithm of the energy was linearly fitted against the depth. This yielded the following relation between depth and energy:

$$v_{\mathrm{energy}} \sim e^{-b_{\mathrm{energy}} z} \tag{5.10}$$

where b_{en} is the coefficient for the attenuation with depth.

The arrival time of the main impact was determined with two algorithms: The STA/LTA method was used, where short and long time averages of the signals are compared and the start is determined as the point where the difference of these averages exceeds a threshold (Withers et al., 1998). In addition, the arrival time of the main impact was determined by AIC picking (Kurz et al., 2005). With the latter method, the arrival time is determined as the minimum of the AIC function which comprises the logarithm of the variance of the signal starting from the beginning and the end of the signal.

The arrival times at the three measurement locations were used to determine the air pressure wave speeds in the respective distance range. The air pressure wave speed between the gas exploder and the first measurement location was determined using the time when the data acquisition started, which was given by the triggering pulse as zero time.

5.2.11 Snowpack characteristics

Snow stratigraphy and layer properties were recorded by observing a full snow profile (Fierz et al., 2009). In addition, density was determined with either a dielectric probe (Denoth, 1994) or a 100 cm^3 density cutter (Proksch et al., 2016).

During the first winter all experiments were performed on 10 and 11 March 2015. Snow depth was approx. 80 cm. The top two centimeters of the snowpack had previously been moist and hence there was a melt-freeze crust at the surface in the morning on both test days. The snowpack was dry during the first half of the day, but relatively warm with average snow temperatures of approx. -2 °C on 10 March and -1 °C on 11 March 2015. During the day the snow temperatures increased and the top few centimeters of the snowpack became moist. This was in particular the case in the afternoon when the experiments were performed. Average snow density was approx. 335 kg m^{-3}. The snowpack did not include any prominent weak layer and stability was classified as ‘good’ according to Schweizer and Wiesinger (2001).

During winter 2015-2016, we performed all experiments between 16 and 18 February 2016. One manual profile was performed on 16 February 2016; on the two consecutive test days conditions were similar apart from a few centimeters of new snow accumulated on 17 February 2016. Snow depth was about 60 to 70 cm. Average snow density was approx. 285 kg m^{-3}. The snowpack was dry, but warm with an average snow temperature of about -1 °C. As in the previous winter snow stability was rated as ‘good’.

In summary, snowpack characteristics were fairly similar between our experiments: a rather shallow and warm snowpack with occasionally slightly moist near-surface layers. Densities were

between 200 and 450 kg m^{-3}, slightly increasing or constant over depth with some lower density layers in ice lenses with high density. In the following, we therefore analyze all measurements jointly.

5.3 Results

5.3.1 Gas mass scaling

A single scaling factor was determined for all gas exploder experiments above snow. The best overall scaling factor was $a_G = 0.65$ with $R^2 = 0.997$. This indicates that doubling the gas quantity leads to the same pressure at about 1.5 times the unscaled distance for the gas quantities employed in our experiments.

The overall scaling factor for the experiments above bare ground was lower $a_{\mathrm{G_{ground}}} = 0.4$ with $R^2 = 0.997$. This indicates that a double gas quantity leads to the same pressure at 1.3 times the original distance above bare ground.

5.3.2 Air pressure above snowpack

A few air pressure measurements were not usable because of microphone malfunction, probably due to loose snow or humidity penetrating the sensor. The air pressure showed a typical sharp increase followed by a steep decrease with a period of negative pressure (or underpressure) (Fig. 5-6).

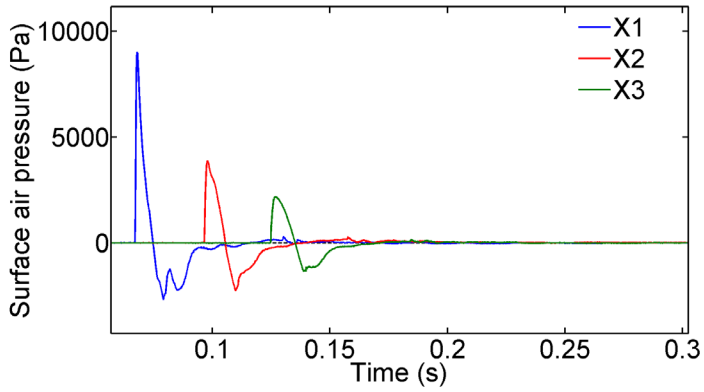

Fig. 5-6: Example of the air pressure signal at the three measuring locations on the X-axis (X1: 16.0 m, X2: 25.6 m, X3: 34.9 m); data from 18 Feb 2016, experiment #5.

The main frequencies of the air pressure signal were in the range of 30 to 40 Hz (Fig. 5-7a and Fig. 5-7b). A clear decay of the energy with distance was observed. However, the main frequencies did not change. The signals were hardly composed of frequencies above 500 Hz.

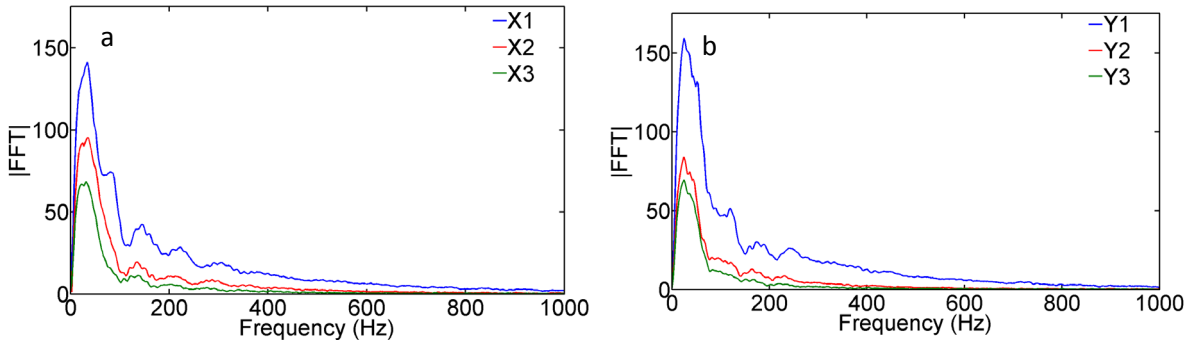

Fig. 5-7: Example of the air pressure frequency content for the three measuring locations on (a) the X-axis and (b) the Y-axis; data from 18 Feb 2016, experiment #5.

Maximum air pressures ranged from 17.5 kPa at a scaled distance of approximately 8 m $kg^{-0.65}$ to 0.3 kPa at a scaled distance of approximately 88 m $kg^{-0.65}$. The average maximum air pressure for all experiments on all test days with snow decayed strongly along the X-axis following a power law with an exponent of about 1.7 (Fig. 5-8a and Table 5-3). Along the Y-axis the maximum air pressure was very similar and also similarly decayed with distance (Fig. 5-8b and Table 5-3). As an example, with the largest gas volume used, i.e. 1.8 kg, the maximum air pressure was 6.1 kPa at 20 m and 0.6 kPa at 80 m along the X-axis. On the Y-axis, the maximum pressures at the same distances were 5.8 and 0.6 kPa.

Table 5-3: Power law coefficients for the decay of the maximum air pressures with distance for all experiments above snow and bare ground along the X- and the Y-axis.

	b		*a*	
	X	Y	X	Y
snow	1.68	1.66	5.69	5.5
bare ground	0.99	0.66	5.12	4.47

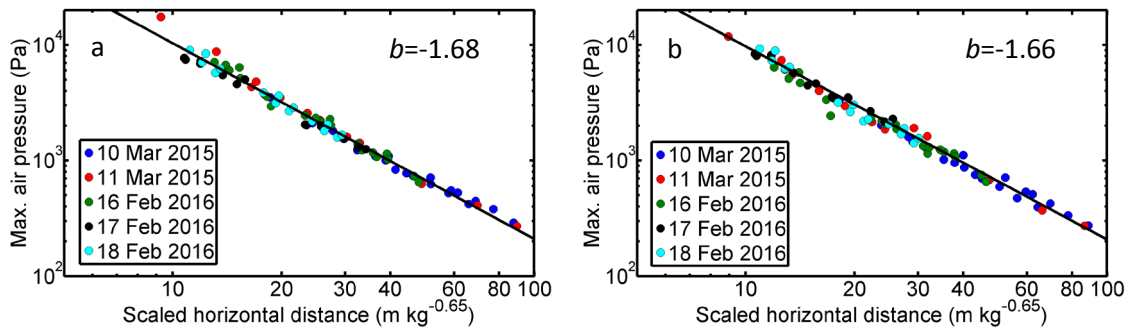

Fig. 5-8: Maximum air pressure for all test days with scaled distance from the point of explosion on (a) the X-axis and (b) the Y-axis.

The maximum derivative of the air pressure $p_{,t_{\max}}$ that is reached at the first steep increase of the air pressure ranged from 7.0×10^7 Pa s^{-1} at a scaled distance of 9 m kg$^{-0.65}$ to 5.5×10^5 Pa s^{-1} at a scaled distance of 88 m kg$^{-0.65}$. As the maximum air pressure, the derivative for all test days above snow decayed strongly with distance from the point of explosion following a power law (Fig. 5-9a and Table 5-4).

The equivalent of the air pressure wave energy p_{ener} ranged from 8.45×10^3 Pa^2 s at a scaled distance of 8 m kg$^{-0.65}$ to 0.59×10^3 Pa^2 s at a distance of 90 m kg$^{-0.65}$ on the X-axis. The absolute values on the Y-axis were similar. The energy decayed strongly with distance from the point of explosion, stronger than the other air pressure measures, but also following a power law (Fig. 5-9b and Table 5-5).

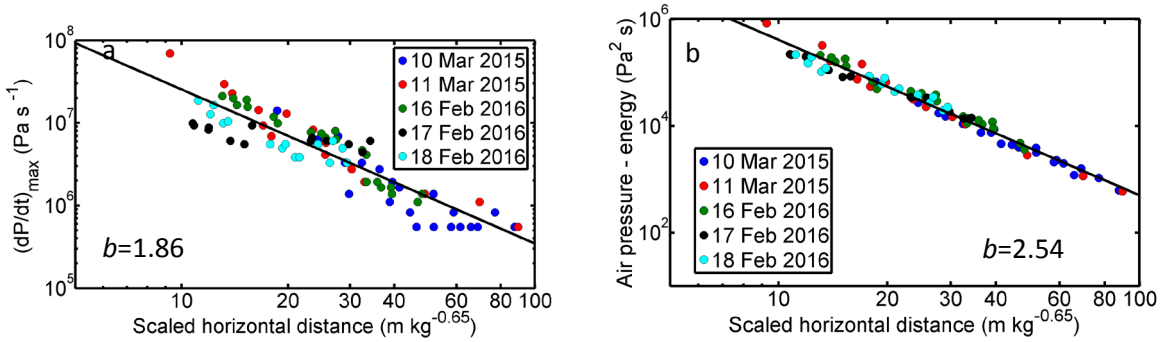

Fig. 5-9: (a) Maximum air pressure derivatives for all test days with scaled distance from the point of explosion on the X-axis, and (b) energy equivalent of the air pressure for all test days with scaled distance from the point of explosion on the X-axis.

Table 5-4: Power law coefficients for the decay of the maximum air pressure derivatives with distance for all experiments above snow and bare ground along the X- and the Y-axis.

	b		*a*	
	X	Y	X	Y
snow	1.86	1.50	9.27	8.78
bare ground		1.18		8.74

Table 5-5: Power law coefficients for the decay of the equivalent of the air pressure wave energy with distance for all experiments above snow and bare ground along the X- and the Y-axis.

	b		*a*	
	X	Y	X	Y
snow	2.54	2.5	8.02	7.9
bare ground	1.87	0.79	7.49	5.72

5.3.3 Accelerations in snowpack

On all test days with snow, snow accelerations were measured at all snow pit locations where also air pressures were measured. In each pit, accelerometers were installed at two different depths below the snow surface. Sensors were buried between 6 and 54 cm below the snow surface. On a given test day, we installed the sensors at approximately the same depths in all snow pits. The sensors were positioned 0.36 to 1.02 m from the snow pit wall into the undisturbed snowpack.

The typical acceleration signals showed a sharp increase at the beginning followed by a sharp decrease and damped oscillation (Fig. 5-10). At the sensors deeper in snowpack the accelerations were smaller; the horizontal components were in general smaller than the vertical accelerations. Maximum vertical accelerations within the snowpack on the X-axis ranged from 132 m s^{-2} at 11.9 m $kg^{-0.65}$ from the point of explosion and approx. 20 cm below the snow surface to 0.8 m s^{-2} at 88 m $kg^{-0.65}$ and approx. 50 cm depth (Fig. 5-11a). On the Y-axis vertical accelerations reached a maximum of 126 m s^{-2} at 10.7 m $kg^{-0.65}$ at approx. 20 cm depth and 0.33 m s^{-2} at a distance of 84 m and approx. 50 cm depth (Fig. 5-12b). Maximum horizontal accelerations ranged from 175 m s^{-2} at a distance of 9.1 m $kg^{-0.65}$ and a depth of approx. 15 cm to 0.2 m s^{-2} at 88 m $kg^{-0.65}$ and a depth of approx. 0.5 m (Fig. 5-13). On the Y-axis, the maximum accelerations ranged from 95 m s^{-2} at a distance of 10.7 m $kg^{-0.65}$ and a depth of approx. 15 cm to 0.2 m s^{-2} [b] at a distance of 84 m $kg^{-0.65}$ and a depth of approx. 50 cm. The maximum accelerations decreased strongly with distance from the point of explosion and depth within the snowpack (Table 5-6 and Table 5-7).

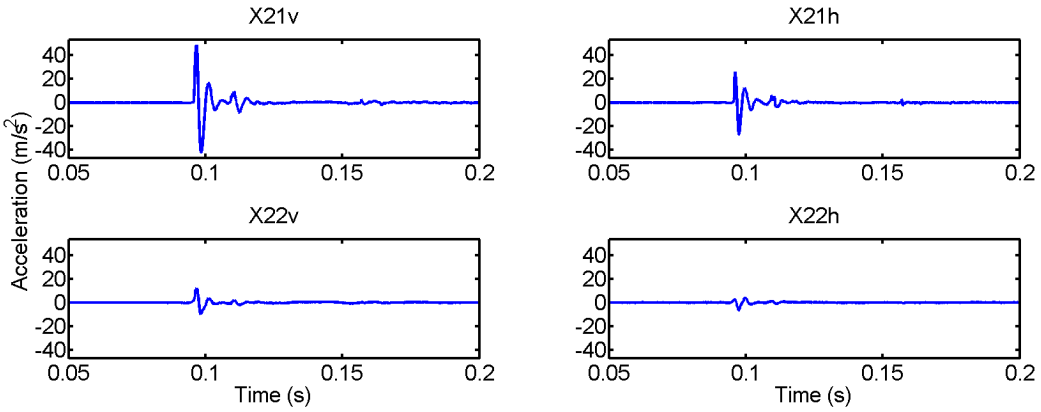

Fig. 5-10: Accelerations at the system X2 (25.6 m from the point of explosion). The top plots show the top sensors (14 cm below snow surface), the bottom plots the bottom sensor (38 cm below snow surface). Left and right plots show the vertical and the horizontal component, respectively; data from 18 Feb 2016, experiment #5.

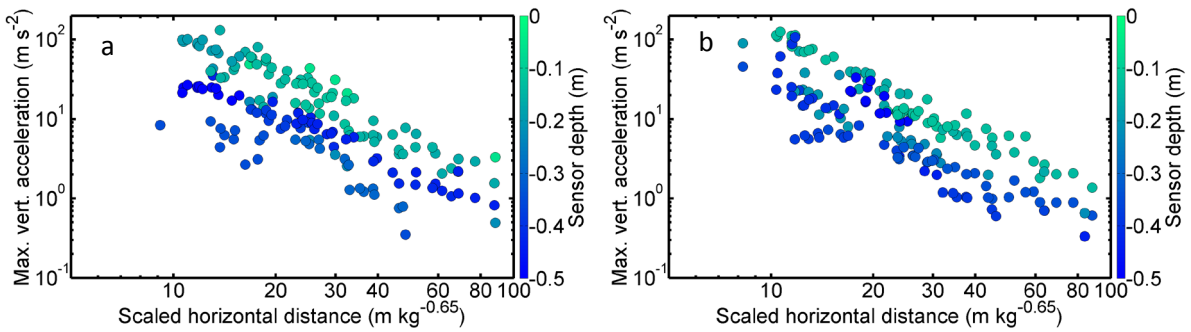

Fig. 5-11: Maximum vertical accelerations of the snowpack with distance from the point of explosion and depth within the snowpack (color scale) along the X-axis (a) and the Y-axis (b).

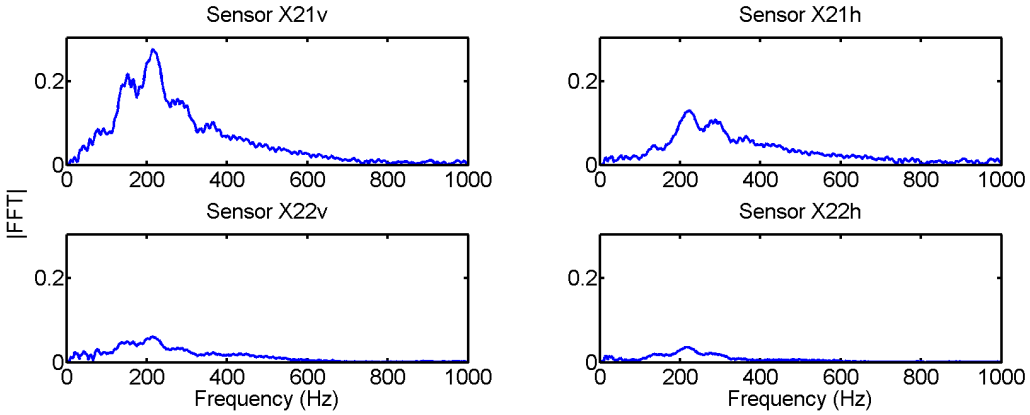

Fig. 5-12: Frequency content of the accelerations at the system X2 (25.6 m from the point of explosion). The top plots show the top sensors (14 cm below snow surface), the bottom plots the bottom sensor (38 cm below snow surface). Left and right plots show the vertical and the horizontal component, respectively; data from 18 Feb 2016, experiment #5.

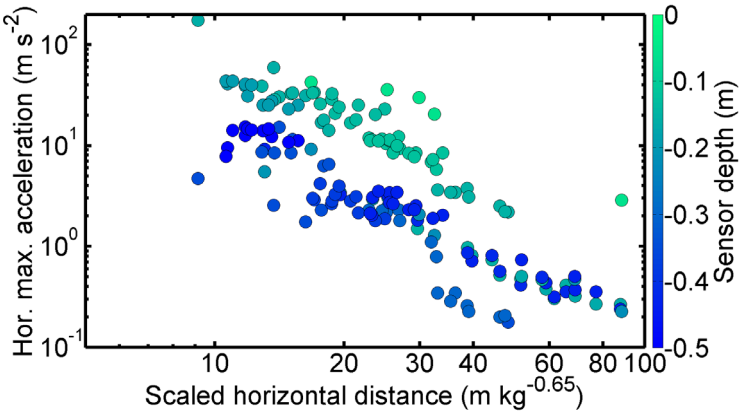

Fig. 5-13: Maximum horizontal accelerations of the snowpack with distance from the point of explosion and depth within the snowpack (color scale) along the X-axis.

Table 5-6: Power law coefficients for the accelerations (acc), displacement velocities (vel) and equivalent of the wave energy (energy) with depth within the snowpack for all experiments.

	b				*a*			
	X		Y		X		Y	
	vert	hor	vert	hor	vert	hor	vert	hor
acc	1.38	1.34	1.16	0.92	0.13	-0.36	0.19	0.05
vel	1.1	1.1	0.79	0.83	-2.65	-3.3	-2.6	-3
energy	1.59	1.14	0.87	0.84	-7	-7.4	-6.93	-7.47

The accelerations measured at different depths in each pit decreased rapidly with depth and followed a power law for the vertical and the horizontal component Table 5-6. For each axis, the decay with distance from the point of explosion was determined at 0.3 m $kg^{-0.65}$ depth using the power law decay with depth. This depth was chosen as it is a typical fracture depth for artificially triggered avalanches. The accelerations showed a strong decay following a power law with distance from the point of explosion at a certain depth within the snowpack for both components and both axes (Table 5-7).

Table 5-7: Power law coefficients for the accelerations with distance from the point of explosion for all experiments (mean), the experiments under dry and moist conditions.

	b				*a*			
	X		Y		X		Y	
	vert	hor	vert	hor	vert	hor	vert	hor
acc	1.96	2.68	2.19	2.82	3.7	4.15	3.84	4.44
vel	2.19	2.96	1.73	1.77	1.07	1.59	0.19	0.01
energy	3.75	4.68	2.81	2.27	-0.94	-0.11	-2.59	-3.79

The main frequencies of the acceleration signal were between 150 and 200 Hz for all depths (Fig. 5-12). Frequencies above 700 Hz were hardly found in the signal. A clear decay of the energy was observed with depth within the snowpack and distance from the point of explosion. The absolute values of the frequency content were lower for the horizontal than for the vertical component.

5.3.4 Displacement velocities in snowpack

Displacement velocities in the snowpack at the positions of the accelerometers were calculated by integrating the acceleration signal over time. As the integrated noise of the acceleration signal would lead to a non-zero velocity, the start and the end of the signals were manually picked to minimize this effect.

The displacement velocities also showed lower values at larger depths and lower values for the horizontal component (Fig. 5-14) Maximum vertical displacement velocities ranged from 0.60 m s^{-1} at 9.1 m $kg^{-0.65}$ distance from the point of explosion and approx. 20 cm depth and 6.5 x 10^{-4} m s^{-1} at 88 m $kg^{-0.65}$ and a depth of approx. 25 cm on the X-axis (Fig. 5-15). On the Y-axis, the respective values ranged from 0.17 m s^{-1} at 8.3 m $kg^{-0.65}$ and a depth of approx. 20 cm to 5.7 x 10^{-4} m s^{-1} at 84 m $kg^{-0.65}$ and a depth of approx. 50 cm.

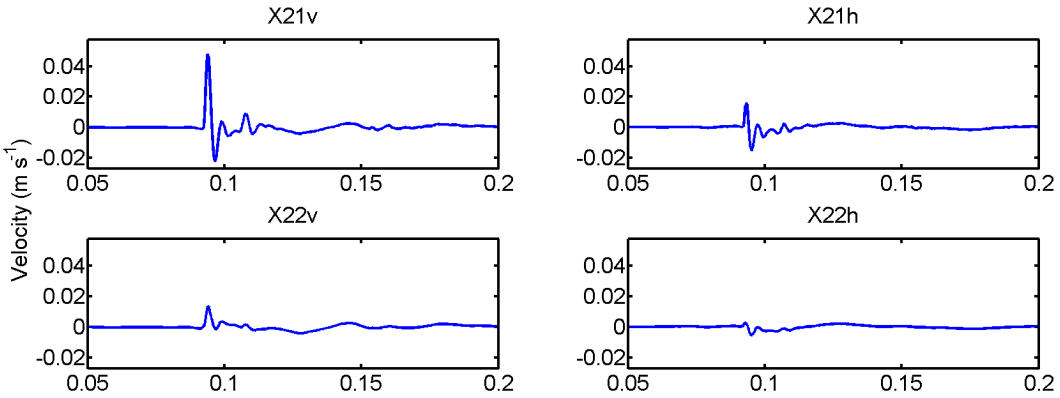

Fig. 5-14: Velocities at the system X2 (25.6 m). The top plots show the top sensors (14 cm below snow surface), the bottom plots the bottom sensor (38 cm below snow surface). Left and right plots show the vertical and the horizontal component, respectively; data from 18 Feb 2016, experiment #5.

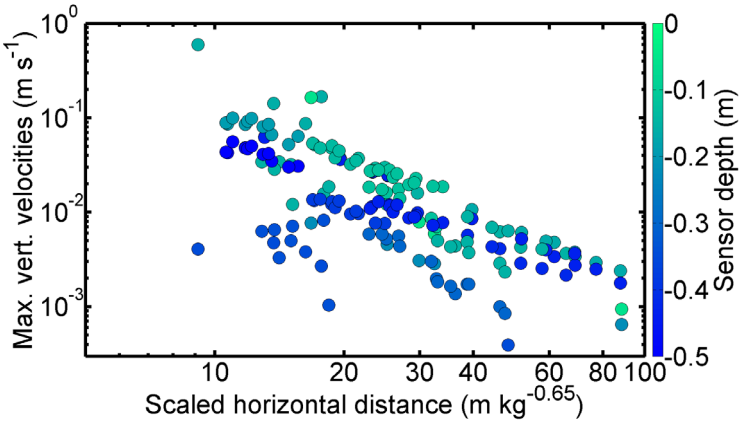

Fig. 5-15: Maximum vertical velocities of the snowpack with distance from the point of explosion and depth within the snowpack (color scale) along the X-axis.

Maximum horizontal velocities ranged from 0.12 m s^{-1} at a distance of 9.1 m $kg^{-0.65}$ and a depth of approx. 15 cm to 2.4 x 10^{-4} m s^{-1} at a distance of 88 m $kg^{-0.65}$ and a depth of approx. 50 cm below the snow surface on the X-axis. On the Y-axis, the respective values ranged from 0.07 m s^{-1} at 11.8 m $kg^{-0.65}$ and a depth of approx. 10 cm to 1.5 x 10^{-4} m s^{-1} at 78 m $kg^{-0.65}$ and a depth of approx. 35 cm.

As for the accelerations, the decay was determined using a power law for each snow pit. The displacement velocities decayed strongly with depth within the snowpack for all pits for both components and all axes (Table 5-6). There was a strong power law decay of the displacement velocities with distance from the point of explosion at the investigated depth of 0.3 m $kg^{-0.65}$ for both vertical and horizontal components and both axes (Table 5-7).

5.3.5 Equivalent of the wave energy in the snowpack

The equivalent of the wave energy in the snowpack, which was calculated from the displacement velocities, yielded curves that increased during passage of the wave and reached at a final value (Fig. 5-16). The values at larger depths and for the horizontal component were lower. Fitting the parameter against the depth using power laws showed a strong decrease with depth within the snow pits for both components and all axes (Table 5-6).

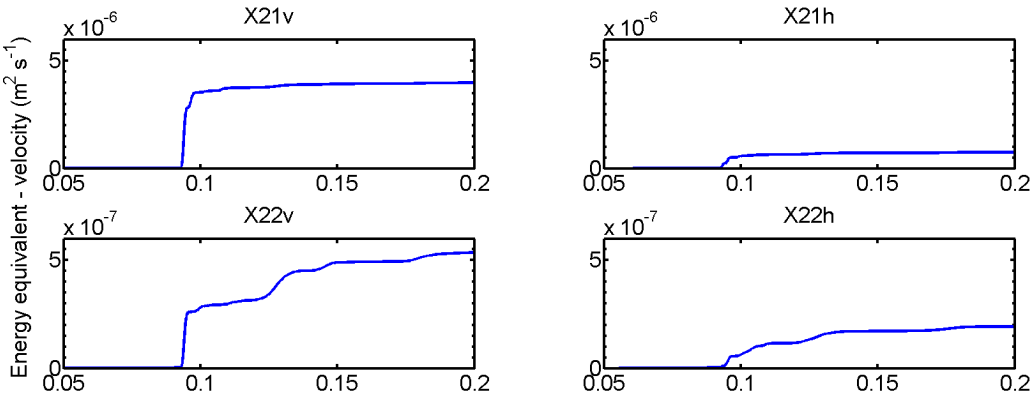

Fig. 5-16: Energy equivalent derived from the velocities at the system X2 (25.6 m). The top plots show the top sensors (14 cm below snow surface), the bottom plots the bottom sensor (38 cm below snow surface). Left and right plots show the vertical and the horizontal component respectively. Note the different scales on the y-axis; data from 18 Feb 2016, experiment #5.

Using these power laws to determine the decay with distance from the point of explosion at a certain depth within the snowpack yielded power laws with a strong decrease from the point of explosion (Table 5-7).

Using the fitting method by Capelli et al. (2016), the coefficient of the energy decay b_{en} was in the range of 2 to 3.

5.3.6 Snowpack displacements

Snowpack displacements were calculated by integrating the picked velocity signal over time. Maximum vertical displacements ranged from 3.7 x 10^{-3} m at 9.1 m $kg^{-0.65}$ and at approx. 15 cm below the snow surface to 2.1 x 10^{-6} m at a horizontal distance of 87.8 m $kg^{-0.65}$ and a depth of approx.

50 cm on the X-axis. On the Y-axis, values ranged from 1.0 x 10^{-3} m at 8.3 m $kg^{-0.65}$ and a depth of approx. 20 cm to 3.6 x 10^{-6} m at a distance of 69 m $kg^{-0.65}$ and a depth of approx. 0.4 m.

The maximum horizontal displacements ranged from 6.4 $\times$ 10^{-4} m at 9.1 m $kg^{-0.65}$ and a depth of approx. 15 cm below the snow surface to 4.4 $\times$ 10^{-9} m at a distance of 87.8 m and a depth of approx. 50 cm on the X-axis. The range on the Y-axis was from 7.9 $\times$ 10^{-4} m at a distance of 12.6 m $kg^{-0.65}$ and a depth of approx. 25 cm to 4.3 x 10^{-9} m at a distance of 88.2 m $kg^{-0.65}$ and a depth of approx. 0.4 m.

5.3.7 Air pressure above bare ground

Air pressure was measured at three different distances ranging from 15 to 31 m from the point of explosion and along two axes including an angle of 89° (Table 5-1). The measurements were not performed at shorter distances because it was expected that the air pressure wave might interrupt data acquisition as the measuring systems could not be protected in a snow pit.

The maximum air pressure ranged from 13.1 kPa at a distance of 12.7 m $kg^{-0.4}$ to 4.5 kPa at 26.8 m $kg^{-0.4}$ from the point of explosion on the X-axis (Fig. 5-17a). On the Y-axis, however, the maximum pressure ranged from 6.8 kPa at a distance of 13.0 m $kg^{-0.4}$ to 2.6 kPa at 28.4 m $kg^{-0.4}$ from the point of explosion (Fig. 21b). The maximum air pressures above bare ground decreased following a power law on both axes (Table 5-3). As an example, the maximum air pressure using 1.8 kg gas reached 8.4 kPa at 20 m and 2.1 kPa at 80 m from the exploder on the X-axis; on the Y-axis, pressures reached 4.8 kPa and 2.0 kPa at the respective distances.

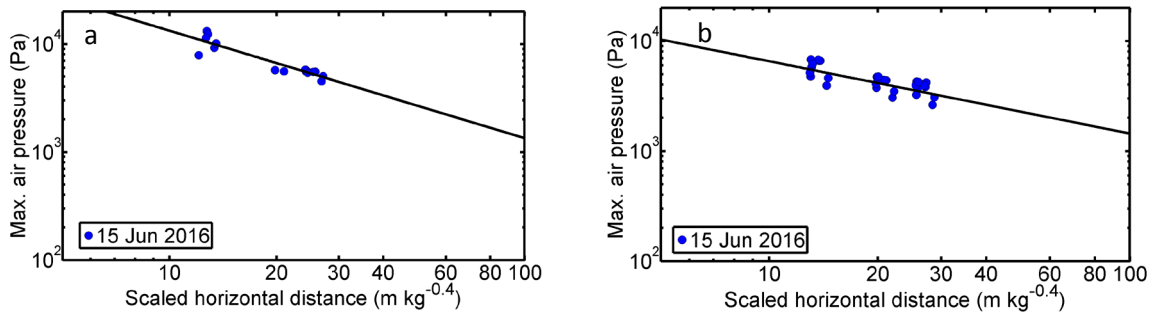

Fig. 5-17: Maximum air pressures above bare ground with distance from the point of explosion (a) along the X-axis, and (b) along the Y-axis (at 89° from X-axis).

The maximum of the air pressure derivative was in the range of 2 $\times$ 10^7 Pa s^{-1} on the X-axis. On the Y-axis, the maximum derivative was 1.9 $\times$ 10^7 Pa s^{-1} at 20.1 m $kg^{-0.4}$ and 8.9 $\times$ 10^6 Pa s^{-1} at a distance of 28.4 m $kg^{-0.4}$. The decay of the air pressure derivative followed a power law on the Y-axis and was similar to the decay of the maximum air pressure (Table 5-4). On the X-axis, the derivative

was only measured correctly at one distance from the explosion and hence no decay could be determined.

The equivalent of the air pressure wave energy p_{ener} ranged from 3.9×10^5 Pa^2 s at a scaled distance of 12.7 m kg$^{-0.4}$ to 6.4×10^4 Pa^2 s at a distance of 27.1 m kg$^{-0.4}$ on the X-axis. The absolute values on the Y-axis were 9.1×10^4 Pa^2 s at a scaled distance of 13.0 m kg$^{-0.4}$ to 2.4×10^4 Pa^2 s at a distance of 28.7 m kg$^{-0.4}$. The energy equivalent decayed following a power law for both axes showing a strong decay (Table 5-5).

5.3.8 Influence of exploder incline and elevation

So far we have analyzed all measurement jointly not considering incline and elevation of the exploder with regard to the snow surface. Comparing all test days with different gas exploder inclines (Table 5-1), the strongest decrease exponents of the air pressure were observed for the lowest and the largest angle and similar exponents for angles between 32 and 37°. However, there were only five angles investigated. When plotting the fitted power law of the air pressure against the distance considering the incline, the air pressures were very similar.

The maximum vertical acceleration decrease with distance at a certain depth within the snowpack for all different exploder inclines showed a decrease of the decay exponent from the lowest to the largest angle on the X-axis. On the Y-axis, the lowest decrease was observed for the lowest incline angle and higher values resulted for the larger angles. The maximum value was reached for an incline of 32°.

The maximum horizontal acceleration decrease at a certain depth with distance on the X-axis showed for all angles a decay exponent of around 2 to 2.4 with an outlier at 30°. On the Y-axis, the lowest decay exponent was observed for the lowest angle (28°); the exponent increased to a maximum at 32° with lower exponents for the largest angles.

With regard to exploder elevation above the snow surface, the comparison of the maximum air pressure decay exponents for different elevations (Table 5-1) did not reveal any tendency. Overall, the maximum air pressures for all experiments above snow were similar without apparent trend. Moreover, there was no tendency observable in the maximum vertical and horizontal accelerations for both axes with different gas exploder elevations.

5.3.9 Effect of snowpack conditions

Snowpack conditions were similar on all test days. The snowpack was well settled and dry, but warm, except in March 2015 when the top centimeters become moist during the experiments. Minor differences between the air pressure and snowpack responses were hence observed between the

days with a moist surface layer and the days with a fully dry snowpack. However, these small differences showed no tendency and were within the measuring uncertainty.

5.3.10 Air pressure wave speeds

Air pressure wave speeds were calculated from the arrival times and the distances between the microphones. The mean air wave speeds measured for each test day was between 322 m and 333 m s^{-1}. Air pressures between the spark plugs in the gas exploder and the first sensor location on each axis were lower. There were no speeds above the speed of sound observed within the measuring range.

5.4 Discussion

5.4.1 Gas quantities and gas scaling

Gas quantities ranged from 0.43 to 1.51 m^3. However, the volume of the gas exploder was approx. 1.25 m^3. This means at least for the larger gas volumes, that the gas mixture had partly flown out of the gas exploder. This is possible because the pipe was not tight at the front. If the pipe would have been closed tightly, an overpressure in the pipe would have resulted possibly causing the pre-blast failure of the plastic cover. This overpressure would not have been representative for the conditions found with operational gas exploders.

The gases flow very rapidly into the gas exploder with a maximum speed of approx. 0.55 m^3 s^{-1}. This probably leads to turbulent flow behavior in the gas exploder. It is hence not clear and not measurable how the gases mix and where they flow. As the gases enter in the back half of the pipe, one may assume that mainly atmospheric air will be pushed out of the pipe. It might also be that always the same proportion of the gas flowed out of the pipe as the gas mixture is heavier than atmospheric air. There was no possibility to check the composition of the gas mixture within the gas exploder due to several reasons. Besides the issue of measuring gas mixtures within an exploder that is suspect to an explosion, the gas mixture will flow rapidly within the gas exploder making it almost impossible to interpret the information about the gas mixture that is changing with time. The influence of the fact that obviously part of the gas mixture is flowing out of the pipe is not considered while determining the gas scaling factor. As the fit is good, the effect of the outflowing gas seems to be of little importance.

The gas scaling factor was determined using the maximum air pressures and gas masses for the experiments, where exact gas measurements were possible. The masses of the experiments without gas measurements were fitted using the results of the experiments with gas measurements. There might be a shift in the distances for experiments above a moist snow surface due to different

behavior of the air pressure decay above the snowpack. However, Simioni et al. (2015; cf. Chap. 4) did not find significant differences for the air pressure propagation above a dry and a moist snowpack.

The best-fit scaling factor above snow was 0.65. The scaling factor was determined for the exploder axis; scaling factors for other directions might be different. The scaling factor was obtained using the maximum air pressures at all distances. As the maximum air pressure decayed with $b_{\mathrm{airp}} = 1.67$ and the maximum air pressure derivative (increase per time) with $b_{\mathrm{airp},t} = 1.66$, it is irrelevant whether the maximum air pressure or the air pressure derivative is chosen to determine the scaling factor.

The obtained scaling factor was almost twice as large as the scaling factor used for solid explosive experiments (Binger and Miller, 2016; Bones et al., 2012; Cooper, 1996; Simioni et al., 2015; cf. Chap. 4) which is commonly assumed to be 1/3 for solid explosives with a spherical expansion. Simioni et al. (2015; cf. Chap. 4) showed that this assumption is valid for solid explosive experiments above a snowpack. The difference between the scaling factors may be due to the following effects: The gas exploder creates a directed explosion which is clearly different from a spherical expansion, but rather a mixture between plane and spherical expansion.

The best scaling factor for the experiments above bare ground was 0.4. The difference to the scaling factor above snow is related to the different properties of the underlying material. The other setup parameters (elevation, incline, gas mixture) were in the same range as for the experiments above a snowpack.

5.4.2 Air pressure

We measured a decay of the air pressure proportional to $x'^{-1.67}$ in the exploder axis (Table 5-3). This is within the range of values reported by Simioni et al. (2015; cf. Chap. 4) for solid explosives ($x'^{-1.1}$ to $x^{-2.1}$). The values were higher than what Gubler (1976) reported, slightly higher than what Ingram (1962) and Mellor (1973) observed, but in excellent agreement with the results from Albert and Hole (2001). The values between $b_{\mathrm{airp}}^{\mathrm{X}} = 1.0$ and $b_{\mathrm{airp}}^{\mathrm{X}} = 2$ show that the decay is stronger than for a spherical expansion ($b = 1$). As the decay of the air pressure is similar up to the investigated angle of approx. 35° from the exploder axis to the side, it can be said that the air pressure – at least within this aperture – is similar to that of an explosion caused by a solid explosive. The air pressure derivative decayed similarly to the maximum air pressure (Table 5-4). This means that the maximum air pressure decay can be used as an approximation for the decay of the maximum increase per time of the air pressure (air pressure derivative) or vice versa.

The calculated equivalent of the air pressure wave energy decayed proportional to approx. $x'^{-2.9}$ (Table 5-5). As the energy is proportional to the pressure amplitude squared, this decrease with

distance is plausible. We are not aware of any previous studies our results on the energy equivalent could be compared to.

The air pressure above bare ground decreased less strongly ($b_{\mathrm{airp}}^{\mathrm{X,bare}} = 1.1$) with distance from the point of explosion than above snow ($b_{\mathrm{airp}}^{\mathrm{X}} = 1.67$) (Table 5-3). The decay above bare ground was close to the decrease of a spherical wave although the directed explosion is not causing spherical expansion at all. The lower exponent above bare ground is rather related to the effect of the different surface properties of snow vs. bare ground. The snowpack absorbs part of the air pressure wave because its impedance – would it be a continuum – is closer to that of air than the impedance of soil. In addition, the open pores of a snowpack decrease the reflectivity of the incoming wave further.

The maximum air pressures above bare ground at 89° from the exploder axis were smaller than in the exploder axis. For example, at 13 m kg$^{-0.4}$, the maximum air pressure was 13.1 kPa on the X-axis and 6.8 kPa on the Y-axis. However, the decrease along the Y-axis was much less strong with $b_{\mathrm{airp}}^{\mathrm{Y,bare}} = 0.66$ compared to the decrease on the X-axis with $b_{\mathrm{airp}}^{\mathrm{X,bare}} = 0.99$. This means that at a distance of 93 m kg$^{-0.4}$, the air pressure on the Y-axis is as large as on the X-axis. Due to the inclined tube the amplitude decay perpendicular to the pipe axis is closer to the decay of a cylindrical wave, whereas the decay along the pipe axis seems to reflect more spherical wave expansion. Whereas the absolute values close to the point of explosion are significantly higher on the X-axis, the values are equal at large distances. Isolines indicating the same pressure will be bulb-shaped close to the explosion but change to a circle at large distance.

The counterweights that almost had to be doubled inhibited experiments at other angles than up to 36° from the exploder axis and below approx. 85° from the axis. It would have been a possibility to build a fixed foundation in the soil. This would – however – have prevented experiments at different locations. Instrumenting the experiments to the back (180° from the gas exploder axis to the front) was not feasible due to the embankment of the road.

5.4.3 Accelerations

On average, the decay with depth within the snowpack at all three distances from the point of explosion was proportional to $x'^{-1.38}$ (Table 5-6). Our results are in good agreement with the results of Binger and Miller (2016) who measured at much closer distances and under conditions they called ‘hard slab snow’. However, scatter in our results was large and caused by the complexity to accurately position the sensors relatively to each other, by the difference between sensor and snow density which existed for layers that were off the average sensor density of 200 kg m^{-3} and the correct coupling of the sensor within the hole.

The maximum vertical accelerations behaved similarly with distance from the point of explosion within the aperture of up to 36° from the exploder axis, with $b_{\mathrm{acc}} = 1.96$ in the gas exploder axis and $b_{\mathrm{acc}} = 2.19$ on the Y-axis (Table 5-7). The maximum horizontal accelerations decreased stronger with distance than the vertical component ($b_{\mathrm{acc}} = 2.68$ and $b_{\mathrm{acc}} = 2.82$ for the X- and Y-axis, respectively). These values are in good agreement with the results for hard slab snow reported in Binger and Miller (2016). The average decrease was stronger than reported in Simioni et al. (2015; cf. Chap. 4). However, as in Simioni et al. (2015; cf. Chap. 4) scatter was large. The maximum horizontal accelerations were smaller. The observed decay is in good agreement with the observations by Bones et al. (2012). Suriñach et al. (2011) did not provide a relation for the decay with distance but reported a decreasing tendency with distance from the point of explosion. They measured at distances larger than 130 m and observed ground accelerations that were in the range of 0.01 to 1 x 10^{-5} m s^{-2} which seem plausible compared to our observations.

5.4.4 Displacement velocities

Velocities within the snowpack showed a strong decay with depth for all pits, more distinct for the vertical than for the horizontal component (Table 5-6). However, scatter was large due to the same reasons as for the accelerations.

Snowpack velocities decayed stronger with distance from the point of explosion at a certain depth than reported by Simioni et al. (2015; cf. Chap. 4) (Table 5-7). Vertical velocities decayed less strongly than horizontal velocities but the decay or their values were similar. Velocities on the Y-axis, out to 36° from the X-axis, decayed less strongly than velocities on the exploder axis. The decay was stronger than what was reported by Gubler (1976).

5.4.5 Equivalent of the wave energy in the snowpack

The energy equivalent, calculated from the snowpack velocities, decreased stronger on the X-axis than on the Y-axis for each pit with increasing depth from the snow surface (Table 5-6). The vertical component decreased slightly stronger than the horizontal component.

The energy equivalent decreased strongly with distance from the point of explosion at a given depth (Table 5-7). We are not aware of any previous results to compare our results of energy equivalent to.

The values of the power law exponent obtained with the method using the fitting to the semi-log-plot ($b_{en} \approx 2$ to 3) were higher than those reported in Capelli et al. (2016) ($b_{en}. \approx 0.35$ to 1.2). The reason is that Capelli et al. (2016) performed their experiments under lab-conditions with a single grain type, a well-known geometry and plane waves. In addition, Our results comprise the effects of an inhomogeneous multi-layered snowpack causing reflections and non-planar

propagation. Furthermore, the wave does not hit the sensors perpendicular to the snow surface and hence a wave arriving at a sensor will not be the same wave that arrives at a lower sensor. The wave arriving at the lower sensor will be transmitted from the air to the snowpack at a shorter distance from the point of explosion. Attenuation measurements in snow seem to be extremely delicate to perform and hence previously reported values vary significantly, in the range of 0.05 to 3.5 dB cm^{-1} (Capelli et al., 2016).

5.4.6 Displacements

Maximum displacement ranged between 10^{-3} m for measurements close to the surface and close to the point of explosion to 10^{-6} m for larger distances and depths within the snowpack. This is in good agreement with the results of Gubler (1976) and Simioni et al. (2015; cf. Chap. 4). No fit parameters for the power law are given for the gas exploder experiments: The absolute displacement values were too small to allow any conclusions based on a power law fit.

5.4.7 Frequency content

The main frequencies of the air pressure signals of the gas exploder experiments (30 to 40 Hz) are in good agreement with the solid explosive experiments (~40 Hz) performed by Simioni et al. (2015; cf. Chap. 4). However, the main frequencies of the accelerations within the snowpack were much higher for the gas exploder experiments (~200 Hz) than for the solid explosive experiments (~40 Hz). As the air pressure frequencies for both types of experiments were similar, it is expected that under given snowpack conditions, the frequency content within the snowpack should be similar, too. The observed difference may be related to snow depth. The snow depth reported in Simioni et al. (2015; cf. Chap. 4) was more than double of the depth observed during our experiments. It seems that the frequency content reflects the vibration behavior of the entire snowpack. Low frequencies and long wave lengths combined with shallow snow depth would support this assumption. The decay of both the air pressure and the acceleration signals was frequency-dependent. The lower frequencies decayed less strongly with distance than the higher frequencies. In snow, this was expected due to non-elastic effects.

5.4.8 Influence of gas exploder incline and elevation

The strongest decrease of the air pressure with distance from the point of explosion was obtained with the lowest gas exploder incline (30°). This is counter-intuitive as one would expect that with a large incline and a directed explosion, pressures would be high close to the surface and decrease rapidly with distance. However, when looking at the absolute values with distance, the differences are small.

There was no influence of the gas exploder elevation observed. Compared to the size of the gas exploder and the distances of the performed measurements, an increase in elevation of approx. 50 cm does not result in significant differences.

5.4.9 Snow conditions

The snowpack during the two experimental periods was rather shallow with snow depths between 60 and 80 cm. Densities were rather high compared to snowpacks usually found when avalanches are triggered artificially and near surface layers often consist of new snow. Furthermore, all experiments were performed under dry, warm snow conditions with only occasionally moist surface layers (during winter 2014-2015). Therefore, considerable differences between experiments due to varying snow conditions could not be expected.

The decrease of the air pressure with distance from the point of explosion was similar independent of if the top layers were moist. A moist part of the snowpack – here the top layers – will change wave propagation above and transmission of waves to the snowpack. However, differences in the snowpack layers other than light wetness might affect the behavior more strongly. Albert and Hole (2001) stated that changes in snowpack conditions considerably influence wave propagation above snow, i.e. that also the transmission of the air pressure wave to the snowpack will vary strongly with differences in snowpack conditions. These changes can happen within a short period of time. If there is a crust or denser layer at the surface, this will have a larger influence on the measured quantities than if there was loose new snow observed due to differences in permeability that are influencing wave propagation in snow (Johnson, 1982). Hence differences that can change within a short period of time have a large influence on the measured air pressure and may explain some of the scatter observed for the air pressure and the derived parameters with distance from the point of explosion.

As for the air pressure, no large differences were observed for the quantities measured within the snowpack with different snowpack conditions. The observed differences did not show any clear tendency. Hence, one can assume that the layering and other properties of the snowpack had a stronger influence than the moist surface layer. Many different layers will cause stronger reflections and hence stronger attenuation measured between two sensors than a snowpack with fewer similar layers due to impedance differences caused by the first. Ice lenses and crusts in combination with other, less dense snow layers will reflect a large part of the energy due to large impedance differences.

An alternative explanation for the low difference in air pressure attenuation and related quantities is that the previously reported low impact under wet-snow conditions may be due to the fact explosions were triggered within the snow (e.g., Gubler, 1977; Johnson et al., 1993). Our results

suggest that for explosions above a snowpack, the impact might be similar – still, the snowpack's response in terms of failure behavior might be different.

5.4.10 Approximation of snowpack loading with other parameters

Snowpack accelerations are difficult to measure and these measurements require a large effort. It is therefore desirable to perform easier measurements such as the one for air pressure and use them as approximation for other parameters. The maximum vertical accelerations decreased with distance at a depth of 0.3 m kg$^{-0.65}$ with $b^{\mathrm{X}}_{\mathrm{acc_{vert}}} = 1.96$ and $b^{\mathrm{X}}_{\mathrm{acc_{hor}}} = 2.68$ (larger scatter for the horizontal component) (Table 5-7). The vertical accelerations were usually larger and will therefore be considered here. The maximum air pressure decreased less strongly than the accelerations $b^{\mathrm{X}}_{\mathrm{airp}} = 1.67$) (Table 5-3). The air pressure derivative decreased in the same way with distance as the maximum air pressure (Table 5-4). The energy equivalent of the air pressure decreased with $b^{\mathrm{X}}_{\mathrm{airp,ener}} = 2.54$ (Table 5-5); the decrease was higher than the decrease of the maximum accelerations. The parameters maximum air pressure and air pressure energy equivalent therefore provide lower and upper bounds, respectively, for the magnitude of the decrease of the accelerations.

The maximum vertical velocities decreased in the same way as the maximum vertical accelerations with distance from the point of explosion at a given depth within the snowpack. Again, the horizontal component decreased much stronger. This might be due to the shallow angle of incidence which might cause waves along the surface or surface waves that have a stronger horizontal component or waves that propagate almost parallel to the snow surface. The air pressure energy equivalent provided a lower bound for the decay of the maximum horizontal accelerations. The maximum air pressure and the air pressure energy equivalent yielded lower and upper bounds for the decrease of the maximum vertical velocities. None of the air pressure parameter decrease coefficients was close to the decrease of the energy equivalent of the snowpack velocities.

The displacements are not considered here due to extremely small values and hence no meaningful fitting parameters were obtained. There was no permanent settling observed.

5.4.11 Air pressure above snow and bare ground

Maximum air pressures, the air pressure derivatives and the air pressure energy equivalents above bare ground were significantly higher than above snow (Table 5-3, Table 5-4 and Table 5-5). Also, their decrease with distance was significantly stronger above a snowpack compared to bare ground. This is expected because the hard soil reflects a higher percentage of the incoming air pressure wave than a porous, compared to soil, soft snowpack does. Albert and Orcutt (1990) reported a similar

effect. Hence, it is essential to perform these types of experiments above snow despite the large operational effort required.

5.4.12 Lateral decrease of the air pressure

Whereas no lateral decrease was observed up to a forward cone of half angle of about 36°, the measurements along an axis perpendicular (89°) to the exploder axis showed that the air pressure and its derived parameters were significantly smaller than in parallel direction (Table 5-3, Table 5-4 and Table 5-5).

However, the decrease was less strong compared to the gas exploder axis. The absolute values of the air pressure above snow cannot be compared to those above bare ground as described above. The relative lateral decrease, compared to the decrease in the axis of the exploder, can be compared as the snowpack is fairly uniform – as is the ground – on the entire study site. With the results from the experiments above bare ground it is now clear why the decrease of the air pressure above the snowpack at up to 36° is slightly less strong than in the exploder axis: Due to effects of the gas exploder geometry, absolute values are smaller at an angle from the exploder axis, but the decay exponent *b* decreases from the exploder axis outwards.

5.4.13 Air pressure wave speed

Air pressure wave speeds between the three measuring pits were in good agreement with the acoustic wave velocity in air and in good agreement with the results of Simioni et al. (2015; cf. Chap. 4) for larger ranges outside the shock zone. Even when considering the exact location of the spark plugs within the gas exploder, speeds between the gas exploder and the first pit were unrealistically low (below 300 m s^{-1}). The reason may be that the zero time determined by the trigger of the gas exploder was not correct. It might be that there was a delay between pushing the trigger button and the ignition of the spark plug. It is therefore not clear, whether the speed of sound was exceeded at shorter distances (up to 12 m from the point of explosion). During solid explosive experiments, shock speeds were observed and the shock limit was in the range of approx. 17 to 30 m from the point of explosion.

5.4.14 Reproducibility

We always performed at least two experiments with approximately the same gas mass. The resulting maximal air pressure varied within 5 to 10 %. Hence the results are well reproducible, even for different days with different snowpack conditions, different exploder setups and scaled gas masses.

5.4.15 Limitations

Our flat field experiments with a prototype gas exploder cannot directly be compared to operational gas exploders. First of all, the recoil of the system might be different since operational gas exploders damp the recoil using gravity and the mass of the pipe. The system we used was tensioned with guy wires that absorb the recoil. This means that the behavior is different. However, both systems are not rigid.

Moreover, the gas masses and the derived gas volumes used with the mobile gas exploder are not the same as usually given as the size of an operational gas exploder in m^3. It is unknown how much gas is used in operational gas exploders as they are calibrated individually via the flow time; moreover, gas amount depends on atmospheric conditions, in particular the elevation where the system is installed.

Still, our gas exploder experiments may be considered as first good approximation of the effect of an operational gas exploder as we reproduced the directed explosion, used a soft system and a similar gas mixture. These results have to be compared to operational gas exploders to assess whether they are transferrable, whether a scaling of the results is required or whether the results are not transferrable at all.

5.5 Conclusions

We performed experiments with a prototype gas exploder above different snowpacks and bare ground. We measured air pressure at different distances from the point of explosion and snowpack accelerations at different depths within the snowpack and distances from the point of explosion.

All measurements were performed in the gas exploder axis and along a second axis to account for the non-radially symmetric shape of the impact. The gas exploder was setup at different inclines and elevations above the ground. We measured the mass of the propane-oxygen gas mixture and determined a scaling factor – for maximum air pressures and gas masses. The scaling factor was 0.65 for experiments above snow and 0.4 for experiments above bare ground, which is higher than what is used with solid explosives (1/3).

The magnitude and decay of the maximum air pressure were similar along the gas exploder axis and the second axis up to angle of 36° from the gas exploder axis. The air pressure derivatives decayed similarly as the maximum air pressure. The energy equivalent decreased stronger with distance than the maximum air pressure or the air pressure derivative. The maximum air pressure values were in good agreement with the results of Simioni et al. (2015; cf. Chap. 4).

Maximum vertical and horizontal accelerations, velocities and the energy equivalent decreased strongly with depth within the snowpack and distance from the point of explosion as previously shown for the case of solid explosives (e.g., Binger et al., 2006; Simioni et al., 2015; cf. Chap. 4).

For our limited range of snowpack conditions we did not find any significant effect of snowpack properties on the air pressure above snow nor the accelerations within the snowpack.

Air pressures decreased significantly faster with distance above a snowpack than above bare ground. The maximum air pressures and other parameters, measured along an axis about perpendicular to the gas exploder axis, were significantly lower at short distances, but decreased less strongly with distance than in the exploder axis. This was also to a very small extent observed for the aperture of up to 36° from the exploder axis above snow, i.e. the measurements above bare ground can be used to determine the proportion of the decay laterally and be used to explain effects above snow. This means, that the effect of the directed gas explosion is causing lower air pressures up to a distance of around 90 m from the explosion at 90° from the exploder axis.

The decay of the maximum air pressure or the air pressure derivative with distance gives a good lower bound for the effects within the snowpack at a certain depth; the decrease of the energy equivalent of the air pressure gives a good upper bound. Maximum displacements were very small and their fit did not lead to meaningful results due to settled snow.

Wave speeds were in the range of the speed of sound at distances larger than approx. 11 m from the point of explosion; the existence of a possible shock-wave close to the point of explosion could not be observed due to the lack of adequate instrumentation.

Due to different solid explosive masses ranging from 2.4 to 10 kg and gas masses ranging from 0.12 to 1.89 kg, experiments with solid explosives and gas mixtures are hard to compare. However, one can conclude that even if absolute air pressure and snowpack parameters would be different, the decay behavior with distance from the point of explosion and depth within the snowpack is similar. Stresses decrease with depth within the snowpack. Together with increasing strength with depth, this leads to a decreasing failure probability for weak layers within the snowpack.

Our study is the first of its kind that comprehensively examines the effect of a directed gas explosion, common to operational gas exploder system, with a measurement setup as previously used for solid explosives. The above findings hence represent an important step towards a better understanding of the effect of an explosion within a snowpack – and eventually of artificially triggering avalanches. However, it remains challenging to relate our measurements to the failure behavior of snow and assess consequences for avalanche release. In the future, we will perform side-by-side experiments allowing the direct comparison between gas explosions and solid explosives.

6 Snowpack response to explosions caused by an operational gas exploder

6.1 Introduction

Artificially triggering snow avalanches by explosions has become a key measure in avalanche mitigation during the past decades. Among the reasons are the economic operation, the charge placing flexibility and the low environmental impact (compared to engineering works). Hand charging can be performed under almost any given condition. Throwing charges from a helicopter allows quick access to many detonation points and in particular remote locations, but is limited to times with good visibility. This means that helicopter bombing cannot be performed during storms and is delayed so that the optimal time for triggering is often missed (McClung and Schaerer, 2006). Fixed avalanche control installations operating with solid explosives or gas mixtures overcome this disadvantage allowing to trigger avalanches at any given daytime and under the most adverse weather conditions – provided there are no other operational constraints. However, for most systems, their fixed location implies low flexibility with regard to the point of explosion. To optimize the application of fixed avalanche control installations it therefore seems crucial to better understand their effect on the snowpack.

Many studies were performed on the effect of explosions on a snowpack. Some of them focused on short distances, i.e. the shock range (less than about 10 to 20 m for small solid explosive masses from the point of explosion), to determine snowpack behavior (Frigo et al., 2012; Johnson et al., 1994; Johnson et al., 1993) and showed the strong compaction and attenuation of the waves within snow. Other studies investigated the effect of solid explosives used in avalanche release on snowpacks (Binger and Miller, 2016; Frigo et al., 2010; Tichota et al., 2010) and showed strong attenuation of the air pressure above and the accelerations within the snowpack with increasing distance and highlighted the advantage of elevating a charge above the ground, in accordance with the studies by Gubler (1977) and Ueland (1993).

Albert et al. (2008), Albert and Hole (2001) and Albert et al. (2013) investigated the effect of different ground conditions on air pressure wave propagation and showed the strong attenuation effect of a snow cover on the blast waves. Furthermore, they reported that ground vibration caused by the air pressure wave hitting the snowpack close to the point of measurement was always larger than the vibration caused by direct ground vibration waves which was also reported by Suriñach et al. (2011).

The effect of solid avalanche explosives was also investigated by Gubler (1977) but at distances more relevant for the effect of an explosion on avalanche release. He showed the strong decay of air pressure with distance from the point of explosion. Simioni et al. (2015; cf. Chap. 4) performed extensive flat field experiments using solid explosives and confirmed the strong attenuation of the air pressure and the snowpack accelerations with distance from the point of explosion but also showed

that the accelerations and all derived parameters decayed strongly with depth within the snowpack. They also reported the existence of two different weak layer failure types.

Simioni et al. (2016c; cf. Chap. 5) performed flat field experiments using a prototype gas exploder above snow and bare ground. They showed a similar behavior as observed by Simioni et al. (2015; cf. Chap. 4). They reported that within a sector of approx. 70° around the exploder axis, loading was not significantly decreasing. However, their results above bare ground indicated that the absolute loading values at an angle of 90° from exploder axis are smaller at short distances but decay less rapidly.

Suriñach et al. (2011) performed ground acceleration measurements at approx. 90° from the axis of an operational gas exploder at large distances (>120 m). They observed small accelerations in the range of 10^{-3} to 10^{-2} m s^{-2} with a larger contribution of the vibration caused by the air pressure wave compared to the direct ground wave. Using a simple stability criterion, they concluded that at these distances avalanche triggering was unlikely. Simioni et al. (2016b; cf. Chap. 7) performed similar experiments at shorter distances from the gas exploder and in the exploder axis. They concluded that under unstable conditions, the induced ground acceleratins might be sufficient to trigger an avalanche. However, in situations when a snowpack was available above the ground, the main ground vibrations were produced by the air pressure wave being partly transferred to the snowpack and hence to the ground. This means that an avalanche would have been directly triggered by the wave in the snowpack and not by a wave being transferred from the ground.

So far almost all studies were performed with solid explosives, many of them at close range. The only exceptions are studies by Suriñach et al. (2011) and Simioni et al. (2016b; cf. Chap. 7) who both focused on the effect of ground accelerations caused by an operational gas exploder, and the one by Simioni et al. (2016a; cf. Appendix F); Simioni et al. (2016c; cf. Chap. 5); the latter studied the effect of a gas explosion on a snowpack. However, their experiments were performed on flat terrain with an experimental gas exploder.

We therefore performed experiments at an operational gas exploder to investigate the effect of the explosion on the snowpack measuring along different axes from the system. We compared our findings to previous results on the effect of ground accelerations and on the snowpack response obtained with flat field gas exploder experiments. Our results will help to better understand the effect of gas explosions on an alpine snowpack and to assess the usefulness of flat field experiments to investigate the effect of explosions.

6.2 Methods

6.2.1 Study site

The experiments were performed at an operational gas exploder at the Jakobshorn ski area in Davos, Switzerland. The gas exploder is located at an elevation of approx. 2480 m a.s.l. at the upper end of a southwest-facing slope above a ski run (46.779° N, 9.850° E). The slope below the gas exploder is between 30° and 40° steep. The gas exploder is installed on a small rock outcrop. The terrain is slightly gully-shaped below the gas exploder. To the side, i.e. 90° from the exploder axis, the terrain is slightly concave but still quite level.

The exploder is the first of four exploders seen from north to south (Fig. 6-1). This exploder was chosen since the terrain was mostly uniform, accessibility to the exploder and the slope was good and the slope was not extremely steep.

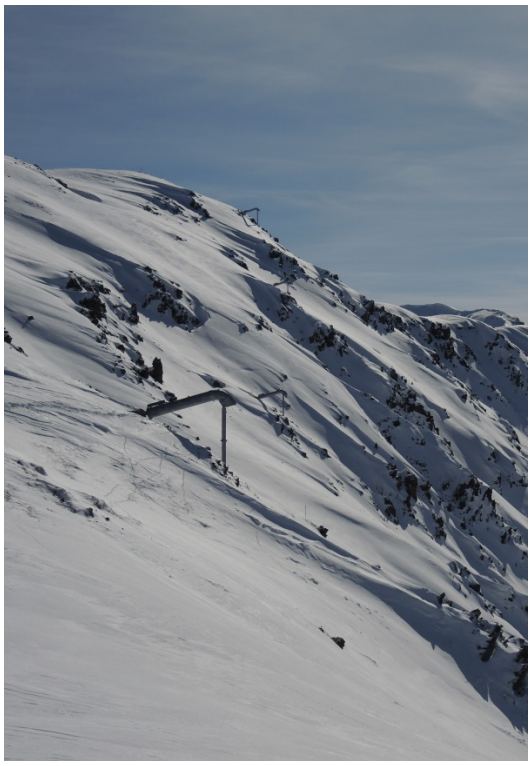

Fig. 6-1: Overview of the slope with the gas exploder. The closest gas exploder was used for the present study. The X-axis was installed on the bottom right of the gas exploder behind the lower rocks. The Y-axis was installed in the front of the picture in the slightly concave terrain. The mini-ridge probably slightly influencing the air pressure wave propagation can be seen directly at the gas exploder.

6.2.2 Gas exploder

The installed avalanche control system is an operational 1.5 m^3 Gazex® produced by TAS. The gas exploder consists of a steel pipe that is bent at the front end such that the opening is directed at an angle of 25 to 45° to the snow surface. The pipe is pivoted at its back end and suspended with a strut

at the front end. The strut is not fixed to the ground, but the gas exploder can move upwards and the recoil is mainly absorbed by the weight of the exploder. The first gas exploder is triggered as a twin shot with the second gas exploder that is located approx. 160 m further south from the first gas exploder. However, the second exploder is not triggered exactly at the same time but shortly before the first exploder. The opening time of the gas valves is set to 10 s. The gas exploder works with a mixture of oxygen and propane.

6.2.3 Experimental setup

The gas exploder causes a directed explosion. This means that the effect on the snowpack is expected to be different in different directions. With solid explosives, the measurements are usually performed in one axis only as the wave propagation behavior is radially symmetric. The measurement setup needs to be adapted for directed explosions. Simioni et al. (2016a; cf. Appendix F); Simioni et al. (2016c; cf. Chap. 5) showed that the magnitude and decay of the air pressure were similar along the gas exploder axis and a second measuring axis as long as the angle from the main gas exploder axis was less than about 36°.

On two test days, the measuring systems were installed in the gas exploder axis only to measure the direct effect and to be able to compare the effect to the results reported by Simioni et al. (2016a; cf. Appendix F); Simioni et al. (2016c; cf. Chap. 5). On one other day, one of the systems was installed in the gas exploder axis and two systems at approx. 90° from the exploder axis (Fig. 6-2). At each measuring location, the air pressure was measured directly above the snowpack. If possible, accelerometers were installed within the snowpack to record the snowpack response.

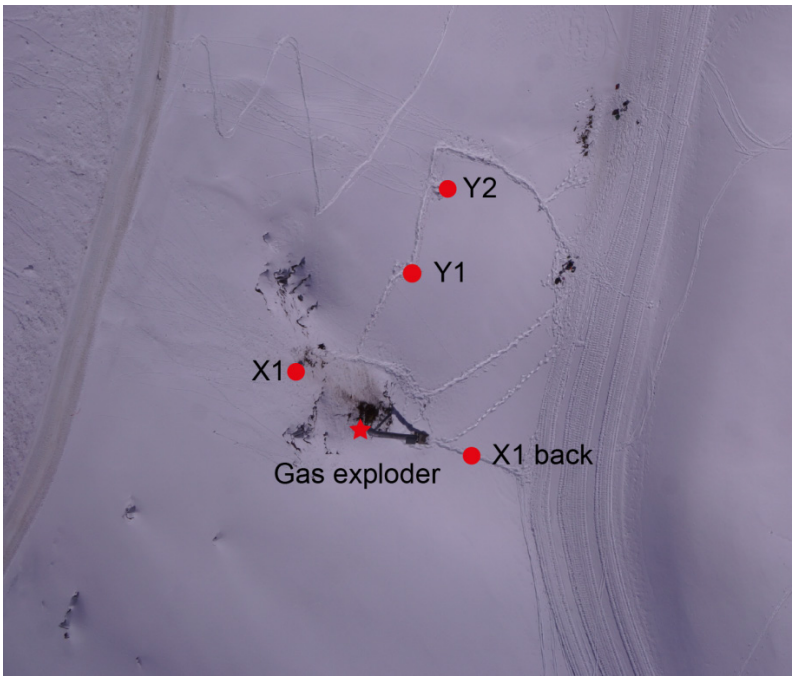

Fig. 6-2: Aerial top view of the experiments on 19 Apr 2016. X1, Y1 and Y2 denote the measuring locations. X1 back denotes the measuring system used for the experiment to measure the influence at 180° from the exploder axis. The crossing ski slope is seen on the left of the picture. The strongest gradient of the slope is towards the left of the picture. On the other test days, all systems were installed in the axis Gas exploder – X1.

The exact locations of the gas exploder and the measuring system were measured using differential GPS. All distances were calculated using the x and y coordinates of the respective location and the elevation as the terrain-parallel distances are relevant for the wave propagation behavior.

6.2.4 Air pressure measurement

The exact same microphones as previously used by Binger and Miller (2016) and Simioni et al. (2015; cf. Chap. 4) with an upper pressure limit of 34.5 kPa were used to measure the air pressure at different distances from the point of explosion above the snowpack. The microphones were installed a few cm above the snow surface.

6.2.5 Acceleration measurement

Dual-axis accelerometers as developed by Simioni et al. (2015; cf. Chap. 4) and used by Simioni et al. (2016a; cf. Appendix F) and Simioni et al. (2016d; cf. Chap. 5) were used to measure snowpack accelerations, usually at one depth within the snowpack. The accelerometers were located in foam cylinders with a density of approx. 200 kg m^{-3} to roughly match snowpack density. It proved to be difficult to accurately install the accelerometers in steep terrain, in particular on the axis at 90° from the exploder axis due to the layout of the dual-axis sensors within the foam cylinder.

6.2.6 Data acquisition

Data were acquired using the same systems and setup as described in Simioni et al. (2015; cf. Chap. 4). These consisted of National Instruments cDAQ systems in every snow pit, independently supplied with power using batteries. The systems were connected with a trigger cable to trigger the systems manually. Data were transferred over LAN cables.

6.2.7 Triggering

The gas exploder was triggered over the gas exploder operation software. As the exact time of triggering was not known and because an automatic triggering of the data acquisition was not possible, the data acquisition was triggered manually. This made it impossible determining the zero time at the explosion.

6.2.8 Data evaluation

Data were evaluated similarly to Simioni et al. (2016a; cf. Appendix F); Simioni et al. (2016c; cf. Chap. 5). The decay of the air pressure was calculated using the slope-parallel distance and the maximum air pressure. This led to power law functions:

$$p_{\mathrm{min,max}}^{\mathrm{X,Y}} = 10^{a} \cdot x^{-b} \ (\mathrm{Pa}) \qquad (6.1)$$

where superscripts X or Y stand for the measuring axis, subscripts min,max for the minimum or maximum value of the measured air pressure, *x* the distance from the point of explosion (m) and *a* and *b* the power law coefficients.

In addition, the maximum increase of the air pressure per time and an equivalent of the air pressure wave energy were calculated according to Simioni et al. (2016a; cf. Appendix F); Simioni et al. (2016c; cf. Chap. 5) and Simioni et al. (2016e; cf. Chap. 8). The decay of these parameters with distance was calculated similarly to equation (1).

Accelerations were integrated once and twice with time to obtain displacement velocities and displacements in the snowpack respectively.

As there were no different gas masses used and the actual gas mass is not known due to the impossibility of measuring it accurately, all distances are given in meters and are not scaled.

6.2.9 Snowpack

The density of the snowpack was measured using a Denoth probe (Denoth, 1989). Manual profiles were not performed.

6.3 Experimental data

A total of 16 experiments were performed during three test days (24 March, 25 March and 19 April 2016). Because of the ski slope crossing below the gas exploder and the operation hours of the ski resort, the experiments had to be conducted during evening hours on the first day and early morning hours on the second day. The measuring equipment was not removed during the night. Only the microphones were taken down due to their sensitivity to moist and cold conditions. The experiments on the third day were performed after the end of the season and hence experiments were performed during the entire day.

*Table 6-1: Number of experiments and test configuration for the three test days. #X and #Y give the number of systems along the respective axis. The * indicates the experiment where one system was installed at the back of the system, i.e. at 180° from the exploder axis.*

Date	Test	#X	#Y
24 Feb 2016	2	2	0
24 Feb 2016	3	2	0
25 Feb 2016	1	2	0
25 Feb 2016	2	2	0
25 Feb 2016	3	2	0
19 Apr 2016	1	1	2
19 Apr 2016	2	1	2
19 Apr 2016	3	1	2
19 Apr 2016	4	1	2
19 Apr 2016	5	1	2
19 Apr 2016	8	1	2
19 Apr 2016	9	1*	2

Seven experiments were performed with two measuring systems in the exploder axis downslope. For six experiments, one system was installed in the exploder axis downslope and two systems at an angle of 90° from the exploder axis in a northern direction at approx. the same elevation as the gas exploder, i.e. along a contour line (Fig. 6-1). One experiment was used to investigate the effect at the back of the system, i.e. 180° from the exploder axis.

Acceleration measurements within and air pressures measurements above the snowpack were performed for all experiments. However, the air pressure measurements in the axis of the exploder were problematic since the microphones were affected by snow sluffing caused by the explosions. Accordingly, during the first two test days, many experiments had to be rejected. Subsequently, we installed the microphones higher than the usual 3-5 cm above the snow surface. For the microphone

positioned at an angle from the exploder axis no significant problems occurred. On average, the microphones were installed 11 cm above the snowpack, with a range of 3 to 23 cm. On average, the acceleration sensors were installed 26 cm below the snow surface, ranging between 18 cm and 35 cm.

6.4 Results

6.4.1 Snowpack densities

Densities ranged between 120 and 410 kg m^{-3} with higher densities for the experiments on 19 April 2016.

6.4.2 Air pressure

The typical wave form showed a steep pressure increase at the beginning of the signal followed by a drop with a longer phase of negative pressure (underpressure, Fig. 6-3). The signal length was approx. 0.05 s. The frequency spectra showed main frequencies around 20 to 30 Hz (Fig. 6-4). All frequencies were attenuated strongly with slightly higher attenuation of higher frequencies.

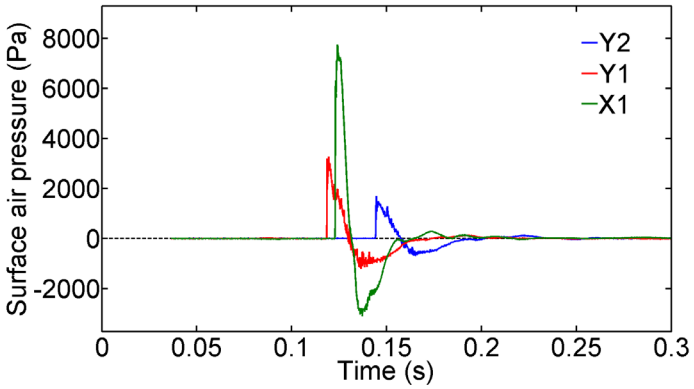

Fig. 6-3: Example of the air pressure wave form at one measuring location on the X-axis (green) and two measuring locations on the Y-axis (red and blue). Data from 19 Apr 2016 test 4.

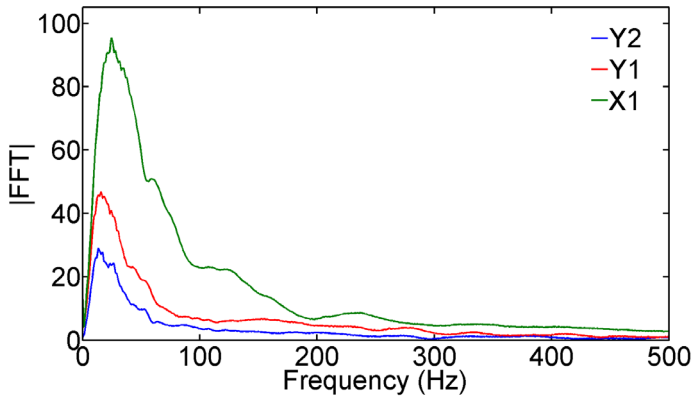

Fig. 6-4: Example of the air pressure frequency content at one measuring location on the X-axis (green) and two measuring locations on the Y-axis (red and blue). |FFT| denotes the absolute value of the fast fourier transform. Data from 10 Apr 2016, test #4.

Maximum air pressures reached 8.2 kPa at a distance of 14.9 m and 3.4 kPa at 29.9 m from the point of explosion in the exploder axis (Fig. 6-5). At an angle of 91° from the exploder axis, maximum air pressures ranged between 3.5 kPa at 15.8 m and 1.7 kPa at 24.5 m (Fig. 6-5). Scatter was small for both axes when values were discarded that were affected by microphone malfunctioning.

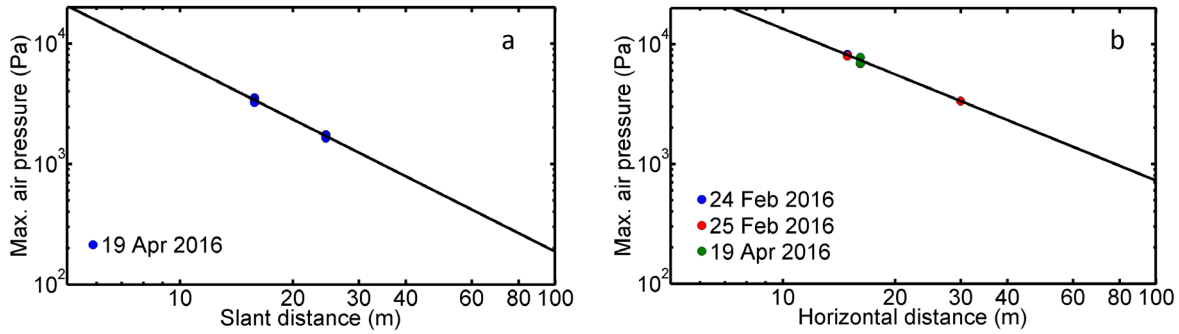

Fig. 6-5: Maximum air pressure (a) along the X-axis for all test days including the best fit (b=1.27) and (b) along the Y-axis for 19 April 2016 including the best fit (b=1.57).

The decay of the maximum air pressures followed a power law for both axes. The decay exponent was larger for the Y-axis than for the X-axis (exploder axis) (Table 6-2: Power law coefficients of the maximum air pressure (p_{max}), the maximum air pressure derivative ($(dp/dt)_{max}$) and the energy equivalent of the air pressure wave (p_{ener}) with distance from the point of explosion.).

Table 6-2: Power law coefficients of the maximum air pressure (p_{max}), the maximum air pressure derivative ($(dp/dt)_{max}$) and the energy equivalent of the air pressure wave (p_{ener}) with distance from the point of explosion.

	b		*a*	
	X	Y	X	Y
p_{max}	1.27	1.57	5.40	5.41
$(dp/dt)_{max}$	0.35	2.54	7.80	10.39
p_{ener}	2.01	2.65	7.87	7.90

The maximum derivative of the air pressure that was reached during the first steep increase of at the arrival of the air pressure wave of the sensor ranged between 6.6 x 10^8 Pa s^{-1} at a distance of 14.9 m and 2.7 x 10^8 Pa s^{-1} at 29.9 m from the explosion on the X-axis (Fig. 6-6). On the Y-axis, the values reached 2.8 x 10^8 Pa s^{-1} at 15.8 m and 1.4 x 10^8 Pa s^{-1} at 24.5 m from the exploder (Fig. 6-6).

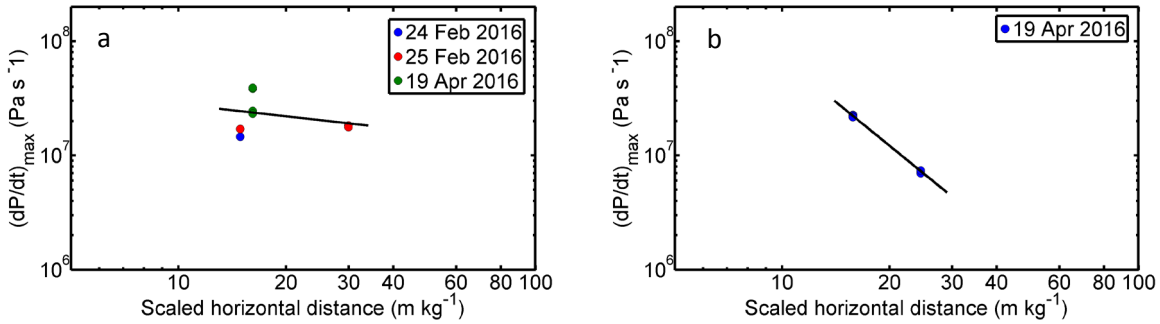

Fig. 6-6: (a) Maximum derivative of the air pressure on the X-axis including the best fit (b=1.27) and (b) on the Y-axis including the best fit (b=1.57).

The maximum derivative of the air pressure decreased following a power law on both axes. The decrease exponents were the same as for the maximum air pressure. The decrease of the parameter was stronger on the Y-axis than on the X-axis (Fig. 6-6).

The equivalent of the air pressure wave energy was between approx. 3.0 x 10^5 Pa^2 s at 14.9 m and 7.8 x 10^4 Pa^2 s at 29.9 m from the gas exploder on the X-axis (Fig. 6-7). On the Y-axis, values between 5.9 x 10^4 Pa^2 s at 15.8 m and 1.8 x 10^4 Pa^2 s at 24.9 m were measured (Fig. 6-7).

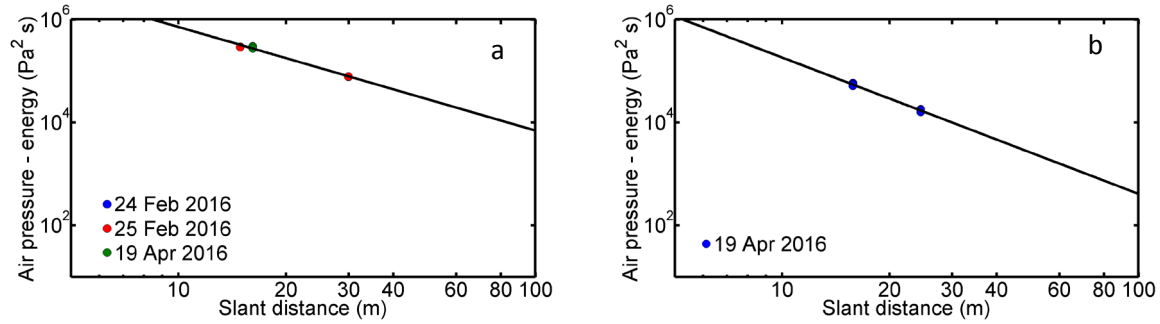

Fig. 6-7: (a) Energy equivalent of the air pressure wave on the X-axis including the best fit (b=2.01) and (b) wave on the Y-axis including the best fit (b=2.65).

The equivalent of the energy decayed following a power law for both axes. The decay was stronger on the Y- than on the X-axis (Fig. 6-7).

The frequency content of the air pressure signal had peak frequencies between 15 and 42 Hz. The signal did hardly contain any frequencies higher than 300 Hz.

The maximum air pressure at the microphone installed at the back of the gas exploder (180° from the gas exploder axis) reached 5’330 Pa at a distance of 10.2 m from the gas exploder opening.

6.4.3 Accelerations

The accelerations showed a sharp higher frequency peak followed by a lower frequency oscillation (Fig. 6-8). Only one wave form could be observed in each signal.

Not all accelerations were measured at the same depth in the snowpack. However, the difference between the depth of the sensor closest to the snow surface and the deepest sensor was rather small with 17 cm.

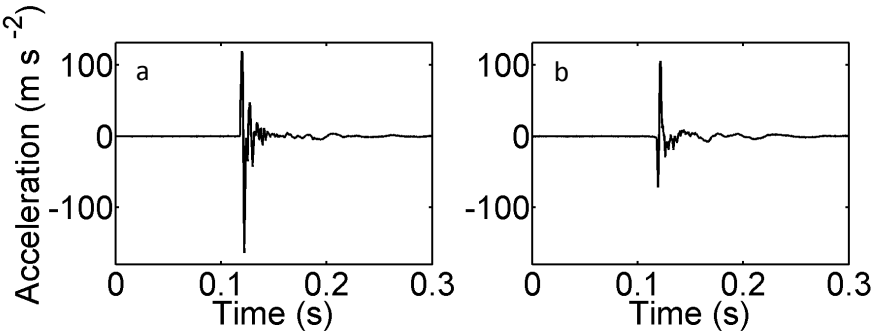

Fig. 6-8: Example of the snowpack accelerations in (a) vertical and (b) horizontal direction at the measuring location Y2. Data from 10 Apr 2016, test 4.

The maximum vertical accelerations were between 79.0 m s^{-2} at 16.1 m and 13.9 m s^{-2} at 29.9 m from the point of explosion on the X-axis (Fig. 6-9). On the Y-axis, the maximum vertical accelerations were between 123 m s^{-2} at 15.8 m and 25 m s^{-2} at 25.1 m with an outlier that was much higher (Fig. 6-9). The maximum horizontal accelerations reached 47.2 m s^{-2} at 16.1 m and 7.5 m s^{-2} at 29.9 m on the X-axis. On the Y-axis, the maximum accelerations reached 102 m s^{-2} at 15.8 m and 29.8 m s^{-2} at 24.5 m.

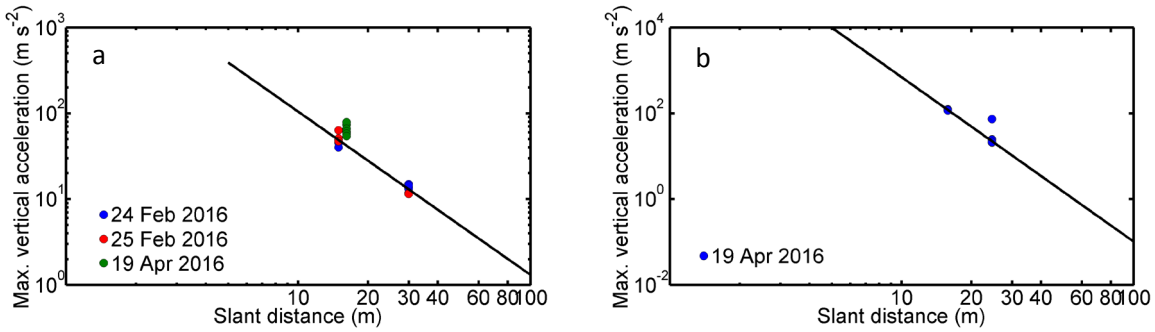

Fig. 6-9: (a) Maximum vertical accelerations in the snowpack on the X-axis including the best fit (b=1.9). The measurements of the 19 Apr 2016 were not included in the fit. (b) Maximum vertical accelerations in the snowpack on the Y-axis including the best fit (b=3.83). The single outlier was not considered for the fit.

The maximum accelerations decayed following a power law on both axes with a much stronger decay on the Y-axis compared to the X-axis. The decay was similar for the horizontal and for the vertical acceleration component.

6.4.4 Displacement velocities

The maximum vertical displacement velocities were between 1.7×10^{-1} m s^{-1} at 16.1 m and 3.4×10^{-2} m s^{-1} at 29.9 m on the X-axis. However, the velocities of the closest sensor were significantly lower than those at the middle distance. The vertical velocities reached 2.2×10^{-3} m s^{-1} at 15.8 m and 6.2×10^{-2} m s^{-1} at 24.5 m on the Y-axis with a higher outlier at 24.5 m. The horizontal component ranged between 1.2×10^{-1} m s^{-1} at 16.1 m and 3.0×10^{-2} m s^{-1} at 29.9. m on the X-axis. On the Y-axis, the horizontal component ranged between 1.3×10^{-1} m s^{-1} at 16.1 m and 2.4×10^{-2} m s^{-1} at 24.5 m with an outlier.

The maximum displacement velocities decayed following power laws for both directions and both components (vertical – horizontal) (Table 6-3). The decay was stronger on the Y- than on the X-axis. The vertical component decreased less strongly with distance than the horizontal component.

Table 6-3: Power law coefficients of the snowpack accelerations (acc), the displacement velocities (vel), the displacements (disp) and the energy equivalent (ener) with distance from the explosion along the X-axis (X) and the Y-axis (Y) for the vertical (vert) and horizontal (hor) component.

	b				*a*			
	X		Y		X		Y	
	vert	hor	vert	hor	vert	hor	vert	hor
acc	1.90	1.86	3.83	4.21	3.92	3.59	6.67	7.01
vel	0.95	1.36	2.96	3.41	0.09	0.46	2.88	3.02
disp	0.83	1.20	1.94	4.18	-2.58	-1.87	-0.92	1.75
ener	2.08	2.29	1.40	6.83	-1.50	-1.38	-2.23	4.12

6.4.5 Equivalent of the displacement velocity wave energy

The equivalent of the energy of the vertical component reached 8.1 x 10^{-4} m^2 s^{-1} at 16.1 m from the point of explosion and 2.9 x 10^{-5} m^2 s^{-1} at 29.9 m on the X-axis. The values for the closest distance were significantly smaller. On the Y-axis, the values reached 1.3 x 10^{-4} m^2 s^{-1} at 15.8 m and 7.7 x 10^{-5} m^2 s^{-1} at 24.5 m. However, for both distances, there was a very high outlier observed.

The horizontal component reached 2.8 x 10^{-4} m^2 s^{-1} at 16.1 m and 2.0 x 10^{-5} m^2 s^{-1} at 29.9 m on the X-axis. The values at the closest sensor were lower than those at the second distance. On the Y-axis, the values ranged between 1.2 x 10^{-4} m^2 s^{-1} at 15.8 m and 5.4 x 10^{-6} m^2 s^{-1} at 24.5 m. Again, there was an outlier at the second distance from the exploder.

The decay of the energy equivalent followed power laws for both axes and both components. The decay was stronger for the X- than for the Y-axis. The horizontal component decayed similarly to the vertical component on the X-axis. However, the decrease of the horizontal component was much stronger than the vertical component on the Y-axis.

6.4.6 Displacements

On the X-axis, the vertical displacements reached 1.1 x 10^{-4} m at 16.1 m from the point of explosion and 2.0 x 10^{-4} m at 29.9 m. The values at the first distance were lower than at the second distance and in the range of the values furthest from the point of explosion. The values reached 6.8 x 10^{-4} m at 15.8 m and 2.8 x 10^{-4} m at 24.5 m from the point of explosion on the Y-axis.

The horizontal component reached 1.3 x 10^{-3} m at 16.1 m and 2.5 x 10^{-4} m at 29.9 m on the X-axis. Values measured at a distance of 14.9 m were lower than those at 16.1 m. On the Y-axis, the displacements ranged between 1.2 x 10^{-3} m at 15.8 m and 1.8 x 10^{-4} m at 24.5 m. At this distance, a high outlier was observed.

The displacements followed power laws for all directions and components (Table 6-3). The decay was strongest for the horizontal component on the Y-axis. The vertical components decreased less strongly than the horizontal components. The vertical component along the Y-axis decreased less strongly than the vertical component on the X-axis. However, the horizontal component on the Y-axis decreased stronger than on the X-axis.

6.4.7 Air pressure wave speed

The speeds of the air pressure wave were determined along the X-axis for experiments, where two measuring systems were installed and the microphones worked without any malfunction. For four experiments speeds were evaluated; the average speed was 335 m s^{-1} with a range between 332 to 336 m s^{-1}, hence very consistent.

On the Y-axis, speeds were determined for the experiments on 19 April 2016, where two measuring systems were installed at an angle of 180° from the exploder axis. The speeds were determined for five experiments between the two microphones. The speeds were very consistent with a mean of 338 m s^{-1} and ranged between 337 and 339 m s^{-1}.

6.5 Discussion

6.5.1 Comparison along different axes

The maximum air pressure and the derived parameters decreased stronger along the Y-axis than the X-axis with the absolute values being smaller on the Y-axis (Fig. 6-5). This was expected due to the shape of the pipe. The maximum air pressure was also smaller for the single experiment where the air pressure was measured behind the gas exploder (180° from the exploder axis) which was plausible. The ratio between the air pressure at the back and in the exploder axis was 40%. This means that the pressure to the back is the smallest compared to all other directions. However, it is only approx. 1'500 Pa smaller at 17.9 m than on the Y-axis at 90°.

The maximum accelerations, displacement velocities and displacements decreased much stronger on the Y-axis than on the X-axis (Fig. 6-9. The absolute values were higher on the X-axis up to distances of 15 to 20 m from the point of explosion. The energy equivalent of the vertical component decreased similarly on the X-axis and the Y-axis with similar absolute values. The horizontal component decreased much stronger for the Y-axis axis than for the X-axis with higher absolute values for the Y-axis for short distances of up to approx. 15 m. The accelerations and the derived parameters have to be assessed critically. Only one measurement was performed per measuring location at one depth within the snowpack. These depths were not exactly the same. With only one sensor, the vertical decay cannot be determined per pit and the values at a certain constant depth with distance from the point of explosion cannot be determined as done by Simioni et al. (2016c; cf. Chap. 5). In addition, the long axis of the sensor was oriented differently for the measurements along the axis at 90°. This was done to always measure the vertical and the radial component with the biaxial sensors. This might influence the results due to the limited accuracy of the sensor placement on the Y-axis. The acceleration measurements have to be considered as indicative only for a certain distance but due to the above-mentioned limitations.

6.5.2 Comparison to flat field gas exploder experiments

The decay exponent of the air pressure along the X-axis is slightly lower for the experiments performed on the operational gas exploder than for the results reported by Simioni et al. (2016a; cf. Appendix F); Simioni et al. (2016c; cf. Chap. 5) with a prototype gas exploder on flat terrain. As an

example, we compared the largest explosion reported by Simioni et al. (2016a; cf. Appendix F); Simioni et al. (2016c; cf. Chap. 5) using 1.9 kg gas with our findings at different distances: At 14.6 m distance, the maximum air pressure of the flat field experiments was 10.3 kPa considering the charge mass whereas it was 8.3 kPa at the operational gas exploder. At a distance of 30 m, the pressure at the operational gas exploder was slightly higher with 3.1 kPa compared to 3.1 kPa for the largest shot with the mobile gas exploder in the flat field (Simioni et al., 2016c; cf. Chap. 5). Overall, there is a good agreement of the results. The largest explosions using the prototype exploder on flat terrain well represent the air pressure results in the axis at the operational gas exploder.

The decay of the maximum air pressure with distance on the Y-axis, at 90° from the exploder axis, was less strong than observed with the prototype gas exploder on flat terrain (Simioni et al., 2016c; cf. Chap. 5), at least up to a distance of approx. 22 m. At larger distances, the pressure on the Y-axis was higher than on the X-axis for the experiments performed with an angle of 90° above bare ground. For the experiments performed at the operational gas exploder, the ratio of the air pressure on the Y-axis and the X-axis was between 0.5 and 0.3 meaning that the pressure was lower on the Y-axis. There are different reasons that might explain this difference: The geometry of the gas exploders at the opening had a different radius and hence the directed explosion was different. The main reason is that the operational gas exploder was standing on a small ridge with concave terrain following along the Y-axis. The air pressure hit the ridge and was therefore probably slightly hindered to propagate freely along the slope to the side. As the experiments in Simioni et al. (2016c; cf. Chap. 5) were only performed at 90° from the exploder axis above bare ground, the absolute values cannot be compared with our findings. Although the ratio between the pressures along different axes should be the same for bare ground or snow, there might be an additional small difference caused by the bare ground. The results of Simioni et al. (2016c; cf. Chap. 5) who performed experiments above almost perfect level terrain or snow with good repeatability are not easily transferrable to the experiments on the operational gas exploder that represent one system at a location where the terrain is not perfectly uniform. The terrain has a large influence on the results. In addition, there are the above-mentioned measuring issues for on-site measurements. The maximum air pressure derivative and the energy equivalent showed the same behavior as the maximum air pressure.

The peak frequencies of the air pressure signal reported by Simioni et al. (2016c; cf. Chap. 5) were in good agreement with our results (15 to 42 Hz with the operational gas exploder compared to 30 to 40 Hz for the flat field experiments).

The maximum vertical accelerations decayed similarly along the X-axis as reported by Simioni et al. (2016c; cf. Chap. 5) at 0.3 m depth within the snowpack – also with regard to the absolute values. All acceleration components agreed well between flat field experiments and the experiments at the operational gas exploder. Displacement velocities and the energy equivalents were decreasing

much stronger for the experiments in the flat field and the absolute values were lower. This comparison can only be made for the X-axis, as the angle between the X- and the Y-axis in the flat field experiments (~35°) does not correspond to the angle between the axes used at the operational gas exploder (90°). Since the frequency contents of the air pressure signals are similar, it is not clear where this difference comes from.

The power law fits of our acceleration measurements allow predicting the accelerations at large distances (>120 m) where Suriñach et al. (2011) performed ground acceleration measurements. Our fit for the Y-axis suggests snowpack accelerations that are at the lower end of the range of observed ground vibrations by Suriñach et al. (2011). However, these values have to be compared carefully as the terrain was not perfectly level in both studies, in particular for the experiments performed by Suriñach et al. (2011). In the exploder axis, our extrapolated values are one order of magnitude higher than those observed by Suriñach et al. (2011) which is plausible as the effect we measured at 90° where they measured was also smaller during the present study. We conclude that at very far distances, the snowpack and ground accelerations are small and avalanche triggering is unlikely unless the snowpack would be extremely unstable.

6.5.3 Test repeatability

Consecutive tests were in good agreement with a few exceptions, mainly caused by microphone malfunction due to sluffing and snow drifting. Even on consecutive days, the results were in good agreement. However, the values of the accelerations obtained with the measurements performed two months after the first experiments, on 19 Apr 2016, were different although air pressure values were in good agreement (Fig. 6-9). The observed differences were likely due to different snowpack conditions.

6.5.4 Importance of flat field and on-site experiments

Our results show that both reproducible flat field experiments and on-site experiments at operational avalanche control systems are important, in particular for gas exploders or other explosions that do not propagate spherically from the point of explosion. Many parameters are in good agreement between the flat field and the experiments on operational systems. The decay at 90° from the exploder axis could not be sufficiently well reproduced with the flat field experiments. This discrepancy is probably due to the difference in terrain. Hardly any avalanche control installation is installed on a uniform slope. This means that the effect will vary the more uneven the actual affected terrain is. In these cases, the flat field measurements provide good first estimates of the expected effect, but the real effect for the given slope configuration can only be determined with direct measurements – as long as there is no suitable numerical model available.

However, there are some major shortcomings of experiments on operational systems. The installation of the measurement equipment within the slope is tedious and risky. Further, the microphones do often not work properly in the axis of the gas exploder due to sluffing and snow drifting.

Alternatively, a model developed on the basis of the flat field experiments could obviate these experiments. However, due to the extremely sophisticated wave propagation process in the porous material snow with different wave modes in the pore space and the ice skeleton (Johnson, 1982), such a model will likely not be available in the near future. Strongly simplifying the processes by employing a continuum approach and parametrizing the attenuation of wave propagation, based on experimental studies, may partly solve this issue.

6.6 Conclusions

We performed experiments on an operational gas exploder during three test days in the winter 2015-2016. We measured air pressures and snowpack accelerations along the gas exploder axis, at an angle of 90° from the exploder axis and at the back of the exploder (180°). The same measuring equipment as in the studies by Simioni et al. (2015; cf. Chap. 4) and Simioni et al. (2016a; cf. Appendix F); Simioni et al. (2016c; cf. Chap. 5) was used.

Air pressures decayed strongly with distance from the point of explosion and were in good agreement with results of experiments performed on flat terrain by Simioni et al. (2016c; cf. Chap. 5) in the exploder axis. At 90° from the exploder axis, the air pressure values were lower than in the exploder axis and decayed stronger which is in disagreement with the findings by (Simioni et al., 2016a; cf. Appendix F) and Simioni et al. (2016c; cf. Chap. 5), who found the absolute values to be lower for short distances but the decay to be less accentuated. The measured air pressure at the back of the system was the lowest of three measured directions. The waveforms and frequency contents agreed well with the results reported by Simioni et al. (2016d; cf. Chap. 5). The accelerations of the snowpack decreased strongly with distance from the point of explosion. As there was only one accelerometer per location installed at not exactly the same depths and accelerations decayed strongly with depth, the results have to be interpreted carefully. Still, the accelerations in the axis agreed well with the flat field experiments. Extrapolating the measurements to larger distances results in values corresponding to the range reported by Suriñach et al. (2011).

Our tests clearly show that flat field experiments are a good, low risk and less tedious way to obtain good estimates of the effect of operational systems, although there were some differences in particular at 90° from the exploder axis – which was measured above bare ground in the flat field experiments. However, the fact that the terrain at operational gas exploders is almost never uniform has to be considered when analyzing the results.

The measurements suggest that for an operational gas exploder, the lines of equal air pressure approximate the form of a bulb with the lowest pressure at the back, a higher pressure at 90° from the axis and by far the highest pressure in the exploder axis. This is in contrast to what we observed in the flat field where the pressure decayed less strongly with distance and hence the shape changes from a bulb to a circle at larger distances (Appendix A), probably due to the terrain characteristics.

Our tests provided insight into the effect of an operational gas exploder. They confirm that the flat field experiments are a good approximation as air pressures and snowpack accelerations agree well in the exploder axis and differences at the other axis were probably caused by the topography. Experiments in steep terrain are difficult, and in particular air pressure measurements are problematic under certain conditions. Tests at an operational gas exploder are only valid for that particular exploder except the terrain configuration at other exploders is very similar.

7 Ground accelerations caused by an operational gas exploder

7.1 Introduction

Preventive triggering of snow avalanches is an important method in avalanche mitigation. Compared to other avalanche mitigation methods such as engineering works, artificial triggering has the advantages of relatively minor economic costs and low visual impact. Avalanche control using explosives has proven to be very effective, especially under dry-snow conditions, as e.g. during the catastrophic avalanche cycle in 1999 in Switzerland. However, this extreme winter also showed that avalanches have to be triggered during storm conditions, at any time of day, to achieve the best effect and to trigger more but smaller avalanches. Avalanches can in fact be triggered most easily during or directly after a storm or snowfall event (Bair et al., 2012). The disadvantage of not being able to trigger avalanches under any conditions has been overcome by the development of fixed avalanche control installations. Nowadays, such installations are widely used. These systems also allow avalanches to be triggered at times of minor economic loss, e.g. at night, and avalanche control work can be performed with increased safety for the personnel. However, due to their fixed position, the advantage of flexible charge placement does no longer exist. It is hence important to better assess the effect of explosions affecting snowpack stability – via the snowpack and the ground.

The influence of ground vibrations on avalanche release has so far only been addressed by few studies. According to Suriñach et al. (2011), the effective radius ranges from 30 to 90 m for a gas exploder if a minimal overpressure of 2.5 kPa is assumed. Ground accelerations caused by a gas exploder are due to blast recoil which is transferred to the foundation and the surrounding rock or soil. For any given explosion above or in the snowpack, i.e. all artificial avalanche control methods, a second source of ground accelerations is the air pressure wave that is transmitted to the snowpack and from there to the ground. Suriñach et al. (2011) installed geophones and seismometers at distances of about 130 to 370 m from a gas exploder at a similar elevation as the exploder to investigate the effect of these vibrations on snow stability. They measured (1) a first complex wave that propagated through the ground at high speeds and (2) a second wave propagating through the air and being transmitted to the snowpack and the soil close to the sensor position. Suriñach et al. (2011) showed that peak ground accelerations were higher for type 2 waves than for type 1 waves. Horizontal components caused by the type 2 wave dominated in amplitude over the vertical components. Suriñach et al. (2011) compared the measured ground vibrations to values calculated with an equation used for critical accelerations for a stable slope and to boundary values obtained by Chernouss et al. (2006). They concluded that an avalanche release beyond the effective radius of a gas exploder was not likely under the conditions they encountered.

Chernouss et al. (2006) measured ground acceleration at different distances from an open pit mine. They calculated a static stability criterion as presented by Suriñach et al. (2011) and a dynamic stability criterion involving cumulative displacement; they showed an example of the effect of ground

shaking on snowpack stability. In addition, they performed tests with a shaking table to show the decrease of snow shear strength caused by ground shaking of the underlying soil.

Simioni et al. (2015; cf. Chap. 4) provided a more detailed review on past research in the field of artificial avalanche control. However, the work by Chernouss et al. (2006) and Suriñach et al. (2011) were the only studies that focused on ground vibration due to an explosion in view of avalanche release. The studies by Suriñach et al. (2011) and Simioni et al. (2016c; cf. Chap. 5) are the only ones that dealt with the effect of a gas exploder which unlike solid explosives causes ground vibrations by the recoil of the system.

Comprehensive measurements of ground accelerations close to an avalanche control system and in particular to gas exploders are missing. Such experiments are required to close the gap to larger distances as investigated by Suriñach et al. (2011).

To investigate whether it is feasible to trigger an avalanche by ground accelerations induced by firing a gas exploder, we installed geophones as used for avalanche detection in an avalanche path at different distances from a gas exploder. We measured displacement velocities and derived ground accelerations with the geophones fixed to the soil and rock. Accelerations were then compared to field data reported by Simioni et al. (2016c; cf. Chap. 5) and Simioni et al. (2015; cf. Chap. 4) which included acceleration measurement and observations on weak layer failure.

7.2 Methods

7.2.1 Study site

A study site with fixed avalanche control installations was chosen to investigate the influence of ground accelerations on avalanche triggering. At the Jakobshorn ski resort above Davos, Switzerland, a ski run traversing a wide slope is controlled by 4 gas exploders (Gazex®, 1.5 m^3). The path below the second gas exploder as counted from the north, or the right, when looking down the slope was chosen for the experiments (Fig. 7-1). The path is characterized by two small gullies that connect to an open slope. The gas exploder is located on a rock outcrop between the two gullies facing slightly into the right gully when looking from below. This gas exploder was chosen for different reasons: The first gas exploder is located on rather flat terrain and avalanches are not often triggered and hence this was not a feasible location for this study. However, the open character of the slope would have been ideal for such experiments. The third and the fourth gas exploder are installed above long narrow gullies and not very representative for the majority of fixed avalanche control installations. However, these devices have the shortest avalanche return periods and would be interesting for this reason. The second and selected gas exploder lies in between the two terrain characteristics and

avalanche frequencies. The slope angle ranges from approx. 45 to 35°. The ground mainly consists of rock and is partly covered with shallow soil.

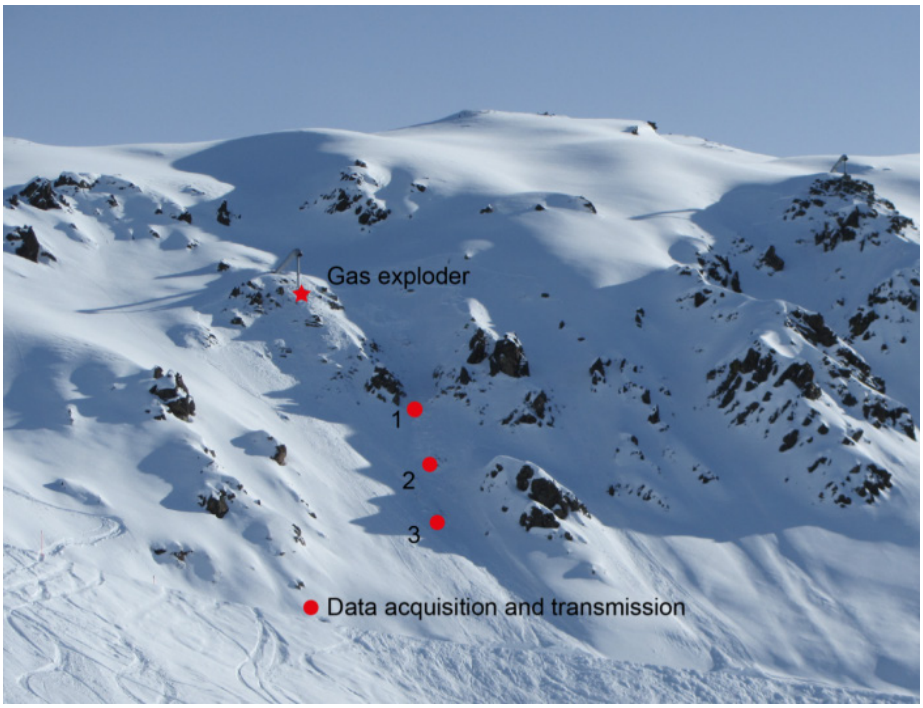

Fig. 7-1: Overview of the slope with the instrumented slope below the investigated gas exploder No. 2.

7.2.2 Avalanche activity and release effectivity

Avalanche control records were provided by the ski patrol in charge of avalanche safety in the ski resort. These records contain information on the number of blasts and resulting avalanches. In addition, pictures from a time lapse camera were used to identify avalanches. The avalanche activity could also be determined by analyzing the seismic signal recorded by the geophones installed in the slope below the gas exploder.

7.2.3 Seismic measurements and avalanche detection

Single axis geophones (SM-6, van Herwijnen and Schweizer (2011)) with a resonant frequency of 8 Hz were installed in the slope below the gas exploder at different distances. The geophones measured the vertical velocity. The geophones were connected to an AD converter and then to a small computer, placed directly besides the ski slope. Power was supplied by the installations for artificial snowmaking that are placed underneath the ski run. Data were continuously acquired at a sampling frequency of about 800 Hz and transferred to the network designed for controlling the snowmaking. Furthermore, a camera was installed to observe the slope of the gas exploder. Data were as well transferred to the snowmaking network.

In addition to measuring ground accelerations to characterize its influence on avalanche release, the seismic data can be used for avalanche detection (St.Lawrence and Williams, 1976) which the system had also been designed for (van Herwijnen et al., 2016c).

7.2.4 Data evaluation

The raw data was saved in 15 minutes segments. For each interval, a spectrogram was directly produced after recording the data (Fig. 7-2). To find explosions and avalanches, all spectrograms were manually evaluated. Evaluation is straightforward due to the distinct power spectrum of an explosion. This procedure allowed other sources to be excluded manually as it is not yet possible to perform this selection automatically. Other sources included explosions caused by hand and helicopter charging, and other fixed avalanche control installations. The remaining explosions were then compared to the gas exploder blasting logs which also list triggered avalanches and sometimes new snow depths and approximate wind speeds.

Wave arrival times to determine wave speeds were calculated using the AIC method (Kurz et al., 2005).

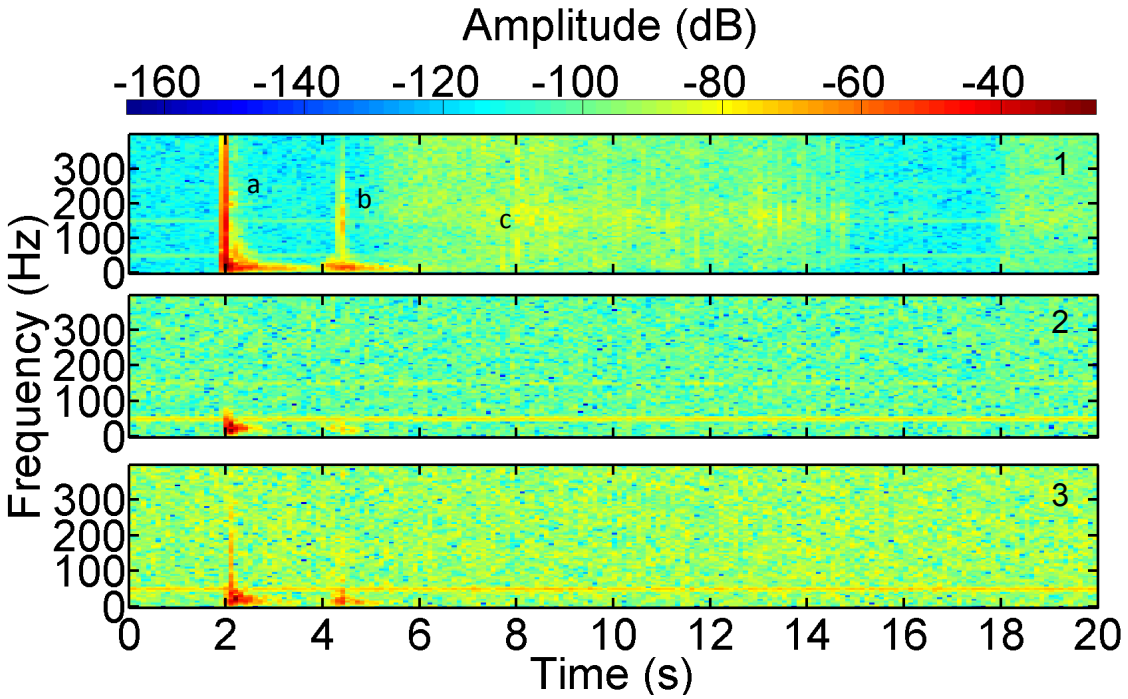

Fig. 7-2: Spectrogram for the three sensors 1 to 3 (from top to bottom) with increasing distance from the exploder. (a) The first high-energy pulse shows the explosion followed by (b) the explosion of the adjacent gas exploder a few seconds later. (c) The avalanche is the low-energy signal between approx. 5 and 14 s. Data from 22 February 2015.

7.2.5 Reference data

The seismic data recorded at the gas exploder were compared to acceleration measurements reported in Simioni et al. (2015; cf. Chap. 4) and Simioni et al. (2016c; cf. Chap. 5). They performed

experiments on a flat study site with elevated solid avalanche control explosives. Acceleration measurements were performed at different distances from the point of explosion and depths within the snowpack. Additionally, failure was recorded with cameras. The lowest acceleration values at the farthest distance where failure could still be observed were taken as a minimum value required for failure in the flat field experiments.

During the winter season 2015-2016, additional experiments were performed at an adjacent gas exploder (Simioni et al., 2016d). Air pressure was measured at different distances from the point of explosion and different angles from the exploder axis (0°, 90° and 180°). Simultaneously, snowpack accelerations within the snowpack were measured at one of the locations where air pressure was measured.

7.3 Data

7.3.1 Geophone installation

During the winter 2013-2014, the geophones were installed in the soil. For the winter 2014-2015, coupling of the sensor with the ground was improved by installing the sensors on rock using bolts glued into boreholes (Fig. 7-3). The change of the sensor locations resulted in slightly different distances between the gas exploder and the geophones. The distances for the winter 2013-2014 were 19, 39 and 63 m for sensors 1 to 3 from the gas exploder and for the winter 2014-2015 18, 29 and 61 m.

Fig. 7-3: Geophone mounted on rock as installed during the winter 2014-2015 seen from above.

7.3.2 Experimental data winter 2013-2014

During the winter 2013-2014, the gas exploder was used during or shortly after almost any snowfall, resulting in 23 shots. In 87 % of the shots (20 shots), an avalanche was triggered with one shot where the outcome is unknown due to the lack of photos and no clear identification in the seismic signal.

Most of the avalanches were small in length and slab thickness (10 to 20 cm) with mainly new snow released, but many of the triggered avalanches reached the ski slope located 95 m from the gas exploder.

All avalanches were dry-snow slab or loose snow avalanches with one exception on 10 March 2014 when wet-snow avalanches were observed. New snow depth in the region was between 10 and 30 cm. Winds, often from the north, led to wind loading in the slopes below the gas exploder.

7.3.3 Experimental data winter 2014-2015

During the winter 2014-2015, the gas exploder was used during or shortly after almost any snowfall. This resulted in 24 shots. Avalanches were released in 88 % of the shots (21 shots). The avalanches for which their size was recorded were small in length (50-80 m), width (20-40 m) and slab thickness (20 to 30 cm), but many reached the ski slope.

7.4 Results

7.4.1 Wave forms winter 2013-2014

In general, typical acceleration wave forms at the first sensor comprised acceleration peaks with a first steep flank followed by a damped oscillation (Fig. 7-4). The wave forms at the further distances did not contain this high-frequency peak but were lower frequency oscillations, with the values at the second sensor often being lower than those at the third sensor. The sensors often registered a precursor wave with low amplitude. The displacement velocity wave forms did not show these sharp peaks with steep increases for either sensor (Fig. 7-5). Residual displacements were observed for sensors 2 and 3 (Fig. 7-6). The wave forms looked slightly differently for each explosion. Frequencies were observed up to approx. 400 Hz for the closest sensor and below 100 Hz for the remaining locations (Fig. 7-8). The timing of the waveforms is relative as the actual zero time could not be determined on an operational gas exploder.

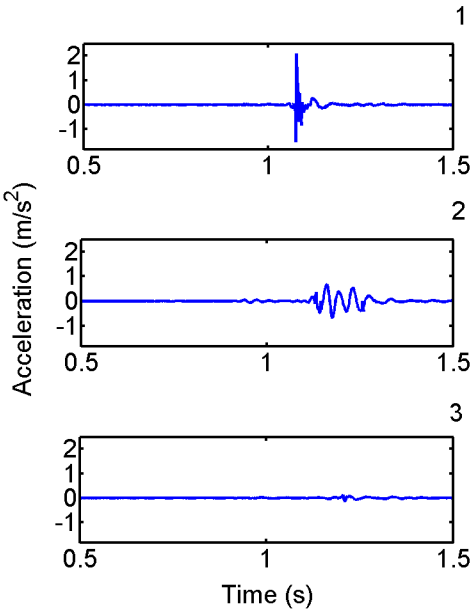

Fig. 7-4: Example of accelerations for sensors 1 to 3 with increasing distance (19.1, 38.6 and 63.0 m, respectively) from the exploder from top to bottom. Data from 24 March 2014.

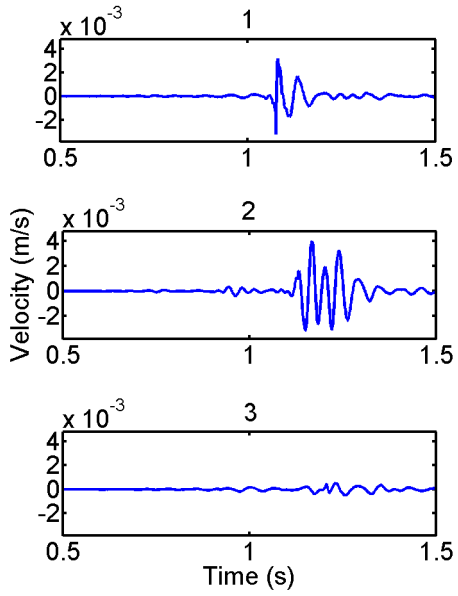

Fig. 7-5: Example of displacement velocities for sensors 1 to 3 with increasing distance (19.1, 38.6 and 63.0 m, respectively) from exploder from top to bottom. Data from 24 March 2014.

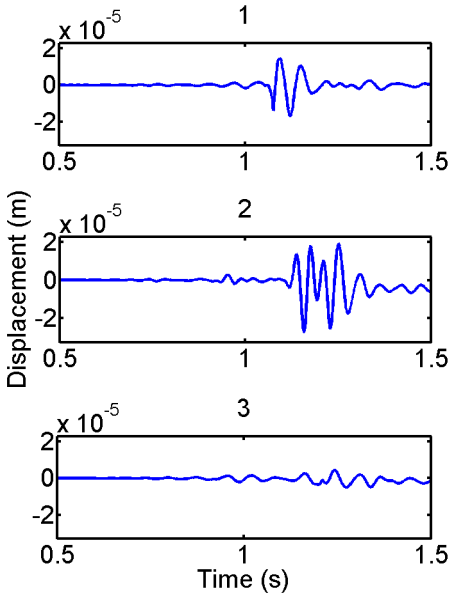

Fig. 7-6: Example of displacements for sensors 1 to 3 with increasing distance (19.1, 38.6 and 63.0 m, respectively) from exploder from top to bottom. Data from 24 March 2014.

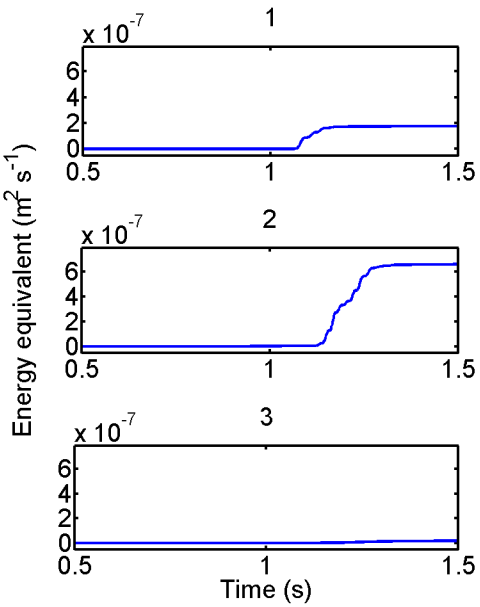

Fig. 7-7: Example of the equivalent of the wave energy for sensors 1 to 3 with increasing distance (19.1, 38.6 and 63.0 m, respectively) from exploder from top to bottom. Data from 24 March 2014.

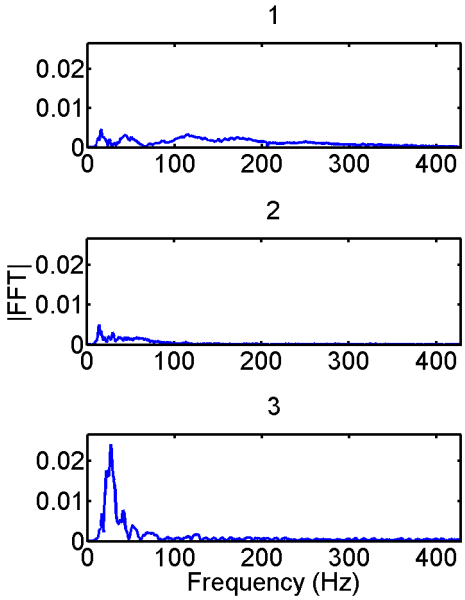

Fig. 7-8: Example of a frequency spectrum for the sensors 1 to 3 (from top to bottom) with increasing distance (19.1, 38.6 and 63.0 m , respectively). Data from 24 March 2014.

7.4.2 Wave forms winter 2014-2015

Usually, the acceleration wave forms showed high frequency peaks with steep increases at the first sensor followed by a damped oscillation (Fig. 7-9). At the other sensors, the acceleration wave forms did not show steep increases or distinct peaks. A similar behavior was observed for the displacement velocities; however, the peaks at the first sensor were less distinct (Fig. 7-10). The displacements showed noticeable damped oscillations towards the end of the signal at the first sensor (Fig. 7-11). The energy equivalent increased steeply during the experiments (Fig. 7-12). The closest sensor showed frequencies of up to more than 400 Hz for the closest sensor and mainly frequencies below 100 Hz for the remaining sensors (Fig. 7-13).

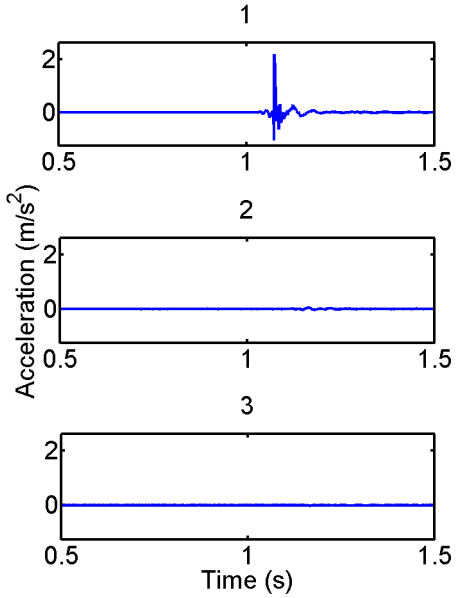

Fig. 7-9: Example of accelerations for sensors 1 to 3 with increasing distance from exploder (16.8, 38.1 and 61.2 m, respectively) from top to bottom. Data from 22 February 2015.

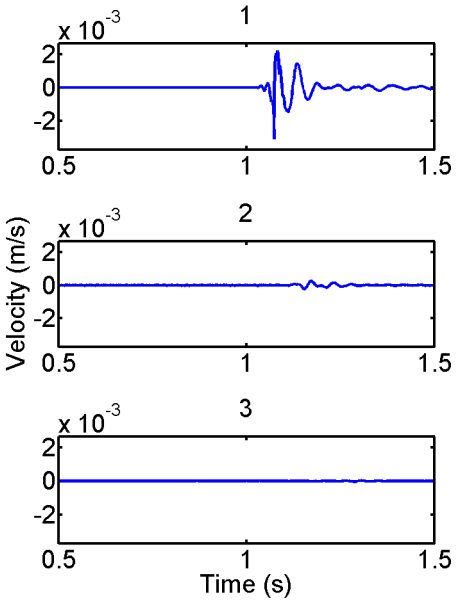

Fig. 7-10: Example of displacement velocities for sensors 1 to 3 with increasing distance (16.8, 38.1 and 61.2 m, respectively) from exploder from top to bottom. Data from 22 February 2015.

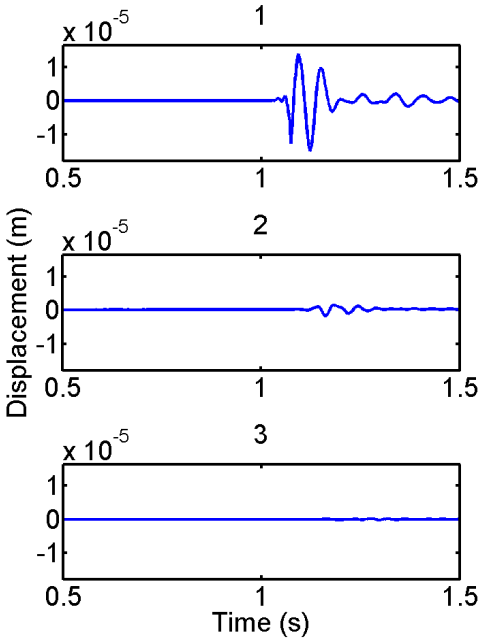

Fig. 7-11: Example of displacements for sensors 1 to 3 with increasing distance (16.8, 38.1 and 61.2 m, respectively) from exploder from top to bottom. Data from 22 February 2015.

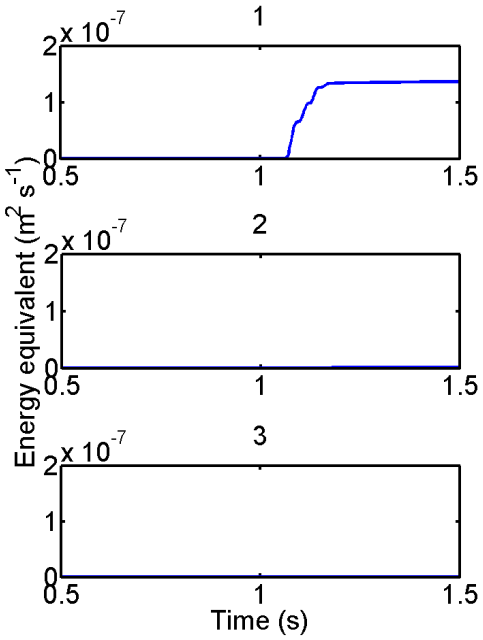

Fig. 7-12: Example of the equivalent of the wave energy for sensors 1 to 3 with increasing distance (16.8, 38.1 and 61.2 m, respectively) from exploder from top to bottom. Data from 22 February 2015.

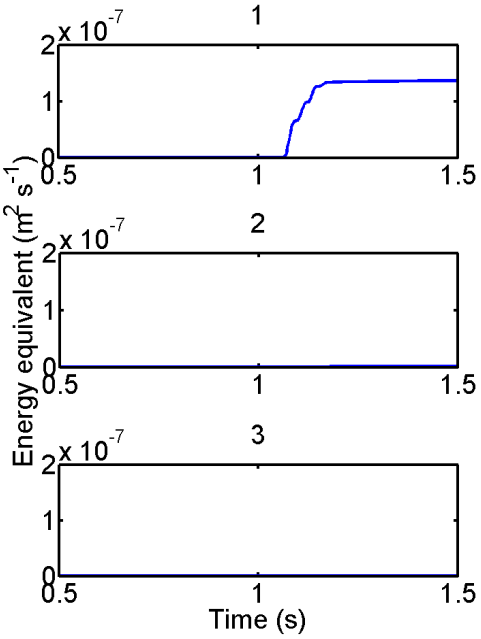

Fig. 7-13: Example of a frequency spectrum for the sensors 1 to 3 with increasing distance (16.8, 38.1 and 61.2 m, respectively) from top to bottom. Data from 22 February 2015.

7.4.3 Acceleration measurements winter 2013-2014

During the winter 2013-2014, maximum accelerations reached 2.1 m s^{-2} at a distance of 19 m to 0.73 m s^{-2} at a distance of 63 m (Fig. 7-14). However, the lowest maximum acceleration values were not reached at the furthest distance, but at the second sensor. The scatter of the maximum acceleration amplitudes was large at the closest measuring location. For one explosion, accelerations were considerably higher for the closest distance (2.1 m s^{-2}) than for all other explosions (max. 1.2 m s^{-2}).

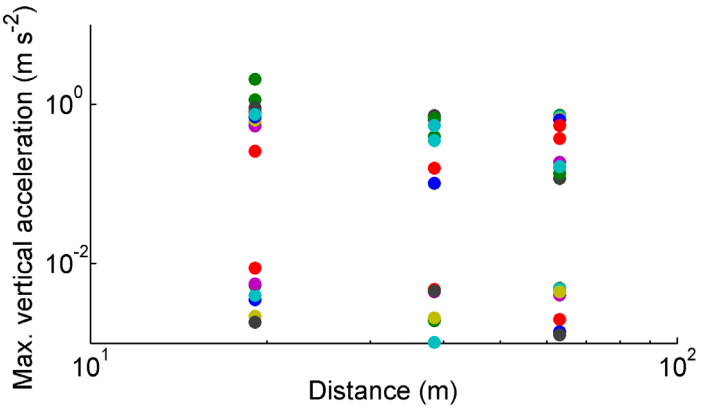

Fig. 7-14: Summary of all maximum accelerations measured during the winter 2013-2014. The different colors of the dots denote different explosions.

7.4.4 Acceleration measurements winter 2014-2015

During the winter 2014-2015, maximum accelerations reached 4.7 m s^{-2} at the closest distance and 0.04 m s^{-2} at the largest distance (Fig. 7-15). Scatter was rather small and outliers were scarce and especially observed at shorter distances. The acceleration values decayed with distance following a power law, where *b* denotes the coefficient describing the decay of the amplitude (*b*=3.68, Simioni et al. (2015; cf. Chap. 4).

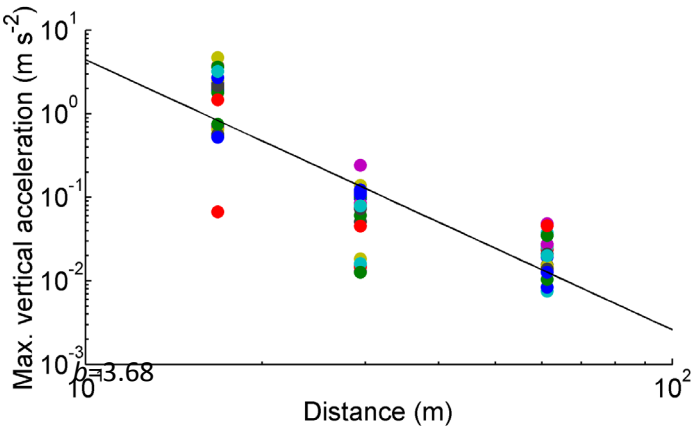

Fig. 7-15: Summary of all maximum accelerations measured during the winter 2014-2015 including best fit.

7.4.5 Displacement velocity measurements winter 2013-2014

Maximum vertical velocities reached between 7.3 x 10^{-4} and 4.5 x 10^{-3} m s^{-1} (Fig. 7-16). However, maximum velocities were observed at the longest distance from the gas exploder. Scatter of the velocities was large, mainly for the closest distance. As for the acceleration, one measurement of the velocity was considerably larger at the closest distance than all others (3.2 x 10^{-3} m s^{-1} compared to 2.2 x 10^{-3} m s^{-1}).

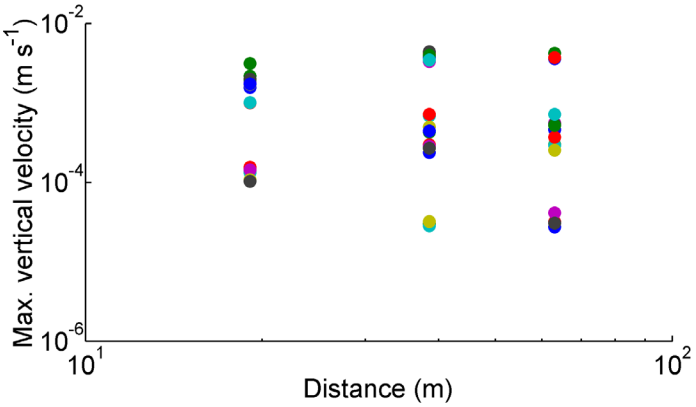

Fig. 7-16: Summary of all maximum displacement velocities measured during the winter 2013-2014 including best fit.

7.4.6 Displacement velocity measurements winter 2014-2015

Maximum vertical velocities reached 2.8 x 10^{-3} m s^{-1} at the shortest distance and 1.5 x 10^{-4} m s^{-1} at the largest distance from the point of explosion (Fig. 7-16). Scatter was small. The maximum displacement velocities followed a power law with distance from the point of explosion (b=3.22). This means that the displacement velocities decreased strongly with distance.

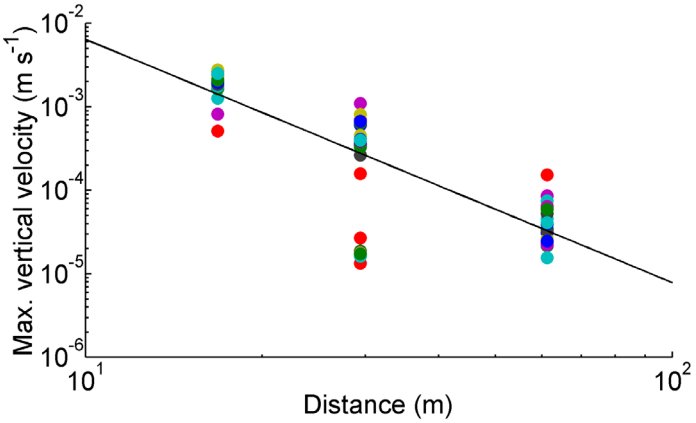

Fig. 7-17: Summary of all maximum displacement velocities measured during the winter 2014-2015 including best fit.

7.4.7 Displacement measurements winter 2013-2014

The maximum vertical displacements ranged between 2.7 x 10^{-5} and 1.5 x 10^{-5} m. Maximum displacements were again not reached at the closest distance, but at the furthest distance from the point of explosion. Scatter was large, especially at the middle and largest distances. In contrast to the velocities and accelerations, not outlier was observed at a distance of 19 m.

7.4.8 Displacement measurements winter 2014-2015

Maximum displacements ranged between 1.5 x 10^{-5} m at the closest distance and 7.1 x 10^{-7} m at the furthest distance from the explosion. Scatter was largest for the closest distance. The displacement decayed following a power law with distance from the point of explosion (*b*=3.32). The behavior was similar as for the displacement velocities.

7.4.9 Equivalent of the wave energy winter 2013-2014

The maximum equivalent of the wave energy reached between 1.8 x 10^{-7} to 8.1 x 10^{-7} m^2 s^{-1}. The largest values were not reached at the shortest distance from the point of explosion. Scatter was large, especially at the furthest sensor, were two clusters could be observed.

7.4.10 Equivalent of the wave energy winter 2014-2015

The final value of the equivalent of the wave energy ranged from 2.0 x 10^{-7} m^2 s^{-1} at the shortest distance to 3.3 x 10^{-10} m^2 s^{-1} at the largest distance with scatter being largest at the shortest distance. The equivalent of the wave energy decayed strongly following a power law with distance (*b*=6.16).

7.4.11 Wave speeds winter 2013-2014

The wave speeds could not be determined for the winter 2013-2014. The signal amplitudes were low and hence the automatic picking of the wave arrival time at the sensors was not reliable.

7.4.12 Wave speeds winter 2014-2015

The automatic arrival time picking yielded accurate results for most experiments (Fig. 7-18). Some wave speeds had to be discarded. The remaining speeds ranged between 211 m s^{-1} and 484 m s^{-1} between the distances of the first and the second sensor. The speeds between the second and the third sensor ranged between 382 and 1298 m s^{-1}. The median between the first and the second sensor was 407 m s^{-1} and between the second and the third sensor 866 m s^{-1}.

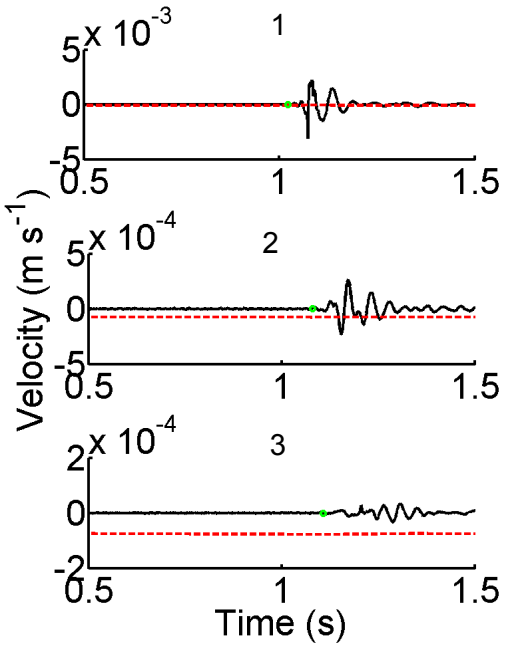

Fig. 7-18: Example of the arrival times (green circles) for sensors 1 to 3 with increasing distance (16.8, 38.1 and 61.2 m, respectively). Data from 22 February 2015.

7.5 Discussion

7.5.1 Influence of sensor placement

During the first winter, the sensors were buried in soil and covered with soil. In the second winter, the sensors were fixed to the rock with bolts. When placing the geophones in soil, the coupling to the ground is not as good as on rock. In addition, with every explosion there might be a small displacement of the soil and the sensor. The displacement of the sensor might be even larger due to the poor coupling. However, if one aims at investigating the effect of ground acceleratins on the snowpack above a soil rather than directly above bare rock, the sensors should be installed in soil bearing in mind the above problems. The increased attenuation of waves in soil compared to rock leads to lower maximum accelerations and derived parameters. This was in particular observed for the closest sensor. The lower damping and the increased coupling observed with rock resulted in higher values. Further from the point of explosion, values for the sensors installed in soil were even higher for some experiments than for the geophones mounted on rock. However, the values for soil were in two groups and scatter was large compared to the sensors mounted on rock.

7.5.2 Wave speeds

During the winter 2014-2015, there was no second wave observed at the sensor in contrast to the first winter. Wave speeds could only be assessed for the second winter. The median wave speed between the first and the second sensor was slightly above the speed of sound in air. The rather low value shows that waves were mainly travelling in air and were transmitted to the snowpack and hence to the rock close to the sensor.

The median speed between the second and the third sensor was much higher (~ 900 m s^{-1}). This can only be explained by the wave being transmitted to the ground close to the point of explosion. For some explosions, the wave speeds were significantly different from other explosions. This may be explained by different depths of the snowpack that influenced the speed.

Close to the point of explosion, there was usually little snow because of the frequent avalanche triggering. At the last sensor the snowpack was usually deeper. This means that at the last sensor, the wave travelling through the air and hitting the snowpack close to the sensor was strongly attenuated over the snowpack depth. The only waves that could reach the sensor were the wave that was transmitted to the ground close to the point of explosion were the snow depth was low or were there even was no snow at all or the wave that was directly transferred over the foundation of the exploder.

7.5.3 Comparison to values within the snowpack

We compared the observed accelerations to the accelerations caused by the largest explosion performed with the mobile gas exploder on a flat study site as reported by Simioni et al. (2016c; cf. Chap. 5). Their lowest maximum snowpack accelerations in the snowpack for 1.9 kg gas at 19 m distance – i.e. the distance of the first geophone in our results – were between 5 and 10 m s^{-2}. This is slightly above the maximum values we measured in the ground. However, maximum accelerations measured by Simioni et al. (2016c; cf. Chap. 5) were around 75 m s^{-2}, i.e. around 18 times larger.

At the distance of the third and furthest geophone, 63 m from the gas exploder, maximum ground accelerations reached 0.73 m s^{-2} in loose soil and 0.04 m s^{-2} on rock. Due to the effects mentioned above, we focus on the measurements on rock. At the same distance, the lowest maximum accelerations in a snowpack reported by Simioni et al. (2016c; cf. Chap. 5) were around 1 m s^{-2}, i.e. around 25 times higher. The lower values at the ground were expected due to the strong attenuation behavior of the snowpack, the wave propagates through before being transmitted to the ground.

7.5.4 Comparison to ground acceleration measurements

Suriñach et al. (2011) measured ground accelerations far from a gas exploder (distance from explosion >100 m). They observed maximum accelerations between 1.3 x 10^{-3} and 2.2 x 10^{-2} m s^{-2}. These values are at least 10 times lower than the values we measured. Applying our power law fit for the maximum accelerations to the distance where they measured their peak values (~ 220 m), our accelerations were approx. one third of the lowest accelerations they measured for the ground wave. The wave that travelled through the air and then through the snowpack to the sensor showed values more than one order of magnitude higher than our results. The higher values observed by Suriñach et al. (2011) might also be due to the fact that the shape of the terrain towards the sensor where they observed the highest value is slightly concave, resulting in a more favorable incident angle of the air pressure wave.

7.5.5 Decay with distance from the point of explosion

The results from the second winter were used to fit power laws of the acceleration and the derived parameters with distance from the point of explosion. The decay was proportional to about $x^{-3.3}$. This is stronger than decay that was observed in Simioni et al. (2016c; cf. Chap. 5) at a certain depth within the snowpack. If the wave would travel through the subsoil only, one would expect that the attenuation would be lower. The combination of the explosion above a snowpack, the transfer through the snowpack and the following transfer to the ground leads to a strong attenuation. Each change of medium – air to snow and snow to ground – implies a difference in impedance. More

energy is reflected when the impedance difference is larger. Other reasons might be that the terrain is not totally level and not perfect.

7.5.6 Probability of avalanche release by ground accelerations

As has been shown, the wave forms observed in the ground – be it soil or rock – cannot be explained by the propagation of the wave through the ground directly from the gas exploder. The wave speeds found were too small. The wave presumably propagated through air and then through the snowpack to the ground. Closer to the point of explosion, no observations could be made. However, we cannot exclude that the indirect loading of the snowpack by ground accelerations caused by the recoil of the gas exploder or by the direct loading of the ground by the explosion at places where usually no snow is left might be sufficient at close range to trigger an avalanche.

Even if the ground accelerations observed would have been caused by the recoil of the system over the foundation or by the impact of the air pressure wave on ground directly at the exploder location, the values would still have been rather low compared to the accelerations in the snowpack. However, in the case of a weak layer near the base of the snowpack, we cannot exclude that these ground accelerations might be sufficient to release an avalanche. For deep snowpacks with a new snow instability, the effect is probably not sufficient.

The frequent triggering observed in our case may be representative for many systems. However, some systems that are installed above infrastructure (railway lines, roads, etc.) are less often used. Hence, a deeper snowpack will usually deposit and ground accelerations will be even smaller.

Suriñach et al. (2011) calculated required peak ground accelerations to cause a block to slide with typical values as reported by Schweizer (1999) and suggested values in the range of 5.82 m s^{-2} to 0.14 m s^{-2}. However, it is not clear, how the snowpack below the sliding block was composed; in particular, how deep it was. The maximum values we observed are in this range. It is not clear though, whether the assumption of a sliding block is correct as the current understanding of avalanche release is different.

7.5.7 Limitations

The analyzed explosions caused by the operational gas exploder are not transferrable to all operational systems. The experiments were performed at a single exploder with a fixed size. In addition, the terrain was not level but a gully (see above). These results hold true for experiments with similar gas exploders and topographies.

7.6 Conclusions

We installed seismic sensors below an operational gas exploder at different distances to investigate the effect of ground accelerations.

Ground accelerations in soil were observed to be lower than on rock due to the strong attenuation of waves in soils. The attenuation of the wave was strong with distance from the point of explosion. In addition, the wave speeds were not sufficiently high. The arriving wave could therefore not be explained by ground accelerations induced close to the exploder or by the recoil of the exploder over the foundation. Instead, it seems that ground accelerations were mainly caused by the air pressure wave hitting the snowpack and being transferred to the ground though the snowpack.

Overall, accelerations observed in the ground were low compared to those measured in the snowpack by Simioni et al. (2015; cf. Chap. 4). Still, because the snowpack in Simioni et al. (2015; cf. Chap. 4) was rather stable and hence failure did only occur close to the point of explosion and at small depths within the snowpack, it seems possible that avalanches may be triggered by the measured accelerations, in particular under conditions when a very fragile weak layer exists. This is also supported by the simple avalanche release model by Suriñach et al. (2011); their results at far distance are in good agreement with ours when scaled to these distances. As the wave is transferred mainly over the snowpack, avalanches will rather be triggered due to the effect within the snowpack than by the ground accelerations. The gas exploder is mounted articulated to the foundation at the back and the front is not stiffly connected to the foundation. The main energy is taken up using the inertia of the gas exploder and hence the transmission of vibrations to the ground by recoil is limited.

8 Small scale field experiments in snow to determine wave propagation principles and mechanical properties

8.1 Introduction

Snow avalanches threaten people and infrastructure in mountainous regions. The hazard can be reduced by various mitigation measures. However, wide-spread engineering works such as defense structures or snow sheds are costly and do often reduce the value of the environment in touristic regions due to their permanent visibility. The deliberate release of snow avalanches has therefore gained significance during the past decades. Whereas in the beginning mainly hand charging was used, the use of helicopter charging and other delivery methods has become increasingly important. Many of these methods cannot be used or only at high risk during bad weather or nighttime – times when artificial triggering might give the best results. The development of fixed avalanche release installations using solid explosives or gas explosives has therefore gained popularity. In contrast to traditional delivery methods, most of these modern systems are bound to a single or just a few points of detonation. It is therefore important to assess the effect of explosions on snowpacks in general. To this end, understanding the propagation characteristics of waves within the snowpack is paramount. In particular, the attenuation of waves above and within snowpacks is crucial.

Many studies, laboratory and field, exist describing the attenuation effect of a snowpack. Johnson et al. (1994) reported high attenuation rates within a snowpack using sheet explosives. However, his experiments were performed in the range of the explosive shock and permanent compaction. Johnson et al. (1993) determined the shock behavior of snow using gas guns and revealed strong attenuation and strain hardening. Binger and Miller (2016) investigated the effect of explosions on a snowpack at short ranges and also showed a strong decrease of the impact with distance from the point of explosion and depth within the snowpack. Many other studies investigated the effect of solid explosive loading on snowpacks (Frigo et al., 2012; Frigo et al., 2010; Gubler, 1977; Tichota et al., 2010). However, most of them did not explicitly focus on wave attenuation within a snowpack.

At a certain distance from the point of explosion, beyond the shock wave range, the wave becomes elastic and hence results from studies on linear acoustic wave propagation in snow can be considered. Different studies used different methods: Reiweger et al. (2015), Ishida (1965) and others determined the attenuation from the transmission loss of snow layers of different thicknesses. Other studies measured the impedance of snow and deduced the attenuation coefficient (Marco et al., 1998). Capelli et al. (2016) performed propagation experiments with small scale samples in the lab, determined the attenuation and compared their findings to data from previous studies. The signal was produced using piezo elements or pencil lead fractures (PLF) and the attenuation was measured using different column lengths. They reported that their results, in the range of 0.35 and 1.2 dB cm^{-1}, were in good agreement with findings from previous studies ranging from 0.05 to 3.5 dB cm^{-1}. However, the comparison between different datasets is difficult due to

different measuring methods, as pointed out by Capelli et al. (2016). With some methods, the attenuation within the pores is measured and with other methods the attenuation in the ice frame. The lower the snow density, the lower the attenuation will be for the waves propagating through the pore space. Mayer (2011) experimented with the localization of pulses via acoustic emissions in small snow samples. He observed the opposite: With lower densities, the localization was difficult due to the strong attenuation whereas the localization quality increased with increasing density. This would mean that he measured the wave within the ice frame rather than the pore space. Hence, in general, studying the attenuation is very complex due to the different wave types observed in porous media (Biot, 1956a) where two longitudinal waves travel in the ice frame and the pore space and an additional shear wave propagates through the ice skeleton. All the three wave types are attenuated differently according to model results (Johnson, 1982).

Various studies were performed to determine the propagation speed of elastic waves in snow. Different speeds were obtained for different measuring methods. Sensors that measured in direct contact with the ice frame resulted in values higher than the speed of sound in air showing increasing speeds with increasing densities (Capelli et al., 2016; Reiweger et al., 2015). Measuring wave speeds not in direct contact with the ice frame resulted in lower values than the speed of sound in air and speeds were decreasing with increasing density (Gudra and Najwer, 2011; Lee and Rogers, 1985). Capelli et al. (2016) reviewed previous research on these wave speeds and showed the dependency of the different speeds on wave type and density. A clear distinction can be made between the waves travelling through the ice frame and the wave within the pore space.

When a weak layer locally fails, an initial crack forms that may spontaneously propagate, depending on weak layer and slab properties, and lead to catastrophic failure. Assessing crack propagation speed is important to e.g. model the dynamic phase of crack propagation and possibly to predict avalanche size. van Herwijnen and Jamieson (2005) and van Herwijnen and Birkeland (2014) developed a method to obtain crack speeds from saw propagation tests using particle tracking velocimetry. Their speeds ranged between 10 and 45 m s^{-1}. Johnson et al. (2004) measured the speed of a whumpf, i.e. a propagating crack, with geophones positioned on the snow surface and reported a value of 20 m s^{-1}. Hamre et al. (2014) determined crack propagation speeds from video stills of the artificial triggering of avalanches with results in the range of 50 to 125 m s^{-1}. However, this might be a mixture between the wave propagation speed in or above the snowpack and the actual crack propagation speed.

None of the above-mentioned studies investigated the attenuation in the elastic range for a natural snowpack in situ, hence in the field with a suitable measuring system. Furthermore, speeds were also mainly measured under laboratory conditions. Only the PTV method has proven to be suitable for extensive field measurements of propagation speeds (van Herwijnen et al., 2016a).

However, the PTV-derived propagation speeds are based on the collapse wave and it is not clear, whether the collapse speed is identical to the preceding crack speed.

Our objectives were therefore to measure the attenuation and speed of waves not only within homogeneous snow but entire snowpacks, but for simple geometries, blocks of snow (~1-8 m^3). These in situ experiments should improve our understanding of wave propagation within snow that are otherwise difficult to assess. In addition, we wanted to explore whether the determination of crack propagation speeds in a snowpack is possible by other means than PTV and assess whether our measuring equipment can be used to measure crack propagation speeds over large distances.

8.2 Methods

8.2.1 Study site

The small scale experiments were performed at three different study sites in the region of Davos, Switzerland.

The study site on the Flüelapass above Davos is located directly besides the road and only accessible during a short period. During the rest of the winter season, the mountain pass is seasonally closed. The study site lies at 2'375 m a.s.l. on flat, almost level terrain. Small scale features are leveled out by frequent snow drifting. The study site is well-suited for experiments including explosions as it is difficult to access and usually rarely travelled during the experimental season. The site is well suited for experiments with solid explosives and larger measuring equipment due to its accessibility.

The second study site is situated around a weather station in the Steintälli at 2442 m a.s.l. (Reuter et al., 2015b). The site was used for experiments where only little measuring equipment was required since it is only accessible on touring skis. The experiments were performed during experiments investigating the temporal evolution of snowpack instability using propagation saw tests (PSTs) (Schweizer et al., 2016b).

The last study site was situated at the Versuchsfeld Weissfluhjoch at 2540 m a.s.l. (Marty and Meister, 2012). The study site is well-accessible on skis as it is situated in a ski area. Every other week, a manual profile including other tests is done to investigate the evolution of the snowpack. During these experiments which included PSTs, the experiments were performed.

8.2.2 Source

Different sources were used to produce the required impulse triggering the waves propagating within the snowpack. For some experiments, solid explosives were used to create the load. This was done to get a better understanding of the wave propagation caused by an explosion which could not

be determined with the large scale experiments performed by Simioni et al. (2015; cf. Chap. 4) who triggered a charge above the snowpack that caused a complex wave field. Small amounts of solid explosives commonly used in artificial avalanche release (approx. 100 g) were detonated. This resulted in a spherical wave that hit the snowpack and was then partly transmitted to the snow. Explosives' regulations, permissions and accessibility of the study site limited this source to experiments at the Flüelapass site.

In addition, hammers were used to create the impulse. A steel plate was hit by different hammer sizes which then caused an approximate plane wave with in the snowpack. The experiments with hammers were easy to perform as the hammer and the steel plate were the only equipment required for the source. This source was mainly used for the experiments at Steintälli and Weissfluhjoch study sites. Different hammer sizes were tested. Hammers with 0.5, 0.8 and 4.5 kg were used for most hammer experiments.

As concurrently PSTs were performed on the test days at Weissfluhjoch and Steintälli, this test geometry was used to also determine crack propagation speeds. For these experiments, the source was the self-propagating crack within the weak layer initiated by cutting along the weak layer with a saw.

8.2.3 Experimental setup

Two different approaches were used for the experimental setup. The first setup included a large block of snow; several meters in length (3-4 m), a few meters in width (2 m) and approx. the top meter of the snowpack. This block was cut from the surrounding snowpack on three sides, the front, the back, and on one side. (Fig. 8-1). The other side was connected to the snowpack. This kind of blocks was mainly used for the experiments with solid explosives. A solid explosive charge was placed at approx. 0.5 to 1 m from the front wall at half the block height. The sensors were placed at different distances from the front of the block and at approx. half the width of the snow block.

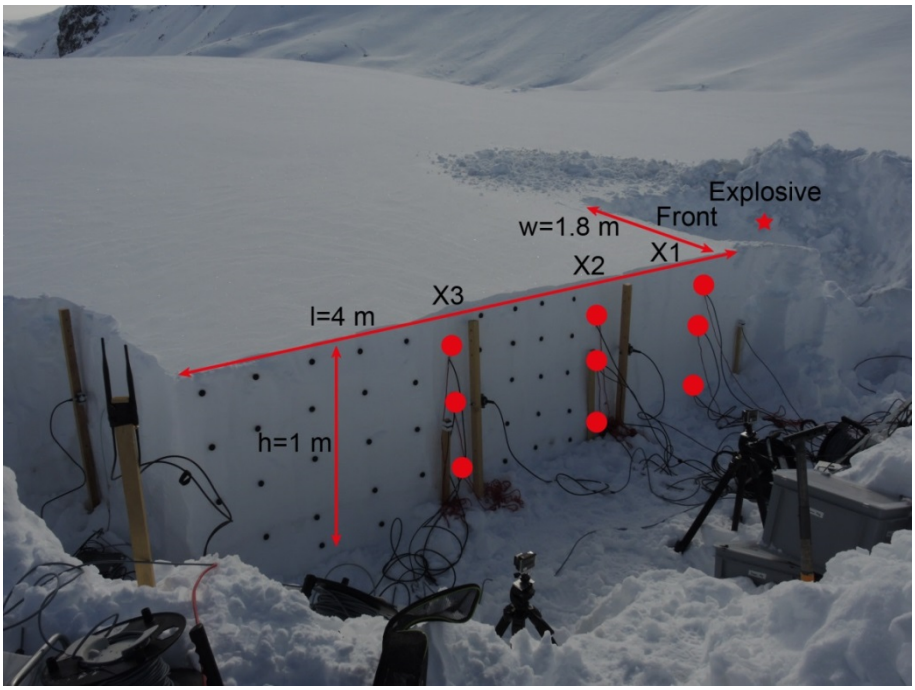

Fig. 8-1: Typical snow block for experiments performed with solid explosives. The solid explosive was placed at the front of the block (red star) at the height of the middle sensor. The sensors were inserted in direction of the arrow from the holes (red dots) on the side. In this case, 3 systems (X1 to X3) and 9 sensors were used at different depths. Picture from 4 February 2015.

The second setup consisted of blocks used for PSTs (Gauthier and Jamieson, 2006) (Fig. 8-3). These blocks were approx. 2 m long and 30 cm wide. Their height depended on snow stratigraphy and corresponded to the height between the relevant weak layer – usually close to the ground – and the snow surface. The steel plate was placed at the front of the block and repeatedly hit with a hammer. The plate was placed at different heights depending on the block height and the apparent layering of the snowpack. This setup was also used to determine crack propagation speeds. For some experiments, the source was placed on or above the snow surface and the accelerometers were installed at different depths within the snowpack below the source.

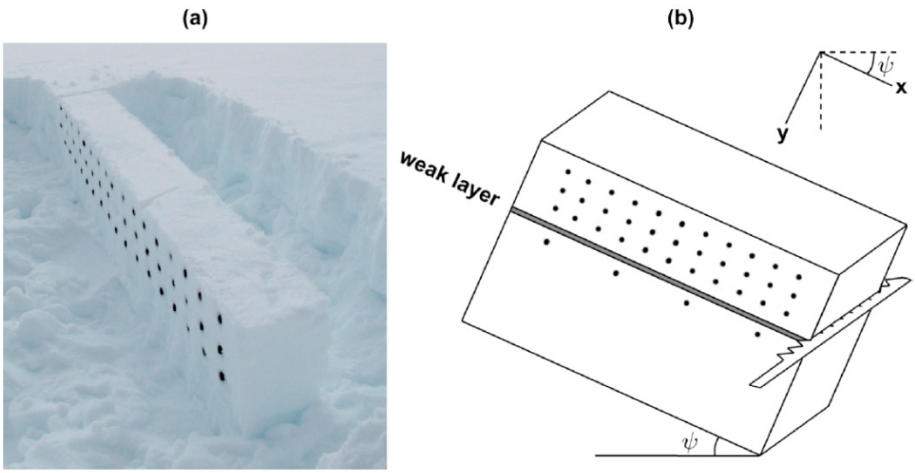

Fig. 8-2: Propagation saw test (PST): (a) Photo of an isolated PST beam with black markers for particle tracking velocimetry. (b) Shematic drawing of the test procedure. (van Herwijnen et al., 2010).

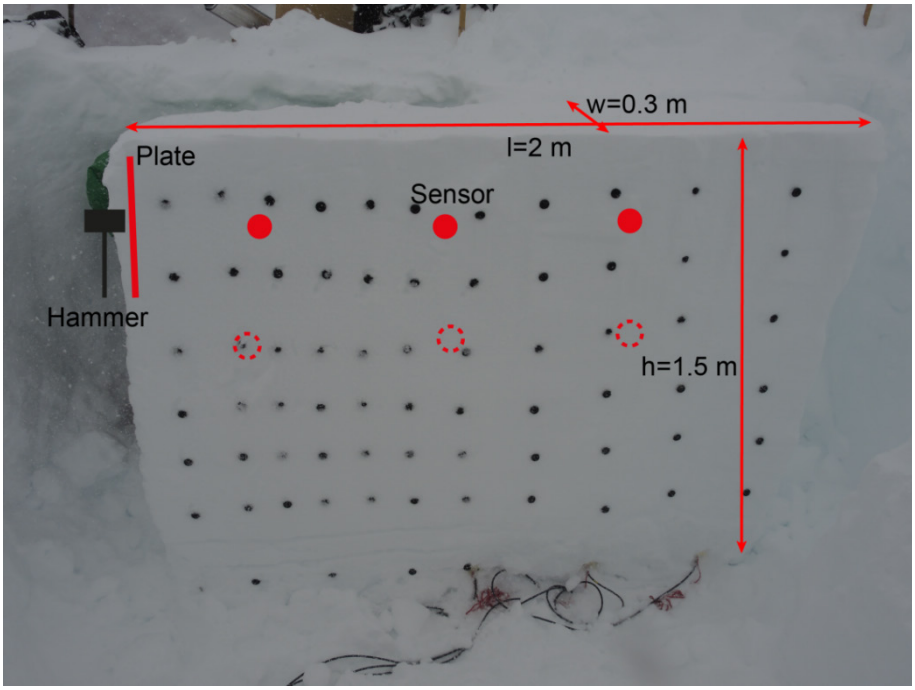

Fig. 8-3: Typical snow block for experiments performed with the hammer. The plate is installed at the front of the block and hit by the hammer. The sensors (red dots) are installed at different distances at the same elevation as the source. The sensors (dashed dots) and the plate are placed at larger depths for subsequent experiments. The black dots are markers for the particle tracking velocimetry and not important for the acoustic experiments.

8.2.4 Acceleration measurements

Accelerations were measured at different locations within the snow blocks. The accelerometers developed by Simioni et al. (2015; cf. Chap. 4) were used. They are placed within a foam cylinder matching an expected average snowpack density of 200 kg m^{-3}. Three to nine accelerometers were used. When using three accelerometers, the sensors were placed at the same depth within the

snowpack at different distances from the front of the block. With nine accelerometers, three accelerometers were installed at three distances and at different depths. The sensors were placed a few centimeters below the weak layer for the experiments where the crack speed in a PST was determined.

8.2.5 Snowpack characterization

Manual profiles were performed to characterize snowpack properties on each test day. In addition, density measurements at every 2 to 5 cm from the snow surface were performed using a Denoth probe (Denoth, 1989). The dielectric constant measured with the Denoth probe depends on liquid water content and density. If liquid water content needs to be determined, the density has to be measured manually with a density cutter which was done on days where the snowpack was expected to be moist or wet.

8.2.6 Data acquisition and triggering

National Instruments cDAQ systems were used to record the data (Simioni et al., 2015; cf. Chap. 4). Depending on the number of accelerometers, one to three systems were used. The data acquisition systems were triggered manually. The solid explosives were triggered from a safe distance after triggering the data acquisition manually. This means, that the exact time of the explosion or the hammer blow could not be determined.

8.2.7 Data evaluation

The acceleration measurements were used for two different purposes. The accelerations were integrated to determine the displacement velocity at each sensor. These velocities were then squared and integrated to receive an equivalent of the energy of the propagating wave. The attenuation coefficient was calculated using the difference of the logarithm of the energy equivalent and the difference of the distances between the sensors. Their ratio corresponds to the attenuation coefficient.

$$\int_{t_0}^{t_1} a_\mathrm{s}\, dt = v\ (\mathrm{m\ s^{-1}}) \tag{8.1}$$

$$\int_{t_0}^{t_1} v^2\, dt = E'(\mathrm{m^2\ s^{-1}}) \tag{8.2}$$

$$\alpha_\mathrm{en} = \frac{\Delta \log E'}{\Delta x}\ (\mathrm{dB\ cm^{-1}}) \tag{8.3}$$

where a_s is the acceleration in m s^{-2}, v the displacement velocity in m s^{-1}, E' the equivalent energy, α_en the damping coefficient and x the position of the sensors.

Two different types of the attenuation coefficient were determined. The first coefficient was determined from experiments where the source was placed at the front of the block. This was done

to perform measurements within a single snow layer or a few similar layers. These measurements were used to determine density-dependent attenuation coefficients. The experiments with the source applied at the top of the snowpack were performed to get an approximation of the attenuation that occurs vertically through a snowpack.

In addition, the attenuation coefficients were determined separately for dry snowpacks, moist snowpacks, experiments using hammers and experiments using solid explosives.

For the experiments where the source was placed at the front of the block and waves were propagating horizontally, i.e. along the layering, through the snowpack, the horizontal attenuation is the attenuation in the main direction of wave propagation and is called the parallel attenuation. The vertical attenuation gives the attenuation of the component perpendicular to the main wave propagation and is hence called the perpendicular attenuation. For the experiments with the source above the snowpack, the vertical component gives the attenuation in the main direction of wave propagation (parallel) and the horizontal component the value perpendicular to the main wave propagation direction.

The arrival times of the waves at the accelerometers were determined using AIC picking (Kurz et al., 2005); further details are given in Simioni et al. (2016c; cf. Chap. 5). With the distances between the first, the second and the third sensors and the arrival times, the wave propagation speed was calculated.

$$c = \frac{\Delta x}{\Delta t}\ (\mathrm{m\ s^{-1}})\ (7) \tag{8.4}$$

where t is the arrival time at the sensors.

The constrained modulus– assuming a longitudinal plane wave in a beam – is given by

$$M = c^2 \rho\ (\mathrm{Pa}) \tag{8.5}$$

The results of the constrained modulus were fitted with an exponential relation vs. density:

$$M_{\mathrm{fit}} = a_{\mathrm{M}} \cdot e^{b_M \rho}\ (\mathrm{Pa}) \tag{8.6}$$

8.3 Results

8.3.1 Experimental data

During the winters of 2014-2015 and 2015-2016, a total of 263 experiments were performed to measure wave propagation speeds and attenuation within the snowpack (Table 8-1). 37 experiments could not be used for the calculation of the attenuation, mainly because of sensors that had a too small range or a too low sensitivity or due to a too weak impulse, i.e. using a too small hammer. 22 experiments were performed under moist snowpack conditions using a hammer. Moist conditions

are defined as wetness index 2 (Fierz et al., 2009). 25 experiments under dry conditions were performed vertically through the snowpack.

In addition, 10 experiments were performed to determine the crack propagation speed using PSTs, where the self-propagating crack originating from a saw cut caused a signal at the sensors. 5 of these experiments resulted in values that were plausible.

For almost all experiments between 4 February 2016 and 4 April 2016 where hammer blows were used, a series of three datasets including three experiments (hammer blows) each were performed with the same setup.

The experiments on the Flüelapass with solid explosives and under dry conditions were performed using three measuring systems with the exception of 2 experiments. This means that the speed and the attenuation were determined at three different depths within the snowpack using the same explosion.

For all other experiments, one measuring system with three sensors was used and the speed and the attenuation were determined at one depth within the snowpack (Table 8-1). This was done for different depths within the snowpack, i.e. the sensors were placed at a different depth for the different experiments.

The experiments under moist snowpack conditions were performed with a hammer.

8.3.2 Snowpack conditions

Densities ranged between 150 and 400 kg m^{-3} for dry conditions and between 370 and 440 kg m^{-3} for moist snowpack conditions. The liquid water content on the only day with moist snowpack conditions, i.e. 29 April 2015, was between 0 and 4 % per volume. The snowpack layering varied strongly with test day and study site. However, two weak layers existed, deeply buried and consisting of faceted crystals, for most of the experiments performed during the winter 2015-2016. These layers were tested with the PST yielding critical crack length between 24 and 90 cm with increasing cut lengths for later test days. Hence, in all tests cracks propagated to the end of the column so that crack speed could be measured.

8.3.3 Solid explosive charges and hammer sizes

The solid explosive charge sizes under dry snowpack conditions were between 0.083 and 0.275 kg. They were located at the depth of the middle sensor where more than one system was used. The distance between the front of the block and the charge size was between 0.32 and 2.25 m.

A hammer with a weight of 0.8 kg and for some experiments of 0.5 kg was used for the experiments at Steintälli and Weissfluhjoch where the tests were performed on PST blocks.

*Table 8-1: Summary of all experiments. The study sites are Flüelapass (FLUE), Steintälli (STEI) and Weissfluhjoch (WEIS). The main wave direction shows whether the source was placed above the snow block (vertical) or at the front of the block (horizontal). The block types shows on which days the experiments were performed on blocks for propagation saw tests (PST, s. block size with *). No. of PSTs shows how many propagation saw tests were performed on the respective day. For the tests without PST experiments, one block per day was used.*

Date	Study site	No. of experi-ments	Source	Main wave direction	Block size *l* x *w* x *h (m)*	Nr. of PSTs	No. of systems
03 Feb 2015	FLUE	1	Explosive	Horizontal	4 x 1.8 x 1		1
04 Feb 2015	FLUE	6	Explosive	Horizontal	4 x 1.8 x 1		3
12 Feb 2015	FLUE	9	Explosive	Horizontal	4 x 1.8 x 1		3
29 Apr 2015	FLUE	17	Hammer	Vertical	0.5 x 0.5 x 1		1
29 Apr 2015	FLUE	5	Explosive	Vertical	0.5 x 0.5 x 1		1
04 Feb 2016	STEI	72	Hammer	Horizontal	2 x 0.3 x 1.3*	4	1
04 Feb 2016	STEI	9	Hammer	Vertical	2 x 0.3 x 1.3*		1
10 Feb 2016	WEIS	28	Hammer	Horizontal	2 x 0.3 x 1.5*	2	1
10 Feb 2016	WEIS	9	Hammer	Vertical	2 x 0.3 x 1.5*		1
24 Feb 2016	WEIS	31	Hammer	Horizontal	2 x 0.3 x 1.6*	2	1
24 Feb 2016	WEIS	6	Hammer	Vertical	2 x 0.3 x 1.6*		1
04 Apr 2016	WEIS	26	Hammer	Horizontal	2 x 0.3 x 1.6*	2	1
04 Apr 2016	WEIS	10	Hammer	Vertical	2 x 0.3 x 1.6*		1

8.3.4 Waves

During the experiments, one principal wave was visible. There were no faster waves as precursors observed. Later waves were observed in some experiments behind the main wave. The measured waves had a vertical and a horizontal component (Fig. 8-4 and Fig. 8-6). The main frequency content was in the range of 300 Hz for the solid explosive experiments with almost no energy above 1000 Hz (Fig. 8-5). The hammer experiments showed main frequencies between approx. 200 and 500 Hz with a much wider frequency spectrum (Fig. 8-7).

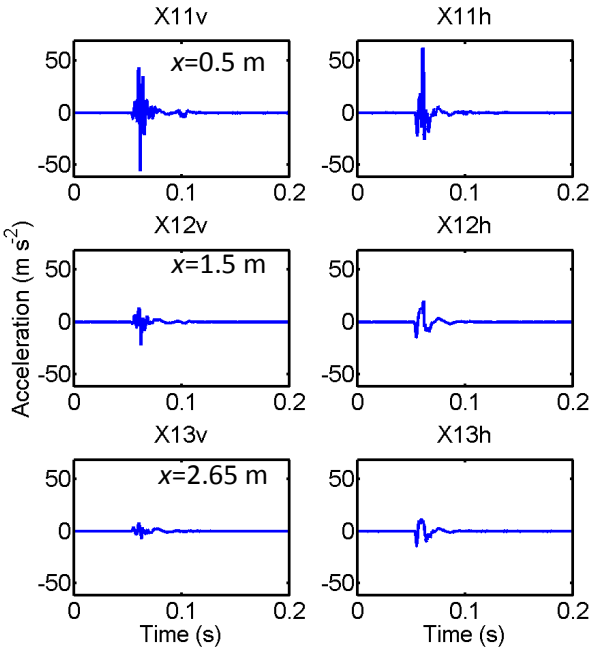

Fig. 8-4: Snowpack accelerations as recorded during a spherical experiment. The vertical (left) and the horizontal (right) component are shown for increasing distances x (from top to bottom) from the source in the block. The strong attenuation of the signal is clearly visible. Data from 04 Feb 2015 test 3_1, solid explosive experiment.

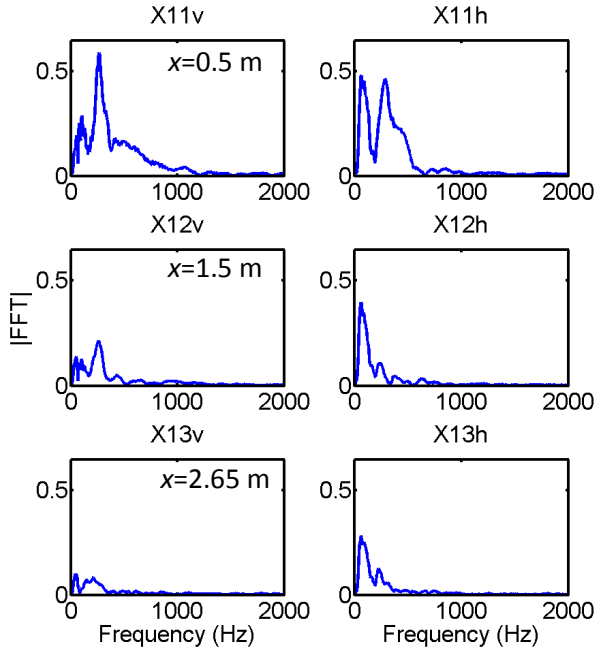

Fig. 8-5: Frequency content of the acceleration signal of an spherical explosive experiment for the vertical (left) and horizontal (right) component for different distances x (top to bottom) from the source. Data from 04 Feb 2015, test 3_1, solid explosive experiment.

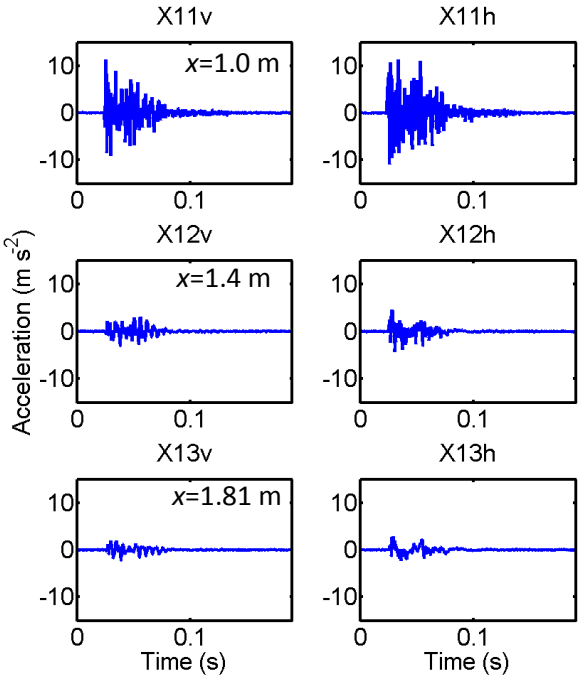

Fig. 8-6: Snowpack accelerations as recorded during a hammer experiment. The vertical (left) and the horizontal (right) component are shown for increasing distances (from top to bottom) from the source in the block. The strong attenuation of the signal is clearly visible. Data from 23 Feb 2016, test 3_1, hammer experiment..

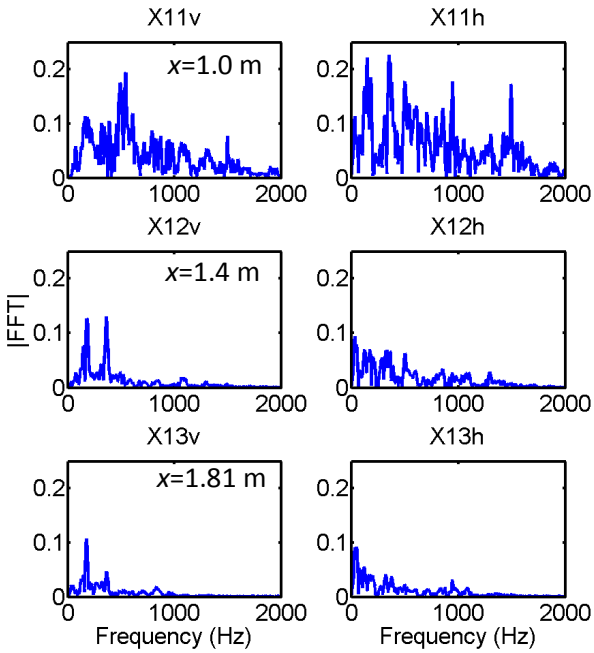

Fig. 8-7: Frequency content of the acceleration signal for the vertical (left) and horizontal (right) component for different distances (top to bottom) from the source. Data from 23 Feb 2016, test 3_1, hammer experiment.

8.3.5 Energy equivalent

The energy, derived from the displacement velocity signal, could not be calculated for all experiments: Depending on the source and the distance from the source, the sensors were saturated for some experiments or the signal had already been attenuated too strongly and hence the sensor was not sufficiently sensitive.

The energies decreased with distance from the source for almost all experiments (Fig. 8-8 and Fig. 8-9). Although the acceleration signals showed similar amplitudes for the horizontal and vertical components, the energies of the two components differed due to differences in the displacement velocities: The component of the energy equivalent of the wave in direction of the main wave propagation was usually larger than the component perpendicular to the propagation direction. Absolute values are not given here as for the damping characteristics of the snowpack, the relation between the energies at different distances is of importance and not the absolute value, which is not an actual energy, but an equivalent.

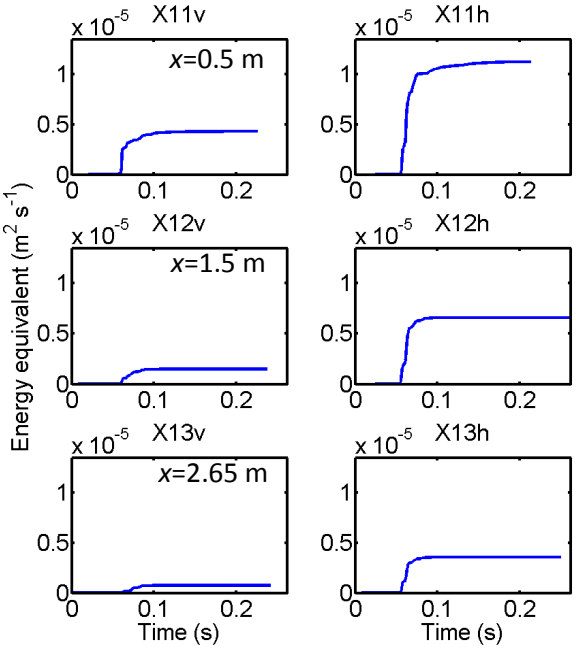

Fig. 8-8: Equivalent of the summed up wave energy for the vertical (left) and horizontal (right) component for different distances x (top to bottom) from the source for a spherical explosive experiment. Data from 04 Feb 2015, test 3_1, solid explosive experiment.

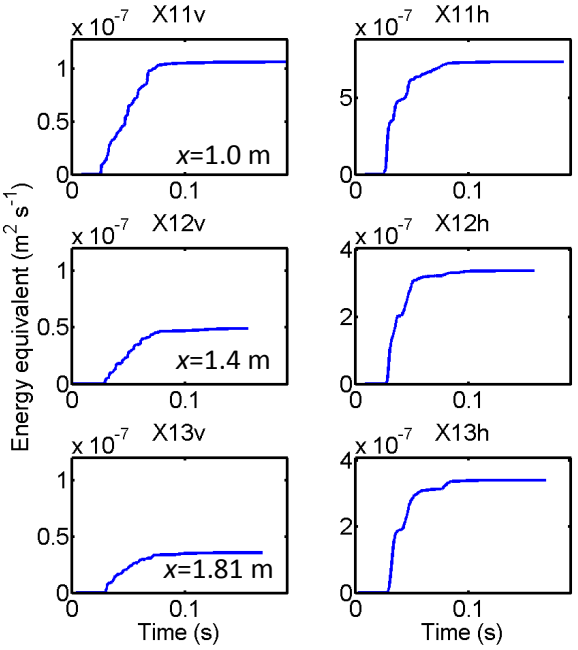

Fig. 8-9: Equivalent of the summed up wave energy for the vertical (left) and horizontal (right) component for different distances (top to bottom) from the source. Data from 23 Feb 2016, test 3_1, hammer experiment.

8.3.6 Attenuation coefficients solid explosive experiments

For the experiments involving solid explosives, the attenuation was measured horizontally through the snowpack within similar layers. The attenuation coefficients ranged between 0.10 and 1.56 dB cm^{-1} (Fig. 8-10). For consecutive tests using the same setup, the coefficients varied. The average of the attenuation of the horizontal component was between 0.27 and 1.04 dB cm^{-1}. There was no density-dependency observed for the attenuation coefficient. The vertical component ranged between 5.3×10^{-2} and 1.3 dB cm^{-1} (Fig. 8-11). The average values were between 0.51 and 0.91 dB cm^{-1}.

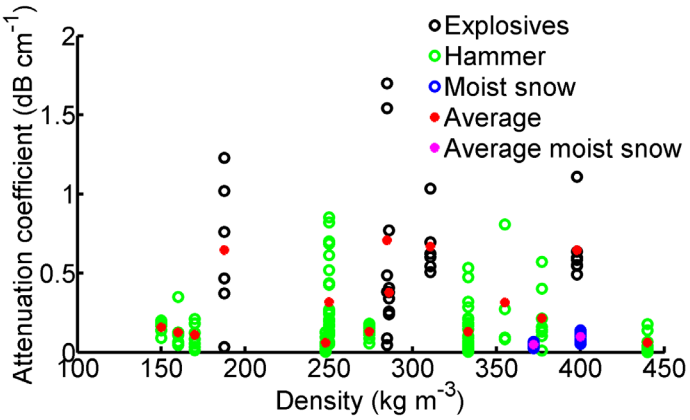

Fig. 8-10: Attenuation coefficient of the horizontal (parallel) component for all experiments performed from the front of a block. All experiments where the wave travelled through different snowpack layers were excluded.

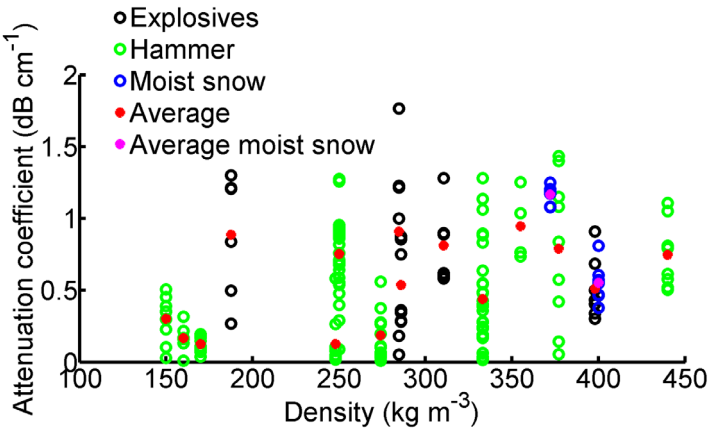

Fig. 8-11: Attenuation coefficient of the vertical (perpendicular) component for all experiments performed from the front of a block. All experiments where the wave travelled through different snowpack layers were excluded.

8.3.7 Attenuation coefficients from horizontal hammer experiments

The horizontal experiments were those where the source was used at the front of the block and the damping was measured within the same layer. The attenuation coefficients ranged from 6 x 10^{-2} to 1.08 dB cm^{-1} for the horizontal component (Fig. 8-10). Consecutive testing at the exact same location led to different coefficients. The average attenuation coefficients for different densities ranged from 0.29 to 0.62 dB cm^{-1}. There was no dependence of the attenuation coefficient on density observed. However, the values for the lowest densities were low compared to the averages at higher densities.

Although the pulse was generated horizontally, there were vertical accelerations observed. Their attenuation coefficients ranged between 7 x 10^{-2} and 1.16 dB cm^{-1} (Fig. 8-11). The attenuation coefficients of the vertical component showed a larger scatter than those for the horizontal component for the single locations. Average values of the coefficients were between 0.11 and 0.97 dB cm^{-1}. No dependence on density was observed.

8.3.8 Attenuation coefficients from vertical hammer experiments

The experiments were the source was placed above or on the snow surface resulted in attenuation coefficients for waves propagating perpendicular to the snowpack layering. The attenuation coefficients were in the range of 2 x 10^{-2} and 1.14 dB cm^{-1} with a median of 0.42 dB cm^{-1} for the horizontal, i.e. perpendicular component, not considering outliers (Fig. 8-12). For the vertical, i.e. parallel component, the values ranged from 0.04 to 0.56 dB cm^{-1} with a median of 0.38 dB cm^{-1}. For consecutive experiments, the values scattered for the same setup. As waves propagated through different snowpack layers, the dependence on density could not be evaluated.

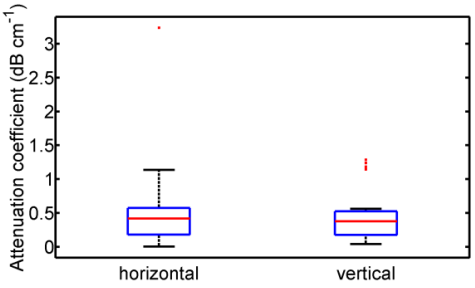

Fig. 8-12: Box plot of the attenuation coefficients of the horizontal (perpendicular, left) and vertical (parallel, right) component for the vertical experiments through different snowpack layers.

8.3.9 Attenuation coefficients for moist snowpack conditions

The attenuation coefficients for moist snowpack conditions ranged between 2.6 x 10^{-2} and 0.14 dB cm^{-1} for the component parallel to the wave propagation (Fig. 8-10). The average attenuation coefficient was between 4.9 x 10^{-2} and 9.9 x 10^{-2} dB cm^{-1}. The vertical component, perpendicular to the wave propagation, was between 0.38 and 0.13 dB cm^{-1} with the average being between 0.55 and 1.2 dB cm^{-1} (Fig. 8-11).

8.3.10 Wave speeds under dry-snow conditions

For the wave speeds, only the experiments where the wave propagated parallel to the snowpack layering were considered, i.e. the source was located at the front of the block. The average wave speeds of the horizontal component ranged between 327 and 1479 m s^{-1}, with rather large variation for some of the consecutive tests under identical conditions (Fig. 8-13). The average wave speeds determined from the vertical component were between about 314 and 1466 m s^{-1} (Fig. 8-14). The speed slightly increased with increasing density.

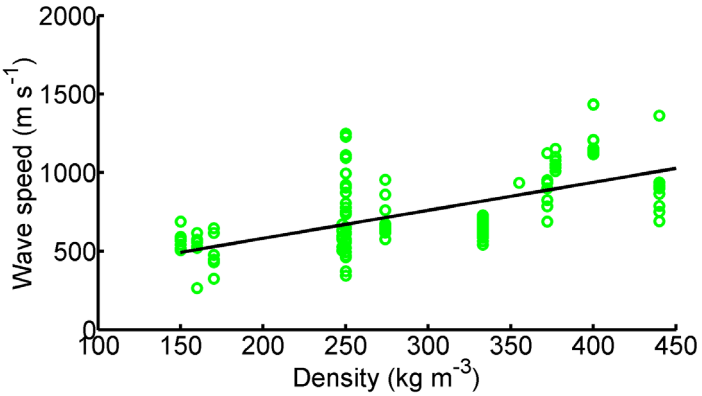

Fig. 8-13: Wave speeds determined from the wave arrival times of the horizontal (parallel) component and distances between the sensors for the experiments with the source at the front of the block. Green dots depict single experiments and the red dots the average of the experiments for a certain density.

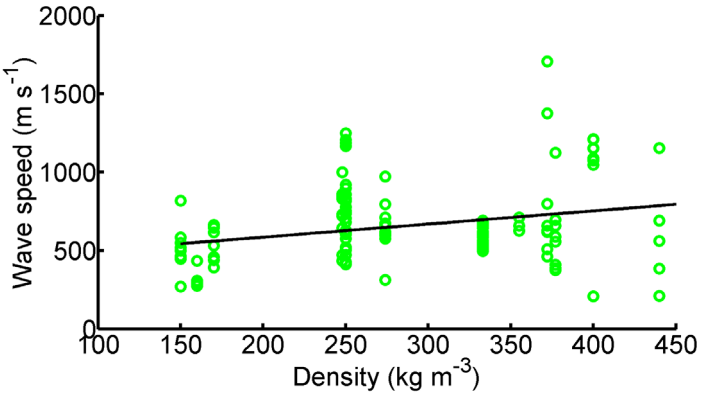

Fig. 8-14: Wave speeds determined from the wave arrival times of the vertical (perpendicular) component and distances between the sensors for the experiments with the source at the front of the block. Green dots depict single experiments and the red dots the average of the experiments for a certain density.

8.3.11 Constrained modulus

The constrained modulus was derived from the wave speeds. The modulus was between 10 MPa for low densities and 500 MPa for densities of approx. 400 kg m^{-3} (Fig. 8-15). The constrained modulus increased with density following an exponential law (eq. 8.7)

$$M = a_{\mathrm{M}} e^{\rho b_{\mathrm{M}}} \ (\mathrm{MPa}) \tag{8.7}$$

with the coefficients

$$a_{\mathrm{M}} = 1.88 \times 10^{7} \tag{8.8}$$

$$b_{\mathrm{M}} = 7.1 \times 10^{-3} \tag{8.9}$$

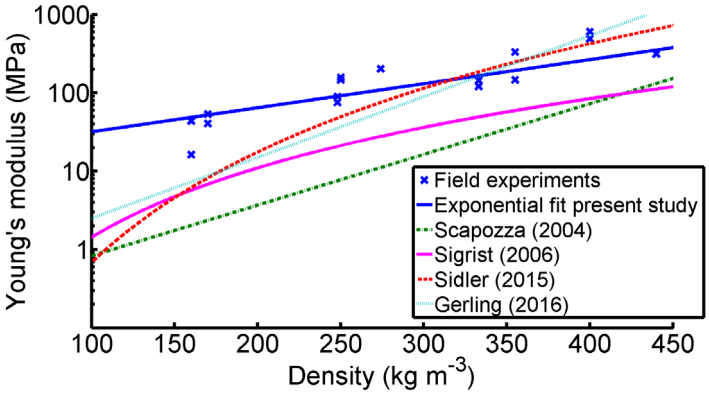

Fig. 8-15: Average Young's modulus (blue crosses) from the field experiments with the best fit with (blue solid line). For comparison, the data from Scapozza et al. (2004) (green dot-dashed line), the fit from Sidler (2015) on data presented by Mellor (1975) (red dashed line) and from Gerling (2016) (cyan dotted line) are given.

8.3.12 Crack propagation speed

For five out of ten experiments, the crack propagation speeds were between 19.0 and 56.8 m s^{-1}. The speeds determined with the arrival time derived from the horizontal and vertical acceleration components were in good agreement for four of the five experiments, all performed on 4 February 2016 (Fig. 8-16). The speeds determined from the horizontal component were always slightly higher (12 to 25%). For some other PSTs, the waveforms looked as if different waves were superimposed with one sharper higher-frequency wave and an additional lower-frequency wave. Due to the superimposition, the signals could not be differentiated and also in the spectrogram no major difference was observed. However, the high-frequency signal led to speeds of several hundred meters per second for those cases where it could be analyzed at the front of the lower-frequency signal.

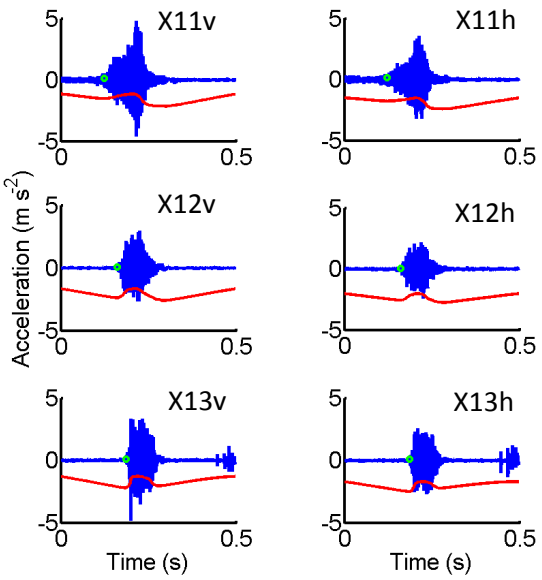

Fig. 8-16: Acceleration measurements during a propagation saw test indicating the arrival time of the wave (green circle) and the AIC function used to pick the arrival time for the vertical (left) and horizontal (right) component. The red curve is the AIC function used to select the start. Data from 4 February 2016, test #1.

Under moist snowpack conditions and for one experiment under dry-snow conditions, the speeds were not consistent between the values determined from the horizontal and vertical component and the speeds were high (several hundred m s^{-1}).

8.4 Discussion

8.4.1 Waves

The waveforms resembled those presented by Simioni et al. (2015; cf. Chap. 4) for the solid explosive experiments (Fig. 8-4 and Fig. 8-6). Frequencies were higher, probably due to the shorter distance of the sensors from the explosion leading to lower dispersion (Fig. 8-5 and Fig. 8-7).

8.4.2 Energy equivalent

Snowpack accelerations were lower for the component perpendicular to the expected main propagation direction of the generated wave. The energy equivalent derived from the displacement velocities, i.e. the integrated accelerations, were lower for the perpendicular component (Fig. 8-8 and Fig. 8-9). In particular for the experiments performed with a hammer, the goal was to create a plane wave propagating in the direction of the greatest extension of the snow block. The non-negligible perpendicular component showed that the waves produced with the plate and the hammer were not perfectly plane. In addition, there were reflections at the layer boundaries which caused perpendicular components. These reflections did not only occur at obvious layer boundaries, but also at subtle changes within a layer otherwise described as uniform having similar density and properties.

8.4.3 Attenuation coefficients

The attenuation coefficients did not show any dependence on density in the investigated range of densities (Fig. 8-10 and Fig. 8-11). The results are in good agreement with the findings by Capelli et al. (2016), who measured wave attenuation at high frequencies of around 10 to 35 kHz. The results agree well with values reported by e.g. Gudra and Najwer (2011) and Buser (1986). Other studies reported increasing attenuation with increasing density (Marco et al., 1998). This finding probably was due to the method that was used to measure the attenuation in snow. Capelli et al. (2016) reported that the magnitude of the observed attenuation was in the range of the attenuation of Biot's slow wave (Biot, 1956a). The attenuation of the other wave modes was much lower. This means that also the main waves we observed with much lower frequencies in the range of 1 to 500 Hz probably corresponded to the slow wave propagating through the pore space.

The attenuation of the component perpendicular to the wave propagation was usually stronger (Fig. 8-10 and Fig. 8-11). This is plausible as the perpendicular component was mainly observed due to an imperfectly created plane wave and by various reflections within the snowpack at layer boundaries. The created P-wave was propagating directly between the sensors whereas the perpendicular component was probably caused by reflected wave modes. It is not clear, which wave modes these waves can be attributed to.

Although the vertical experiments with the source above the snowpack did not allow evaluating attenuation coefficients for specific densities, they provided overall attenuation coefficients (Fig. 8-12). The coefficient for the vertical experiments was varying strongly between the different test days but was similar during single test days. This means that the layering which was different for the different test days had a strong influence on the attenuation. The vertical component was attenuated similarly to the perpendicular component with the exception of one test day, when the perpendicular component was attenuated less strongly. Overall, the attenuation coefficients for the vertical experiments were in the same range as for the horizontal experiments. This is rather surprising as one would expect higher attenuation coefficients for the vertical experiments. The wave propagates through many different layers including ice layers with significant impedance differences that would reflect a portion of the wave energy and lead to strong attenuation. As the snowpack was rather uniform in the horizontal direction, this cannot be the explanation for the similar attenuation coefficients. It might be that the anisotropic snow behavior led to the difference to some degree. The non-perfect planar wave during the horizontal experiments leading to a vertical wave component might be another reason.

The attenuation of the parallel (horizontal) component during the horizontal experiments with moist snowpack conditions was at the lower end of the overall attenuation coefficients (Fig. 8-10). Until now, it was assumed that attenuation under moist or wet-snow conditions would be stronger due to the observations during artificial triggering where many more detonation points are required to control a slope during wet compared to dry snowpack conditions. It seems that this observation is not related to the attenuation of the impact. In any case, if the charge penetrates the snowpack and is triggered within the snowpack, the attenuation is extremely strong. This means that the minor effect during wet-snow conditions is rather due to different crack propagation and avalanche release propensity, i.e. snowpack stability conditions, than due to the stronger decay of the effect of the charge. It makes sense that the decay during moist or wet-snow conditions is not stronger than during dry conditions: During wet-snow conditions, the pores are (partly) filled with water. The difference between water as a pore fluid compared to air and the ice skeleton is lower regarding wave propagation and hence the attenuation should not be stronger.

8.4.4 Wave speeds

The average wave speeds were between approx. 400 and 1100 m s^{-1} (Fig. 8-13 and Fig. 8-14). The obtained results are in good agreement with the longitudinal waves within the ice skeleton measured and reviewed by Capelli et al. (2016). The speeds cannot be those of the transversal wave because they were too high. They also cannot correspond to the longitudinal wave within the pore space due

to two reasons: The values were too high and did not decrease with density as is expected for this wave mode due to the increasing tortuosity with increasing density as reported by Ishida (1965).

8.4.5 Wave modes

The typical signal length measured with the hammer experiments was approx. 0.05 to 0.1 s (Fig. 8-6). Distances between the sensors were between 0.5 and maximum 1.5 m. Taking typical speed values for the different wave modes, it is not possible to distinguish between the different wave modes as arrival time differences are small, on the order of a few milliseconds. Hence the different signals are superimposed. Different wave modes are probably superimposed. Measuring at larger distances would help to distinguish between the different modes. However, the strong attenuation limits measurements at larger distance. The wave amplitude and the sensitivity of the sensor would be too low. We conclude that the speeds we measured are those of the fast wave through the ice skeleton which shows low attenuation. Biot's model and earlier studies (Capelli et al., 2016) indicate that our speeds correspond to this waves or are even above whereas the other waves are much slower. Rhe attenuation we measured on the other hand seems to be the attenuation corresponding to the slow longitudinal wave within the pore space. Applying Biot's model to snow and earlier experiments (Capelli et al., 2016) show that the other wave modes have much lower attenuation coefficients and that our attenuation data are in good agreement with these earlier findings.

8.4.6 Constrained modulus

Our results showed high constrained moduli derived from the wave speeds compared to earlier studies performed under laboratory conditions (Gerling, 2016; Scapozza, 2004; Sidler, 2015; Sigrist, 2006). This was in particular observed at lower densities, whereas the agreement was good for higher densities compared to laboratory experiments performed with acoustic emissions or at higher frequencies, i.e. also with a wave pulse (Gerling, 2016). Scatter in our data was rather large as snow with the same density may have different physical properties depending on the grain type. These differences were not considered for this study. Earlier studies performed experiments in the laboratory where snow of the same type can be produced under controlled conditions. We, on the other side, used natural snowpacks. The results were hence of good quality considering these limitations.

8.4.7 Crack propagation speed

The crack speeds were always higher than those derived from the deformation recorded by a high speed camera for the same experiments that were between 31 and 45 m s^{-1} with one higher value of 77 m s^{-1}. However, the error of the speeds determined using particle tracking velocimetry is approx.

± 5 m s^{-1}. If we assume that our error is in the same range or slightly higher, the higher values reported in our studies are plausible.

The measured crack propagation speeds were in good agreement with the results reported by van Herwijnen and Jamieson (2005) and van Herwijnen and Birkeland (2014) who measured the speeds using high-speed photography, i.e. particle tracking velocimetry, for extended column tests (ECT) and PSTs. The results agree well with the speeds determined by van Herwijnen and Schweizer (2011) who determined the speed from seismic signals and the known size of an avalanche and reported 40 m s^{-1}. The agreement is also good with the findings by Johnson et al. (2004) who were able to measure the speed of a whumpf with seismic instruments on the snow surface. Our speeds are at the low end of those reported by Hamre et al. (2014). However, they measured the values from video frames and it is not entirely clear whether these speeds are a mix of wave propagation speeds through the air and the snowpack and crack propagation speeds.

For those cases where it was possible to analyze the high-frequency signal, much higher speeds were measured. It is assumed that these are the actual crack propagation speeds and that the other wave is the collapse wave which is slower due to the inertia of the slab.

8.4.8 Source and sample geometry

In principal, all sources were suited for the performed experiments. The solid explosives were mainly used to better understand the propagation characteristics of waves caused by an explosion for simple geometries as opposed to the complex wave propagation on real-scale experiments as performed by Simioni et al. (2015; cf. Chap. 4). The solid explosives have one disadvantage also at the small scale: The wave spreads spherically from the point of explosion and hits the snowpack. This means that there is no plane wave propagation within the snow block and the measured attenuation is a mixture of material damping and geometrical spreading. However, the differences between two- and three-dimensional expansion are small at the distances from the point of explosion we investigated.

Using the hammer and a steel plate, the produced waves were assumed to be plane. However, due to the layering and imperfections described above, the waves did not propagate perfectly plane. The geometry that was used for the hammer experiments was a block, about 2 m long. Hence, the sample height or the height of the investigated snowpack layer was smaller than the wave lengths (>0.5 m) at the observed frequencies (approx. 1 to 1500 Hz). In addition, the block was higher than the steel plate and the experiments were performed at three depths on the block. This certainly had an influence on the wave propagation as well. However, we are not interested in the propagation and attenuation behavior of a perfectly homogeneous snow sample, but in the overall behavior of a snowpack. Given the rather large scatter observed in laboratory experiments (Capelli et al., 2016)

and the fact that the attenuation coefficients we observed were in the same range as their results, we conclude that our sources and sample geometries were well-suited. The geometry of the sample and the source, and imperfections associated with those, seem to have a minor effect on the attenuation coefficients and propagation speeds we observed. However, there are reflections that lead to additional signals or superimpose the main wave signal.

8.4.9 Test repeatability

Consecutive tests with the same setup often showed variable results. In particular for the hammer experiments, this could not be explained by non-elastic effects. Plastic deformation was certainly happening directly at the plate to a small extent. However, this should not influence the attenuation coefficients between two sensors located some tens of centimeters from the frontal block wall. We conclude that already small differences in the source lead to large differences in the attenuation behavior. Even for laboratory experiments on small samples, the scatter was large for much more consistent sources like piezo-elements or PLFs.

After each explosion, a few centimeters of the front wall were removed due to visible plastic deformation. For these experiments, the charge size, the charge location and the block length were not consistent for consecutive experiments. The attenuation within the block is material dependent and a function of the wave type. Although the differences in the source location were small, this seems to have been sufficient to cause part of the scatter of the attenuation coefficients.

8.4.10 Measuring setup

The same measuring setup was used as in Simioni et al. (2015). One or three systems were used with three or nine accelerometers. The system worked reliably. It was well-suited to use at study sites with good accessibility. However, the measuring system was not ideal for experiments at remote study sites due to the large and heavy casing of the systems especially manufactured for solid explosive testing. The system itself including the hardware filters has small dimensions and would easily fit into a small casing portable in a backpack.

The accelerometers were well-suited for all types of experiments described here. The main difficulty was the choice of the best-fitting sensor regarding maximum range and sensitivity. To only determine the wave speeds, the maximum range is unimportant but a sufficiently high sensitivity is desirable. To determine the attenuation coefficient, a sufficiently large peak range is important. A limiting factor in the measurement setup is the distance, up to which reasonable measurements are possible. The strong attenuation prevents measurements at larger distances. This was already observed in the lab for small samples and low energy sources (Mayer, 2011).

For very low densities, a firm coupling of the foam cylinders to the snowpack was sometimes difficult to achieve. Inserting the sensors into medium density snow did not cause any problems. For high densities, an instrument to pre-drill a hole, similar to Simioni et al. (2015; cf. Chap. 4) but smaller and better portable would be advantageous. In addition, smaller sensors would be convenient.

8.5 Conclusions

During two winters we performed in situ wave speed and attenuation experiments on snow blocks of different geometries, cut out of the natural snowpack.

Experiments were performed using small solid explosive charges and hammers with a steel plate as source. We measured acceleration wave forms, amplitudes and wave arrival times at different distances from the source and different depths within the snowpack. From the signals we derived an energy equivalent which was then used to determine the attenuation of the wave energy parallel and perpendicular to the propagating main wave. Furthermore, we calculated the wave propagation speed through the snowpack from the arrival times.

The measured attenuation did not depend on snow density regardless of the direction of the measurement compared to the main propagation direction or the source. Within the investigated range of snow densities, the attenuation we measured corresponded to the attenuation of the slow wave within the ice pores which is in good agreement with earlier findings. However, increasing attenuation with increasing density was not observed. The attenuation does not correspond to the fast wave within the ice skeleton that is much less attenuated than our results suggest.

The attenuation using solid explosives was slightly stronger on average than for the experiments with a hammer. We assume that this result is mainly due to the effect of the spherical expansion caused by the solid explosive. However, the wave was not perfectly plane for the hammer experiments mainly due to the strong layering of the snowpack. This finding is supported by the fact that there was a wave component perpendicular to the main wave propagation direction caused by reflections. The attenuation measured under moist snow conditions was similar to the one under dry-snow conditions. Scatter was large, mainly for the experiments involving solid explosives. This was probably due to plastic effects caused by the strong solid explosive wave. Overall attenuations were in the range of 5×10^{-2} to 0.7 dB cm^{-1}. These values are in good agreement with previous studies which was almost exclusively performed under laboratory conditions. However, comparison with other studies is difficult due to different measuring techniques used resulting in the attenuation of different wave types. Independent of the measuring method, in all previous studies scatter was as well rather large. Our field experiments on the attenuation of waves within similar snowpack layers and through different layers are a good alternative to sophisticated laboratory experiments.

Although the measurements provided attenuation coefficients for entire (or parts of) snowpacks, the findings agreed well with laboratory experiments. The combination of laboratory experiments on homogeneous small scale samples and field experiments is a good way to understand the processes within a snowpack caused by wave propagation.

The densities in our experiments were in the range of earlier studies. The results suggest that we measured the speed of the fast wave through the ice skeleton. The wave propagation speeds were linearly dependent on snow density with increasing speeds for increasing snow densities. The values of constrained modulus derived from density and wave speed were in good agreement with earlier results also obtained with dynamic measuring methods. The modulus was on the order of 100 MPa for a snow density of about 250 kg m^{-3}.

Our results suggest that the decay of the slow wave and the speed of the fast wave were measured. Although we only observed one major wave, this is not unreasonable. The arrival time difference at short distances is small, such that the different wave types are superimposed. Unfortunately, they cannot be distinguished with experiments using longer blocks as the waves are attenuated too strongly to be detected at far measuring locations.

The measured crack propagation speeds were in the range of earlier findings derived with different methods. The results show that crack propagation speeds can be measured with simple field methods. However, for snow blocks of the size of propagation saw tests, the PTV method is probably more accurate due to the more precise determination of the bending of the slab. Still, our method has potential, in particular to determine crack speeds at larger ranges, where the PTV method is not feasible. Some of the results indicate that the speed of the collapse wave as observed in the PST experiments with the PTV method might not be identical to the real crack propagation speed.

Our experimental results support previous findings that the effect of an explosion strongly decreases with depth within the snowpack and distance from the explosion as observed by Simioni et al. (2015; cf. Chap. 4). The results pave the way for modeling wave propagation in snow which has shown to be difficult for large scale explosions.

9 Conclusions and outlook

9.1 Summary of conclusions

The aim of this study was to assess the effect of various artificial avalanche triggering methods by developing a measuring system, measuring wave propagation in snowpacks caused by explosions, and recording and evaluating failure due to explosions.

During three winter seasons we were able to collect and analyze a large dataset to address our objectives. In the following we summarize the findings first with regard to the three main objectives and then report other significant results.

(a) Develop measuring equipment and layout to assess the effect of explosions

We developed a modular data acquisition system for one to nine measuring locations with simultaneous data recording. The systems were robust but still handy enough to use one system at a time at remote field sites. Each system was built such that several acceleration sensors, microphones and other sensors could be used. Triggering was either performed manually or automatically. LEDs were used to indicate the trigger time to the cameras that monitored failure. Batteries were used to provide the systems with power and to reduce the number of cables. Data transmission was performed wirelessly or over network cables. Depending on the data transmission, only one or two different cables were required between the systems. Data was acquired using a simple laptop.

Depending on the needs, we used a different number of systems ranging from one for small scale experiments investigating crack propagation and attenuation to six plus three for days when we performed gas exploder and solid explosive experiments.

Biaxial sensors in foam cylinders were developed to measure snowpack accelerations in the snowpack. Air overpressure was measured using low-cost microphones. For the solid explosive experiments, the ignition signal was taken from the blast machine as zero time. The developed measuring layout proofed successful for the comparison of different types of explosions under repeatable and directly comparable conditions.

(b) Quantify wave propagation above and in a snowpack caused by explosions

In principal, we performed two types of experiments. First, we report on the small scale experiments to study wave propagation characteristics. Second, we describe our findings on the large scale experiments where we assessed the effect of explosions on a snowpack in view of artificial triggering of avalanches.

For the small scale experiments we adapted the above-described measuring equipment and layout. We conducted experiments at different test sites using solid explosives and hammers as sources to develop a measuring procedure. We measured accelerations and snowpack densities and performed experiments within layers of similar

snowpack characteristics and perpendicular to the snowpack layering. Using automatic picking, we determined the start of the signals and determined wave velocities depending on density. This method employing elastic waves is believed to be the only measurement yielding the true constrained modulus without any plastic deformation. Average wave speeds ranged between approx. 500 and 1000 m s^{-1} which corresponds to the speed of the longitudinal wave in the ice skeleton. We used the acceleration signals to derive wave attenuation within the snowpack for the first time in field experiments. We showed that we measured the amplitude of the slow wave in the pore space due to the strong attenuation but the speed of the fast wave in the ice skeleton. Attenuations were in the range of 0.1 to 1 dB cm^{-1} with no density dependency which is in good agreement with earlier studies. Due to the strong attenuation, measurements could not be performed at larger distances and hence the amplitude and shape of the fast wave could not be distinguished from the slow wave. The small scale measurements also yielded an exponential law to describe the constrained modulus with density. The values were high for low densities and in agreement with other measurements at higher densities in the range of a few hundred MPa also using pulse propagation. The small scale field experiments were a good supplement to complex lab experiments and bridge the gap between the lab and large scales.

Some of the small scale experiments were performed concurrently with experiments on the crack propagation propensity of the snowpack. We used our measuring equipment to measure the wave caused by crack propagation with accelerometers and picking of the start of the arriving wave. Crack propagation speeds slightly exceeded the speeds determined using particle tracking velocimetry with values in the range of 20 to 60 m s^{-1}. For some tests the crack propagation speed was significantly higher than what had been reported so far in the range of a few hundred m s^{-1}. The analysis of the signals showed that there were different waves measured. They were mainly superimposed but for some experiments a wave with a steep first flank was observed at the beginning of the signal. Based on these preliminary data, we suggest the signal included different processes: A wave corresponding to the advance of the crack in the weak layer and a second wave corresponding to the settling of the slab due to weak layer failure (collapse wave).

During three winter seasons we performed large scale experiments – at the scale of several tens of meters – using solid explosives and a mobile gas exploder at Hinterrhein. The results show the strong decay of the air pressure above a snowpack compared to other underlying materials. The accelerations and the derived parameters decayed strongly with distance from the point of explosion and depth within the snowpack with

values between x^{-1} and x^{-2} with stronger decays for the energies, where x is the distance or the depth. Air pressure speeds exceeded the speed of sound in the vicinity of the explosion, i.e. up to around 20 m indicating a shock wave. Accelerations in the snowpack were in the region of a few hundred m s^{-2} at close distances and depths down to approx. 1 to 2 m s^{-2} at larger distances and depths. We performed the first experiments with a mobile prototype gas exploder running on oxygen and propane. This gas exploder caused a directed explosion similar to some types of operational avalanche control systems. The influence of the gas exploder incline on the air pressure above the snowpack was small. Within an angle of approx. 36° from the exploder axis, air pressures and snowpack accelerations did not decrease significantly with the angle from the exploder axis. At 90° from the exploder axis, air pressure values were smaller at shorter distances compared to the exploder axis but equaled those values at larger distances due to a less distinct decay. The analysis of these air pressure data revealed that the isolines of equal air pressure were elliptically-shaped close to the point of explosion and became circular-shaped at large distances (Appendix B). Air pressures and all derived parameters were similar for the different explosions comparing the maximum gas mass used to common solid explosive charge sizes. Accelerations and derived parameters were similar for the directed gas and spherical explosions. We developed scaling factors for the influence of charge and gas masses.

Furthermore, we recorded weak layer failure in snowpacks caused by explosive loading. We used high-speed cameras that had been applied for crack propagation measurements within the snow pits where we installed our acceleration sensors. Because of different snowpack conditions during two seasons we were able to observe two different kinds of snowpack failure. Due to the time delay between the arrival of the air pressure wave at the surface and the failure of the weak layer at the point of observation we concluded that one type of failure was caused by weak layer failure closer to the point of explosion and subsequent crack propagation. For the experiments where the failure was almost immediate after the arrival of the air pressure wave, it was clear that the failure had been caused directly by the air pressure wave hitting the snowpack close to the point of observation. The latter failure was mainly observed for stable snowpack conditions where the snowpack was not prone to crack propagation and up to a maximum distance of 20 m. The second scenario might be representative of the case when the absolute effect of an explosion is important to trigger a possible weak layer that is not present close to the point of explosion. The detection of failure was difficult due to the blowing snow and the strong air pressure caused by the explosion that slightly moved the cameras.

(c) Measure the effect of an explosion caused by operational avalanche control systems on snowpacks and ground

We performed measurements near an operational gas exploder to measure the air pressure and snowpack accelerations. The results agreed well with the flat field experiments in the exploder axis with similar air pressures in the range of several kPa. However, at 90° from the gas exploder axis, the decay was much stronger than in the field. The differences at the second axis were attributed to the fact that the terrain at the operational gas exploder was not uniform which influenced the air pressure wave propagation. The results obtained with this gas exploder are only representative for cases of similar topography. We therefore concluded that flat field experiments are the best solution to assess the general effect of artificial avalanche release avoiding the influence of the terrain. In addition, experiments on operational systems are very cumbersome and are not recommended further except to perform additional verification on uniform slopes.

Geophones installed in the ground at different distances from an operational gas exploder were used to assess whether an avalanche can be triggered by ground accelerations. Ground accelerations and the derived parameters were small compared to accelerations within the snowpack measured during the flat field experiments. Maximum ground accelerations were in the range of 10 to 0.01 m s^{-2}. The decay with distance of the ground accelerations was stronger than observed for the accelerations within snow as measured in flat field experiments. Scatter was large depending on the depth of the snowpack which has a strong influence on attenuation. The main ground acceleration amplitudes were caused by the wave travelling through the air and the snowpack rather than through the foundation and directly through the ground. We concluded that at distances where avalanches may be triggered by the air pressure wave transferred onto the snowpack, the ground accelerations were insufficient to be relevant for avalanche triggering – unless the stability of the snowpack is so poor that any given additional load may trigger an avalanche. The installation of the sensors on rock and soil showed the strong attenuation behavior of soil and hence the lower probability of failure within a snowpack above soil rather than rock due to ground accelerations.

In addition to the main objectives, other interesting findings can be reported:

(a) Comparison of solid explosives (Appendix A)

Due to the change of the solid explosive type used in fixed avalanche control installations from Alpinit to Riomon T1 during this project, we had to perform comparison tests between the solid explosives to ensure that the results of our main experimental series were applicable to new solid explosives. Although the solid explosives' specifications differed slightly, the results obtained with the different solid explosives were in very good agreement. This could even be confirmed for experiments performed during different winters with different snowpack conditions. In summary, no significant difference was found between the effects of the two types of solid explosives.

(b) Modeling of wave propagation (Appendix E)

We compared the results of our experiments to a complex model where we provided the data and part of the discussion. The complex model performed fair. Still there were some issues mainly due to the snowpack properties used for the model: Whereas the wave forms measured agreed well with the modeled waveform of the slow wave in the pore space, the amplitudes of the accelerations were significantly overestimated by the model. The reason probably is the parameterization, based on density only, of the mechanical properties of snow needed to solve the Biot's equations.

9.2 Outlook

Whereas the thesis presents new and important findings on the effect of explosions and wave propagation within snowpacks, we suggest the following points to be considered for future research:

1) Improving the measurement equipment
    - The wireless connection only worked flawlessly during the first main experimental series at the field site of Hinterrhein. During later experiments the network often malfunctioned probably due to interference with local networks. This was the reason for changing to network cables. To simplify the experiments and the need for cables, it would be desirable to set up a fast and stable wireless connection between the data acquisition systems.
    - For the solid explosive experiments we were able to determine the start point of the explosion using the trigger impulse. This did not work for the gas exploder experiments as the ignition of the spark plug was delayed and as it was not clear whether the gas mixture was triggered with the first ignition.

      In addition, we planned to investigate the accuracy of the measuring system using a shaker table. Unfortunately, no suitable shaker table could be organized for this study. It would be of interest to assess the simultaneity of the system and the performance of the microphones and the accelerometers.
    - The data acquisition system should be built smaller and handier for small scale field experiments at remote locations for which the systems were not initially designed.
    - The cameras used were chosen to record high frame rates at low costs with the possibility of triggering the cameras wirelessly. As the wireless connection did not work over the required distance as opposed to the camera specifications, cameras are needed that have a high frame rate and can be triggered over the data acquisition system.

2) *Additional experiments*
    - Additional large scale experiments under unstable snowpack conditions and less dense snowpacks would be of interest to assess weak layer failure and the influence of low-density snow on wave propagation in more detail.
    - It would be ideal to have measurements at the back of the gas exploder and at angles where experiments were obstructed due to the counterweights. However, this would require a different anchoring of the gas exploder and a different suspension to have an undisturbed snowpack at the back of the exploder.
    - The gas mass measurement and calculation should be assessed in more detail as we observed gas volumes that were exceeding the actual pipe size. More detailed

measurements or calculations are required. Sensors as flow meters were not an option due to the required extremely fast response time and the resulting high costs.

- Small scale experiments should be performed under snowpack conditions where large parts of the snowpack are uniform including similar densities and grain types.
- Additional small scale experiments are desirable with many acceleration sensors and possibly load sensors as a basis for understanding stresses and stability in more detail.
- To investigate the different wave types we observed in crack propagation experiments, it would be advantageous to perform additional experiments also on longer snow beams to investigate whether these two wave types can be detected for all experiments and whether the wave with the steep flank is travelling faster and can be measured at the wave front at larger distances.

3) Modeling

- Now that experimental data are available, the next big and most important step is to assess the effect of the explosions on snowpack stability. This has to be done using numerical models, as wave propagation in snow is fairly complex. Many FE models did not work due to the following reasons: All models lacked the probability of modeling wave propagation in porous media unless the differential equations are integrated by the user. The models using continua were lacking good possibilities to implement wave dependent damping and were only able to predict one wave type. However, the longitudinal wave of the second kind might be the most important for stability considerations which would again justify the use of a continuum. A special FE code for explosions encountered issues with modeling a low density and low strength material such as snow. The porous model described before works with some limitations as the implementation of more complex geometries is difficult and the model is not ideal to model an explosion. It is clear that a suitable model requires simplifications of the problem. Yet it is not known which approach is the best. An ordinary FE code would be preferred as this would also give the opportunity to engineering consultants to perform calculations before installing expensive fixed avalanche control installations.
- The additional small scale experiments mentioned above should be used to investigate stability and snowpack stresses more accurately.

Appendix A Comparison of solid explosives

A.1 Introduction

During the flat field experiments at the study site of Hinterrhein, we tested solid solid explosives as commonly used in fixed avalanche control installations and for conventional charges. During the winter season 2013-2014, when the main experiments using solid explosives were performed with different charge sizes and elevations, the solid explosive Alpinit was the only solid explosive used in fixed avalanche control installations. Alpinit is a slurry explosive. For different reasons, the solid explosive type was changed for the winter season of 2014-2015. Since then, Riomon T1, a powder explosive is used in remote avalanche control systems. It was therefore required to compare the effect of the different solid explosives to evaluate whether the tests from the first and the following winters could be analyzed jointly.

A.2 Specifications of solid explosives

Riomon T1 and Alpinit are two different solid explosives regarding their chemical properties: Whereas Alpinit is a slurry with some moistness, Riomon T1 is a powder explosive that is dry. The two solid explosives differ slightly in their explosives' properties (Table A-1). Alpinit has a slightly higher density, a higher detonation speed and a higher explosive heat per kg. This should result in a higher energy release per time.

Table A-1: Solid explosive characteristics of Riomon T1 (www.maxam-deutschland.com)

Explosive name	Riomon T1	Alpinit
Explosive type	Powder	Slurry
Explosive density (kg m^{-3})	1'100	1'200
Explosive heat (kJ kg^{-1})	4'082	5'610
Detonation speed (m s^{-1})	4'600	4'900

A.3 Test procedure

During the experiments where the effect of solid explosives on the snowpack was tested (Simioni et al., 2015; cf. Chap. 4), the two different solid explosives were compared. This was done during the period when the old solid explosive (Alpinit) was still on stock and the new solid explosive (Riomon T1) was already available. The two solid explosives were not delivered in exactly same charge sizes. Resizing the charges to equal masses was not feasible. The geometries of the charges were very similar, both capsule-shaped with similar lengths. The lengths ranged between 420 and 460 mm and the diameter between 75 and 110 mm. We used similar charge sizes of different explosives for consecutive shots to be able to compare the explosives under similar conditions. The results were

scaled with the cube root of the charge size according to Cooper (1996) and Simioni et al. (2015; cf. Chap. 4). For consecutive shots, the charges were placed at the same elevation.

A.4 Data and results

We performed more than 30 experiments with the different solid explosives on the same days. From these experiments, we obtained 9 acceptable air pressure measurements at different distances from the point of explosion with the explosive Alpinit and 19 with the explosive Riomon T1. From the air pressure signal, we calculated the frequency content, the steepest increase of the air pressure per time and an equivalent of the energy of the air pressure wave according to Simioni et al. (2015; cf. Chap. 4), Simioni et al. (2016c; cf. Chap. 5) and Simioni et al. (2016e; cf. Chap. 8). The results were used to fit power law relations for the different measures with the scaled distance from the point of explosion as in e.g. Simioni et al. (2015; cf. Chap. 4).

In addition, we compared the results of the different solid explosives over two different seasons with different snowpacks. We used the results from the first main experimental season 2013-2014 Simioni et al. (2015; cf. Chap. 4) and the results were we compared the solid explosive effect to the effect of a gas exploder on flat terrain during the winter 2015-2016.

The maximum air pressure showed similar signals for the two different explosives for two consecutive tests (Fig. A–1). The frequency content of the air pressure signal was very similar for two consecutive tests (Fig. A–2).

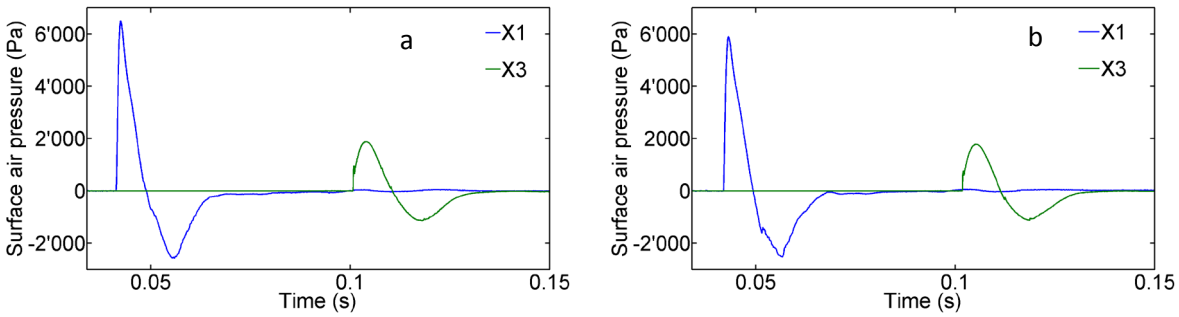

Fig. A–1: Example of the air pressure signal for two consecutive tests using (a) Alpinit and (b) Riomon T1. Data from 17 Feb 2015, tests #3 and #4.

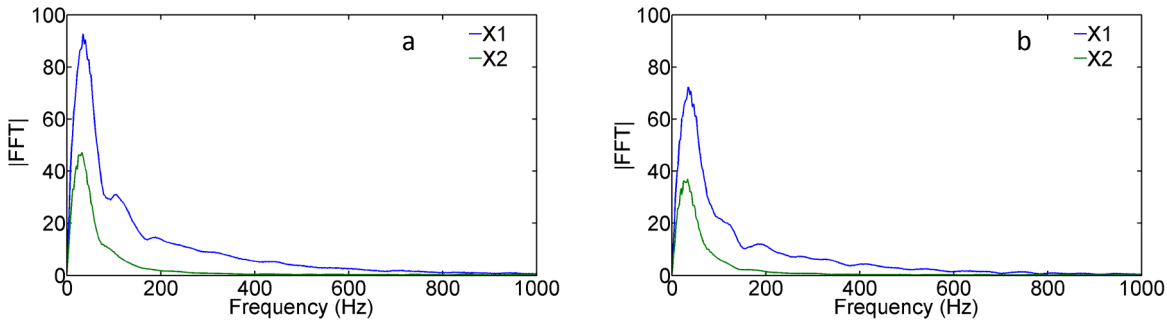

Fig. A–2: Example of the air pressure frequency content for two consecutive tests using (a) Alpinit and (b) Riomon T1. Data from 17 Feb 2015, tests #3 and #4.

The decay of the different measures with distance from the point of explosion was similar for the test series dedicated to the comparison of the different solid explosives (Table A-2, Fig. A–3, Fig. A–4 and Fig. A–5). Whereas the maximum air pressure and the equivalent of the wave energy showed small scatter, there was larger scatter observed in the data of the maximum increase per time $(dP/dt)_{max}$.

Table A-2: Power law coefficients for the different solid explosives determined from specific test series to compare different solid explosives during the winter 2014-2015 for the maximum air pressure (p_{max}), the steepest increase of the air pressure per time $(dP/dt)_{max}$ *and the energy equivalent of the air pressure wave.*

	a		*b*	
	Riomon T1	Alpinit	Riomon T1	Alpinit
p_{max}	5.58	5.56	1.66	1.63
$(dP/dt)_{max}$	8.44	9.15	1.35	2.03
energy	7.91	7.85	2.48	2.39

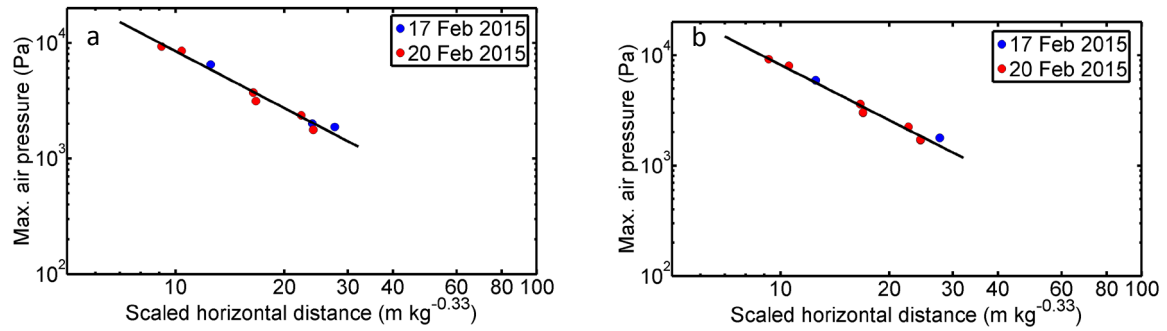

Fig. A–3: Comparison of the decay of the maximum air pressure for (a) Alpinit and (b) Riomon T1 for the test days in winter season 2014-2015.

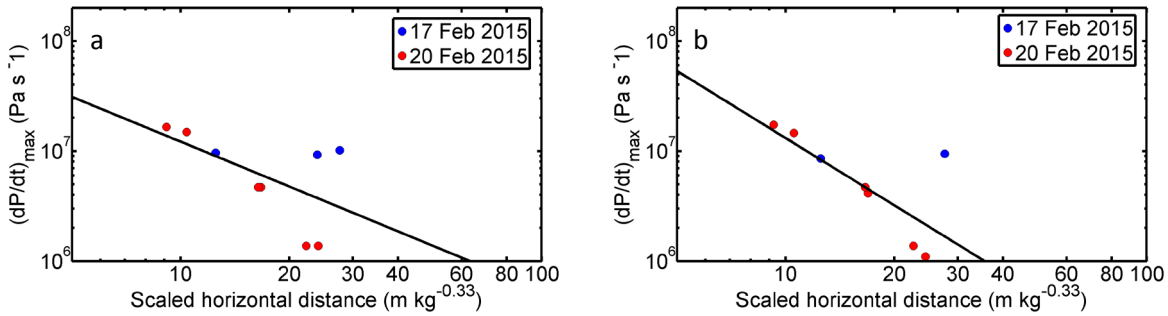

Fig. A–4: Comparison of the maximum air pressure increase per time for (a) Alpinit and (b) Riomon T1 for the test days in winter season 2014-2015.

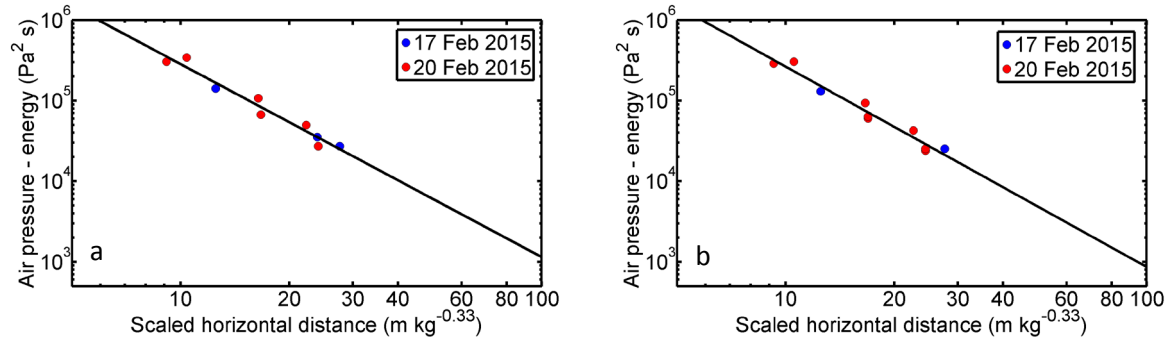

Fig. A–5: Comparison of the energy equivalent of the air pressure wave for (a) Alpinit and (b) Riomon T1 for the test days in winter season 2014-2015.

The results compared between the two different seasons showed larger differences than for the dedicated measuring series, but are still in good agreement (Table A-3).

Table A-3: Power law coefficients for the different solid explosives determined from the main experimental series during the winter 2013-2014 (Alpinit) and 2015-2016 (Riomon) for the maximum air pressure (p_{max}, the steepest increase of the air pressure per time (p_{diff}) and the energy equivalent of the air pressure wave.

	a		*b*	
	Alpinit	Riomon T1	Alpinit	Riomon T1
p_{max}	5.61	5.9	1.70	1.88
$p_{,t\ max}$	8.57	9.30	1.51	1.92
energy	8.05	8.12	2.56	2.53

The results showed that although there are differences between the two solid explosives' properties, the differences in the recorded air pressure are very small, i.e. the agreement between the different solid explosives is extremely good. For the dedicated test series, the power law coefficients are almost equal. For the other comparison, the power law coefficients were very similar. The strong effect of the snowpack on the pressure wave propagation seemed to mask the effect of the different solid explosive types and even the differences in charge elevation. Differences

in the snowpack as observed between the winters of 2013-2014 and 2015-2016 did only result in small differences in the recorded air pressure response. The only differences – within the same type of solid explosives – were observed for the maximum increase of the air pressure per time. The reason for this is unclear.

A.5 Conclusion

We performed comparison tests with different solid explosives since the type of solid explosives used in fixed avalanche control installations changed in the course of our study. The results showed that there was no significant difference between the different solid explosives used although their specifications slightly differ. The fitted power law relations showed that the decay of the maximum air pressure, the steepest increase of the air pressure per time and the equivalent of the air pressure energy were very similar for consecutive tests performed on the same day and still similar for experiments performed on different test days. The reason is probably that the influence of the snowpack properties on the attenuation of the air pressure wave above snow is so large that the small differences between the two types of solid explosives become unimportant.

Appendix B Air pressure isolines

B.1 Introduction

In Simioni et al. (2015; cf. Chap. 4) and Simioni et al. (2016c; cf. Chap. 5) we investigated the effect of an unconfined explosion using solid explosives and a direct gas explosion. The aim was to derive the air pressure and the effect within the snowpack at different distances from the point of explosion and different depths within the snowpack. We reported that experimentally the effect of a directed gas exploder did not change within a forward cone with an aperture of approx. 70°. This angle was limited by the counterweights of the gas exploder. To overcome this problem we performed experiments above bare ground in the gas exploder axis and along an axis at 89° from the exploder axis which was not feasible under conditions with a snowpack. We used these results to derive isolines of equal pressure above the snowpack to compare the affected area of different types of explosions.

B.2 Methods

For the solid explosive, the method was straight-forward: We used the power law relation describing the decay of the maximum air pressure with distance from the point of explosion. The plot of this relation at any given angle resulted in isolines around the explosion.

For the gas exploder results, the method was more complex: We calculated the relation between the air pressure above bare ground with distance along the gas exploder axis and the second axis at 89°. Although the decay of the air pressure is significantly different between conditions with snow and bare ground, the relation between the air pressures at different angles from the exploder axis is assumed to be identical, as the snowpack properties should not be anisotropic in the two different horizontal directions. The relation derived above bare ground was then used to calculate the air pressure above snow at 89° from the air pressure above snow along the exploder axis. Together with the maximum angle at which we measured above snow, we derived air pressure data in a horizontal plane with the decaying air pressures with distance from the point of explosion. We used an interpolation of simple complexity (function ‘griddata’ implemented in Matlab 2013b). Using a less complex interpolation method resulted in unrealistic isolines, functions of higher complexity did not show satisfying results because of the few data points available.

B.3 Data and results

The fits of the maximum air pressure for the gas explosion from Simioni et al. (2016c; cf. Chap. 5) were used to describe the decay of the air pressure with distance from the point of explosion (Table B-1: Power law coefficients a and b of the maximum air pressure above snow derived from the experiments using the mobile gas exploder along the exploder axis (0°) and the largest angle from the exploder axis investigated (36°). and Table B-2). We used 1.9 kg gas, the maximum mass, and

4.8 kg solid explosives for the comparison as this gas mass correspond best with a 4.8 kg charge that is often employed in fixed avalanche control systems. The smaller parameter *a* along the axis at 89° led to lower air pressures close to the point of explosion. However, also the parameter *b* was smaller along this axis which then led to a circular isoline at some distance. This means that close to the point of explosion, the isolines were oval-shaped (Fig. B–1) assuming a lower effect at the back of the exploder as observed during the experiments on the operational gas exploder Simioni et al. (2016d; cf. Chap. 6). At larger distances, the isolines were almost circular-shaped and corresponded to the shape of an unconfined explosion (Fig. B–2). Far from the point of explosion, there was a dent in the isoline at 36° from the exploder axis. This is due to the fact that the values at 89° were derived from the relation above bare ground.

Table B-1: Power law coefficients a and b of the maximum air pressure above snow derived from the experiments using the mobile gas exploder along the exploder axis (0°) and the largest angle from the exploder axis investigated (36°).

	a	*b*
0°	5.69	1.68
36°	5.5	1.66

Table B-2: Power law coefficients a and b of the maximum air pressure above bare ground derived from the experiments using the mobile gas exploder along the exploder axis (0°) and the largest angle from the exploder axis investigated (89°). The last row (89°/0°) gives the power law for the relation between the two axes. Note the negative sign of b in the last row due to the definition of the power law ($p = 10^a \cdot x^{-b}$).

	a	*b*
0°	5.12	0.99
89°	4.47	0.66
89°/0°	0.22	-0.33

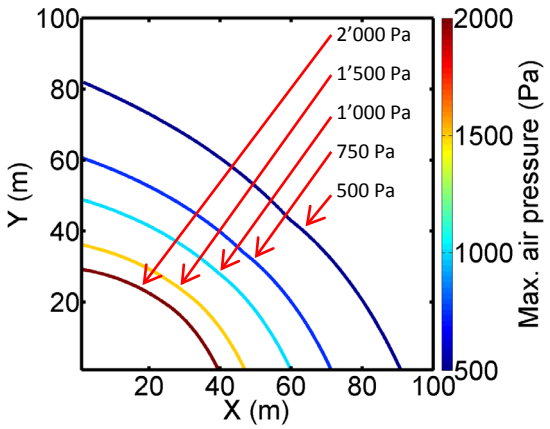

Fig. B–1: Topview of the isolines indicating the maximum air pressure from the experiments with a gas exploder scaled for a gas mass of 1.9 kg (largest shot). The X-axis(unscaled) is oriented in the direction of the gas exploder axis and is the symmetry axis. The gas exploder is located in the bottom left of the figure. Values to the back are not given as no measurements could be performed at the back of the gas exploder.

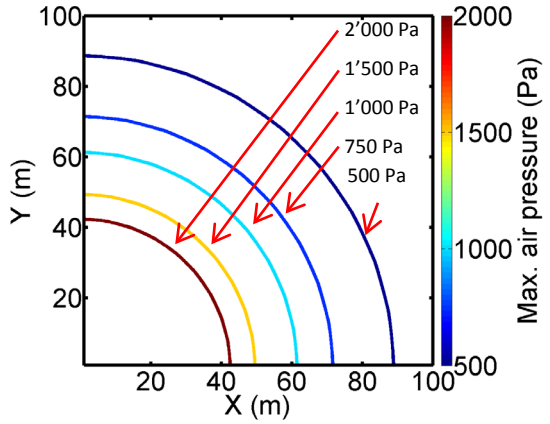

Fig. B–2: Topview of the isolines indicating the maximum air pressure from the experiments with solid explosives scaled for a solid explosive charge of 4.8 kg Riomon T1. The isolines are circular-shaped. The charge is located in the bottom left of the figure. X- and Y-axes (unscaled) are symmetry axes.

B.4 Conclusion

Based on the results of the gas exploder and the solid explosive experiments we determined the area affected with at least a certain air pressure. We showed that for the gas exploder, the isolines of maximum air pressure were oval-shaped up to a certain distance (about 80 m) and then circular-shaped as experienced with unconfined solid explosives. As the accelerations and other parameters may well be approximated with the decay of the maximum air pressure (Simioni et al., 2016c; cf. Chap. 5), these results also give an idea on the impact of the air pressure wave within the snowpack.

It is crucial to know that the absolute maximum air pressure value at a certain distance from the point of explosion is in most avalanche situations not the most critical parameter. To release an avalanche, weak layer failure and subsequent crack propagation are required (cf. Chap. 1). It is therefore sufficient in many situations to fail a weak layer at a shorter distance from the point of

explosion. In some situations the snowpack may not be prone to crack propagation at short but at larger distances or a remote snowpack may be detached from the snowpack around the explosion due to rocks or other terrain features. In these cases, the absolute values of the maximum air pressure or one of its derivatives at a large distance may be decisive. However, the impact beyond 100 m is rather small (surface air pressure < 400 Pa) and likely not sufficient to trigger an avalanche except under very unstable conditions – when typically the spatial variations in stability at the slope scale are not particularly large. Hence, additional points of explosion may be required.

Appendix C Assessing weak layer failure and changes in snowpack properties due to avalanche control by explosives

Published as 'Simioni, S. and Schweizer, J., 2013. Assessing weak layer failure and changes in snowpack properties due to avalanche control by explosives. In: F. Naaim-Bouvet, Y. Durand and R. Lambert (Editors), Proceedings ISSW 2013. International Snow Science Workshop, Grenoble, France, 7-11 October 2013. ANENA, IRSTEA, Météo-France, Grenoble, France, pp. 775-778.'

Abstract

Avalanche control by explosives is among the key temporary preventive measures and today fixed avalanche control installations are widely used. Hitherto, little is known about the effect of a blast onto the snow cover. In order to optimize charge location and type it is important to know what the processes caused by an applied load from an air blast wave onto the snow cover are and whether a weak layer is likely to fracture. In the winter 2012-2013 we performed first field experiments on a flat site with a rather uniform snow cover. Cameras located in snow pits capturing the pit wall allowed for recording the blast wave and detecting possible weak layer failure. Accelerometers were used to record the waves penetrating and propagating through the snowpack. Accelerations were strongly attenuated with depth within short distances in the wet snow cover. Consecutive tests did not influence acceleration amplitudes. The video images suggest that the crack initiated near the detonation point and propagated from there to the location of observation (snow pit). The weak layer did not appear to fracture due to the direct impact of the air pressure wave penetrating the snowpack at the snow pit location.

C.1 Introduction

Avalanche control by explosives is among the key temporary preventive measures. An explosion may trigger an avalanche due to the air pressure wave penetrating the snowpack or by ground accelerations. A weak layer can fail due to one of these mechanisms. Past experiments show that blasts above the snow surface are most effective in triggering avalanches (Gubler, 1977). With a charge position above the snow cover, accelerations within the snowpack increase significantly with increasing height of the detonation point as reported by Bones et al. (2012) for short distances from the blast. An air pressure wave reaching the snow surface is partly transferred into the snowpack. Biot's theory indicates that there exist different types of waves within the snow cover and that impedance of a snow cover and the adjacent atmosphere have similar values for low density snow (Johnson, 1982). Air pressure waves penetrate a dry snow cover almost unchanged whereas amplitudes are strongly attenuated under wet snow conditions (Gubler, 1977). Recent numerical modelling confirms past experimental findings such as blast height influence and provide insight into probable snowpack response and failure mechanism (Miller et al., 2011).

The effectiveness of avalanche control depends on the stresses and strain rates caused by the penetrating waves and on snow stability, i.e. the slab and weak layer properties at the time of applying the control method.

van Herwijnen et al. (2008) showed that particle tracking velocimetry allows to record and characterise fracture behaviour of a weak layer.

The aim of this study was to characterise weak layer failure and wave propagation within the snowpack caused by detonation of an explosive charge and to improve our understanding of the processes that cause fracture. We installed video cameras, if available with high speed recording, within snow pits at different distances from an explosion in a plane in order to record possible weak layer failure by avalanche control during two test days in February and April with dry and wet snow conditions, respectively. In addition, we used accelerometers to characterise the waves penetrating the snowpack.

C.2 Methods

C.2.1 Study site

The avalanche control experiments were performed at the military firing range in Hinterrhein (Switzerland) at an elevation of 1680 m a.s.l. (Fig. C–1). The plane, level field was chosen to allow repeated measurements under similar snow conditions. The study site is suitable for performing experiments with different avalanche control methods in parallel with short time delay.

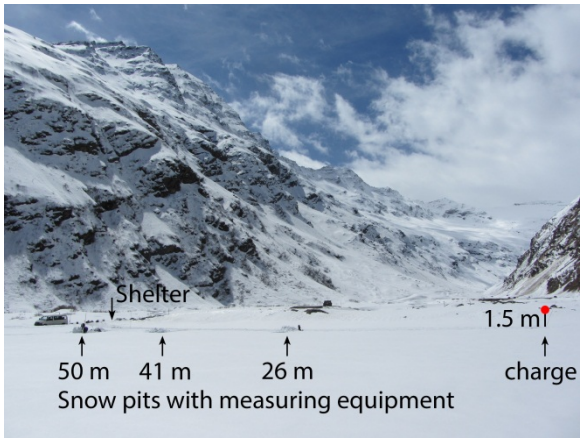

Fig. C–1: Overview of the study site at Hinterrhein showing distances of the snow pits from the detonation point and height of the charge above snow surface. The snow pit at 15 m is not shown since it was dug after the first experiment.

Inclined slopes would not allow for such tests because of the avalanche danger when entering the site to install measuring equipment and because of the potential loss of measuring equipment in the case of triggering an avalanche.

During winter 2012-2013, snow depth at the nearby observation station Splügen usually was below average and reached 70 cm on the test days at the firing range. Manual profiles including density measurements were taken on the days of the experiments, as well as SMP profiles.

C.2.2 Explosive charges, detonator and triggering

A widely employed explosive in avalanche control in Switzerland and in particular in fixed avalanche control installations was used for this tests (Table C–1).

Table C-1: Explosive characteristics

Explosive name	Alpinit
Explosive type	Slurry
Explosive mass (kg)	4.25
Explosion heat (kJ/kg)	5610
Detonation velocity (m s^{-1})	4900

Electric detonators were used for these experiments for safety reasons instead of pyrotechnic detonators that are otherwise commonly used.

Charges were mounted on a pole approximately 1.5 m above the snow surface which is below the height of best effectiveness for explosions above the snow surface (Gubler, 1977; Johnson et al., 1994).

C.2.3 Measuring equipment

Snow pits were dug at different distances from the detonation point, slightly offset in order to not disturb wave propagation caused by the preceding snow pit.

Commercially available SLR and compact cameras with acquisition rates between 24 and 250 frames per second were installed in snow pits aiming at the pit wall parallel to the direction of the propagating pressure wave (Fig. C–2). The cameras were triggered manually.

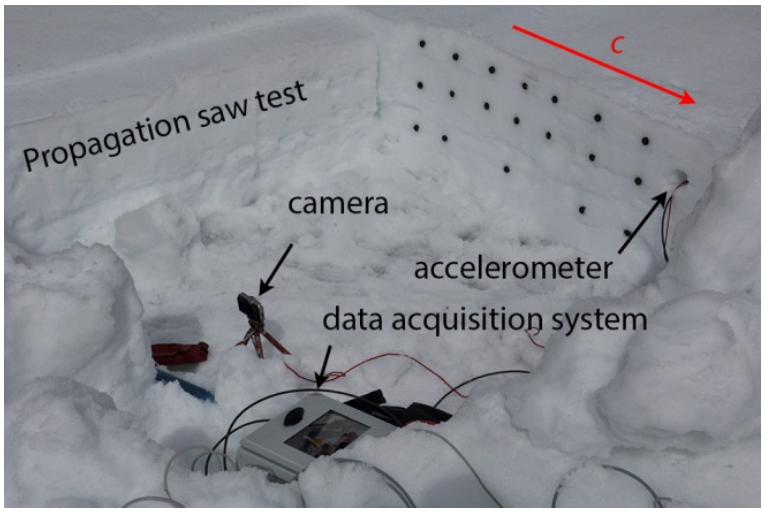

Fig. C–2: Snow pit showing measuring equipment, direction of air pressure wave with velocity c and a stability test to assess crack propagation propensity.

Acceleration sensors or geophones were buried at different distances from the detonation point at different depths within the snow cover to measure snow accelerations or snow displacement velocities, respectively. A microphone was used for one series of experiments to measure air pressure at the snow surface. Data acquisition was performed with National Instruments cDAQ systems (Fig. C–2).

Snow micro-penetrometer (SMP) measurements (Schneebeli and Johnson, 1998) were performed before and after the experiments along a line starting from the detonation point in a certain interval. However, due to malfunctioning of the instrument and possibly effects of small scale spatial variability, no results can be reported here.

C.2.4 Processing of the data

The movies allowed to qualitatively assess weak layer fracture and its cause.

Displacements, displacement velocities, accelerations and frequency contents were determined from the accelerometer and geophone data.

C.3 Results and Discussion

During winter 2012-2013, a total of six tests were performed, mainly to evaluate the measuring layout and equipment.

Three tests were performed under dry snow conditions using geophones for all tests and video acquisition with one camera for one test. Geophones were placed at 50 m and a camera at 25 m from the explosion for one test.

Three tests on one day were performed under wet snow conditions using accelerometers, a microphone and three cameras placed in snow pits at distances ranging from 26 to 50 m from the blast. These tests were performed consecutively at the same position.

C.3.1 Snow accelerations

Accelerations from the tests under wet snow conditions showed decay of the amplitude with depth within the snow cover following a power law and were strongly attenuated which is in agreement with results reported by Gubler (1977). Amplitudes were attenuated by as much as 88% within a distance of 0.3 m (Fig. C–3).

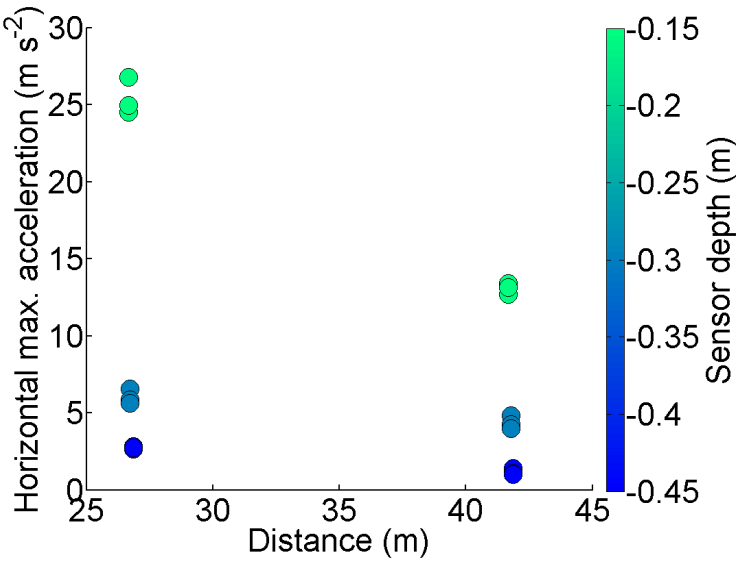

Fig. C–3: Maximum horizontal accelerations at different distances and depths for the experiments under wet snow conditions. The strong attenuation with depth within the snow cover is clearly visible.

Consecutive testing at the same detonation point did not have a significant influence on the measured accelerations within the snow cover at distances between 26 and 50 m in agreement with Gubler (personal communication). A blast 1.5 m above the snow surface only produced a small crater of a few centimetres in depth close to the detonation point. There was no visible plastic deformation at the distances of the snow pits and accelerometers. The snowpack at these distances did not experience plastic deformation that could influence the signal of consecutive blasts. There was large plastic deformation in case of a weak layer fracture, but this could not be seen in the signal.

C.3.2 Weak layer failure

The acquired video for dry snow conditions at a distance of 26 m from the blast revealed that the weak layer did not fracture due to the direct impact of the air pressure wave on the snow surface which caused the loose snow on the surface to be blown away. The weak layer fractured with a time delay after the arrival of this wave. We assume that the stress wave penetrating the snowpack near the detonation point caused the fracture of the weak layer which then propagated along the weak layer. In other words, we assume that the fracture observed in the snow pit was not caused by direct impact of the stress wave penetrating the snowpack at the location of the snow pit but by crack propagation through the weak layer. Typical crack propagation velocities in snow are 20 to 40 m s^{-1} (Birkeland and van Herwijnen, 2012) whereas the air pressure wave travels at supersonic speed close to the detonation point and as an elastic wave at sonic speed at distances at which our measuring equipment was installed.

For the tests under wet snow conditions three cameras were installed at distances ranging from 15 to 50 m from the detonation point (Fig. C–2). The effect of fracture time delay after the

arrival of the air pressure wave could not be shown for these experiments since the arrival of the air pressure wave did not cause any visible snow transport (due to the wet snow conditions) and the microphone that was installed in one of the snow pits was not synchronised in time with the camera. The videos only allow for a qualitative interpretation whether the weak layer had fractured at this distance or not.

The first explosion caused a slab fracture at 25 m and no fracture at further distances. The second explosion caused a fracture (resulting in the collapse of the weak layer) at 15 m and no fracture at larger distances. No camera was installed at 15 m for the first test. The weak layer did either not fracture during the first test, the slab changed within the delay of one hour from first to second test due to wetting, the weak layer did not collapse totally during the first test or the missing support of the slab at the side of the snow pit for the second test had an influence on fracturing.

Particle tracking velocimetry could not be applied possibly due to movement of the camera and distortion of the picture, and due to snow particles blown into the visual field of the camera.

C.4 Summary

We installed accelerometers, geophones and cameras within snow pits in order to characterise wave propagation and weak layer failure within the snow cover on a flat study plot.

Accelerations were strongly attenuated with depth within short distances in the wet snow cover. Consecutive tests did not influence acceleration amplitudes.

The video images suggest that the crack initiated near the detonation point and propagated from there to the location of observation (snow pit). The weak layer did not appear to fracture due to the direct impact of the air pressure wave penetrating the snowpack at the snow pit location.

In the future, we plan to monitor changes in snowpack properties, in particular in density and snow layer thickness before and after an explosion.

Acknowledgment

The study is partly funded by the Swiss Federal Office for the Environment (FOEN).

We thank Werner Preisig of the military firing range for logistical support, Alec van Herwijnen, Lino Schmid and Ben Reuter for help with the field work, and Dan Miller for helpful discussions.

Appendix D Field experiments on weak layer failure and crack propagation due to explosions

Published as 'Simioni, S., Schweizer, J. and Dual, J., 2014. Field experiments on weak layer failure and crack propagation due to explosions. In: P. Haegeli (Editor), Proceedings ISSW 2014. International Snow Science Workshop, Banff, Alberta, Canada, 29 September - 3 October 2014, pp. 185-188.'

Abstract

Avalanche control by explosives is among the key temporary preventive measures and fixed avalanche control installations are frequently installed today. Hitherto, little is known about weak layer failure and crack propagation due to an explosion. In the winter 2013-2014 we performed field experiments on a flat study site. We triggered slurry explosive charges ranging from 4.25 to 5 kg as used in avalanche control at different heights above the snow surface. At three different distances from the point of explosion we measured surface air pressure and accelerations within the snowpack at various depths. Cameras were placed in the snow pits for recording weak layer failure and crack propagation and to monitor the snowpack deformation by particle tracking velocimetry. We assessed whether weak layer failure occurred and if so whether it was caused by crack propagation or the direct impact of the air pressure wave above the point of observation (pit). We compared these results to the data recorded by the accelerometers and microphones to obtain magnitudes required to cause weak layer failure in a given snowpack. First results show loading conditions using explosives required to fail a weak layer given a certain snowpack.

D.1 Introduction

Avalanche control by explosives is among the key temporary measures and fixed avalanche control installations are frequently installed and successfully used today. Pressure waves originating at the point of detonation propagate through the air and are partly transferred into the snowpack. The latter propagate through the ice lattice and the pore space and are supposed to cause weak layers to fail so that an avalanche releases.

In order to assess whether an explosion had an effect on snowpack stability, one has to know whether a possible weak layer has failed. As weak layer failure is associated with collapse (e.g. van Herwijnen et al., 2010), failure can be determined by evaluating vertical snowpack displacement. Snowpack deformation caused by explosions can either be measured by sensors buried in the snowpack (Bones et al., 2012; Gubler, 1977; Simioni and Schweizer, 2013; cf. Appendix C) or by particle tracking velocimetry (PTV) using video cameras (van Herwijnen et al., 2010). These methods usually require a snow pit for device installation but allow for high frequency real-time measurement of the dynamic deformation. A penetration profile acquired with a high resolution snow micro-penetrometer (SMP) would allow for semi non-destructive measurements (Schneebeli and Johnson, 1998) but only just before and after the explosion. Assuming a linear-elastic constitutive behavior of the snowpack, compressional stresses can easily be calculated (Kolsky, 1953) as previously shown by Gubler (1977).

Displacement can either be caused by weak layer failure leading to collapse or snow compaction due to the impact of the explosion. Acceleration sensors and particle tracking

velocimetry are restricted to certain points within the snowpack or at the pit wall, respectively. However, whether weak layer failure occurred or not, can simply be determined by visual inspection of the PTV camera images.

The aim of this study was to compare accelerometer data and PTV images during explosions. Furthermore, it was intended to qualitatively assess weak layer failure. From these results loading conditions required to fail a weak layer given a certain snowpack when using explosives were estimated.

D.2 Methods

D.2.1 Study site

The military firing range in Hinterrhein (Switzerland) was used for the experiments. It is characterized by various plane level study sites at an elevation of 1680 m a.s.l. with a rather uniform snowpack.

Snow depth at the nearby snow observation station of Splügen was above average for the period of the experiments in winter 2013-2014. Snow depth at the study plot reached 180 cm on the test day investigated.

D.2.2 Explosive charges, triggering

An explosive charge usually used in fixed avalanche control installations in Switzerland was employed for these experiments. The slurry explosive charges, ranging from 4.25 to 5 kg were put directly on the snow surface or fixed to a pole elevated between 1 and 3 m above the snow surface to achieve best effectiveness (Gubler, 1976; Johnson et al., 1994). The charges were triggered by electronic detonators.

D.2.3 Measuring equipment

In order to install the measuring equipment, snow pits (usually 3) were dug at different distances from the point of explosion.

Accelerometers were installed by introducing them from the pit wall at different distances from ground zero and at different depths into the snowpack. Microphones were placed at the snow surface to measure the air pressure resulting from the explosion. Data acquisition was automatically triggered at the time of the explosion.

Cameras manufactured by GoPro were placed inside the snow pits and used in high speed mode to record the pit wall which was equipped with markers. This allowed for recording the displacement within the snowpack.

A manual profile was taken in one of the snow pits. Density was measured in each snow pit using a capacitive sensor (Denoth, 1989).

D.2.4 Failure initiation

One can discriminate between weak layer failure due to crack propagation and due to the direct impact of the air pressure wave at the location of observation due to different wave propagation velocities and a resulting time delay. Crack propagation happens at much lower speed than propagation of the air pressure wave through the atmosphere with subsequent propagation through the snowpack to the weak layer (Birkeland and van Herwijnen, 2012; Gubler, 1977; Simioni and Schweizer, 2013).

D.2.5 Failure mechanism and identification

The air pressure resulting from an explosion hits the snowpack with a positive and a negative pulse which lead to corresponding loading of the snowpack. During the positive compressive pulse, a weak layer will fail if the compressive strength or rather the shear strength are exceeded (Simioni et al., 2014b). The negative peak stresses will be lower than the positive maximum stresses and in most cases not cause failure.

Assessing the video stills of an experiment allowed to identify whether there had happened weak layer failure or not.

D.2.6 Deformation and loading

Accelerations were directly measured by the installed accelerometers. Displacement velocities and displacements were derived by integration. Air pressure was measured with the installed microphones at the snow surface.

Stresses were calculated assuming a linear elastic material behavior. This is a strong simplification of the complex wave propagation behavior in snow which would be described most accurately by Biot's theory (Johnson, 1982). We measured density ρ at different depths within the snowpack. We derived the wave propagation velocity c_p inside the snowpack based on the wave arrival times at two vertically separated sensors in a pit. The elastic modulus E can then be obtained: $E = {c_p}^2 \rho$.

Normal stresses were calculated using the relation

$$\sigma = \frac{v_{\text{disp}}}{c_p} E$$

where v_{disp} is the displacement velocity (Kolsky, 1953).

D.3 Results and discussion

We performed 37 experiments during the winter 2013-2014. In the following, we mainly present the exemplary results of one experiment (25 February 2014). However, the qualitative observations we report have been observed in several experiments.

D.3.1 Weak layer failure

Snow depth in the study area was considerably above average and contributed to good snowpack stability without persistent weak layers (Schweizer and Wiesinger, 2001). Nevertheless, weak layer failure could be recorded at distances close to the explosion and in near-surface layers, especially with new snow conditions.

During the negative impulse of the wave, weak layers and the above snowpack were lifted if failure happened in layers close to the surface and at observation points close to the explosion, e.g. below the new snow. This allowed for clear identification of failure. If failure happened in deeper snowpack layers, the failure could usually still be identified due to the sudden displacement of the snowpack above the weak layer.

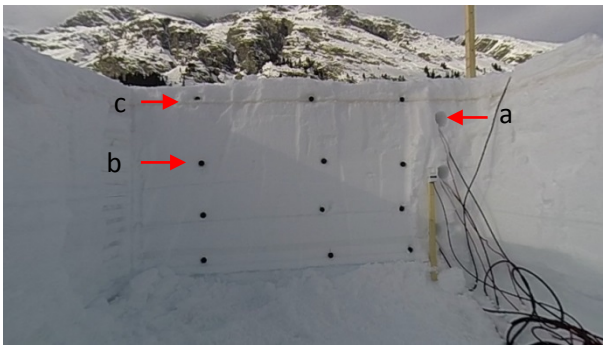

Fig. D–1: Snow pit wall with a) markers, b) holes for accelerometers, c) weak layer (failure). The snowpack above the weak layer c) was lifted due to the negative pressure impulse.

Although loading was higher due to larger charges and measuring closer to the point of explosion compared to the preceding season (Simioni and Schweizer, 2013; cf. Appendix C), no crack propagation through the weak layer triggered close to the detonation point could be observed during the experiments. Crack propagation was likely not observed since the snowpack was stable and no prominent weak layer was present. Failure mainly happened below the uppermost layer consisting of new snow or decomposed and fragmented precipitation particles.

In order to release an avalanche, slab and weak layer must be prone to crack propagation (Reuter et al., 2013). Crack initiation is expected to occur close to the detonation point where the impact is largest. If near the detonation point no suitable slab and weak layer combination exists so that crack propagation cannot occur, a running crack may still be initiated further from the detonation point where the snowpack is more prone to propagation. In that case it is important to know whether the impact of the air pressure wave at the point of observation is still large enough to cause weak layer failure and subsequent crack propagation.

D.3.2 Air pressure

Air pressure at the investigated pit showed the distinct shape of a blast wave, with a positive peak pressure of 17.5 kPa and a negative peak of -5.34 kPa at a distance of 12 m from the point of explosion.

D.3.3 Accelerations

The accelerations reached 135 m s^{-2} at the uppermost accelerometer. These values decreased significantly with depth down to 28 m s^{-2} for the lowest sensor around 80 cm below the snow surface. The vertical acceleration at the depth of the failed weak layer was derived by extrapolation of the lower sensors and reached 270 m s^{-2}.

D.3.4 Stresses

The elastic modulus, calculated with measured densities and propagation velocities, was in the range of 60 to 90 MPa, i.e. high – as expected for an estimate derived from a highly dynamic loading experiment.

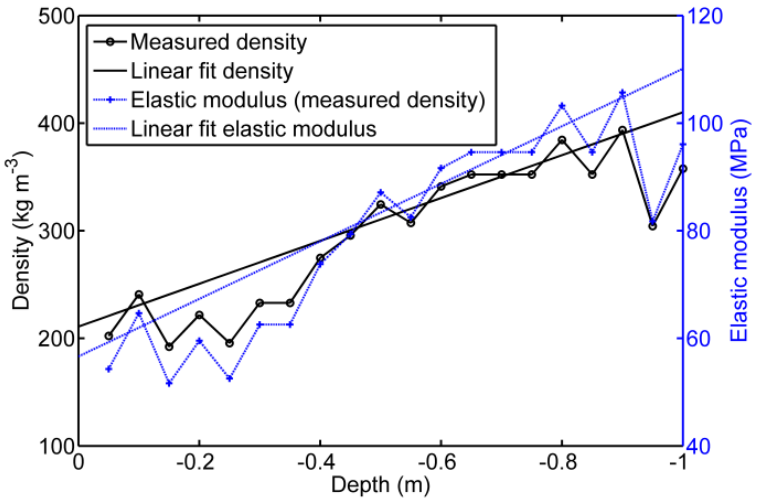

Fig. D–2: Density and corresponding elastic modulus vs snow depth. The green line indicates linear fit to density.

In our experiment, the weak layer failure occurred approximately 12 cm below the snow surface. The uppermost accelerometer was buried 19 cm below the surface. The peak normal stress at 19 cm was 8.8 kPa. This value is rather low compared to typical values of compressive strength but above tensile strength of snow (Shapiro et al., 1997). Slightly higher, at the depth of the weak layer, the compressive stresses were probably larger. However, as shear stresses could not be determined, it is not possible to say whether the respective strength was exceeded. Deeper in the snowpack, layers generally have higher density and higher strength, if there are no persistent weak layers, and the stresses calculated in these layers were low and hence likely insufficient to cause failure.

However, other experiments with larger charges, in closer distance to the point of explosion and/or different elevation of the charge did cause failure of layers deeper in the snowpack.

So far we could not calculate the shear stresses since we were unable to determine the shear waves and their amplitudes in the accelerometer signal as the measurements were performed very close to the detonation point and the shear wave was not delayed sufficiently so that the different wave modes could be separated.

D.4 Summary

We performed experiments to assess the impact of an explosion on the snowpack. We measured air pressure, accelerations and monitored the snow pit wall with cameras to detect failure and derive loads required to fail a weak layer.

We detected failure below a layer of recently fallen snow by evaluating the camera stills. For the single experiment analysed here, we observed that the surface layer was lifted up – indicating failure between the surface layer and the underlying snowpack. Normal compressive stress was about 9 kPa, i.e. within the order of magnitude of compressive strength. Close to the surface, the compressive stresses were in the order of magnitude of the surface air pressures.

In the next winter, we will perform experiments again if possible under more unstable snowpack conditions, and plan to compare the effect of different kinds of explosions.

Acknowledgements

The study was partly funded by the Swiss Federal Office for the Environment (FOEN). We thank Werner Preisig and the personnel of the military firing range for logistical support, and Lino Schmid, Matthias Heck, Achille Capelli, Johan Gaume, Martin Proksch, Philip Crivelli, Thomas Thüring and Oliver Pelzer for help with the field work.

Appendix E Field measurements and modeling of wave induced weak layer failure due to an explosion

Published as 'Simioni, S., Sidler, R., Schweizer, J. and Dual, J., 2014. Field measurements and modeling of wave induced weak layer failure due to an explosion. In: P. Haegeli (Editor), Proceedings ISSW 2014. International Snow Science Workshop, Banff, Alberta, Canada, 29 September - 3 October 2014, pp. 722-726.'

Abstract

Little is known about the mechanisms involved when triggering avalanches artificially by explosions. Here we test the hypothesis that weak layer failure is mainly initiated by wave induced stresses exceeding the strength of the specific layer. We therefore performed experiments with explosives on a flat study site in winter 2013-2014 in wet and dry snowpacks. At three different distances from the point of explosion we measured surface air pressure and accelerations within the snowpack at various depths. We evaluated snow density and dielectric properties with conventional methods in snow profiles and used this information together with empirical relationships to build a Biot-type porous model of the snowpack. Acoustic wave propagation was simulated by solving Biot's equations numerically with a pseudo-spectral approach. Failure in the snowpack was modelled if compressional and shear stresses exceeded the strength limits for the corresponding snow density. Modelled failure locations were compared to the actual appearance of fractures in the field measurements. The results are a promising step towards models including more complex geometries which will help to improve planning of fixed avalanche control installations.

E.1 Introduction

Fixed avalanche control installations have gained popularity during the past years primarily to protect infrastructure. For an informed decision on where to locate installations in the release zone to have adequate coverage and hence to reduce the residual risk to a target level, it is desirable to know how far away from an explosion a weak layer is still likely to fail.

Since the pioneering work by Gubler (1977), flat field experiments on avalanche control have been performed by Ueland (1993) who focused on far distances, and Bones et al. (2012) who studied the effect of an explosion on the snowpack near the point of detonation. Gubler (1976), Johnson et al. (1994) and Mellor (1973) found that best effectiveness was obtained for an explosion a certain height above the snowpack. Small scale experiments were performed by Johnson et al. (1992) and revealed the principle behavior of snow under dynamic loading. Johnson (1990) developed a simple model to predict shock wave attenuation in snow, focusing on short distances from the explosion. Biot's theory, which describes wave propagation in porous media, had previously been applied on snow by Johnson (1982). A finite element model for rapid loading was developed by Haehnel and Shoop (2004). Miller et al. (2011) developed a numerical model to study the response of snow to explosions. Recently, a pseudo-spectral model for porous materials solving Biot's equations with a pseudo-spectral approach was developed (Sidler et al., 2010).

The aim of this study was to explore whether weak layer failure initiated by wave induced stresses can be adequately modeled. We compared results of field experiments to numerical simulations based on a Biot-type porous model of the snowpack. The stress field of the simulation

was evaluated based on the failure criterion to obtain the locations where snowpack failure had occurred; those were then compared to the failure locations found in the field experiments.

E.2 Methods

E.2.1 Field experiments

The field experiments were performed on a plane, level study site at an elevation of 1680 m a.s.l. (Simioni and Schweizer, 2013; cf. Appendix C). The experiments during the preceding winter showed a very uniform snowpack (Simioni and Schweizer, 2013; cf. Appendix C).

During winter 2013-2014, snow depth at a nearby observation station was well above the average. Snow depth at the study site reached 180 cm during this season. A manual profile including snow density measurements with a capacitance probe (Denoth, 1989) was observed on the day of the experiments and indicated good stability (Schweizer and Wiesinger, 2001).

For the explosive source we chose Alpinit, a slurry explosive widely employed in avalanche control installations in Switzerland (Simioni and Schweizer, 2013; cf. Appendix C).

Charges ranging from 4.25 to 5 kg were fixed to a pole at elevations of 2 and 3 m above the snow surface. The charges were triggered with electric detonators.

Measuring equipment was placed in three snow pits at different distances from the detonation point. Acceleration sensors were buried in two of the snow pits at different depths. Microphones were installed above all three snow pits to measure the resulting pressure in the air above the snowpack. All measurement installations were automatically triggered at the exact time of explosion. Cameras manufactured by GoPro were installed in all snow pits to visually identify the failure of weak layers.

E.2.2 Numerical modeling of wave propagation

A poroelastic model of wave propagation is much better suited to describe wave propagation in snow than the conventional elastic or viscoelastic models commonly applied in seismology (Johnson, 1982). To this end we solved Biot's (1962) equations of motion with a pseudo-spectral approach which is known to be accurate and efficient (Sidler et al., 2010). We also consider the wave propagation in the air above the snowpack and in the ground below the snow.

Compressive and shear strength were parameterized depending on snow density (Jamieson and Johnston, 2001; Shapiro et al., 1997). Failure occurs if the modeled stresses exceed the strength at a given point within the snowpack.

A Friedlander wavelet was used to model the pressure source with parameters based on the field measurements of air pressure (Fig. E–1).

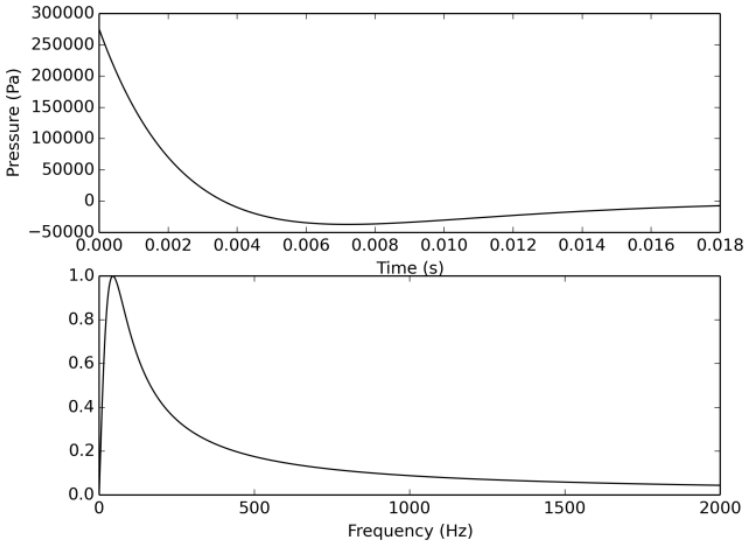

Fig. E–1: Waveform and frequency content of the Friedlander wavelet used as pressure source in the simulation. The source is located in the acoustic layer above the poroelastic snow layer.

E.3 Results

E.3.1 Acceleration

The accelerations of the snowpack showed a clear attenuation with depth and distance from the blast. Acceleration for three different depths at a distance of 27 m from the source can be seen in Fig. E–2.

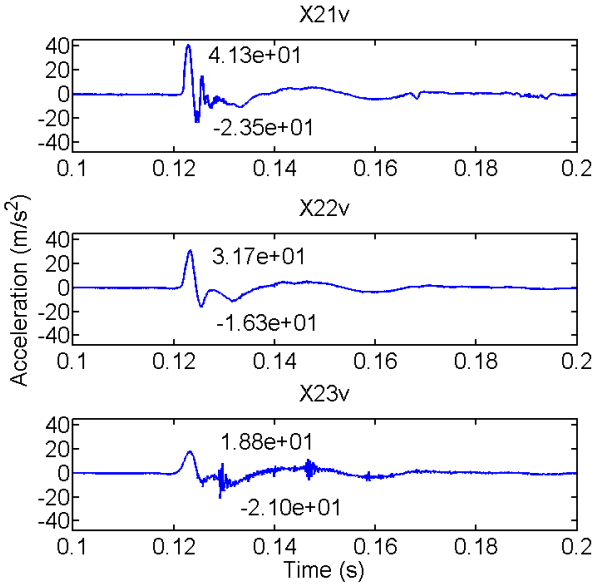

Fig. E–2: Vertical accelerations for sensors at a distance of 27 m from the point of explosion and three different depths (21, 50 and 78 cm below the snow surface).

The typical waveform consists of a first dominant sharp pressure wave followed and superposed by pressure and shear waves with smaller amplitudes arriving at the sensor. This corresponds well with a Friedlander source waveform that is often associated with explosive sources in air. The corresponding waveform and frequency content are shown in Fig. E–1.

E.3.2 Air pressure

As the air pressure wave propagates from the point of detonation it is subject to geometrical spreading and interference with reflected and transmitted wave modes. The measured air pressure for the modeled experiment decreased exponentially from approx. 17 kPa at a distance of 12 m from the blast to 4 kPa at 22 m. The attenuation of the air pressure wave amplitude in the field experiments varied between $x^{-1.5}$ and $x^{-2.5}$, where x is the distance from the point of explosion.

E.3.3 Weak layer failure

The stills from the videos recorded in the snow pits during explosion revealed that weak layer failure mainly occurred below the top layer consisting of new snow and partly decomposed and fragmented precipitation particles. We attribute the absence of failure in deeper layers to the stable structure of the snowpack; persistent weak layers were not present.

E.3.4 Model

We simulated the propagation of an acoustic wave by 2D wave propagation on a 1D snowpack model based on the density profile observed in the snow pit. We simulated the air above the snowpack as a purely acoustic medium supporting only one pressure wave mode and used the appropriate open pore boundary conditions at the air-snow interface. For the ground underlying the snowpack we used the properties of unconsolidated, water-saturated sand with considerably higher wave velocities. The model for porosity is shown in Fig. E–3.

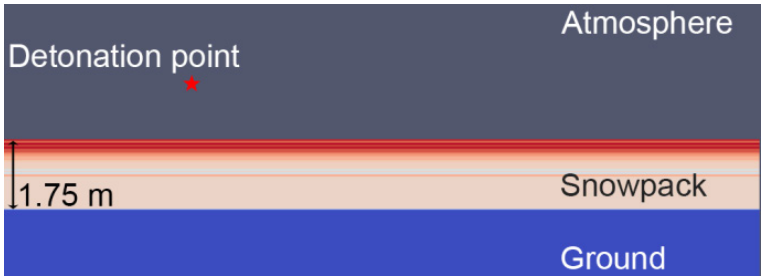

Fig. E–3: Porosity model for the numerical modeling. The snowpack is a one-dimensional model based on measured density and is displayed in different shades of red. Gray indicates air and a water saturated sandy subsurface below the snowpack is shown in blue color. The model is 19 m long and snow depth is 175 cm.

E.3.5 Simulation

During the time of the simulation snapshots of the stress fields are written out in short time intervals and evaluated for maximal stress conditions that the snowpack can withstand. We therefore distinguished between deviatoric (shear) and axial (bulk) stress fields. The corresponding stress fields 2.7 milliseconds after the start of the simulation are shown in Fig. E–4 and Fig. E–5, respectively. The model suggests that the snowpack mainly failed in shear near the uppermost layers of the snowpack. Due to the considerably higher wave velocities of the sand underlying the snowpack the waves were strongly transmitted into the ground and the sand layer behaved almost like an absorbing boundary.

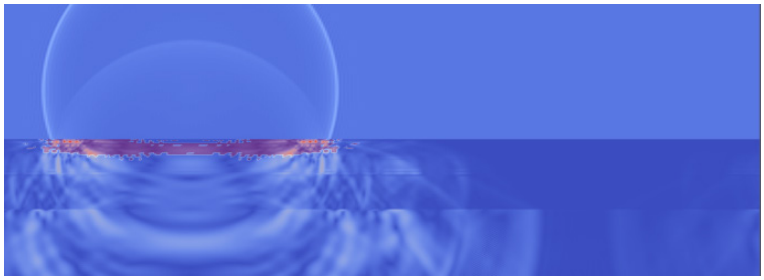

Fig. E–4: Snapshot after 2.7 ms showing the pressure in the air above the snowpack, the deviatoric (shear) stress in the subsurface (blue for positive stresses) and the locations where the maximum shear stress exceeded the strength (in red) during the time of the simulation.

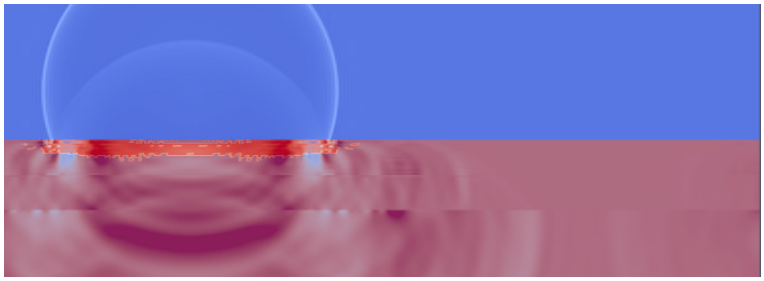

Fig. E–5: Same as Fig. E–4 but uniaxial (bulk) stress (ruby for negative stresses) is shown instead of deviatoric stress and locations where strength is exceeded (luminous red).

E.4 Summary

We performed field experiments with explosives and recorded air pressure, snowpack acceleration, stratigraphy and density. We used density and air pressure measurements as input for a Biot-type porous representation of the snowpack. We then solved Biot's equations with a pseudo-spectral approach and compared the locations of the stress field exceeding the maximum strength of the snowpack to the locations where snowpack failure was identified in the field experiments.

The modeled air pressure was in good agreement with the values measured in the field experiments, considering the error of a 2D model compared to the spherical expansion of the wave in the experiment. Defining the correct shape and values of the input wavelet including amplitude

and frequency content based on the air pressure measurements is crucial to obtain a modeled snowpack response similar to the measured response. Although using smaller charges, the air pressures modeled by Miller et al. (2011) were higher than those modeled here but nevertheless in the same order of magnitude. A shear stress concentration was observed above the weak layer as detected in the explicit model used by Miller et al. (2011).

The model suggests that weak layer failure occurs mainly due to shear loading in the uppermost part of the snowpack as observed from the camera stills.

In the future, we will refine the model with data from more field experiments and compare the results to those that can be obtained with the explicit model developed by Miller et al. (2011).

Acknowledgements

This research has been supported by the Swiss National Science Foundation and the Swiss Federal Office for the Environment (FOEN). We thank Werner Preisig and the team of the military firing range for logistical support, and Lino Schmid, Matthias Heck, Achille Capelli, Johan Gaume, Martin Proksch, Philip Crivelli, Thomas Thüring and Oliver Pelzer for help with the field work.

Appendix F Artificial avalanche release: flat field experiments using a gas exploder

Published as 'Simioni, S., Dual, J. and Schweizer, J., 2016. Artificial avalanche release: flat field experiments using a gas exploder. In: E. Greene (Editor), Proceedings ISSW 2016. International Snow Science Workshop, Breckenridge CO, U.S.A., 3-7 October 2016, pp. 405-409.'

Abstract

Fixed avalanche control installations are frequently used today due to their various advantages to artificially trigger avalanches. Gas mixtures or explosives are ignited to create the required overpressure on the snowpack which is then transferred to the snowpack and may cause weak layer failure. Hitherto, extensive research has been conducted on explosives. However, comprehensive gas exploder experiments have so far been lacking and the detailed effect of gas explosions on a snowpack is poorly known – although it is no question that gas exploders are successfully operated throughout the world. We performed experiments with a mobile prototype gas exploder on a flat level study site. In total, 35 experiments with different gas quantities consisting of propane and oxygen were conducted. Similar to previous experiments, we measured surface air pressure with microphones at different distances from the point of explosion and snowpack accelerations at different depths within the snowpack and different distances from the explosion. Measurements were performed along two different axes to consider the effect of a directed explosion. As it is the case with explosives, air pressure and accelerations within the snowpack decay strongly with distance from the point of explosion and depth within the snowpack. The test procedure is well suited as a standard procedure to compare different avalanche release methods. Our findings will help to better understand the effect of different fixed avalanche control installations.

F.1 Introduction

The artificial release of avalanches is a key active control measure in avalanche mitigation. Hundreds of fixed avalanche control installations have been installed during the last decade – and are successfully operated. Still, a number of questions on the effectiveness remain unanswered.

To release avalanches artificially, an explosion is either caused by explosives or a gas mixture. In the snowpack, the explosion leads to peak stress and strain within a fraction of a second and might cause the failure of a weak layer. A subsequent avalanche release is probable if the snowpack is prone to crack propagation. Within the scope of this research, we focus on gas explosions.

Different studies were performed on the effect of explosions on snowpacks, many of them investigated the effect close to the point of explosion, i.e. within the shock region, and showed the strong attenuation of waves within a snowpack (e.g., Frigo et al., 2012; Johnson et al., 1993). Tichota et al. (2010) and Binger and Miller (2016) developed a measurement setup to record air overpressures above and accelerations within the snowpack at short distances from the explosion and showed a strong decrease of the measured parameters with distance from the point of explosion and depth within the snowpack.

At larger distances, more relevant for the effectiveness of artificial release, Gubler (1977) performed an extensive study with explosives used for artificial avalanche release. He showed,

among other findings, the influence of charge placement and the increased effect of a charge elevated above the snowpack. Other studies observed the effect of a snowpack on the propagation of acoustic wave above the snow surface (e.g., Albert and Hole, 2001). Simioni et al. (2014a) recorded a weak layer failure caused by an explosion. Also using explosives, Simioni et al. (2015; cf. Chap. 4) performed extensive field studies to study the impact on a snowpack and reported that air pressures decayed strongly, proportional to $x^{-1.6}$, where x is the distance from the explosion. Snowpack accelerations decreased significantly with depth within the snowpack and distance from the explosion.

Liebermann et al. (2002) described the principle of a fixed avalanche control system working with gas. Berthet-Rambaud (2009) performed first investigations on this kind of release systems. The effect of ground accelerations induced by a gas exploder at far distances was investigated by Suriñach et al. (2011). They concluded that ground accelerations caused by a gas exploder was not sufficient to trigger avalanches at distances greater than 120 m.

Many of the studies on the impact of explosions were performed at short ranges and with explosives only. Only one study was particularly dedicated to gas exploders, however at large distances (>120 m) (Suriñach et al., 2011). We are not aware of any published studies investigating the effect of gas explosions on a snowpack.

The aim of this work was to assess the impact of a directed gas explosion on the snowpack. We used a mobile prototype gas exploder and measured air pressures above and accelerations within the snowpack.

F.2 Methods

F.2.1 Study site

We performed the experiments at the military firing range in Hinterrhein (Switzerland) (Simioni et al., 2015; cf. Chap. 4). Snow depth at the level study site was between 70 and 80 cm; the snowpack was predominately dry and spatially rather uniform.

F.2.2 Measuring equipment

The measurement setup was similar to the one used by Binger and Miller (2016). Microphones were installed above the snow surface to measure the air pressure and accelerometers within the snowpack to measure snowpack accelerations (Simioni et al., 2015; cf. Chap. 4). The instruments were installed at different distances ranging from 11.6 to 49.2 m from the point of explosion. Measurements were performed along different axes from the point of explosion to account for the fact that the effect of the directed gas explosion is not radially symmetric.

F.2.3 Mobile gas exploder

A mobile prototype gas exploder, provided by TAS, the manufacturer of the Gazex® system, was used to perform the experiments. The gas exploder consists of a steel tube open on one side (length: 2.5 m, inner diameter: 80 cm); it is suspended from a crane and anchored to the ground with steel wires to absorb the recoil. The two gases (oxygen and propane) are stored in tanks at a pressure of 6.5 and 1.4 bar, respectively). The gas then flows for a certain period of time from the tanks into the gas exploder where it is mixed. A plastic lid prevents the gas from flowing out of the tube before the explosion. This is required since the oxygen-propane mixture is heavier than the ambient air. The gas mixture is ignited using spark plugs.

The gas exploder was installed at different elevations from the snow surface and angles between the snow surface and the exploder.

Fig. F–1: Gas exploder during explosion.

F.2.4 Gas quantities and scaling

The released gas quantity m_G (in kg) is calculated using the ideal gas law:

$$m_{\mathrm{G}} = \frac{\Delta p_G \, V_{\mathrm{tank}}}{R_s \, T}$$

where Δp_G is the pressure difference between before and after releasing the gas from the tank (Pa), V_{tank} is the volume of the pressure reduction tank (m^3), R_s is the specific gas constant of the respective gas ($J\ kg^{-1}\ K^{-1}$) and T is the gas temperature (K).

The gas volume is calculated from the gas mass using air temperature and the ambient air pressure.

For explosives, the influence of the charge mass is usually considered by scaling the distances from the point of explosion with the cube root of the charge size (Cooper, 1996). For a directed gas

explosion, this relation might not hold true. Therefore, the scaling factor was determined from the air pressure results. The scaling factor was varied within a certain range and the best fit of the air pressure vs. the scaled distance was chosen.

$$x' = x\, {m_\mathrm{G}}^{-c_\mathrm{G}} \quad (\mathrm{m\,kg^{-}}^{c_\mathrm{G}})$$

where c is the scaling factor and the subscript G stands for gas.

The acceleration data were integrated with time to obtain displacement velocities and displacements. In addition, an energy equivalent was calculated by integrating the square of the displacement velocities with time, similar to the air pressure energy equivalent.

Air pressure data were fitted against scaled distance with a power law relation, e.g.:

$$p_\mathrm{max} = 10^\mathrm{a}\, {x'}^{-\mathrm{b}}$$

where a and b are the coefficients of the power law. The coefficient b describes the magnitude of the decay of a certain parameter with distance or depth.

Accelerations and derived parameters were first fitted with depth within the snowpack. This fit was used to calculate the decay with distance at a certain depth within the snowpack – again with a power law.

F.3 Results and discussion

We performed 35 gas exploder experiments above dry and partly moist snowpacks during the winters 2014-2015 and 2015-2016.

The angles between the axis of the gas exploder tube and the second measuring axis ranged between 23 and 37° above snow and 89° above bare ground. The elevation of the tube bottom edge and the snow/ground surface was between 1.4 and 1.8 m.

The quantities of the gas mixture were between 0.4 and 1.45 kg. Exact gas quantity measurements were only performed during the winter 2015-2016. The quantities of the first season were determined using the air pressure measurements and the scaling factor from the second season.

F.3.1 Scaling factor

The best scaling factor c_G was 0.65 for experiments above snow and 0.4 for experiments above bare ground. This shows the influence of two different surfaces on air pressure propagation.

F.3.2 Air pressure

The maximum air pressure decayed on average with ${x'}^{-1.67}$. This is in good agreement with or slightly higher than reported by earlier studies that, however, all used explosives (Albert and Hole, 2001; Gubler, 1977; Ingram, 1962; Mellor, 1973). Up to the maximum angle of 37° from the exploder axis, no lateral decrease was observed. The maximum derivative of the air pressure decreased

similarly as the maximum air pressure. The energy equivalent decreased stronger than the air pressure with distance. This is plausible, since the energy of a wave decays following the square of the amplitude decay.

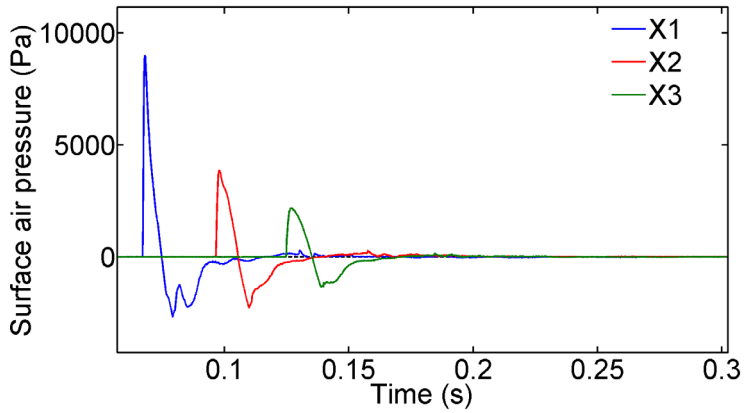

Fig. F–2: Example of the air pressure signal at the three measuring locations on the x-axis, data from 18 Feb 2016, experiment 5. Distances for X1, X2 and X3 are 16.0, 25.6 and 34.9 m, respectively.

F.3.3 Acceleration, displacement velocity and displacement

The accelerations decreased strongly with depth proportional to $z^{-0.9}$ to $z^{-1.4}$. This is in the same range as observed in other studies using explosives (Binger et al., 2006). Displacements were small ranging from 10^{-3} m to 10^{-6} m and were in good agreement with previous results by, e.g., Gubler (1977).

The incline and the elevation of the gas exploder did not have a significant effect on the measured quantities. Compared to the distances at which we measured, the slight change of elevation and the change of incline within a range of only 10° are expected to have a minor influence. The incline was not changed to more extreme values as the tested inclines were similar to those for operational gas exploders.

The strength of the air pressure decay was similar to the decay of the maximum vertical accelerations. This finding means, that the behavior of the air pressure can be used as an approximation for the behavior within the snowpack. The propagation speed of the air pressure wave never exceeded the speed of sound in air for locations larger than approx. 11 m. At shorter distances, no measurement was possible to prove the existence of a shock wave with higher speeds.

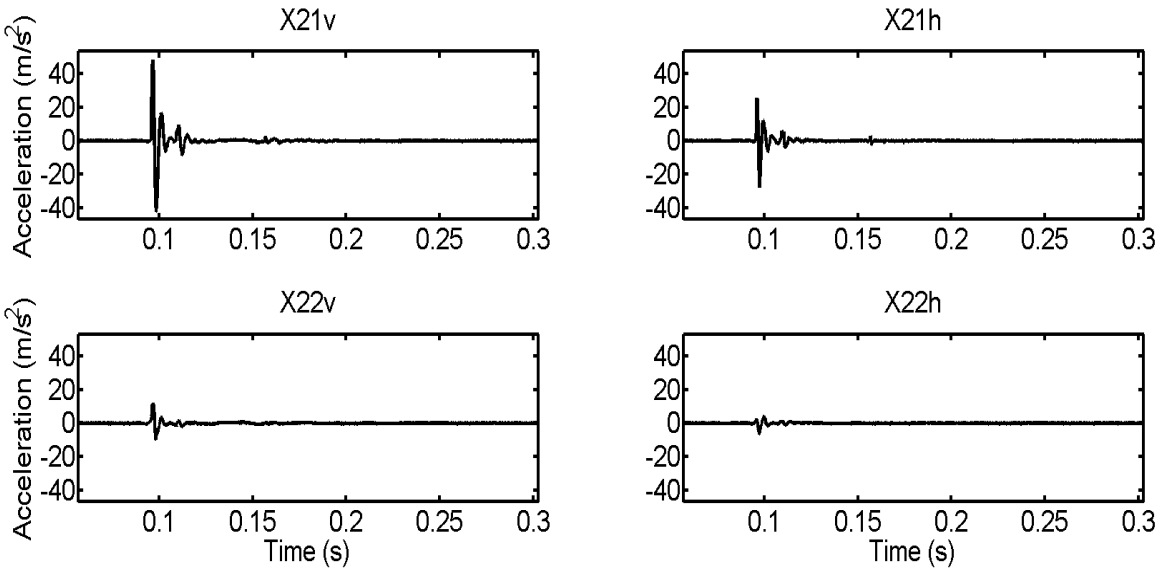

Fig. F–3: Example of the vertical (left) and horizontal (right) accelerations at two depths (top: 14 cm, bottom 38 cm) within the snowpack at 25.6 m from the gas exploder. Data from 18 Feb 2016, experiment #5.

F.4 Summary and Outlook

We performed the first extensive measuring campaign with a mobile gas exploder to investigate the effect of gas explosions on a snowpack.

We observed an air pressure of 1 kPa at approx. 57 m with 1.8 kg of gas which is similar to what we observed with a 4.5 kg explosive charge. This shows that the impact of a gas exploder is clecomparable to the impact obtained with solid explosives.

Within an opening angle of approx. 70° no lateral decay of the impact was observed. However, it is expected that the decay will be different at larger angles due to character of the directed explosion. Slight changes of incline and elevation of the gas exploder had no influence on air pressures above and accelerations within a snowpack. The snowpack accelerations decreased similarly as the maximum air pressure or the air pressure derivative with distance from the point of explosion. The decay of the latter parameters might therefore be useful as approximations to assess the behaviour within the snowpack.

All the relevant quantities are clearly sufficient to trigger an avalanche – as far as our understanding goes. In particular at close distances the impact is extremely high. The size of the resulting avalanche might rather be related to crack propagation propensity than a high impact at large distances.

These results help to understand the effect of a directed gas explosion on snowpacks. The findings might be used to assess differences in the effect of different explosions.

F.5 Limitations

Our results obtained with a prototype gas exploder cannot directly be compared to an operational Gazex®. The gas masses and volumes measured during the experiments do not correspond to the size of an operational gas exploder given in m^3.

Conflict of interest statement

None of the authors has any affiliations with or involvement in any organization or entity with any financial interest or non-financial interest in the subject matter or materials discussed in this manuscript.

Acknowledgements

The study was partly funded by the Swiss Federal Office for the Environment (FOEN). We thank the Swiss Armed Forces for logistical support. Our thanks go to TAS for providing the mobile gas exploder and operating supplies. We thank Lino Schmid, Matthias Heck, Achille Capelli, Bettina Richter and Alec van Herwijnen for help with the field work.

Appendix G Publications and planned publications

Some of the chapters of this thesis were published, are submitted or planned to be published with some adaptions.

- Chapter 4 was published with adaptions as
  Simioni, S., Sidler, R., Dual, J. and Schweizer, J., 2015. Field measurements of snowpack response to explosive loading. Cold Regions Science and Technology, 120: 179-190.
- The content of chapter 5 is in preparation to be submitted as
  Simioni, S., Dual, J. and Schweizer, J., 2016. Snowpack response to directed gas explosions on level ground. in preparation.
- The content of chapter 6 is in preparation to be submitted as
  Simioni, S., Dual, J. and Schweizer, J., 2016. Small scale field experiments in snow to determine wave propagation principles and mechanical properties
- The remaining chapters are planned to be published individually, in combination or in combination with other studies on the same topic.
- Appendix C was published as
  Simioni, S. and Schweizer, J., 2013. Assessing weak layer failure and changes in snowpack properties due to avalanche control by explosives. In: F. Naaim-Bouvet, Y. Durand and R. Lambert (Editors), Proceedings ISSW 2013. International Snow Science Workshop, Grenoble, France, 7-11 October 2013. ANENA, IRSTEA, Météo-France, Grenoble, France, pp. 775-778.
- Appendix D was published as
  Simioni, S., Schweizer, J. and Dual, J., 2014. Field experiments on weak layer failure and crack propagation due to explosions. In: P. Haegeli (Editor), Proceedings ISSW 2014. International Snow Science Workshop, Banff, Alberta, Canada, 29 September - 3 October 2014, pp. 185-188.
- Appendix E was published as
  Simioni, S., Sidler, R., Schweizer, J. and Dual, J., 2014. Field measurements and modeling of wave induced weak layer failure due to an explosion. In: P. Haegeli (Editor), Proceedings ISSW 2014. International Snow Science Workshop, Banff, Alberta, Canada, 29 September - 3 October 2014, pp. 722-726.
- Appendix F was published as
  Simioni, S., Dual, J. and Schweizer, J., 2016. Artificial avalanche release: flat field experiments using a gas exploder, Proceedings ISSW 2016. International Snow Science Workshop, Breckenridge CO, U.S.A., 3-7 October 2016.

List of symbols and abbreviations

Symbol	Description	Unit
A	area	m^2
A_r, A_s, A_t	Amplitudes of reflected P-, transmitted S- and transmitted P-wave	Pa
C	elastic constant, Biot theory	Pa
E	Young's modulus	Pa
I_3	second moment of inertia	m^4
N	shear modulus solid, Biot theory	Pa
E'	Energy equivalent	$m^2\ s^{-1}$
M	constrained modulus	Pa
Q	coupling of volume change, Biot theory	-
R	pressure on fluid, Biot theory	Pa
R_s	Specific gas constant	$J\ kg^{-1}\ K^{-1}$
T	gas temperature	K
T_{atm}	ambient air temperature	K
$\underline{U}$	displacement vector fluid	m
V_{GAS}	gas volume	m^3
V_{tank}	gas tank volume	m^3
X	first axis (from point of explosion)	
Y	second axis (from point of explosion)	

Symbol	Description	Unit
a_s	snowpack acceleration	m s^{-2}
a	power law coefficient	-
a_G	scaling factor gas	-
a_K	power law coefficient constrained modulus	-
b	power law coefficient	-
b_K	power law coefficient constrained modulus	-
c_1	longitudinal wave speed	m s^{-1}
c_f	longitudinal wave speed fluid	m s^{-1}
c_2	transversal wave speed	m s^{-1}
c_0	longitudinal wave speed structures/plane wave	m s^{-1}
c_b	flexural wave speed	m s^{-1}
k	wave number	m^{-1}
m_GAS	gas mass	kg
p	air pressure	Pa
p_energy	air pressure energy equivalent	Pa^2 s
p_{GAS}	gas tank pressure	Pa
$p_{,t_\mathrm{max}}$	maximum air pressure derivative	Pa s^{-1}
t	time	s
$\underline{u}$	displacement vector (solid)	m
v	displacement velocity	m s^{-1}
v_energy	energy equivalent from displacement velocity	m^2 s^{-1}
x	distance	m
x'	scaled distance	m kg^{-a}
z	depth	m

Symbol	Description	Unit
α_{en}	attenuation coefficient	dB cm^{-1}
ε_{ij}	strain	-
ε_{ijk}	permutation symbol	-
η	Nondimensional frequency parameter, Biot theory	-
Θ	angle of wave propagation	rad
λ	Lamé parameter	Pa
λ_f	Lamé parameter fluid	Pa
μ	Lamé parameter	Pa
ρ	density	kg m^{-3}
ρ_f	fluid density	kg m^{-3}
$\rho_{11}, \rho_{12}, \rho_{22}$	coefficient of inertial effects of moving fluid, Biot theory	-
σ_{ij}	stress	Pa
φ	scalar potential	-
$\underline{\psi}$	vector potential	-
ω	angular frequency	s^{-1}

References

Achenbach, J.D., 1973. Wave propagation in elastic solids. Applied Mathematics and Mechanics. North-Holland, Elsevier, Amsterdam, The Netherlands, 425 pp.

Albert, D.G., 1983. Review of the propagation of inelastic pressure waves in snow. CRREL Report 83-13, US Army Cold Regions Research and Engineering Laboratory, Hanover NH, U.S.A.

Albert, D.G., 2001. Acoustic waveform inversion with application to seasonal snow covers. Journal of the Acoustical Society of America, 109(1): 91-101.

Albert, D.G., Decato, S.N. and Carbee, D.L., 2008. Snow cover effects on acoustic sensors. Cold Regions Science and Technology, 52(2): 132-145.

Albert, D.G. and Hole, L.R., 2001. Blast noise propagation above a snow cover. Journal of the Acoustical Society of America, 109(6): 2675-2681.

Albert, D.G. and Orcutt, J.A., 1990. Acoustic pulse propagation above grassland and snow: Comparison of theoretical and experimental waveforms. Journal of the Acoustical Society of America, 87(1): 93-100.

Albert, D.G., Taherzadeh, S., Attenborough, K., Boulanger, P. and Decato, S.N., 2013. Ground vibrations produced by surface and near-surface explosions. Applied Acoustics, 74(11): 1279-1296.

Bair, E.H., 2013. Forecasting artificially-triggered avalanches in storm snow at a large ski area. Cold Regions Science and Technology, 85: 261-269.

Bair, E.H., Simenhois, R., Birkeland, K. and Dozier, J., 2012. A field study on failure of storm snow slab avalanches. Cold Regions Science and Technology, 79-80: 20-28.

Berthet-Rambaud, P., 2009. Comparison of shock waves provoked by various artificial avalanche release techniques, and of their effects on the snowpack. In: J. Schweizer and A. van Herwijnen (Editors), Proceedings ISSW 2009. International Snow Science Workshop, Davos, Switzerland, 27 September - 2 October 2009. Swiss Federal Institute for Forest, Snow and Landscape Research WSL, pp. 328-329.

Binger, C., Nelsen, J. and Olson, K.A., 2006. Explosive shock wave compression in snow: effects of explosive orientation and snowpack compression. In: J.A. Gleason (Editor), Proceedings ISSW 2006. International Snow Science Workshop, Telluride CO, U.S.A., 1-6 October 2006, pp. 592-597.

Binger, J.B. and Miller, D.A., 2016. Soft and hard slab snow dynamic response to explosives used in avalanche hazard mitigation. Journal of Cold Regions Engineering, 30(2): 04015003 (17 pp.).

Biot, M.A., 1956a. Theory of propagation of elastic waves in a fluid-saturated porous solid. I. Low-frequency range. Journal of the Acoustical Society of America, 28(2): 168-178.

Biot, M.A., 1956b. Theory of propagation of elastic waves in a fluid-saturated porous solid. II. Higher frequency range. Journal of the Acoustical Society of America, 28(2): 179-191.

Biot, M.A., 1962. Mechanics of Deformation and Acoustic Propagation in Porous Media. Journal of Applied Physics, 33(4): 1482-1498.

Birkeland, K.W. and van Herwijnen, A., 2012. Using high-speed video to better understand Extended Column Tests, Proceedings ISSW 2012. International Snow Science Workshop, Anchorage AK, U.S.A., 16-21 September 2012, pp. 98-103.

Bones, J., Miller, D. and Savage, S., 2012. An experimental dynamic response study of hard slab seasonal snow to explosive control, Proceedings ISSW 2010. International Snow Science Workshop, Anchorage AK, U.S.A., 16-21 September 2012, pp. 142-148.

Bouzidi, Y. and Schmitt, D.R., 2012. Incidence-angle-dependent acoustic reflections from liquid-saturated porous solids. Geophysical Journal International, 191(3): 1427-1440.

Brown, R.L., 1981. A method for evaluating shock wave propagation in snow. Cold Regions Science and Technology, 5: 151-156.

Buser, O., 1986. A rigid frame model of porous media for the acoustic impedance of snow. Journal of Sound and Vibration, 111(1): 71-92.

Capelli, A., Kapil, J.C., Reiweger, I., Or, D. and Schweizer, J., 2016. Speed and attenuation of acoustic waves in snow: laboratory experiments and modelling with Biot's theory. Cold Regions Science and Technology, 125: 1-11.

Cardu, M., Chiaravalloti, L., Chiaia, B., Cornetti, P. and Frigo, B., 2008. A coupled stress and energy criterion for natural and artificial triggering of dry snow slab avalanches, 42nd US Rock Mechanics Symposium and 2nd U.S.-Canada Rock Mechanics Symposium, San Francisco, U.S.A., 29 June - 2 July 2008. American Rocks Mechanics Association, pp. ARMA-08-2003.

Chernouss, P., Fedorenko, Y., Barashev, N. and Mokrov, E., 2006. A study of blasting-induced snow instabilities and avalanche releases. In: A. Gleason (Editor), Proceedings ISSW 2006. International Snow Science Workshop, Telluride CO, U.S.A., 1-6 October 2006, pp. 598-606.

Chernouss, P., Mokrov, E., Fedorenko, Y., Husebye, E. and Beketova, E., 2002. Russian-Norwegian project on seismisity-induced avalanches. In: J.R. Stevens (Editor), Proceedings ISSW 2002. International Snow Science Workshop, Penticton BC, Canada, 29 September-4 October 2002, pp. 25-30.

Cooper, P.W., 1996. Explosives engineering. Wiley-VCH, New York, 480 pp.

Denoth, A., 1989. Snow dielectric measurements. Advances in Space Research, 9(1): 233-243.

Denoth, A., 1994. An electronic device for long-term snow wetness recording. Annals of Glaciology, 19: 104-106.

Deresiewicz, H. and Rice, J.T., 1962. The effect of boundaries on wave propagation in a liquid-filled porous solid: III. Reflection of plane waves at a free plane boundary (general case). Bulletin of the Seismological Society of America, 52(3): 595-625.

Fierz, C., Armstrong, R.L., Durand , Y., Etchevers, P., Greene, E., McClung, D.M., Nishimura, K., Satyawali, P.K. and Sokratov, S.A., 2009. The International Classification for Seasonal Snow on the Ground. HP-VII Technical Documents in Hydrology, 83. UNESCO-IHP, Paris, France, 90 pp.

Frigo, B., Chiaia, B. and Cardu, M., 2012. Snowpack effects induced by blasts: experimental measurements vs theoretical formulas, Proceedings ISSW 2012. International Snow Science Workshop, Anchorage AK, U.S.A., 16-21 September 2012, pp. 943-947.

Frigo, B., Chiaia, B., Cardu, M., Giraudi, A., Godio, A. and Rege, R., 2010. Experimental analysis of snowpack effects induced by blasts, International Snow Science Workshop ISSW, Lake Tahoe CA, U.S.A., 17-22 October 2010, pp. 66-71.

Gauthier, D. and Jamieson, J.B., 2006. Towards a field test for fracture propagation propensity in weak snowpack layers. Journal of Glaciology, 52(176): 164-168.

Gerling, B., 2016. Determination of the elastic modulus of snow by acoustic methods and comparison to penetrometer measurements and numerical simulations, unpublished.

Gubler, H., 1976. Künstliche Auslösung von Lawinen durch Sprengungen. 32, Swiss Federal Institute for Snow and Avalanche Research, Davos, Switzerland.

Gubler, H., 1977. Artificial release of avalanches by explosives. Journal of Glaciology, 19(81): 419-429.

Gubler, H., 1983. Künstliche Auslösung von Lawinen durch Sprengungen: Eine Anleitung für den Praktiker, Swiss Federal Institute for Snow and Avalanche Research, Weissfluhjoch/Davos, Switzerland.

Gubler, H., 1993. Artificial release of avalanches, Proc. Int. Symp. on Avalanche Control, Nagaoka, Japan, 11-12 September 1992. Japanese Society of Snow and Ice, Nagaoka, Japan, pp. 102-130.

Gudra, T. and Najwer, L., 2011. Ultrasonic investigation of snow and ice parameters. Acta Physica Polonica A, 120(4): 625-629.

Haehnel, R.B. and Shoop, S.A., 2004. A macroscale model for low density snow subjected to rapid loading. Cold Regions Science and Technology, 40(3): 193-211.

Hamre, D., Simenhois, R. and Birkeland, K., 2014. Fracture speeds of triggered avalanches. In: P. Haegeli (Editor), Proceedings ISSW 2014. International Snow Science Workshop, Banff, Alberta, Canada, 29 September - 3 October 2014, pp. 174-178.

Herrmann, W., 1971. Constitutive equations for compaction of porous materials.

Ingram, L.F., 1962. Air blast in an arctic environment. Technical Report no. 2-597, US Army Waterways Experiment Station, Vicksburg, MS, U.S.A.

Ishida, T., 1965. Acoustic properties of snow. Contributions from the Institute of Low Temperature Science, A20: 23-63.

Jamieson, J.B. and Johnston, C.D., 2001. Evaluation of the shear frame test for weak snowpack layers. Annals of Glaciology, 32: 59-68.

Johnson, B.C., Jamieson, J.B. and Stewart, R.R., 2004. Seismic measurement of fracture speed in a weak snowpack layer. Cold Regions Science and Technology, 40(1-2): 41-45.

Johnson, J.B., 1980. A model for snow-slab failure under conditions of dynamic loading. Journal of Glaciology, 26(94): 245-254.

Johnson, J.B., 1982. On the application of Biot's theory to acoustic wave propagation. Cold Regions Science and Technology, 6(1): 49-60.

Johnson, J.B., 1990. Estimates of shock wave attenuation in snow. Report 90-8, US Army CRREL, Hanover NH, U.S.A.

Johnson, J.B., Brown, J.A. and Gaffney, E.S., 1992. Shock response of snow. Report 92-12, US Army CRREL, Hanover NH, U.S.A.

Johnson, J.B. and Schneebeli, M., 1999. Characterizing the microstructural and micromechanical properties of snow. Cold Regions Science and Technology, 30(1-3): 91-100.

Johnson, J.B., Solie, D.J. and Barrett, S.A., 1994. Response of seasonal snow to explosive loading. Annals of Glaciology, 19: 49-54.

Johnson, J.B., Solie, D.J., Brown, J.A. and Gaffney, E.S., 1993. Shock response of snow. Journal of Applied Physics, 73(10): 4852-4861.

Kolsky, H., 1953. Stress waves in solids. Oxford University Press, London, 211 pp.

Kurz, J.H., Grosse, C.U. and Reinhardt, H.-W., 2005. Strategies for reliable automatic onset time picking of acoustic emissions and of ultrasound signals in concrete. Ultrasonics, 43(7): 538-546.

LaChapelle, E.R., 1977. Alternate methods for the artifical release of snow avalanches. Journal of Glaciology, 19(81): 389-397.

Lee, S.M. and Rogers, J.C., 1985. Characterization of snow by acoustic sounding: A feasibility study. Journal of Sound and Vibration, 99(2): 247-266.

Liebermann, E., Schippers, J. and Liebermann, S.C., 2002. The "Gazex" avalanche release system. In: J.R. Stevens (Editor), Proceedings ISSW 2002. International Snow Science Workshop, Penticton BC, Canada, 29 September-4 October 2002, pp. 46-48.

Löwe, H. and van Herwijnen, A., 2012. A Poisson shot noise model for micro-penetration of snow. Cold Regions Science and Technology, 70: 62-70.

Marco, O., Buser, O., Villemain, P., Touvier, F. and Revol, H.P., 1998. Acoustic impedance measurement of snow density. Annals of Glaciology, 26: 92-96.

Marty, C. and Meister, R., 2012. Long-term snow and weather observations at Weissfluhjoch and its relation to other high-altitude observatories in the Alps. Theoretical and Applied Climatology, 110(4): 573-583.

Mayer, K., 2011. Acoustic emission analysis of snow, Graz University of Technology, Graz, Austria, 87 pp.

McClung, D.M. and Schaerer, P., 2006. The Avalanche Handbook. The Mountaineers Books, Seattle WA, U.S.A., 342 pp.

Meister, R., 2002. Avalanches: warning, rescue and prevention. Avalanche News, 62: 37-44.

Mellor, M., 1965. Explosions and snow. Cold Regions Science and Engineering, Part III, Section A3a. CRREL, Hanover NH, U.S.A., 34 pp.

Mellor, M., 1973. Controlled release of avalanches by explosives. In: R. Perla (Editor), Advances in North American avalanche technology: 1972 Symposium. USDA Forest Service, General Technical Report RM-3, pp. 37-49.

Mellor, M., 1975. A review of basic snow mechanics, Symposium at Grindelwald 1974 - Snow Mechanics, IAHS Publ., 114. Int. Assoc. Hydrol. Sci., Wallingford, U.K., pp. 251-291.

Mellor, M., 1977. Engineering properties of snow. Journal of Glaciology, 19(81): 15-66.

Miller, D.A., Tichota, R.G. and Adams, E.E., 2011. An explicit numerical model for the study of snow's response to explosive air blast. Cold Regions Science and Technology, 69(2-3): 156-164.

Nicolas, J., Berry, J.-L. and Daigle, G.A., 1985. Propagation of sound above a finite layer of snow. Journal of the Acoustical Society of America, 77(1): 67-73.

Pérez-Guillén, C., Tapia, M., Furdada, G., Suriñach, E., McElwaine, J.N., Steinkogler, W. and Hiller, M., 2014. Evaluation of a snow avalanche possibly triggered by a local earthquake at Vallée de la Sionne, Switzerland. Cold Regions Science and Technology, 108: 149-162.

Podolskiy, E.A., Chambon, G., Naaim, M. and Gaume, J., 2013. A review of finite-element modelling in snow mechanics. Journal of Glaciology, 59(218): 1189-1201.

Podolsky, E., Chernous, P., Abe, O. and Nishimura, K., 2008. Experimental study of short-term loading influence on shear strength. In: C. Campbell, S. Conger and P. Haegeli (Editors), Proceedings ISSW 2008, International Snow Science Workshop, Whistler, Canada, 21-27 September 2008, pp. 701-708.

Proksch, M., Rutter, N., Fierz, C. and Schneebeli, M., 2016. Intercomparison of snow density measurements: bias, precision, and vertical resolution. The Cryosphere, 10(1): 371-384.

Reiweger, I., Mayer, K., Steiner, K., Dual, J. and Schweizer, J., 2015. Measuring and localizing acoustic emission events in snow prior to fracture. Cold Regions Science and Technology, 110: 160-169.

Reuter, B., Proksch, M., Löwe, H., van Herwijnen, A. and Schweizer, J., 2013. On how to measure snow mechanical properties relevant to slab avalanche release. In: F. Naaim-Bouvet, Y. Durand and R. Lambert (Editors), Proceedings ISSW 2013. International Snow Science Workshop, Grenoble, France, 7-11 October 2013. ANENA, IRSTEA, Météo-France, Grenoble, France, pp. 7-11.

Reuter, B. and Schweizer, J., 2009. Avalanche triggering by sound: myth and truth. In: J. Schweizer and A. van Herwijnen (Editors), Proceedings ISSW 2009. International Snow Science Workshop, Davos, Switzerland, 27 September - 2 October 2009. Swiss Federal Institute for Forest, Snow and Landscape Research WSL, pp. 330-333.

Reuter, B., Schweizer, J. and van Herwijnen, A., 2015a. A process-based approach to estimate point snow instability. The Cryosphere, 9: 837-847.

Reuter, B., van Herwijnen, A., Veitinger, J. and Schweizer, J., 2015b. Relating simple drivers to snow instability. Cold Regions Science and Technology, 120: 168-178.

Scapozza, C., 2004. Entwicklung eines dichte- und temperaturabhängigen Stoffgesetzes zur Beschreibung des visko-elastischen Verhaltens von Schnee. Ph.D. Thesis, ETH Zurich, Zurich, Switzerland, 250 pp.

Scapozza, C. and Bartelt, P., 2003. Triaxial tests on snow at low strain rate. Part II. Constitutive behaviour. Journal of Glaciology, 49(164): 91-101.

Scapozza, C., Bucher, F., Amann, P., Ammann, W.J. and Bartelt, P., 2004. The temperature-and density-dependent acoustic emission response of snow in monoaxial compression tests. Annals of Glaciology, 38: 291-298.

Schmid, L., 2015. Deriving snow properties with upward-looking radar systems. Ph.D. Thesis, ETH Zurich, Zurich, Switzerland, 156 pp.

Schneebeli, M., 2002. The importance of the microstructure of snow in nature and engineering. In: C.A. Brebbia, L.J. Sucharov and P. Pascolo (Editors), Design and Nature 2002: Comparing Design in Nature with Science and Engineering. Design and Nature. WIT Press, Southampton, U.K., Udine, Italy, 10-12 September 2002, pp. 87-93.

Schneebeli, M., 2004. Numerical simulation of elastic stress in the microstructure of snow. Annals of Glaciology, 38: 339-342.

Schneebeli, M. and Johnson, J.B., 1998. A constant-speed penetrometer for high-resolution snow stratigraphy. Annals of Glaciology, 26: 107-111.

Schweizer, J., 1999. Review of dry snow slab avalanche release. Cold Regions Science and Technology, 30(1-3): 43-57.

Schweizer, J. and Jamieson, J.B., 2010. Snowpack tests for assessing snow-slope instability. Annals of Glaciology, 51(54): 187-194.

Schweizer, J., Reuter, B., van Herwijnen, A. and Gaume, J., 2016a. Avalanche release 101. In: E. Greene (Editor), Proceedings ISSW 2016. International Snow Science Workshop, Breckenridge CO, U.S.A., 3-7 October 2016, pp. 1-11.

Schweizer, J., Reuter, B., van Herwijnen, A., Richter, B. and Gaume, J., 2016b. Temporal evolution of weak layer and slab properties in view of snow instability. The Cryosphere Discussion: in review.

Schweizer, J. and Wiesinger, T., 2001. Snow profile interpretation for stability evaluation. Cold Regions Science and Technology, 33(2-3): 179-188.

Shapiro, L.H., Johnson, J.B., Sturm, M. and Blaisdell, G.L., 1997. Snow mechanics - Review of the state of knowledge and applications. Report 97-3, US Army CRREL, Hanover, NH, U.S.A.

Sidler, R., 2015. A porosity-based Biot model for acoustic waves in snow. Journal of Glaciology, 61(228): 789-798.

Sidler, R., Carcione, J.M. and Holliger, K., 2010. Simulation of surface waves in porous media. Geophysical Journal International, 183(2): 820-832.

Sigrist, C., 2006. Measurement of fracture mechanical properties of snow and application to dry snow slab avalanche release. Ph.D. Thesis, ETH Zurich, Zurich, Switzerland, 139 pp.

Simioni, S., Dual, J. and Schweizer, J., 2016a. Artificial avalanche release: flat field experiments using a gas exploder. In: E. Greene (Editor), Proceedings ISSW 2016. International Snow Science Workshop, Breckenridge CO, U.S.A., 3-7 October 2016, pp. 405-409.

Simioni, S., Dual, J. and Schweizer, J., 2016b. Ground accelerations caused by an operational gas exploder. in preparation.

Simioni, S., Dual, J. and Schweizer, J., 2016c. Snowpack response to directed gas explosions on level ground. in preparation.

Simioni, S., Dual, J. and Schweizer, J., 2016d. Snowpack response to explosions caused by an operational gas exploder. in preparation.

Simioni, S., Gebhard, F., Dual, J. and Schweizer, J., 2016e. Small scale field experiments in snow to determine wave propagation principles and mechanical properties. in preparation.

Simioni, S. and Schweizer, J., 2013. Assessing weak layer failure and changes in snowpack properties due to avalanche control by explosives. In: F. Naaim-Bouvet, Y. Durand and R. Lambert (Editors), Proceedings ISSW 2013. International Snow Science Workshop, Grenoble, France, 7-11 October 2013. ANENA, IRSTEA, Météo-France, Grenoble, France, pp. 775-778.

Simioni, S., Schweizer, J. and Dual, J., 2014a. Field experiments on weak layer failure and crack propagation due to explosions. In: P. Haegeli (Editor), Proceedings ISSW 2014. International Snow Science Workshop, Banff, Alberta, Canada, 29 September - 3 October 2014, pp. 185-188.

Simioni, S., Sidler, R., Dual, J. and Schweizer, J., 2015. Field measurements of snowpack response to explosive loading. Cold Regions Science and Technology, 120: 179-190.

Simioni, S., Sidler, R., Schweizer, J. and Dual, J., 2014b. Field measurements and modeling of wave induced weak layer failure due to an explosion. In: P. Haegeli (Editor), Proceedings ISSW 2014. International Snow Science Workshop, Banff, Alberta, Canada, 29 September - 3 October 2014, pp. 722-726.

SLF (Editor), 2000. Der Lawinenwinter 1999 - Ereignisanalyse. Swiss Federal Institute for Snow and Avalanche Research, Davos, Switzerland, 588 pp.

Sommerfeld, R.A., 1982. A review of snow acoustics. Reviews of Geophysics and Space Physics, 20(1): 62-66.

St.Lawrence, W.F. and Williams, T.R., 1976. Seismic signals associated with avalanches. Journal of Glaciology, 17(77): 521-526.

Stoffel, L., Nairz, P., Kleemayer, K., Procter, E., Kogelnig, A., Urschler, R., Larghi, M. and Sauermoser, S., 2015. Artificial release and monitoring technologies for avalanches. In: F. Rudolf-Miklau, S. Sauermoser and A. Mears (Editors), The Technical Avalanche Protection Handbook. Wilhelm Ernst & Sohn, Berlin, pp. 325-361.

Stoll, R.D. and Kan, T.-K., 1981. Reflection of acoustic waves at a water-sediment interface. Journal of the Acoustical Society of America, 70(1): 149-156.

Strange, J.N., Denzel, C.W. and McLane, T.I., 1961. Cratering from high explosive charges: Analysis of crater data. Technical Report No. 2-547, Corps of Engineers - U.S. Army Engineer Waterways Experiment Station, Vicksburg MS, U.S.A.

Suriñach, E., Vilajosana, I., Kleemayer, K. and Rammer, L., 2011. Study of the wavefield generated by a gas exploder used for artificial avalanche release. Cold Regions Science and Technology, 66(1): 17-29.

Tichota, R.G., Miller, D.A., Larson, R. and Richmond, D., 2010. An experimental investigation of explosives and snowpack dynamic response, International Snow Science Workshop ISSW, Lake Tahoe CA, U.S.A., 17-22 October 2010, pp. 418.

Tschirky, F., Brabec, B. and Kern, M., 2000. Lawinenunfälle in den Schweizer Alpen - Eine statistische Zusammenstellung mit den Schwerpunkten Verschüttung, Rettungsmethoden und Rettungsgeräte. In: W. Ammann (Editor), Durch Lawinen verursachte Unfälle im Gebiet der Schweizer Alpen. Eidgenössisches Institut für Schnee- und Lawinenforschung SLF, Davos, Switzerland, pp. 125-136.

Ueland, J., 1993. Effects of explosives on the mountain snowpack, Proceedings International Snow Science Workshop, Breckenridge, Colorado, U.S.A., 4-8 October 1992. Colorado Avalanche Information Center, Denver CO, USA, pp. 205-213.

van Herwijnen, A., Bair, E.H., Birkeland, K.W., Reuter, B., Simenhois, R., Jamieson, B. and Schweizer, J., 2016a. Measuring the mechanical properties of snow relevant for dry-snow slab avalanche

release using particle tracking velocimetry. In: E. Greene (Editor), Proceedings ISSW 2016. International Snow Science Workshop, Breckenridge CO, U.S.A., 3-7 October 2016, pp. 397-404.

van Herwijnen, A. and Birkeland, K.W., 2014. Measurements of snow slab displacement in Extended Column Tests and comparison with Propagation Saw Tests. Cold Regions Science and Technology, 97: 97-103.

van Herwijnen, A., Gaume, J., Bair, E.H., Reuter, B., Birkeland, K.W. and Schweizer, J., 2016b. Estimating the effective elastic modulus and specific fracture energy of snowpack layers from field experiments. Journal of Glaciology, 62(236): 997-1007.

van Herwijnen, A., Heck, M. and Schweizer, J., 2016c. Forecasting snow avalanches by using avalanche activity data obtained through seismic monitoring. Cold Regions Science and Technology, 132: 68-80.

van Herwijnen, A. and Jamieson, B., 2005. High-speed photography of fractures in weak snowpack layers. Cold Regions Science and Technology, 43(1-2): 71-82.

van Herwijnen, A. and Jamieson, J.B., 2007. Snowpack properties associated with fracture initiation and propagation resulting in skier-triggered dry snow slab avalanches. Cold Regions Science and Technology, 50(1-3): 13-22.

van Herwijnen, A. and Schweizer, J., 2011. Seismic sensor array for monitoring an avalanche start zone: design, deployment and preliminary results. Journal of Glaciology, 57(202): 267-276.

van Herwijnen, A., Schweizer, J. and Heierli, J., 2010. Measurement of the deformation field associated with fracture propagation in weak snowpack layers. Journal of Geophysical Research, 115: F03042, doi:10.1029/2009JF001515.

Vollmann, J. and Dual, J., 2012. Wave propagation in elastic solids. ETH Zürich, Unpublished, pp. 100.

Wilhelm, C., Wiesinger, T., Bründl, M. and Ammann, W.J., 2001. The avalanche winter 1999 in Switzerland - an overview, Proceedings International Snow Science Workshop, Big Sky, Montana, U.S.A., 1-6 October 2000. Montana State University, Bozeman MT, USA, pp. 487-494.

Withers, M., Aster, R., Young, C., Beiriger, J., Harris, M., Moore, S. and Trujillo, J., 1998. A comparison of select trigger algorithms for automated global seismic phase and event detection. Bulletin of the Seismological Society of America, 88(1): 95-106.

Wooldridge, R.E., Hendrikx, J., Miller, D.A. and Birkeland, K., 2012. The effect of explosives on the physical properties of snow, Proceedings ISSW 2012. International Snow Science Workshop, Anchorage AK, U.S.A., 16-21 September 2012, pp. 1033-1039.

Acknowledgments

During my PhD studies at the WSL Insitute for Snow and Avalanche Research in Davos I had a great time and learnt a lot. This experience would not have been possible without the help and support of many. It is my pleasure to express my gratitude:

I owe my deepest gratitude to my supervisor Dr. Jürg Schweizer for taking time for me and my work. I am thankful for many discussions and helpful input over the last years as well as a very kind personal relationship. It is with immense gratitude that I acknowledge the support of my Professor Jürg Dual for accepting me as a PhD student, for fruitful discussions and valuable input. Prof. Dual impressed me at any occasion with his knowledge, experience and his ability to deduct new insight within shortest time. I thank Prof. Patrick Jenny for serving on my PhD committee.

I would like to thank Prof. Dan Miller for his input especially in the beginning of this thesis. My thanks go to Rolf Sidler for the modelling work and to Prof. Vilem Petr for his ideas.

I would like to show my gratitude to the Swiss Army and the Armed Forces Logistics Organisation. In particular, my thanks go to Jürg Preisig and his team from the firing range in Hinterrhein for the permission to perform the experiments. Big thanks go to Johannes Aliesch, Peter Furger and team for their logistical support during the experiments in Hinterrhein. Thanks to Jakob Bosshard for driving the mobile crane. I would like to thank Francesco Piffaretti and Hans-Rudolf Gisler from the Territorialregion 3 for leaving no stone unturned to provide a suitable crane. My thanks go to Nicolas Roduit and his soldiers Ciaran Parks and Marius Gächter for organizing and performing the crane mission.

I thank André Zahnd and his team from Spiez Laboratory for lending us their measuring equipment.

My thanks go to Jürg Ritter and Peter Daetwyler for the support regarding handling and storing of explosives.

I would like to thank Arthur Jenal and Serafin Siegele and their teams from Samnaun and Ischgl cablecars for their support.

I thank Michael Frei and Jürg Ambühl from Davos Klosters Mountains for their support. My sincere thanks go to Vali Meier and his team from the rescue service at the Jakobshorn in Davos. Vali Meier supported our work in any possible way which was extremely valuable.

Big thanks go to Martin Hiller and his apprentices from the institute's electronics department for the development and the production of the measuring equipment. Thanks to Andi Tröger,

Christian Simeon, Silvio Burger and their apprentices for the tedious production of the accelerometers and other measuring equipment in the mechanical workshop. I thank Marco Collet for the design of the foam cylinder and further support. Thanks to Martin Gentner for his support with the explosives warehouse.

I thank the advisory board comprised of Thomas Rentsch, Pius Henzen, Clo Gregori, Peder Caviezel, Romano Meier, Romano Pajarola and Reto Baumann from the Federal Office for the Environment for their valuable input and for supporting this project.

Big thanks go to the manufacturers of the fixed avalanche control installations for providing the systems and operating supplies: David Poulet, Vincent Hélary, Ernesto Bassetti and their team from TAS; Sam Wyssen and his team from wyssen avalanche control; Jürg Knobel and his team from Inauen-Schätti.

I very much enjoyed the work and spare time with my colleagues at SLF: Thank you Lino Schmid for the good times, your Matlab support and the adverse weather conditions during all field work, Matthias Heck for field work assistance and the best bike runs, Fabiano Monti for your warm welcome every morning. I thank Ben Reuter, Achille Capelli, Bettina Richter, Alec van Herwijnen, Stephan Harvey, Stephanie Mayer, Rouven Stourny, Oliver Pelzer, Franziska Zahner, Johan Gaume, Christoph Mitterer, Basti Gerling, Fabian Vogler, Thomas Thüring, Severin Olloz: Besides your friendship, your support in the office and the field were crucial to complete this work. I would also like to thank Martin Proksch and Jürg Trachsel from outside my team and all the others at SLF that supported me in any way.

During my time in Davos I maintained good contact with my friends from Winterthur and would like to thank them for their friendship. In particular thank you Leo for countless “huhu” and all our on- and off-topic discussions.

I most sincerely thank my family who supports me in everything I have done, do and will do.

My biggest thanks go to my wife Katrin and my son Mio. I am really lucky to have you!